UNIVERSITY OF ALBERTA

PROTON INDUCED NUCLEAR PION PRODUCTION AT
INTERMEDIATE ENERGIES

BY

MUNASINGHE ARACHCHIGE PUNYASENA ©
B. Sc. (Hons), University of Kelaniya, Sri Lank. (1990)
M. Sc. University of Alberta, Edmonton, Canada (1993)

A thesis
submitted to the Faculty of Graduate Studies and Research
in partial fulfillment of the requirements for the degree of

DOCTOR OF PHILOSOPHY

DEPARTMENT OF PHYSICS

EDMONTON, ALBERTA

FALL 1996

The author has granted an irrevocable non-exclusive licence allowing the National Library of Canada to reproduce, loan, distribute or sell copies of his/her thesis by any means and in any form or format, making this thesis available to interested persons.

L'auteur a accordé une licence irrévocable et non exclusive permettant à la Bibliothèque nationale du Canada de reproduire, prêter, distribuer ou vendre des copies de sa thèse de quelque manière et sous quelque forme que ce soit pour mettre des exemplaires de cette thèse à la disposition des personnes intéressées.

The author retains ownership of the copyright in his/her thesis. Neither the thesis nor substantial extracts from it may be printed or otherwise reproduced without his/her permission.

L'auteur conserve la propriété du droit d'auteur qui protège sa thèse. Ni la thèse ni des extraits substantiels de celle-ci ne doivent être imprimés ou autrement reproduits sans son autorisation.
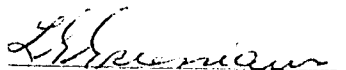
ISBN   0-612-18095-6

Canada

UNIVERSITY OF ALBERTA
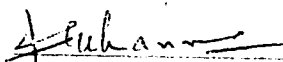
FACULTY OF GRADUATE STUDIES AND RESEARCH

The undersigned certify that they have read, and recommend to the Faculty of Graduate Studies and Research for acceptance, a thesis entitled **PROTON INDUCED NUCLEAR PION PRODUCTION AT INTERMEDIATE ENERGIES** submitted by Munasinghe Arachchige Punyasena in partial fulfillment of the requirements for the degree of DOCTOR OF PHILOSOPHY.
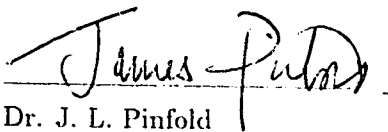
Dr. William. C. Olsen (Supervisor)
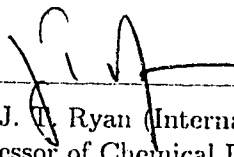Professor of Physics
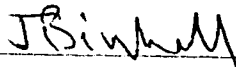
Dr. L. G. Greeniaus (Co-Supervisor)
Professor of Physics

Dr. F. C. Khanna (Committee Chairman)
Professor of Physics

Dr. J. L. Pinfold
Professor of Physics

Dr. J. Ryan (Internal-External Examiner)
Professor of Chemical Engineering
University of Alberta

Dr. J. Birchall (External-External Examiner)
Professor of Physics
University of Manitoba, Canada

Date : Aug. 7 1996

UNIVERSITY OF ALBERTA

Library Release Form

NAME OF THE AUTHOR : Munasinghe Arachchige Punyasena

TITLE OF THE THESIS : *Proton Induced Nuclear Pion Production at Intermediate Energies*

DEGREE : Doctor of Philosophy

YEAR THIS DEGREE GRANTED : 1996

Permission is hereby granted to the University of Alberta Library to reproduce single copies of this thesis and to lend or sell such copies for private, scholary or scientific research purposes only.

The author reserves all other publication and other rights in association with the copyright in the thesis, and except as hereinbefore provided neither the thesis nor any substantial portion thereof may be printed or otherwise reproduced in any material from whatever without the author's prior written permission.

H. A. Punyasena

Department of Physics,
University of Kelaniya,
Kelaniya,
Sri Lanka.

Date : 12th August, 1996

This Thesis is Dedicated
to My Beloved Late Parents

ABSTRACT

Proton-induced nuclear pion production $[A(p, \pi^{\pm})A+1]$ is not a very well understood branch of nuclear physics. Initially the variety of differential cross section distributions held out the promise that exclusive pion production could be used as a tool to understand nuclear phenomenon. Topics such as inter-nucleon interactions, pion interactions in the nuclear medium, and Δ-nuclear interactions were all quoted as possible aspects of the nuclear field which could be revealed by the (p, π) probe. It was also pointed out that due to the high momentum transfer involved in this reaction, these studies would be sensitive to high-momentum components of the nuclear wave function and to short-range correlations between nucleons in nuclei. All these attributes of the (p, π) reaction were shown to be unfounded as theoretical studies were unable to reproduce the experimental data. Hence the goal of most (p, π) studies since the initial experiments has been to look for signatures of the reaction mechanism.

The goal of this experiment is no different from those of the recent past, that is, to look for signatures of the reaction mechanism in nuclear pion production. Recent work has shown that the $NN \rightarrow NN\pi$ can be considered as the primary reaction mechanism due to the many signatures that can be found in the experimental data for this reaction. This work extends the investigation of these signatures into the 220 to 400 MeV beam energy region for nuclei which have not previously been studied thoroughly. In addition previous works have been limited to 1p-shell nuclei (i.e., A < 16), however in this work it will be shown that (p, π) on heavier nuclei, at least for the ^{40}Ca nucleus, also displays $NN \rightarrow NN\pi$ signatures in the experimental data.

TRIUMF's newly commissioned Second Arm Spectrometer (SASP) system comprises a quadrupole-quadrupole-dipole magnet combination which is associated with multi-wire drift chambers and scintillator paddle detectors. The SASP was used for this study on proton induced nuclear pion production on p- and d- shell light nuclei at intermediate energies (200-400 MeV). Both the differential cross section and the analyzing power angular distributions have been determined with polarized protons for the reactions $^{12}C(p, \pi^{+})^{13}C$,

$(p, \pi^-)^{13}$ and $Ca(p, \pi^+)^{41}Ca$ at 250 and 280 MeV. The (p, π^-) reaction on ^{13}C has been measured at three beam energies (221, 280, and 350 MeV) with polarized protons. The cross section and analyzing power angular distributions have been measured for both the exclusive final states and the continuum region in each reaction.

The $NN \to NN\pi$ signatures which were studied are the analyzing power angular shapes for the continua, the discrete final states of the mirror nuclei, ^{14}C and ^{14}O, the analyzing power angular distributions for the high-spin, two-particle one-hole (2p1h) stretched states and the energy dependence of the (p, π^-) reaction as compared to the (p, π^+) reaction. These results show that the $(p, \pi^\pm)$ reaction on nuclei can be viewed as a $NN \to NN\pi$ process occurring within the nuclear medium.

It is noted that the (p, π) reaction, due to its high-momentum transfer to the residual nucleus, preferably excites high-spin 2p1h stretched states. Hence the (p, π) reaction can be used as a quasi-spectrographic tool as the dominant peaks in the (p, π) spectrum can be associated with the highest J^π configurations that can be reached from the ground state configuration. Several J^π assignments are made on this basis, notably for peaks seen in the ^{41}Ca spectrum.

ACKNOWLEDGEMENTS

Contents

List of Tables

List of Figures

Chapter 1

Introduction

The atomic nucleus is a bound system of interacting protons and neutrons. The strong inter-nucleon interaction is known to be mediated by the exchange of mesons. The long-range part of the nucleon-nucleon (NN) interaction is mainly governed by the exchange of pions due to their low mass of 140 MeV, while the exchange of heavier mesons (ρ, ω,...., etc.) dominate the short-range part. The NN interaction, which is the basic ingredient for any microscopic calculation of nuclear reactions, must be well understood to discuss the physics of the nucleus.

Experiments related to the scattering of particles from nuclei have been performed for many years to investigate the NN interaction and nuclear structure. Theoretical calculations and the accumulated data still do not provide precise explanations for many aspects of this complicated system—the nucleus. Low-energy proton and neutron beams were utilized in the early scattering experiments, but afterwards, with the availability of modern particle accelerators, similar studies became possible at higher energies. Also, the meson factories [e.g. LAMPF in USA and TRIUMF in Canada, SIN in Switzerland] supplied meson beams to enhance the scope of the scattering studies, opening a new era, permitting the experiments to be done with lighter particles. After the development of high-resolution meson spectrometers, it became possible to study reactions in which pions are produced in the final state.

Proton-induced pion production reactions, $A(p,\pi)A+1$, are very useful because they provide a unique probe to aid in the understanding of pion interactions in the nucleus. Extensive effort, both experimentally and theoretically, has been devoted to establish the systematics of the (p,π) reaction. The main goal of these studies is to extract new information about the reaction mechanisms and related nuclear structure.

The experimental studies of pion production have been done using the (p, π^+) and (p, π^-) reactions. The charged pions are easily detected in modern pion detectors. The (p, π^0) reaction has not been studied as extensively due to the difficulty of neutral pion detection. The (p, π^+) reaction cross section is roughly an order of magnitude higher, and has more pronounced features, than for (p, π^-). Hence most of the pion production investigations until the early 1980's were limited to the studies of the (p, π^+) reaction. A fairly large body of (p, π^+) data is now available over a wide energy range and on many nuclear targets. Due to its small cross section and nearly featureless angular distribution, the (p, π^-) reaction did not originally arouse the interest of early experimentalists.

The microscopic model calculations developed thus far for $A(p, \pi)A+1$ reactions consider mesonic and isobaric degrees of freedom and have been able to account qualitatively for only a small fraction of the data. One requires a thorough understanding of the underlying reaction mechanism, the resonant channels if there are any, and the nuclear structure effects of the process. In particular, the reaction involves high momentum transfer ($q \sim 450 - 700$ MeV/c near threshold) to the residual nucleus. In principle, (p, π) reactions probe nuclear wave functions at momenta well in excess of the Fermi momenta of the individual nucleons, and might therefore be used to investigate states or components of states not easily accessible in other reactions. However, because of this large momentum transfer, the theoretical treatment is complicated and the reaction mechanism is not well understood. Hence, nuclear pion production still remains one of the less understood topics in intermediate-energy nuclear physics. An experimental study involving both the (p, π^+) and the (p, π^-) reactions at intermediate energy will address some of the yet-unanswered questions, leading us towards a better understanding of the process.

The current $A(p, \pi)A+1$ data show that the reaction seems to involve only two active nucleons in the initial state, while the rest of the nucleus acts as a spectator. The final state consists of these two nucleons bound in well-defined orbitals of the residual nucleus, and the emitted pion. This quasi-free process ($NN \to NN\pi$) is known as the two-nucleon mechanism (TNM). If the TNM is assumed to be the dominant process, only a single channel ($pn \to pp\pi^-$) contributes to the (p, π^-) reaction, while (p, π^+) can go through the $pp \to pn\pi^+$ and $pn \to nn\pi^+$ processes. The struck target neutron in the (p, π^-) reaction must be changed into a proton, and therefore the residual nucleus will be left preferentially in a 2p1h state. In the (p, π^+) reaction, the holes produced in the final state can be filled by the incident proton, thus limiting the selective 2p1h high-spin states (see section 2.2.1). This advantage of the (p, π^-) reaction compared to (p, π^+) stimulated much interest in studying the production of negative pions.

The commissioning of a high-resolution pion spectrometer at the Indiana University Cyclotron Facility (IUCF) paved the way for several $(p, \pi^{\pm})$ studies. These showed that negative pion production in proton-nucleus collisions at intermediate energies could be used as a more powerful probe than (p, π^{+}) to understand the underlying reaction mechanism and the nuclear structure. However, the maximum proton beam energy available at IUCF is only 206 MeV, which limited the studies to low energy pions. In order to obtain a deeper insight into the (p, π^{-}) process, it is essential to study it over a larger energy range. TRIUMF, with an energy range (200-500 MeV), together with the newly constructed Second Arm Spectrometer (SASP), constitute an ideal facility for a comprehensive $(p, \pi^{\pm})$ experimental survey.

These circumstances led us to carry out the present experimental program at TRIUMF where a complete study of the $(p, \pi^{\pm})$ reaction on light nuclei is attempted. We have made $(p, \pi^{\pm})$ exclusive cross section and analyzing power measurements over most of the angular range available for SASP $(25° - 135°)$. The incident bombarding protons were taken in the form of a vertically-dispersed and polarized beam to the nuclear target. The (p, π^{+}) data were taken at two bombarding energies (250 and 280 MeV) on two different p-shell nuclei (^{12}C and ^{13}C) and a d-shell nucleus (^{40}Ca), while the (p, π^{-}) measurements were made using ^{13}C at three energies (221, 280, and 350 MeV).

The Δ-isobar resonance in the intermediate state of the (p, π) reaction is expected to be dominant in this selected energy range. The kinematically-transformed cross section and analyzing power data of $(p, \pi^{\pm})$ from nuclei compared to results for free two-nucleon case would reveal any similarity of the nuclear pion production reaction with the quasi-free cases ($pp \rightarrow d\pi^{+}$ and $pn \rightarrow pp\pi^{-}$), providing solid information on the reaction mechanism of the process. Mapping of the energy dependence of the $(p, \pi^{\pm})$ cross section and analyzing power angular distributions in the Δ-isobar region would test current (p, π) microscopic model calculations, and provide critical constraints on their physics input.

A general discussion of the (p, π) reaction is given in Chapter 2 where the past and the present status of the subject is briefly reviewed. Chapter 3 gives a brief review of the theoretical description of the reaction mechanism in the pion production process, and the relevant expressions for the experimental observables such as its reaction cross sections and analyzing powers for the transitions. Chapter 4 provides a detailed description of the present experiment. Methods of data analysis and results extraction are explained in Chapter 5, while the final results of the experiment are displayed in Chapter 6. The physics interpretation of these results is given in Chapter 7. Chapter 8 discusses the conclusions of this experimental project.

3

Chapter 2

Pion Production

Pions are the lightest members of the meson family. All other mesons have masses greater than twice the pion mass. Pions are spin-zero particles with negative intrinsic parity, isospin 1, and appear in the three charge states +1, 0, and −1, denoted by π^+, π^0, and π^-. One or several pions can be produced in a collision when a projectile proton with sufficiently high kinetic energy hits a target nucleus. A single pion in the final state is the simplest case of the pion production reaction. Pions are detected using a pion spectrometer to extract information about the nuclear reaction $A(p,\pi)A+1$. This reaction mechanism seems to be dominated by a basic elementary collision between two nucleons. Therefore, some features of the pion production in nucleon-nucleon collisions are discussed next.

2.1 Pion Production in Nucleon-Nucleon Collisions

The threshold energy for the production of a single pion in a nucleon-nucleon collision is about 280 MeV in the laboratory. The two-pion production threshold is approximately 600 MeV, however the cross section is too small for useful measurements below energies of about 1 GeV. At higher proton energies, it is possible to produce heavy mesons which then decay into pions. At 4.6 GeV, for example, production of up to five pions was observed [Al67]. The intrinsic spin of the pion was determined to be zero in early (p,π) studies where cross sections of the reactions $pp \to d\pi^+$ and $\pi^+d \to pp$ were compared by using detailed balance to determine $(2S_\pi + 1)$ [Du51]. The negative intrinsic parity of the pion was established by observing the reaction $\pi^-d \to nn$ for pions captured from an atomic s-state [Pa51]. The 2:1 cross section ratio predicted by isospin invariance was confirmed for the two reactions, $pd \to {}^3H\pi^+$ and $pd \to {}^3He\ \pi^0$ [Ha60].

4

Table 2.1: Isospin decomposition for the total cross-sections of the proton-induced single pion production.

Reaction		Isospin Decomposition
$pp \to d\pi^+$	:	$\sigma_{10}(d)$
$pp \to pn\pi^+$	:	$\sigma_{10}(np) + \sigma_{11}$
$pn \to nn\pi^+$	:	$\frac{1}{2}[\sigma_{11} + \sigma_{01}]$
$pn \to pp\pi^-$	:	$\frac{1}{2}[\sigma_{11} + \sigma_{01}]$
$pp \to pp\pi^0$	:	σ_{11}
$pn \to d\pi^0$	:	$\frac{1}{2}\sigma_{10}(d)$
$pn \to pn\pi^0$	:	$\frac{1}{2}[\sigma_{10}(pn) + \sigma_{01}]$

Since pion production takes place through the strong interaction, which is invariant under isospin symmetry, it is useful to classify the various pion production channels using isospin symmetry. Isospin invariance of the strong interaction requires that the total isospin of the initial state be the same as that of the final state. The total isospin (T) of the initial nucleon pair is either 0 or 1. Since the final state consists of a pion which has isospin 1, the total isospin (T') of the final state nucleon pair can also be either 0 or 1, as allowed by isospin invariance. The relevant pion production channels in nucleon-nucleon collisions are given in Table 2.1 with the isospin decomposition of the total cross sections ($\sigma_{TT'}$) for each channel. Here, $\sigma_{TT'}(d)$ and $\sigma_{TT'}(np)$ denote the cross sections in which the final state contains the deuteron and the unbound proton-neutron pair, respectively.

In addition to the reaction channels given in Table 2.1, the other possible channels are $nn \to nn\pi^0$ and $nn \to np\pi^-$ in which both the initial interacting nucleons are neutrons. These two channels are not included in the above isospin decomposition table because they are not relevant for (p, π) studies. It is seen from Table 2.1 that all seven reaction channels can be described using only three cross sections, namely σ_{10}, σ_{11}, and σ_{01}. We also see that the cross section for deuteron production in the proton-neutron reaction is half that for the proton-proton reaction. Phase shift analyses of free $NN \to NN\pi$ data [Ar96] reveal that σ_{10} is substantially larger than σ_{11}, which in turn is much larger than σ_{01}. Consequently, the cross section for $pp \to (np)_{T'=0} \pi^+$ is large compared to those for $pn \to nn\pi^+$ and $pn \to pp\pi^-$.

It is widely believed that the (p, π) reaction goes through an intermediate state involving a Δ-isobar ($j^\pi = \frac{3}{2}^+$, $T = \frac{3}{2}$) which then decays to a nucleon and a pion to form

the final state: i.e., $N + N \to N + \Delta \to N + N + \pi$. Since the nucleon has $T = \frac{1}{2}$, the total isospin of the intermediate state is 1 or 2. Therefore, in this mechanism, isospin invariance requires that the initial state must be $T = 1$, predicting that the σ_{01} cross section is zero. The largest cross section near threshold is $\sigma_{10}(d)$. This implies that the low-energy (p, π^+) reaction goes mostly via $pp \to d\pi^+$.

2.2 $A(p, \pi)A+1$ Reaction

The (p, π) reaction on nuclei is a useful tool for learning about nuclear structure and pion-nuclear interactions. One of the interacting nucleons is inside the nucleus so that the collision is more complex than the free nucleon-nucleon case. The wavelength of the incident proton at energies above the pion production threshold is shorter than the average distance between the nucleons in the nucleus. For example, the inter-nucleon distance is 1.9 fm whereas the wavelength (λ) of a 500 MeV proton is 0.19 fm so that the pion production in nucleon-nucleus collision is normally the result of a single nucleon-nucleon collision within the nuclear medium. The nucleon inside the target nucleus also has Fermi momentum, so pion production can take place at a lower incident proton energy than that required in a free nucleon-nucleon collision. Multiple interactions can occur in the many-nucleon environment, and shadowing effects can reduce the effective number of nucleons for the process. The identity of a particle may easily change in the nuclear medium in some transitions of the process (a proton can charge exchange to become a neutron or a π^+ into a π^-, etc.). An emitted pion may quickly be absorbed by a nucleon pair because its mean free path is smaller than the size of the nucleus.

The first exclusive measurements of the $A(p, \pi^+)A+1$ reaction were reported in the pioneering studies of nuclear pion production at Uppsala [Da71] with an incident beam energy of 185 MeV. In these studies, the differential cross sections for proton capture to the ground and excited states were measured for the reactions $^{12}C(p, \pi^+)^{13}C$ and $^{9}Be(p, \pi^+)^{10}Be$. Further studies [Au78, Ja82, Vi82, Fa85, Ko89] were later undertaken with more sophisticated facilities at other laboratories including IUCF, LAMPF, and TRIUMF. These experiments detected the pions using magnetic spectrometers with a typical resolution of about 200 keV, good enough to distinguish different excited states in the residual nucleus. Several reviews of the early studies on (p, π) reaction are found in the literature [Fe81, Be82].

Theoretical calculations of the (p, π) reaction have been done mainly using two microscopic models [Iq85, Al88, Ku89]. The first model assumes that the incident proton

is stopped by the target nucleus by capturing it into a certain orbital. The decelerating incoming nucleon emits a pion in the same way that an accelerated charge radiates photons. In this case, most of the momentum transfer is taken up by the bound nucleon. This process in which the pion is produced directly from the projectile in a stripping- or bremsstrahlung-like reaction is called the one-nucleon mechanism (ONM) because there is only one active nucleon treated explicitly in the process. The other microscopic model assumes that the pion is produced in a collision between the incident proton and a nucleon in the target nucleus. During the collision, one of the nucleons may go to an intermediate isobaric excited state. This process is known as the two-nucleon mechanism (TNM) because there are two active nucleons participating in the reaction process. The residual nucleus in ONM is left in an excited state with a one-particle (1p) configuration compared to the ground state of the target nucleus. Two-particle one-hole (2p1h) configurations can be excited in general through TNM.

The incoming proton and the outgoing pion interact with the nucleus before and after the pion production process. These interactions are taken into account by using distorted waves for the proton and the pion irrespective of the basic ONM or TNM elementary process. These two processes are illustrated diagrammatically in Fig. 2.1, where (a) shows a stripping- or bremsstrahlung-like process (ONM) and (b) shows a process producing a pion in a collision between the incident proton and a target nucleon (TNM). When more data became available, it was realized that the TNM could explain many more features of the reaction mechanism than the ONM as discussed below.

The (p, π^+) reaction was studied at TRIUMF using incident polarized protons [Au78] to measure the cross section and analyzing power angular distributions at 200 MeV bombarding energy for ^{12}C and ^9Be, the same nuclei used at Uppsala. The sign and angular dependence of the analyzing power data were found to be similar to the corresponding data for the $pp \rightarrow d\pi^+$ reaction [Jo77]. Thus, the analyzing power in the nuclear pion production reaction appeared to reflect the basic $NN \rightarrow NN\pi$ process, supporting the TNM model rather than the ONM model.

Several (p, π^-) studies at IUCF [Vi82, Ja82] with 200 MeV protons also confirmed that the reaction was dominated by the two-nucleon mechanism. These included the measurements of broad-range momentum spectra for (p, π^-) reactions on a number of target nuclei with $13 \leq A \leq 92$ which showed a striking and systematic selectivity for one or a few low-lying discrete states in the residual nuclei. The same group observed the possible signatures of the two-nucleon pion production processes in $A(p, \pi^-)A+1$ reactions near threshold. Measurements of cross section and analyzing power angular distributions

(a) One nucleon mechanism (ONM):
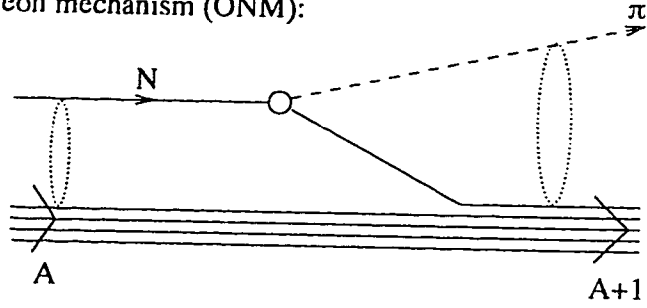
(b) Two nucleon mechanism (TNM):
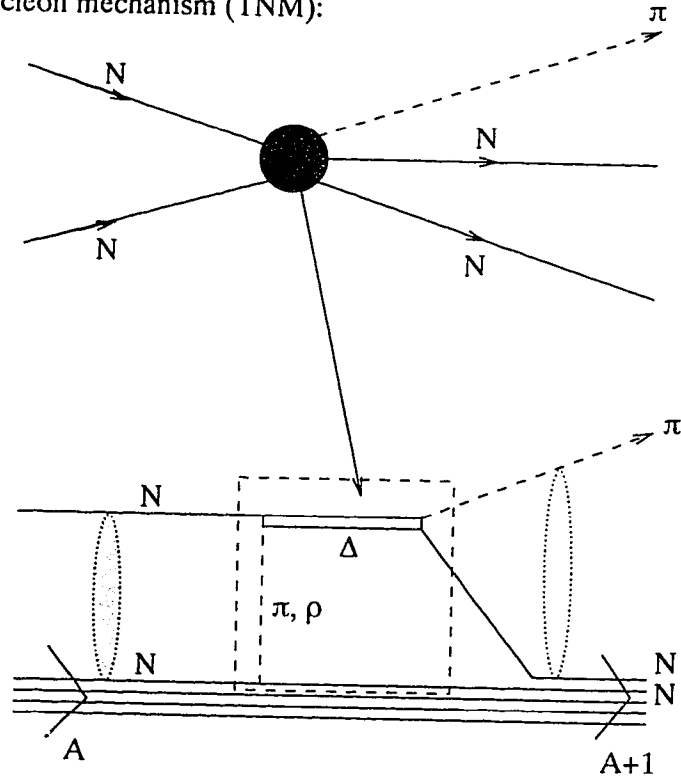
Figure 2.1: Two mechanisms to describe the nuclear pion production reaction. (a) A stripping- or bremsstrahlung-like process, in which the pion is produced directly from the projectile nucleon (ONM), and (b) a process in which the pion is produced in a collision between the incident nucleon and a target nucleon (TNM).

for $^{12,13}C(p,\pi^-)^{13,14}O$ reactions [Ko89] exhibit the above features, supporting the view that the fundamental $NN \to NN\pi$ process dominates in nuclear pion production.

The relative strengths of the final state transitions in (p,π^-) reactions on $1f_{\frac{7}{2}}$-neutron sub-shell nuclei were predicted by theoretical calculations [Br83] in which a plane wave, zero-range reaction model combining 2-proton stripping with 1-neutron pickup processes (the basic ingredients of the $NN \to NN\pi$ process) was used. The results of these calculations for the low-lying discrete states showed qualitative agreement with the experimental data [Th87, Sc86], and many detailed aspects of the spectra could be understood for the first time, thus providing evidence to support the two-nucleon mechanism. Several new microscopic calculations of the (p,π) reaction based on the TNM which explicitly include some of the higher-order processes have been reported [Iq85, Al88, Ku89].

Iqbal and Walker [Iq85] have performed calculations using only the dominant TNM amplitudes. The model includes the initial-state NN interaction via the exchange of virtual pions and ρ-mesons, which proceeds through the Δ-isobar excitation in the nuclear medium, and decay to the emitted real pion and the bound nucleon in the final state. The model applied by Alons et al. [Al88] incorporates both the pions and the ρ-mesons as the intermediate exchange particles. The Δ-nucleus interaction is included in the Δ propagator. This also has the flexibility of including both the ONM and the TNM amplitudes in the calculation. Kume [Ku89] has performed (p,π^-) calculations within the two-nucleon production model assuming 2p1h amplitudes. This study has shown that the two-body process with the final protons coupled to a spin singlet state, $pn \to (pp)^{S=0}\pi^-$, dominates the reaction cross section and that the analyzing power in spin singlet channel $(S=0)$ takes a large positive value, which is mainly due to the pion distortion effect. Although the contribution to the reaction cross section from the spin-triplet channel $(S=1)$ is about an order of magnitude smaller than that of the spin-singlet channel, the spin-triplet contribution to the analyzing power is appreciable due to the interference with the spin-singlet contribution [Ku89]. These model calculations differ from each other mainly by which interaction diagrams they include. Hence, the area of application in each case is very selective. Each of these models has had a certain measure of success within their limited areas of applications. However, none has been able to produce quantitative agreement with the large body of available data.

The discrepancy between the microscopic model calculations and the data is partly due to the great sensitivity of the (p,π) reaction to both the reaction mechanism and nuclear structure. Therefore, an explicit treatment of the microscopic nature of the reaction dynamics should involve at least mesonic and isobaric degrees of freedom to achieve quan-

titative agreement between the theoretical predictions and the experimental results. Some qualitative agreement can be found in the studies using polarized protons near threshold [Ja82, Vi82, Br83, Sc86], where the TNM is able to explain the pronounced selectivity observed for discrete high-spin, two-particle one-hole (2p1h) states [Ja82, Vi82], the shape and target dependence of the continuum [Br83], and even some cross section and analyzing power features for selected weak transitions [Ja82].

Using 200 MeV incident protons, the isospin-dependence of the $NN \to NN\pi$ processes inside nuclei was investigated by comparing cross sections and analyzing powers for the $^{13}C(p, \pi^{\pm})$ continuum production to those for corresponding processes in the free case [Ko89]. These results favor the dominance of a quasi-free, two-nucleon mechanism in nuclear pion production. The comparison of $^{13}C(p, \pi^{\pm})$ cross section and analyzing-power angular distributions also confirms the dominance of the two-nucleon mechanism. The same authors also have seen, for the first time, the isolated anomalous features exhibited by strong $^{12,13}C(p, \pi^{+})$ transitions to two highly-excited discrete states in ^{13}C and ^{14}C at 21.4 and 23.3 MeV excitations, respectively.

Similar studies [Hu88] at and above the Δ-resonance region also gave strong indications of the quasi-free nature of the (p, π) reaction inside nuclei. This quasi-free nature is particularly evident in the case of the (p, π^{+}) reaction. Here the relative strengths of the discrete final states, the energy dependence of the cross section, and some features of the analyzing power behavior are in qualitative agreement with expectations based on the dominance of a quasi-free $pp \to d\pi^{+}$ process. The $pp \to d\pi^{+}$ observations at 450 MeV bombarding energies [Jo84], and $pp \to np\pi^{+}$ data [Fa85] typically show a large, negative analyzing power behavior over most of the angle range, with relatively little difference between the two-body and three-body final states. At present, there is not as much data available for the (p, π^{-}) reaction so that similar conclusions for this reaction are somewhat speculative.

2.2.1 Comparison of (p, π^{-}) and (p, π^{+})

As stated in the previous section, only one two-nucleon process $(pn \to pp\pi^{-})$ involving the interaction between the projectile proton and a target neutron can contribute to the (p, π^{-}) reaction, whereas the (p, π^{+}) reaction can proceed via a one-nucleon mechanism (ONM) as well as the two-nucleon mechanism (TNM). The (p, π^{-}) reaction has another striking difference compared to (p, π^{+}). Both final state nucleons have an isospin projection which differs from the struck target nucleon and are unable to fill the hole cre-

ated by the NN interaction. In this light, once the final 2p1h state of the (p, π^-) transition is identified, the shell model orbital of the struck neutron is uniquely determined. Despite the experimental disadvantage of its low cross section, which is significantly lower compared to (p, π^+), one can argue that the (p, π^-) reaction is potentially easier to understand than the (p, π^+) since NN processes play a dominant role [Vi82, Br83, Ko87, Ko89].

Since a process like $p \to p\pi^- (n\pi^-)$ does not exist, the one-nucleon mechanism must predict a zero cross section for the (p, π^-) reaction. This implies that the proton-induced negative pion production should involve only 2p1h final states, which in turn can be explained only by the two-nucleon mechanism. This particular nature of the reaction mechanism in (p, π^-) agrees with the observations of pronounced selectivity of the stretched 2p1h states of the final nucleus [Gr84, Th87].

According to the TNM model, the stretched 2p1h states are also expected to be excited in (p, π^+) reactions with an absolute strength roughly comparable to those observed in (p, π^-). However, there cannot be a similar pronounced selectivity of these states relative to other peaks in the (p, π^+) spectrum. Transitions with lower angular momentum transfer and less optimal momentum sharing may be of comparable strength in this case because several NN processes (as indicated in Table 2.1), involving target nucleons from a variety of orbitals, can contribute coherently to the total (p, π^+) amplitude. Since a large momentum is transferred to the residual nucleus, the high-spin 2p1h excited states are favoured in $A(p, \pi^\pm)A+1$ reactions by momentum sharing. However, transitions to these states in (p, π^+) are accessible only via a restricted set of reaction paths. The accessible reaction channels for (p, π^-) are even more restricted. For example, the incident proton is constrained to interact, for all (p, π^-) transitions, with a target neutron from a specific (high angular momentum) orbital to excite only 2p1h states in the residual nucleus. Compared to this, the contributing NN processes are inherently very restricted so that the relative strength of $A(p, \pi^-)A+1$ peaks should be more clearly dominated by momentum-matching considerations.

The observed $^{12,13,14}C(p, \pi^-)$ transitions to the ground state of $^{13,14,15}O$ show that the reaction is consistently more sensitive than (p, π^+) to details of the nuclear transitions involved [Ja82]. The analyzing-power angular distributions of the nuclear transitions in $^{13,14}C$ have opposite sign to those in ^{12}C. This phenomenon is explained in a simple TNM model ($pn \to pp\pi^-$) as a direct consequence of the difference in the struck target neutron orbitals, $p_{\frac{1}{2}}$ versus $p_{\frac{3}{2}}$ in the different target nuclei [Ja82].

The continuum region of the (p, π) spectrum, which reflects contributions from a large number of nuclear transitions, is also important because it represents an average

over many nuclear structure effects. A linear rise of the continuum with excitation energy has been observed in a number of studies where stable angular distribution shapes are found [Ko89, Th87, Hu87]. These studies further indicate that the analyzing powers (A_y) exhibit remarkably stable angular distributions which are almost completely insensitive to the excitation energy and to the target nucleus.

The $\Delta(1232)$ isobar excitation in the intermediate state of the (p, π^-) reaction is not as strong as that in the (p, π^+). The analyzing-power data for the (p, π^-) reaction on nuclei, together with the recent phase shift analysis [Pi86] of cross section data for π^- absorption on a $^1S_0$ proton pair in ^{3}He, suggest [Vi87] that the elementary two-nucleon process responsible for π^- production is dominated by the transition $pn(^3D_1, T = 0) \rightarrow pp(^1S_0)+\pi^-$, for which an intermediate $\Delta+N(T = 1, 2)$ state is forbidden by isospin conservation. Thus, one concludes that there is probably an additional dynamical suppression of (p, π^-) transitions, assuming that the two final state protons in the process $pn \rightarrow pp\pi^-$ are constrained by the short-range nature of the interaction to be in a $^1S_0$ state.

Unfortunately, a definite conclusion cannot be drawn about the underlying reaction mechanism of (p, π^-) regarding the dominant resonant channels and the corresponding analyzing-power behaviour because of the lack of sufficient data over the Δ-resonance region. The TNM model calculations developed so far assume a Δ-isobar excitation in the reaction which is peaked within the bombarding energy range of 320 - 350 MeV. However, (p, π^-) data above 200 MeV exist only for ^{7}Li with polarized incident protons, and for ^{13}C with unpolarized protons [Hu87. Hu88]. These experiments were carried out at TRIUMF with the MRS spectrometer, and were very time consuming due to the small MRS solid angle. The energy dependence of the cross section for the ^{7}Li(p, π^-) data seem to indicate an important role for the Δ resonance in some discrete transitions, while the observations of ^{13}C(p, π^-) have shown just the opposite. The observed analyzing-power angular distributions tend to be more negative as the energy increases. Because of poor statistics, this information is inadequate to draw a solid conclusion on the (p, π^-) reaction. Comprehensive $(p, \pi^\pm)$ data, especially at TRIUMF energies, should provide a quantitative understanding of the pion production mechanism, leading to a possible extraction of new information about nuclear structure. These data should simultaneously reveal the role of the Δ-isobar excitation and the effects of the nuclear medium on the underlying reaction process.

12

Chapter 3

A(p,π)A+1 Reaction Theory

It follows from the general introduction to the (p, π) reaction in the previous chapters that (p, π^-), which goes only by $pn \to pp\pi^-$ channels, can be explained only in terms of the two-nucleon mechanism (TNM). This particular model assumes that the pion is produced in a single collision between the projectile proton and a target nucleon. The process may go through an intermediate state by creating a Δ-isobar inside the nuclear medium. The isobar immediately decays to a nucleon and a pion through the strong interaction; the nucleon gets bound in a certain orbital in the nucleus, while the pion is emitted. Thus, the two-body final state consists of the residual nucleus which is left in a two-particle one-hole (2p1h) state with respect to the ground state of the target nucleus and the outgoing pion. The effects due to soft proton-nucleus and pion-nucleus interactions before and after the production process are considered in the calculation as proton- and pion-nuclear distortions. The following calculation is based on the TNM assuming a Δ-isobar intermediate state in the A(p, π)A+1 reaction.

3.1 Microscopic Input for TNM

The significant contributions to the Δ rescattering process are shown in Fig. 3.1. In the Two-Nucleon model, the pion emission process is referred to as projectile emission (PE) if the pion starts from the projectile proton and rescatters from the target nucleon, while it is called target emission (TE) if the pion starts from the target nucleon. Fig. 3.1 illustrates that the two initial nucleons interact by exchanging a pion or a ρ-meson resulting in one of the nucleons being excited into a virtual Δ-isobar intermediate state. The Δ particle immediately decays to the emitted pion and the bound nucleon in the

13

final state. The angular momentum state of the initial target nucleon is denoted by j_β, while those of the final nucleons are denoted by j'_β and j'_α. The different labelling in each case is due to the antisymmetrization of the final nuclear wave function. This figure illustrates the post pion emission where, (a) and (b) represent two projectile emission diagrams (direct and exchange), while (c) and (d) represent two target emission diagrams (direct and exchange).
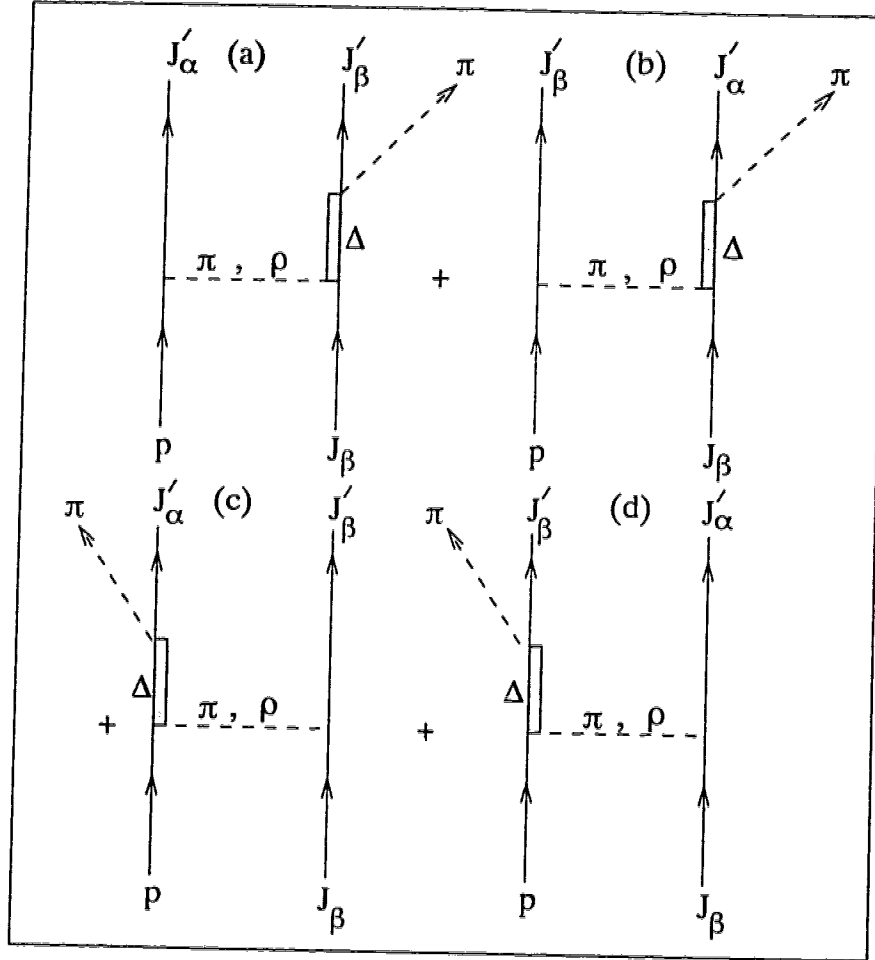
Figure 3.1: The post-emission diagrams for intermediate Δ-isobar formation in the two-nucleon mechanism: (a) and (b) show the direct and exchange projectile emission while (c) and (d) show the direct and exchange target emission, respectively.

3.1.1 πNN and $\pi N\Delta$ Interaction

The two-nucleon mechanism assumes that the $A(p, \pi)A+1$ reaction proceeds through the NN interaction (the incident proton and the target nucleon). At intermediate energies below 500 MeV, it is sufficient to consider this interaction to be mediated by π and ρ exchange. First we consider the pion exchange in the initial NN interaction for which the static form of the interaction Hamiltonian at the $NN\pi$ vertex [Al88] is written as

$$H_{\pi NN}^{int} = \frac{f_\pi(q^2)}{m_\pi}\, \sigma \cdot q\, \tau \cdot \hat{\phi} \, , \tag{3.1}$$

with $q = (q_0, q)$ representing the four-momentum of the intermediate pion and m_π its rest mass. $\hat{\phi}$ is the pion field which is a scalar in spin space and a unit vector in isospin space. The off-shell form factor at the $NN\pi$ vertex is denoted as $f_\pi(q^2)$. The σ and τ are the usual matrix representations of the operators which connect the two-component spinors in spin and isospin space, respectively.

The second vertex of the NN interaction is the $\pi N\Delta$ vertex for which the interaction can be obtained from eqn. (3.1) [We77] by substituting

$$f \to f^- \, , \qquad \sigma \to S^\dagger \, , \qquad \tau \to T^\dagger \, , \tag{3.2}$$

where $S^\dagger$ and $T^\dagger$ are the transition spin and isospin operators connecting spin-isospin $\frac{1}{2}$- and $\frac{3}{2}$- states [Su68] and are defined from

$$\langle \frac{1}{2} \parallel S \parallel \frac{3}{2} \rangle = \langle \frac{1}{2} \parallel T \parallel \frac{3}{2} \rangle = 2 \, ,$$

$$\langle \frac{3}{2} \parallel S^\dagger \parallel \frac{1}{2} \rangle = \langle \frac{3}{2} \parallel T^\dagger \parallel \frac{1}{2} \rangle = -2 \, .$$

The corresponding interaction Hamiltonian involving $\pi N\Delta$ coupling, written for the case of meson-annihilation and Δ-isobar creation is therefore,

$$H_{\pi N\Delta}^{int} = \frac{f_\pi^-(q^2)}{m_\pi}\, S^\dagger \cdot q\, T^\dagger \cdot \hat{\phi} \, , \tag{3.3}$$

where the off-shell $\pi N\Delta$ vertex form factor is denoted by $f_\pi^-(q^2)$.

3.1.2 ρNN and $\rho N\Delta$ Interaction

To include ρ exchange in the initial NN interaction, one needs to consider the ρNN vertex and the $\rho N\Delta$ vertex. The ρ is a spin-1 isospin-1 particle, hence the interaction is

not the same as in the case of one pion exchange, the pion being a pseudoscalar particle. The interaction Hamiltonian for the ρNN coupling is given by,

$$H_{\rho NN}^{int} = -\frac{f_\rho(q^2)}{m_\rho} \, \sigma \times q \, \tau \cdot \hat{\rho} \, ,$$

(3.4)

where, the ρ field is represented by $\hat{\rho}$ which is a vector both in spin space and isospin space. Now for the second vertex, the corresponding $\rho N\Delta$ interaction Hamiltonian is obtained (as for pion exchange) as

$$H_{\rho N\Delta}^{int} = -\frac{f_\rho^*(q^2)}{m_\rho} \, S^\dagger \times q \, T^\dagger \cdot \hat{\rho} \, .$$

(3.5)

3.1.3 Coupling Constants and Off-Shell Corrections

The off-shell continuation of the vertex function must be taken into account because the exchanged mesons are far off-shell in the rescattering amplitudes. However, the nucleons involved are not far from their mass-shell and their off-shell behavior is presumably accounted for through their bound state wave functions and the distorted waves for the projectile. The form factors, which are functions of the squared four-momentum of the exchanged meson only, can be used conveniently for the off-shell corrections to the vertex functions. Some theoretical basis has been given [Br83] for the use of monopole form factors, leading to the following off-shell parameterization of the coupling constants in eqns. (3.1) and (3.4):

$$f_x(q^2) = f_x(m_x^2)\frac{\Lambda_x^2 - m_x^2}{\Lambda_x^2 - q_0^2 + q^2} \, ,$$

(3.6)

where x denotes the intermediate meson (π or ρ) and $f_x(m_x^2)$ represents the on-shell value of the coupling constants ($f_{\pi NN}$, $f_{\rho NN}$, etc.). Table 3.1 shows typical values of the parameter, Λ_x, used in (p, π) calculations. Both the structure of the vertex and the off-shell correction to the exchanged meson are taken into account by the form factor. The ratio of the couplings is predicted in the simplest SU(2)×SU(2) quark model as [Ha74],

$$\frac{f_{\pi N\Delta}}{f_{\pi NN}} = \frac{f_{\rho N\Delta}}{f_{\rho NN}} = \frac{6}{5}\sqrt{2} \, .$$

(3.7)

Typical values of these coupling constants are given in the Table 3.1, which shows that the ratio of those used for the ρ meson exchange is in close agreement with the quark model predictions, while it is higher for the pion exchange.

16

Table 3.1: Typical values of the coupling constants used to calculate the form factor at each vertex by Alons *et al.*, [Al88].

x	f_{xNN}/m_x (fm)	$f_{xN\Delta}/m_x$ (fm)	Λ_x (MeV)
π	1.42	3.05	1200
ρ	2.02	3.44	1500
Δ			500

3.2 Construction of the TNM Operator

The pion-nucleon scattering amplitude is dominated by s- and p-waves at pion energies below 300 MeV, and hence by ignoring the higher partial waves, the interaction can be written as

$$H_{NN \to NN\pi}(i,j) = H_s(i,j) + \left[\; H_p^N(i,j) + H_p^\Delta(i,j) \; \right] , \qquad (3.8)$$

where the p-wave contribution is separated into a non-resonant, nucleon-dominated piece $H_p^N(i,j)$ and a resonant, Δ-isobar-dominated piece $H_p^\Delta(i,j)$ [Al88]. The TNM calculations for the (p, π^+) reaction show that the non-resonant contributions are negligible compared to the resonant contributions for incident proton energy greater than 200 MeV [Iq85]. It is assumed also that the non-resonant p-wave contributions are small. By assuming a smooth off-shell energy dependence and by taking the ratio of the squares of the off-shell and on-shell pion momenta involved, it follows from the structure of the πN amplitude that under the extreme off-shell conditions encountered in TNM, the p-wave part is enhanced by more than an order of magnitude as compared to the on-shell situation, thus greatly reducing the importance of the s-wave piece [Al88, Iq85]. These assumptions have not been supported experimentally for the (p, π^-) reaction, because of the lack of data in the Δ-resonance region.

The expressions described above are combined with propagators for the pion, ρ-meson, and Δ-isobar to obtain the TNM operator which is written in momentum space as

$$H_p^\Delta(i,j) = \frac{f_\pi^*(m_\pi^2)}{m_\pi} S_j \cdot k_\pi T_j \cdot \hat{\phi} \left\{ \; V_\pi(q_0, q) + V_\rho(q_0, q) \; \right\} D_\Delta(\omega) . \qquad (3.9)$$

17

Here the interaction potentials for the π- and ρ-mesons in momentum space are defined by

$$V_\pi(q_0, q) = \frac{f_\pi(q^2) f_\pi^*(q^2)}{m_\pi^2} \left[\; \sigma_i \cdot q S_j^\dagger \cdot q \tau_i \cdot T_j^\dagger \; \right] D_\pi(q^2) \;, \tag{3.10}$$

$$V_\rho(q_0, q) = \frac{f_\rho(q^2) f_\rho^*(q^2)}{m_\rho^2} \left[\; (\sigma_i \times q) \cdot (S_j^\dagger \times q) \tau_i \cdot T_j^\dagger \; \right] D_\rho(q^2) \;. \tag{3.11}$$

The propagators of Δ, π, and ρ are denoted by $D_\Delta(\omega)$, $D_\pi(q^2)$, and $D_\rho(q^2)$. Using standard angular momentum algebra, the operator quantities appearing in the pion interaction potential can be written as

$$\sigma_i \cdot q S_j^\dagger \cdot q = \frac{1}{3} \sum_{\lambda=0,2} C_\lambda^\pi(q) \left[Y_\lambda(\hat{q}) \times (\sigma_i \times S_j^\dagger)^\lambda \right]^{00} \;, \tag{3.12}$$

where $C_0^\pi(q) = -\sqrt{(12\pi)}q^2$, and $C_2^\pi(q) = \sqrt{(24\pi)}q^2$ for the λ values of 0 and 2, respectively. Similarly for the case of ρ exchange,

$$(\sigma_i \times q) \cdot (S_j^\dagger \times q) = \frac{1}{3} \sum_{\lambda=0,2} C_\lambda^\rho(q) [Y_\lambda(\hat{q}) \times (\sigma_i \times S_j^\dagger)^\lambda]^{00} \;, \tag{3.13}$$

where $C_0^\rho(q) = -\sqrt{(48\pi)}q^2$, and $C_2^\pi(q) = -\sqrt{(24\pi)}q^2$ for the λ values of 0 and 2, respectively. The notation "00" denotes the total angular momentum and its projection for the couplings involved. Once the transition potentials are determined, the TNM operator $H_p^\Delta(i,j)$ has to be Fourier transformed to configuration space in order to calculate the transition amplitudes. Taking the static limit of the transition potentials where the energy of the exchanged meson is ignored, i.e., at the limit of $q_0 = 0$, one can write the transition amplitude as

$$V_p^\Delta(r_i - r_j) = \int \frac{dq}{(2\pi)^3} H_p^\Delta(i,j) \exp\left[\; iq \cdot (r_i - r_j) \; \right] \;. \tag{3.14}$$

The explicit wave function for the pion produced in the final state is written as

$$(k_\pi \hat{\phi}) \to i \left(\; \nabla \chi_\pi^{(-)*}(k_\pi, r) \; \right) \hat{\phi} \;, \tag{3.15}$$

where $\chi_\pi^{(-)*}(k_\pi, r) = \chi_\pi^{(+)}(-k_\pi, r)$ is a pion distorted wave (simply $\exp(-ik_\pi \cdot r)$ in the case of plane waves). We discuss the pion distortions in the final state later under the section on distortion effects. The partial wave expansions for the plane waves appearing in the TNM operator in eqn. (3.14) are expanded as

$$\exp[iq \cdot r_i] = 4\pi \sum_{\lambda_i \mu_i} i^{\lambda_i} j_{\lambda_i}(qr_i) Y_{\lambda_i}^{\mu_i}(\hat{r}_i) Y_{\lambda_i}^{\mu_i}(\hat{q})^* \;, \tag{3.16}$$

18

$$\exp[-i\boldsymbol{q} \cdot \boldsymbol{r}_j] = 4\pi \sum_{\lambda_j \mu_j} i^{-\lambda_j} j_{\lambda_j}(qr_j) Y^{\mu_j}_{\lambda_j}(\hat{r}_j) Y^{\mu_j}_{\lambda_j}(\hat{q})^* . \tag{3.17}$$

Using standard angular momentum algebra, the explicit result for the PE contribution of the TNM operator can be obtained by using $i = 0$ and $j = 1$ in the above expressions. Similarly, the TE contribution is obtained by using $i = 1$ and $j = 0$ in the relevant expressions.

3.2.1 The Propagators

The non-static propagators for the intermediate π and ρ in the nucleon-nucleon inelastic interaction may be written as

$$D_\pi(q^2) = \frac{1}{q^2 - m_\pi^2 + i\varepsilon} = \frac{-1}{\boldsymbol{q}^2 + m_\pi^2 - q_0^2 - i\varepsilon} , \tag{3.18}$$

$$D_\rho(q^2) = \frac{1}{q^2 - m_\rho^2 + i\varepsilon} = \frac{-1}{\boldsymbol{q}^2 + m_\rho^2 - q_0^2 - i\varepsilon} , \tag{3.19}$$

where $q_r^2 = q_0^2 - \boldsymbol{q}^2$ is the four-momentum squared of the exchanged x-meson. q_0 is the energy of the exchanged meson which is put to zero at the static limit. Assuming a local effective Δ-nucleus interaction, $V_{\Delta A}(r)$, in the many-nucleon environment one can obtain the Δ propagator in configuration space by solving the following differential equation [Iq85]:

$$\left\{ M_N + \omega - M_\Delta + (i/2)\Gamma_\Delta(E_\Delta) - T_\Delta - V_{\Delta A}(r) \right\} G_\Delta(r, r'; \omega) = \delta(\boldsymbol{r} - \boldsymbol{r}') . \tag{3.20}$$

Here $E_\Delta = M_N + \omega + T_\Delta$, where $M_N + \omega$ is the center-of-mass energy of the pion-nucleon system inside the nuclear medium with M_N being the nucleon mass (neglecting its binding energy) and $\omega = T_p$ the projectile kinetic energy in the proton-nucleus centre-of-mass system. T_Δ is the kinetic energy operator of the Δ while M_Δ and Γ_Δ represent the mass and the width of the delta, respectively.

3.3 Distortion Effects

The incoming proton interacts with the strong nuclear field before making the nuclear transition, as does the outgoing pion after the production process. Therefore, the wave functions of the proton and the pion cannot be taken as the plane waves and the distortion effects in the initial and final states have to be considered in the microscopic calculation of the (p, π) reaction.

19

3.3.1 Initial State Interaction

The initial state is described adequately by the interaction between the projectile proton and the target nucleus before the projectile makes its transition to a certain bound state. The proton distorted waves can be calculated by means of a standard non-relativistic optical model approach. The proton distorted wave function in the initial state is expanded as

$$
\begin{aligned}
\Psi_{m_{s_1}}(k_p, r_0) &= (\frac{4\pi}{k_p}) \sum_{L,M} (i)^L \frac{U_L(k_p, r_0)}{r_0} Y^*_{LM}(\hat{k}_p) Y_{LM}(\hat{r}_0) \chi^{\frac{1}{2}}_{m_{s_1}} \\
&= (\frac{4\pi}{k_p r_0}) \sum_{L,M} \sum_{j,m} (i)^L U_L(k_p, r_0) \\
&\quad \times Y^*_{LM}(\hat{k}_p) (L M \frac{1}{2} m_{s_1} \mid j m) \mid L \frac{1}{2} j m) .
\end{aligned}
\tag{3.21}
$$

where k_p denotes the momentum of the incident proton and r_0 is its coordinate vector. $U_L(k_p, r_0)$ is the radial part, and $\chi_{m_{s_1}}$ the spin part of the proton distorted wave function. $U_L(k_p, r_0)$ is obtained using the following Schrodinger equation:

$$
\left\{ -\frac{\hbar^2}{2\mu} \frac{d^2}{dr^2} + \frac{\hbar^2 l(l+1)}{2\mu r^2} + V(L, j, r) \right\} U_L(k_p, r) = E U_L(k_p, r) .
\tag{3.22}
$$

The reduced mass of the proton-nucleus system is denoted by μ in the proton-nucleus center-of-mass, and the corresponding energy related to the wave number k_p is E which satisfies

$$
\hbar^2 k_p^2 c^2 = E^2 - \mu^2 c^4 .
$$

$V(L, j, r)$ is the proton-nucleus optical potential which is given in a phenomenological parameterized form as

$$
\begin{aligned}
V(L, j, r) &= V_C(r, R_C) + V_1 f(r, R_1, a_1) + i W_2 f(r, R_2, a_2) \\
&\quad - \frac{2}{r} \left[V_3 \frac{df}{dr}(r, R_3, a_3) + i W_4 \frac{df}{dr}(r, R_4, a_4) \right] (l \cdot \sigma) .
\end{aligned}
\tag{3.23}
$$

In this expression $V_C(r, R_C)$ is the Coulomb potential arising from a uniform charge distribution and the nuclear optical potential. The parameters V_1 and W_2, represent the strengths of real and imaginary parts of the central part. V_3 and W_4 are the corresponding strengths of the spin-orbit part of the optical potential. The f's represent the form factors which are usually considered in Woods-Saxon form,

$$
f(r_i, R_i, a_i) = \frac{1}{1 + \exp[(r_i - R_i)/a_i]} .
$$

Here, $R_i = r_i A^{1/3}$ is the mean radius of the nuclear potential well, while the skin thickness is denoted by a_i. The optical potential is usually obtained in a phenomenological parametarized form by fitting to experimental data, for example, taken from proton-nucleus elastic scattering at a compatible energy range.

3.3.2 Nuclear Ground State

Consider a reaction on a closed-shell target nucleus for simplicity (for example, ^{12}C, ^{40}Ca). The closed-shell of the nuclear ground state can be considered as a particle in a state $|\, j\, m \rangle$ coupled to the rest of the nucleus, which itself is represented as a hole in the state $|\, j\, m \rangle$. Now suppressing the isospin variables, one can write the nuclear ground state as

$$
\begin{aligned}
|\, \Psi^{0^+}(r_1, \xi) \rangle &= \sum_{j,m} |\, \Psi_{jm}(r_1), \Phi_{j\,-m}(\xi) \rangle \\
&= \sum_{j,m} R_{nlj}(r_1) \,|\, j\, m \rangle \Phi_{\bar{j}}(\xi) \,|\, j\, -m \rangle \, .
\end{aligned}
\tag{3.24}
$$

In this equation, r_1 and ξ are the coordinate vectors of the target nucleon and the remaining nuclear core, respectively. The radial part of the wave function of the target nucleon is represented by $R_{nlj}(r_1)$ which is obtained by solving the Schrodinger equation with an appropriate nuclear potential. $\Phi_{\bar{j}}(\xi)$ denotes the nuclear core wave function. The nuclear ground state formed above has to be coupled with the distorted wave of the incident proton to form the overall initial state which is a proton coupled to a closed-shell, $J = 0$, $m_j = 0$ nucleus. Thus we form the total initial state as

$$
|\, \Psi_i \rangle_{m_{s_1}} = A \,|\, \Psi_{m_{s_1}}(k_p, r_0), \, \Psi^{0^+}(r_1, \xi) \rangle \, ,
\tag{3.25}
$$

where A represents the antisymmetrization of the total wave function of the initial state.

3.3.3 Final State Interaction

The final state consists of a real pion and the nucleus with an extra bound nucleon. If this additional nucleon is bound in the angular momentum state $|\, j_f\, m_f \rangle$, the state of

21

the nucleus can be written as

$$\begin{aligned}
| \Psi_{m_f}(r_0, r_1, \xi) \rangle &= A' | \Psi_{j_f m_f}(r_0),\ \Psi^{0+}(r_1, \xi) \rangle \\
&= A' R_{n_f l_f j_f}(r_0) | j_f m_f \rangle \sum_{j', m'} R_{n' l' j'}(r_1) | j'\, m' \rangle \\
&\quad \times \Phi_{\bar{j}'}(\xi) | j' - m' \rangle\ ,
\end{aligned}$$
(3.26)

where $R_{n' l' j'}(r_1)$ represents the radial part of the wave function of the bound nucleon after the decay of the delta, and $R_{n_f l_f j_f}(r_0)$ represents the bound state of the incident nucleon. The wave function of the nuclear core (i.e., the hole state) is represented by $\Phi_{\bar{j}'}(\xi) | j' - m' \rangle$. A' denotes the antisymmetrization of the wave function in the final state.

The pion distorted wave can be expanded in a partial wave decomposition as

$$\chi^{(-)*}(k_\pi, r_2) = \frac{4\pi}{k_\pi} \sum_{l_\pi, m_\pi} (i)^{l_\pi} \frac{\Phi_{l_\pi}(k_\pi, r_2)}{r_2} Y_{l_\pi m_\pi}(\hat{r}_2) Y^*_{l_\pi m_\pi}(\hat{k}_\pi)\ .$$
(3.27)

where k_π and r_2 are the momentum of the outgoing pion and its coordinate vector, respectively. $\Phi_{l_\pi}(k_\pi, r_2)$ is the radial part of the pion distorted wave function for which the solution is obtained by solving the Schrodinger equation as in the case of proton distortions in the initial state [see eqn. (3.22)]. However in this case, the potential is taken as the Coulomb potential plus the pion-nuclear optical potential. This potential has been used by Iqbal and Walker [Iq85] as a modified Kisslinger potential which is written for a nucleus of atomic number A as

$$V_{opt}(r) = -Ab_0 k^2 \rho(r) + Ab_1 \nabla \cdot \rho(r) \nabla - \left(\frac{A}{2} \right) \left[\frac{T_\pi + m_\pi}{M} \right] b_1 \nabla^2 \rho(r)\ .$$
(3.28)

Here, T_π and m_π denote the kinetic energy and the rest mass of an emitted pion with wave number k. The nucleon mass is M while b_0 and b_1 are parameters related to the S- and P- wave pion-nucleon phase shifts. $\rho(r)$ is the nucleon density at a distance r from the nuclear center. A phenomenological parameterized form of this optical potential can be obtained by fitting to pion-nuclear elastic-scattering data at a compatible energy range. Since the pion distortion effects $(k_\pi \hat{\phi})$ are included in the TNM operator itself [see eqn. (3.9)], the final state of the reaction is taken as the 2p1h nuclear state of the residual nucleus. Thus, we have

$$| \Psi_f \rangle_{m_f} = A' | \Psi_{m_f}(r_0, r_1, \xi) \rangle\ .$$
(3.29)

3.4 Transition Matrix Elements

The transition amplitudes in the two-nucleon mechanism are evaluated by coupling the nuclear states of one active nucleon in the initial ground state nucleus and two active nucleons in the final state residual nucleus to the same nuclear-core wave function. Once the initial and final state wave functions are obtained, the matrix element of the nuclear transition can be written with the TNM operator sandwiched between them as follows:

$$| \langle f \,|\, T_{p,\pi} \,|\, i \rangle | \;=\; \langle \Psi_f \,|\, H_{NN \to NN\pi}(0,1) \,|\, \Psi_i \rangle$$

$$= A'' \sum_{j,m} \sum_{j',m'} \langle \Psi_{j_f m_f}(r_0),\ \Psi_{j'm'}(r_1) \,|\, H_{NN \to NN\pi}(0,1) \,|$$
$$\times \,|\, \Psi_{m_{s_1}}(r_0),\ \Psi_{jm}(r_1) \rangle \times \langle \Phi_{j\,-m}(\xi) \,|\, \Phi_{j'\,-m'}(\xi) \rangle$$

$$= A'' \sum_{j,m} \langle \Psi_{j_f m_f}(r_0),\ \Psi_{jm}(r_1) \,|\, H_{NN \to NN\pi}(0,1) \,|$$
$$\times \,|\, \Psi_{m_{s_1}}(r_0),\ \Psi_{jm}(r_1) \rangle \,. \tag{3.30}$$

where the orthonomality of the nuclear-core states, $\langle \Phi_{j\,-m}(\xi) \,|\, \Phi_{j'\,-m}(\xi) \rangle = \delta_{jj'}$, has been used. The wave functions of the nuclear-core in the initial and the final states are taken to be the same, otherwise the matrix elements would vanish. A'' again represents an appropriate antisymmetrization factor.

3.5 Experimental Observables in the A(p,π)A+1 Reaction

The cross section and the analyzing power are the typical observables for this type of reaction studies. They are determined for the selected reaction channels that are well understood.

3.5.1 Differential Cross Section

In the case of the $A(p,\pi)A+1$ reaction, the differential cross section has to be calculated considering a two-body initial state and a two-body final state. Once the transition amplitude of the reaction is known, the differential cross section is given by

$$\frac{d\sigma}{d\Omega} = \frac{\alpha_1 \alpha_2}{(2\pi)^2} \frac{1}{|v_p - V_i|} \int dk_\pi k_\pi^2 \frac{1}{(2s_p+1)} \frac{1}{(2j_i+1)} \sum_{m_s} \sum_{M_i} \sum_{M_f}$$

$$\times \int dk_{A+1} \delta(E_f - E_i)\delta(P_f - P_i) |\langle f | T_{p,\pi} | i \rangle|^2 , \tag{3.31}$$

where $\alpha_1 = (m_p/E_p)$ and $\alpha_2 = \frac{1}{2E_\pi}$ are the fermion and boson normalization factors in the initial state and the final state, respectively. The relative velocity of the incoming nucleon channel is given by $(v_p - V_i)$. j_i is the initial angular momentum state of the target nucleus. The quantities E_i, E_f, P_i, and P_f represent the initial and final total energies and momenta. The final expression for the differential cross section is obtained in terms of the reduced T-matrix elements $\langle | T_{p,\pi} | \rangle$ with the relative velocity expressed in terms of the kinematical variables in the centre-of-mass, and by performing integration over k_π and k_{A+1}. Thus, we have

$$\frac{d\sigma}{d\Omega} = \frac{\alpha_1}{(4\pi)^2} \left(\frac{k_\pi}{k_p} \right) \frac{E_p E_A E_{A+1}}{(E_p + E_A)^2} |\langle | T_{p,\pi} | \rangle|^2 , \tag{3.32}$$

where k_p and k_π represent the magnitude of momentum of the incident proton and the outgoing pion, respectively. E_p, E_A, and E_{A+1} are the total energies of the incident proton, target nucleus, and the residual nucleus, respectively. The reduced T-matrix element is written as

$$|\langle | T_{p,\pi} | \rangle|^2 = \frac{1}{(2s_p+1)} \frac{1}{(2j_i+1)} \sum_{m_s} \sum_{M_i} \sum_{M_f} |\langle f | T_{p,\pi} | i \rangle|^2 , \tag{3.33}$$

which is averaged over all the initial spin projections of the projectile proton and the angular momentum projections of the target nucleus, and summed over all the final states containing pion and the residual nucleus. If a polarized proton beam is used, the initial proton spin averaging is not required.

Chapter 4

The Experiment

The present measurements of A$(p. \pi^{\pm})$A+1 reactions were carried out in two separate TRIUMF experiments, E417 and E635. The former includes the (p, π^{+}) studies while the latter consists of measurements for the study of (p, π^{-}). Both were performed using the same facility at the TRIUMF laboratory in Vancouver, Canada. This chapter includes a detailed description of the experiment and major parts of the instrumentation involved in the measurements.

Accelerated particle beams are used as probes in most of the present experiments in subatomic physics to study the details of nuclear reactions and thereby exploit the nature of interactions between the constituents of the nucleus. Different types of particle accelerators such as cyclotrons, synchrotrons, linear accelerators, or accelerating rings in various geometries are made available for these purposes at different laboratories around the world. Subatomic experiments performed at TRIUMF make use of a primary beam of accelerated protons produced by a variable energy cyclotron. All other secondary beams are derived from this primary beam.

4.1 Experimental Facilities

The TRIUMF laboratory provides proton, neutron and meson beams for various types of experimental studies depending on the application. An initial beam of H^{-} ions of 300 keV is first injected into the main cyclotron, which then delivers proton beams from three different extraction ports. Three primary beam transport systems carry the proton beams in well-defined achromatic or dispersed beam configurations to the different

experimental areas in the laboratory.

4.1.1 The TRIUMF Cyclotron

The TRIUMF particle accelerator is a six-sector, isochronous cyclotron which accelerates H^- ions to a maximum energy of 520 MeV. The main advantage of the design is that the extracted proton beam is continuously variable in energy from 183 MeV to 520 MeV. A thin graphite foil is used to strip the electrons from the H^- ions at the beam extraction port. The subsequent positively charged particles (protons) are bent out of the machine by the magnetic field that guides the H^- ions. A pure proton beam is thus extracted into the external beamline.

The entire cyclotron operation is computer controlled. The position and angle of the stripping foil can be varied as desired. Its radial position determines the extracted beam energy, and the beam intensity depends on how much of the beam the foil intercepts. Several extraction ports allow the extraction of two or more beams simultaneously and independently. Since H^- ions are accelerated, an appreciable beam loss can occur in the machine due to electric dissociation. Therefore, the size of the cyclotron is large (30 feet in diameter) to minimize the peak magnetic field, and hence the beam loss. More details of the facility can be found in reference [Cr77].

The general layout of the laboratory is shown in Fig. 4.1. Beams through BL1 and BL4 are extracted simultaneously using two stripper foils which are 180° apart in azimuth, and are individually adjustable, thus providing two independent beams. Beamline BL2 is the third independent proton beam and is utilized for the production of radio isotopes and cancer treatment. Beamline BL1 transports the proton beam to the Meson Experimental Hall where secondary meson beams are produced for meson experiments. Beamline BL4 is divided into two arms, namely BL4A and BL4B, using a bending magnet, and hence only one of the two can be operated at a time. BL4B transports the beam to the proton hall where the present experiment was performed. The details of the transport magnetic elements on BL4B can be found in reference [Pu92]. The experimental arrangement is shown in Fig. 4.2. This includes the external beamline, its associated major components, and the Dual Arm Spectrometer System (DASS) in the proton hall (see section 4.2.2).
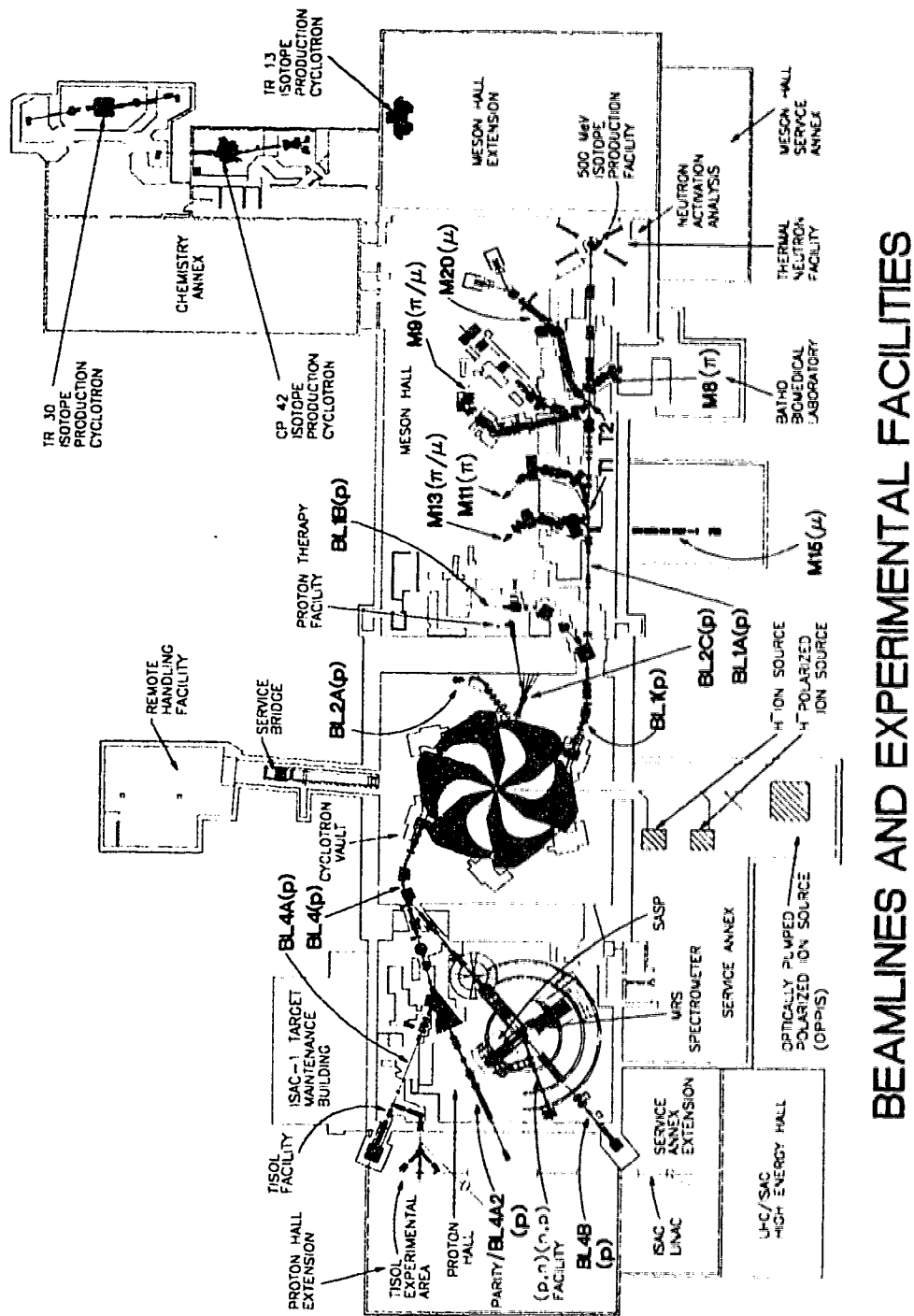
Figure 4.1: General layout of the TRIUMF laboratory showing the different experimental areas that are connected to the main cyclotron by the beamlines indicated.

27
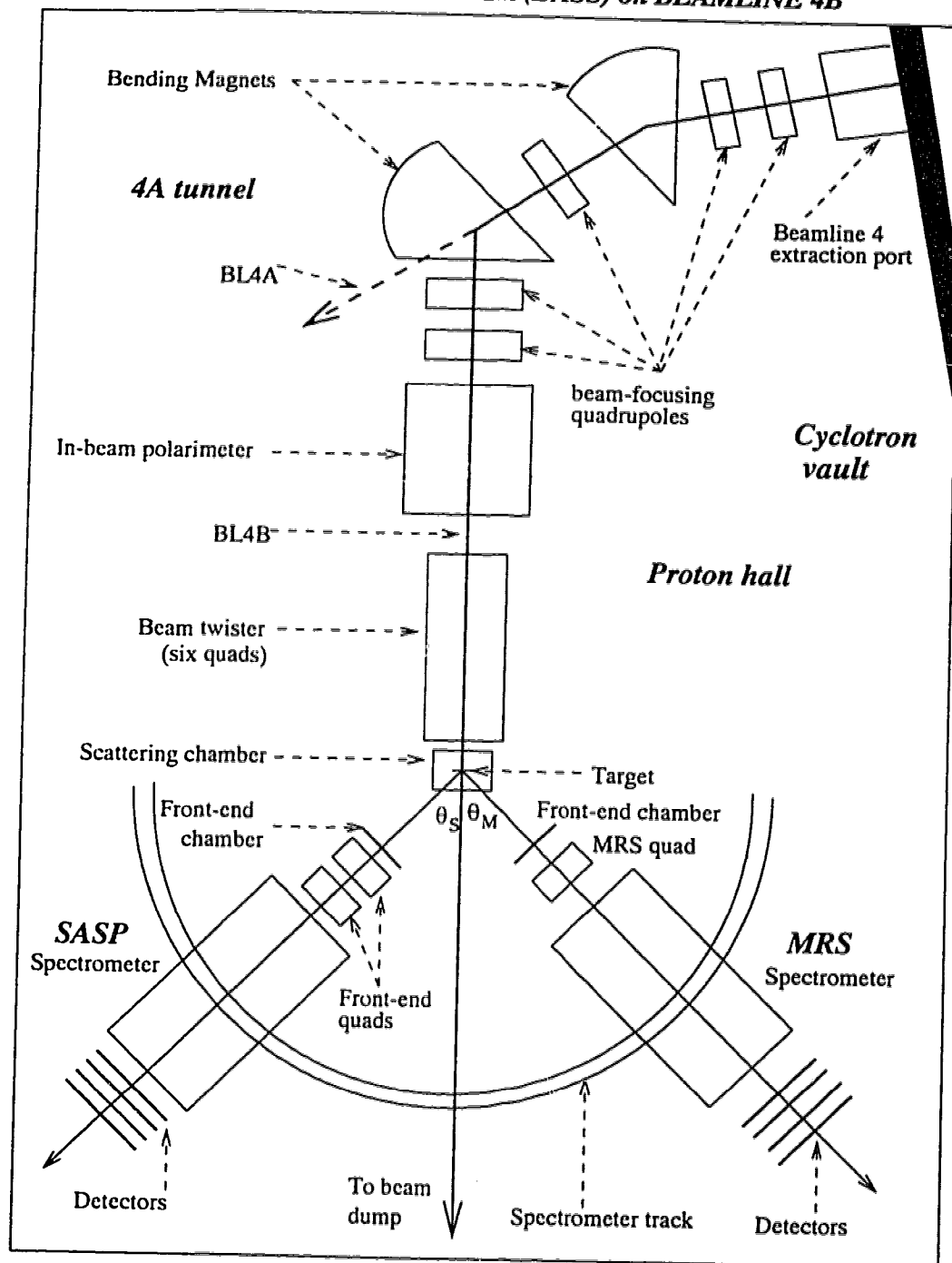
Figure 4.2: Plan view of the experimental arrangement which shows the external beam and its associated major beamline elements and the spectrometer arrangement in the proton hall.

28

4.1.2 Polarized Proton Beam

The proton beam in BL4B is available either in polarized or unpolarized form. The polarization vector can be vertical, transverse, or longitudinal. The beam polarization is reversible, and is typically about 75%. A dispersed, vertically-polarized beam of protons was used in the present measurements with a vertical momentum dispersion of -11 (cm/%). The beam polarization was continually measured by the In-beam Polarimeter (IBP).

The In-beam Polarimeter (IBP)

The IBP, one of the major BL4B elements, is situated upstream of the beam twister (see next section) in the proton hall. Inside the polarimeter, a thin, hydrogen-rich target, typically 1.334 mg/cm^2 of CH$_2$ is exposed to the incoming proton beam. The subsequent $pp \rightarrow pp$ elastic scattering events can be detected in two opposite directions (left and right) to measure the asymmetry. A schematic diagram of the IBP is shown in Fig. 4.3(a) and its associated electronics logic is shown in Fig. 4.3(b). Three scintillation counters are used to detect pp elastic events scattered to the left, and another three for the events scattered to the right. Consequently, there are 12 scintillation counters installed in the IBP including those for the measurement of up-down asymmetry. In our measurements, the left-right asymmetry is used to obtain the spin-up and spin-down polarization of the incident beam. Protons scattered to the left and right at 17° lab angle are detected in coincidence with their corresponding recoil protons, which are scattered in the opposite side at 68.9°. In addition, a second signal from the recoil detector, delayed by 43 ns, is used in coincidence with the small angle detectors to obtain the number of accidental coincidences. These are subtracted from the left (N_L) and right (N_R) counts to determine the true number of scatterings. The accidental coincidences are due to the events coming from different beam bunches which are separated by 43 ns in the incident proton beam.

According to the set-up in Fig. 4.3 (using the known analyzing power of the reaction), the left-right asymmetry provides the transverse polarization components (spin-up and spin-down) of the beam while the sideways polarization is obtained using the top and bottom asymmetry. Thus, spin-up (+) and spin-down (−) polarizations are determined by

$$P^+ = \frac{\varepsilon^+}{A_{IBP}} \; , \; P^- = \frac{\varepsilon^-}{A_{IBP}} \; , \tag{4.1}$$

where, the ε's are the left-right asymmetries for spin-up and spin-down polarizations cor-
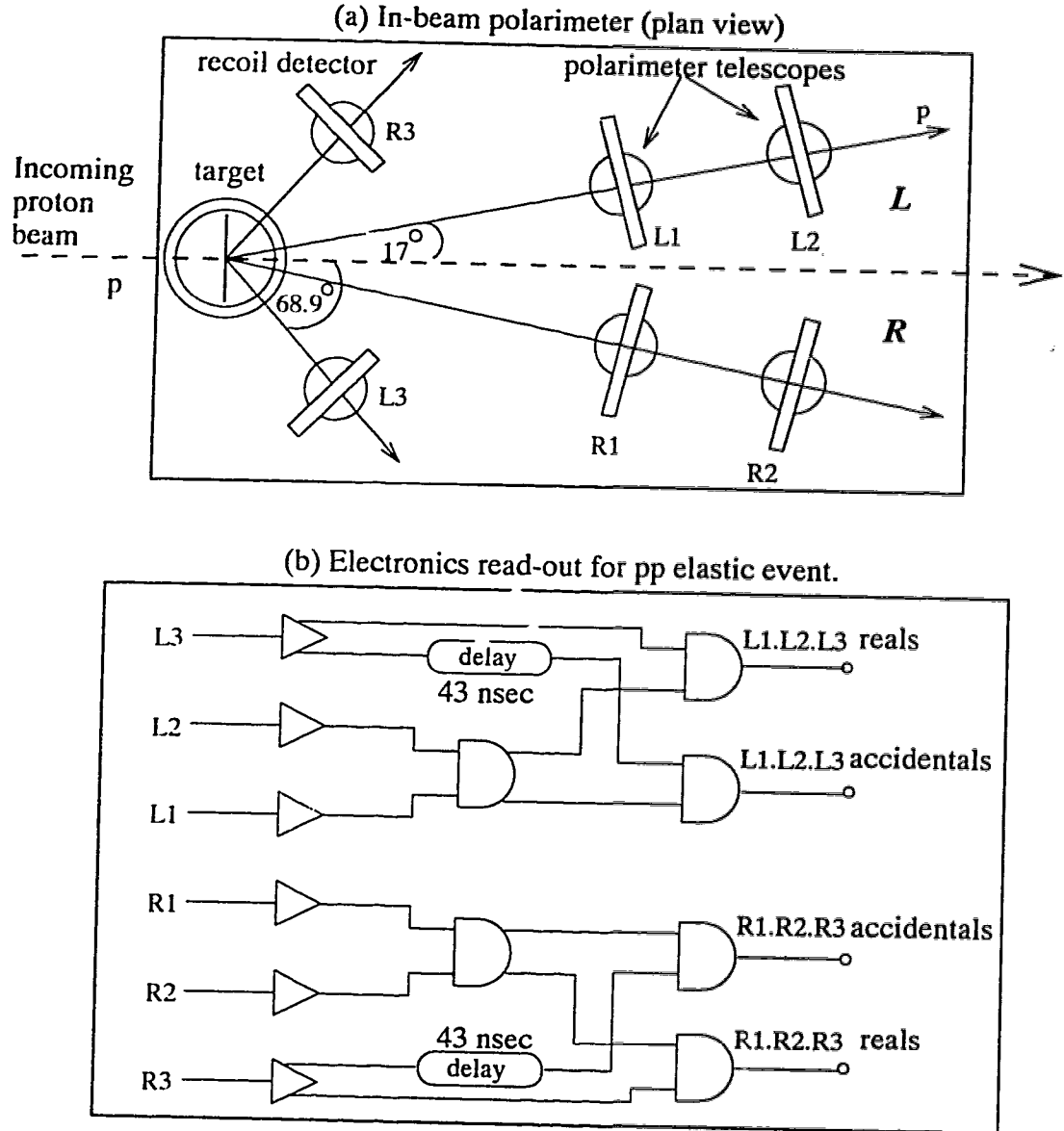
Figure 4.3: Schematic diagram of the In-beam polarimeter used for the measurement of beam polarization. The detector set-up is shown in (a) while (b) shows the electronics logic for pp elastic events.

rected for the instrumental asymmetry, and are calculated as

$$\varepsilon = \frac{[L(real) - L(acc)] - [R(real) - R(acc)]}{[L(real) - L(acc)] + [R(real) - R(acc)]} - \varepsilon_0 \ . \tag{4.2}$$

Here, ε_0 is the instrumental asymmetry and is determined from polarimeter data taken with an unpolarized incident beam. The accidental-to-real ratio of polarimeter counts was kept at approximately 0.1%/nA/(mg/cm). A substantially larger value of this ratio is an indication of excessive beam spill somewhere upstream in the beamline. A_{IBP} is the analyzing power of the IBP including correction for $C(p, 2p)$ background [Wa96].

4.1.3 Dispersion Matching Mode

The beam has a horizontal energy dispersion at the extraction port due to the finite size of the stripping foil. However, the spectrometer, which bends particles in the vertical plane, requires a vertically-dispersed beam at the target for optimum resolution. A beam twister located upstream of the target chamber on BL4B, rotates the phase space of the incoming beam by 90° to change the horizontal dispersion into a vertical dispersion. The beam twister is a set of six 4-inch quadrupole magnets mounted in a frame that allows the ensemble to be rotated around the beam axis. The relative distances between the quadrupoles also can be changed if desired. The unit magnification of the device is such that it is +1 in the vertical and -1 in the horizontal. The achromatic beam tune requires the quads to be in their normal orientation (rotated 45°) to focus/defocus in the horizontal and vertical directions. When the beam is horizontally dispersed, the ensemble is rotated about the beam axis to the zero setting. The opposite signs of the two magnifications have the effect of twisting the horizontal dispersion into a vertical dispersion as required by the spectrometer.

Once a vertically dispersed beam is achieved, one can proceed to matching the beam dispersion with that of the magnetic spectrometer to improve the resolution in the observed spectra. The better the resolution achieved, the more precise is the interpretation of physics. If the beamline and the spectrometer are perfectly dispersion matched, then the resolution will be independent of the momentum spread in the incident beam, and will be mainly a function of the target thickness. The relatively low cross section of (p, π) reactions requires thick targets and hence energy straggling in the target is the main contributor to the resolution.

The dispersion matching is achieved as follows. If a non-monoenergetic beam of protons is placed at a point of the focal plane, and is directed back through the spectrometer,

31

it will emerge with a dispersion of $\Delta X'$ which depends on the initial momentum spread of the beam and is given by

$$\Delta X' = \frac{D_s(P'_H - P'_L)}{M_s P'} \, , \tag{4.3}$$

where $D_s(M_s)$ is the dispersion(magnification) of the spectrometer and $P'_H(P'_L)$ is the highest (lowest) momentum component of the beam. The average momentum of the beam is denoted by P'. Conversely, a beam of particles incident on the spectrometer with a position spread of ΔX and a momentum spread of $(P_H - P_L)$, is focussed at a single point on its focal plane. Experimentally, the vertical spread of the incident beam is similarly,

$$\Delta X = \frac{D_t(P_H - P_L)}{P} \, , \tag{4.4}$$

where P and D_t represent the average momentum and the dispersion of the incident beam after passing through the target, respectively. The dispersion-matching condition is thus, $\Delta X = \Delta X'$ which leads to

$$\frac{D_t(P_H - P_L)}{P} = \frac{D_s(P'_H - P'_L)}{M_s P'} \, . \tag{4.5}$$

Neglecting the momentum spread induced by the target yields $P_H = P'_H$ and $P_L = P'_L$, and hence the final dispersion matching condition is obtained as

$$D_t = \frac{D_s}{M_s} \, . \tag{4.6}$$

Therefore, the incident proton beam has to be tuned to satisfy the above condition. A nominal 170 keV resolution in the focal plane spectra can be achieved for π-detection in the dispersion-matching mode for this spectrometer at 250 MeV.

4.2 The Experimental Arrangement

The experimental arrangement for the measurements of nuclear reactions is a complicated assembly installed in the proton hall on beamline BL4B. The main components include a target chamber, a magnetic spectrometer, and its associated detectors and electronics. A schematic diagram of the experimental layout is shown in Fig. 4.4.

4.2.1 Nuclear Targets

The choice of targets depends on the nuclear reactions to be studied. Typically, several nuclear targets are used in an experiment. A maximum of 6 targets are loaded on
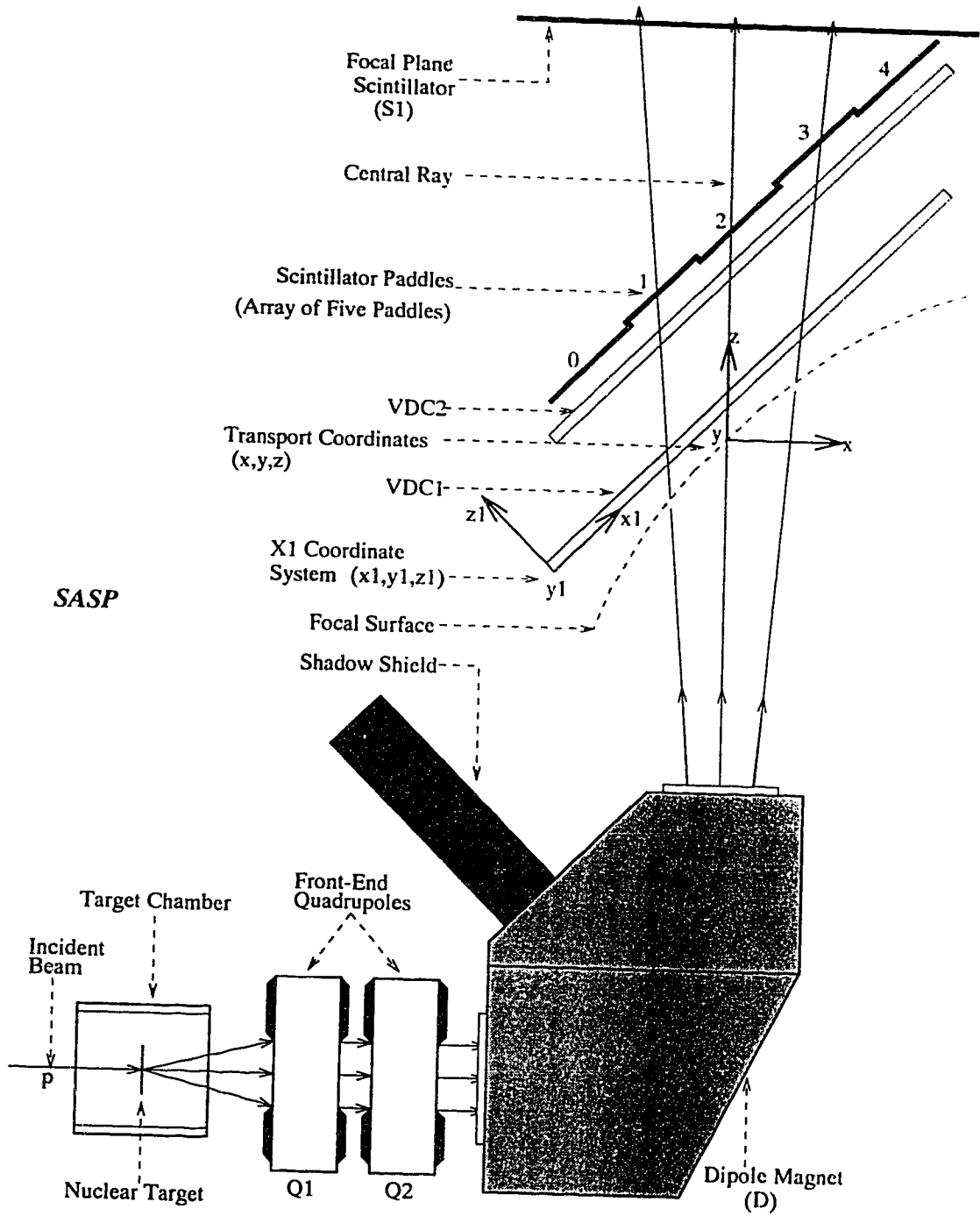
Figure 4.4: A schematic diagram which shows the layout of the SASP spectrometer. Only the major components are shown. The FEC is inserted between the target chamber and Q1, if necessary. Detailed information is found in reference [Wa96].

a metal-framed target ladder located inside the vacuum-sealed target chamber. Among these, one is usually a scintillating screen (ZnS) used to monitor the size (cross section) of the beam before inserting the primary target of interest. An empty target is also available for the measurement of background events. The target ladder motion is completely controllable remotely so that a particular target, at any desired target angle, can be exposed to the incoming beam. The outgoing nuclear reaction products are analysed by the spectrometer located immediately downstream of the target chamber.

Table 4.1: Different nuclear targets and their thicknesses as used in the measurements.

Nuclear Target	Thickness (mg/cm^2)	Comments
^{12}C	50.02	Natural Carbon
^{13}C	96.00	98.90 % Enriched
^{26}Mg	97.20	99.42 % Enriched
^{40}Ca	15.68	99.00 % Enriched
CH$_2$	48.06	–
ZnS	—	Scintillation Screen

4.2.2 Second Arm Spectrometer (SASP)

SASP (see Fig. 4.4) is a newly-commissioned magnetic spectrometer which can be operated either as a single arm spectrometer or as a second arm spectrometer (SASP) in conjunction with the existing medium resolution spectrometer (MRS) in a dual arm system (DASS). The DASS facility has been designed for both spectrometers to share a common pivot, thus allowing for the use of a common target chamber. Each spectrometer can be rotated independently around the pivot to detect reaction products at different scattering angles. The maximum angular range of SASP is 23° to 135° in the normal operating mode.

The SASP solid angle is 14 msr at its central momentum, and it has a flight path of 7 m. Outgoing particles from the nuclear reaction are focused by the front-end quadrupoles into the dipole magnet which bends the particles by 90° in the vertical plane (bend plane) with respect to the initial beam direction. The particles emerging from the dipole magnet go through the focal plane detection system which consists of two large vertical drift chambers (VDCs), a scintillation hodoscope of five paddles, and a large single scintillator (S1) installed at the top of the detector tower (see Fig. 4.4). Position information of

34

the reaction particles is obtained from the VDCs. The energy loss of each particle is provided by the scintillator array for particle identification. The top-end scintillator is used to purify the final trigger signal. The larger solid angle and the shorter flight path compared to MRS makes SASP a better pion spectrometer than MRS, the other half of DASS. The use of Front-End chambers, which limits the count rate, is optional in SASP operation. The absence of the front-end chamber allows a relatively high beam intensity on the target. This particular feature in SASP is an advantage, especially in low cross section measurements such as nuclear pion production.

Three magnetic elements are used in SASP. Two front-end quadrupole magnets focus the outgoing reaction products into the dipole bending magnet which then analyses the momenta of the particles in the vertical (bend) plane, and focuses them onto the focal surface below the VDCs. The dipole magnetic field can be tuned to observe a desired momentum range of the scattered particles at the focal plane. Reversing the coil current permits the detection of either π^+ or π^-. The π^+ spectra contain low energy protons in the background, while the π^- spectra are free of this contamination.

(p, π^-) data were taken at 221, 280, and 350 MeV with five different scattering angles, while the data for (p, π^+) were accumulated at 250 and 280 MeV at eight scattering angles. The front-end chamber was inserted at higher scattering angles where the event rates are relatively low. However, most of the data taking were completed using a high beam intensity in the absence of the front-end chamber.

4.2.3 SASP Detection System

The flight path of the particles through the spectrometer is illustrated in Fig. 4.4. It also shows the layout of the various detectors in the system. In the case of this experiment, the reaction pions were detected in multiwire drift chambers and scintillators as schematically shown in the figure. Signals from the wire chambers positioned at the front and top ends of the spectrometer provide spatial and time-of-flight information for ray tracing of a particle passing through SASP. Particle identification is achieved by the combined information of energy loss of particles in the top-end scintillators and their times-of-flight through the spectrometer. The cyclotron radio frequency (RF) signal is used in combination with scintillator signals for the particle identification in the absence of the front-end chamber.

35

Front-End Chamber (FEC)

The front-end chamber has two sets of two orthogonal wire planes labelled as X_0, X_0', Y_0, and Y_0' which are perpendicular to the central particle ray. Each plane consists of sixteen pairs of alternating active anode and cathode wires in between cathode planes. The distance between the two adjacent anode and cathode wires is 2.5 mm. There is an offset between the primed and unprimed planes which equals half the anode wire spacing. The usual gas mixture used in the front-end chamber consists of a 50/50 mixture of argon and isobutane by volume at a total pressure of one third of an atmosphere.

When a charged particle passes through the gas, a small region is ionized, and the subsequent electrons start drifting towards the nearest anode wire. each of which is connected to an independent discriminator and time-to-digital converter (TDC). A charge pulse on an anode causes the TDC to start. All the TDCs are stopped together at a fixed time after the SASP event-trigger is satisfied so that longer drift times correspond to smaller TDC values and vice versa. The wire arrangement of the front-end chamber is illustrated in Fig. 4.5(a) where the unprimed and primed planes are labelled in opposite order from each other. The absolute address of a particular wire is taken as a word in the data stream which is called as chn.

If $FIRST$ and $LAST$ are the lowest and highest absolute addresses respectively, for a given wire plane, then [see Fig.4.5(a)],

$$N = chn - FIRST, \; for \; X_0.Y_0 \; (FIRST = 0, \; LAST = 15).$$

$$N' = LAST - chn', \; for \; X_0'.Y_0' \; (FIRST = 16, \; LAST = 31).$$

The position of a charged particle in the chamber is then calculated as the average of the positions in the two planes. This is shown in Fig. 4.5(b) where one anode-cathode cell is illustrated with an ionizing particle passing through the chamber. Suppose that the cathode-anode separation in each plane is l, and the drift time from cathode to anode is Δ. The parameters X, t, X', t' are shown in the figure for each plane. In terms of these, one can write the drift distances X and X' as

$$X = \frac{tl}{\Delta}, \; and \; X' = \frac{(\Delta - t')l}{\Delta},$$

where $t(t')$ is the drift time in the unprimed(primed) plane [see Fig. 4.5(b)]. In terms of

36

(a) Wire arrangement inside the front-end chamber.

(b) Single cell illustrating the position calculation.
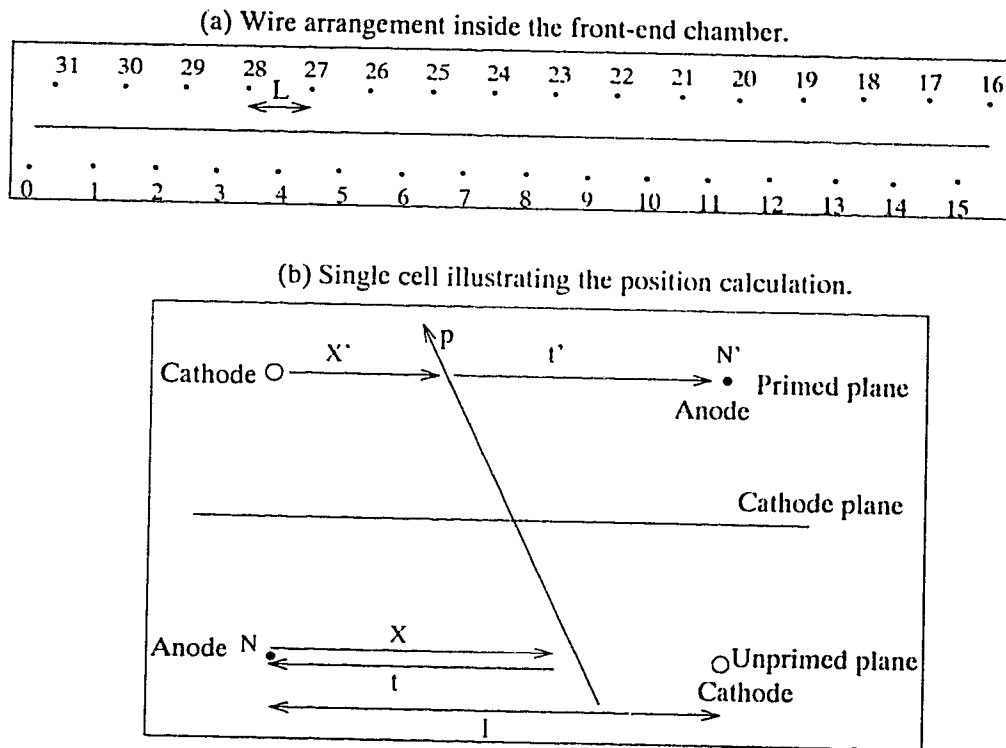
Figure 4.5: The front-end chamber geometry which consists of two identical wire planes, each containing 16 active wires. L is the anode separation.

the anode wire spacing L (where $L = 2l$), the average measured distance $\bar{X}$ is given by

$$\bar{X} = \frac{X + X'}{2} = \left(\frac{t - t' + \Delta}{4\Delta}\right) L .$$ (4.7)

Since the TDCs are operating in a common stop mode, resulting in a longer TDC time for a shorter drift time, the average measured position $\bar{X}$ can be written in terms of the corresponding TDC time $T = t_0 - t_{drift}$ where $t_0 =$ common stop time, as

$$\bar{X} = \left(\frac{T' - T + \Delta}{4\Delta}\right) L .$$ (4.8)

The staggering of the planes is useful to decide whether the passing particle is either to the left or right of an anode wire, and hence whether the average position is to be added or subtracted from the wire number N. According to the wire arrangement, one can see that a particle coming to the right of an unprimed wire with $N' = N$ will result in $2(N' - N) + 1 = +1$. and similarly a particle to the left of an unprimed wire with $N = N' + 1$ will result in $2(N' - N) + 1 = -1$. Therefore, this quantity is used to decide the correct side of the struck wire. The absolute average position of an ionizing event in the FEC is then calculated as

$$SX0 = \left\{ N + [2(N' - N) + 1] \left[\frac{T' - T + \Delta}{4\Delta}\right] \right\} L .$$ (4.9)

The anode spacing is $L = 500$ in units of 50 μm.

Focal Plane Drift Chambers (VDC)

Two large vertical drift chambers (VDCs) are located immediately above the focal plane of the spectrometer to determine the particle trajectories. These VDCs are parallel to each other, and inclined by 45 degrees to the outgoing central ray from the dipole exit. Each VDC consists of two wire planes which are called the X plane and the U plane. The angle between X plane wires and U plane wires is 30°. X and U planes are separated by a common cathode plane, which is a thin aluminized mylar foil. The set of these two planes is then sandwiched by another pair of similar mylar cathode planes. The gas in the VDCs is a 50-50 mixture (by volume) of Argon and Isobutane at atmospheric pressure. Gold-plated 20 μm tungsten wires spaced 6 mm apart are used for the anode wires. There are two field-shaping guard wires between any two adjacent anode wires in each plane of the VDCs as shown in Fig. 4.6(a). Fig. 4.6(a) also illustrates the passage of a charged particle through a plane, and the corresponding drift times, T_i, to the struck wires.

38

(a) Position calculation from the VDC.

(b) Wire arrangement inside the VDC.

(c) Transformation of U into Y coordinates.
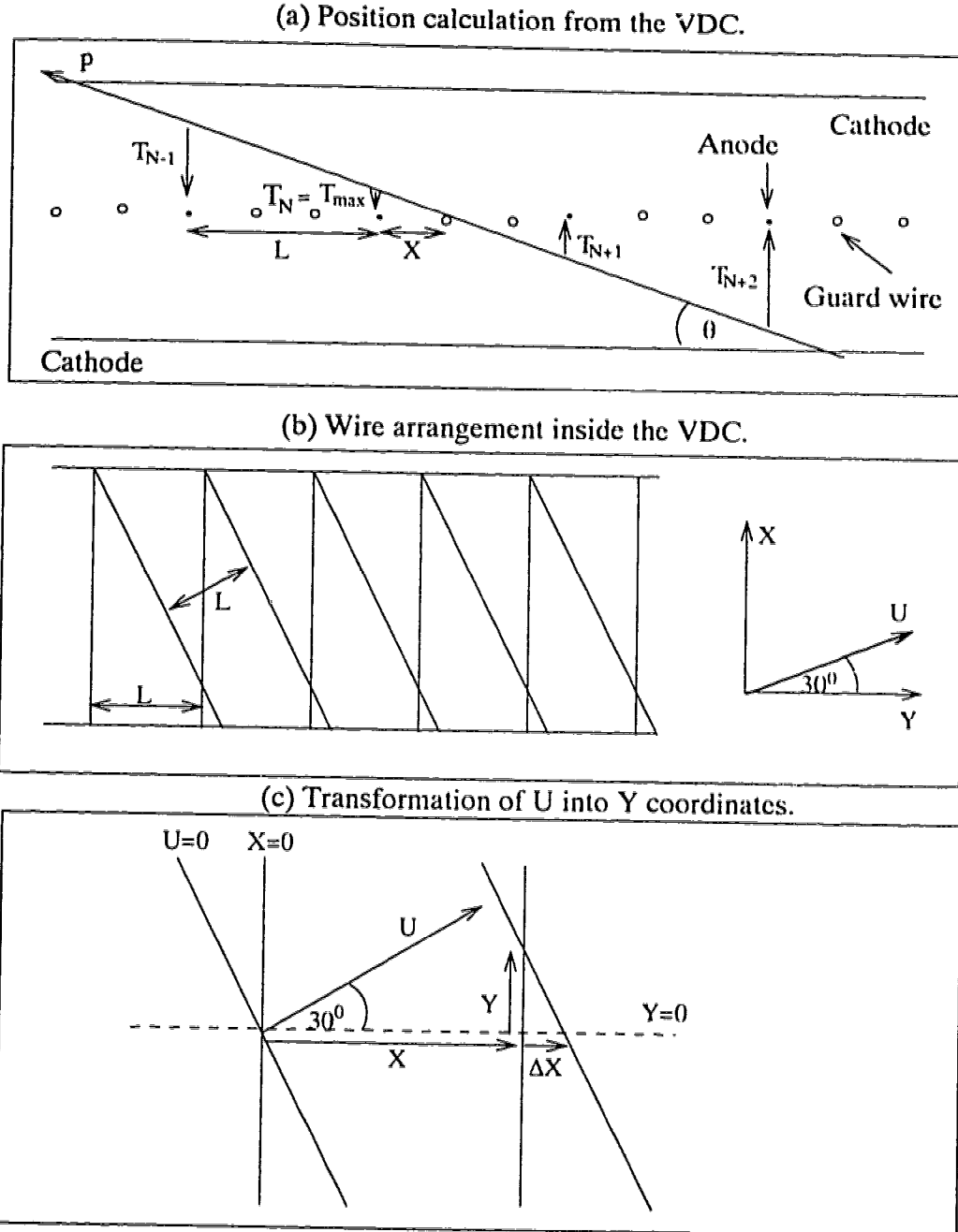
Figure 4.6: The geometry of the vertical drift chambers installed to trace the particles back to the focal plane. (a) shows how the anode and field shaping or guard wires are arranged in a single plane. The angular orientation of the wires in the X and U planes are illustrated in (b). (c) shows how the U coordinate is transformed to the Y coordinate.

39

The VDCs operate in the common stop mode (as does the FEC) so that large drift times correspond to small TDC times. Electrons released due to the ionization of the VDC gas by a traversing charged particle drift towards the anodes. A valid hit requires that at least three adjacent wires be struck. There can be more struck wires, however, only the one with the minimum drift time (maximum TDC time) and its two adjacent neighbours are used in the position calculation.

Defining T_{max} = largest TDC value, N = wire # with the largest TDC value, T_{min} = smaller of T_{N-1} and T_{N+1}, and $d_{min(max)}$ = drift distance for $T_{min(max)}$, and X = the distance from the anode to where the particle trajectory crosses the plane [see Fig. 4.6(a)], one can write,

$$\tan\theta = \frac{d_{min} - d_{max}}{L} = \frac{d_{N+1}}{(L - X)} , \tag{4.10}$$

which leads to

$$\frac{X}{L} = \frac{d_{max} - d_{min} + d_{N+1}}{d_{max} - d_{min}} . \tag{4.11}$$

Also we have $\tan\theta = d_{max}/X$, so that

$$\frac{X}{L} = \frac{-d_{max}}{d_{max} - d_{min}} . \tag{4.12}$$

Thus, combining the above results leads to

$$\frac{X}{L} = \frac{d_{N+1} - d_{min}}{2(d_{max} - d_{min})} . \tag{4.13}$$

Using the relation $d_{drift} = v_{drift} \times t_{drift}$, one can transform the drift distances to drift times, t_{drift}. Letting $T = t_0 - t_{drift}$, where t_0 is the common stop time, $d = v(t_0 - T)$. Therefore, X can be written as follows;

$$X = \frac{L(T_{min} - T_{N+1})}{2(T_{min} - T_{max})} . \tag{4.14}$$

The absolute position of the ionizing event in the chamber from its reference end is therefore,

$$X_{tot} = LN + \frac{L(T_{min} - T_{N+1})}{2(T_{min} - T_{max})} , \tag{4.15}$$

where $L = 1200$ in 50 μm units.

40

Transformation of (X, U) to (X, Y)

The design of the VDCs is such that the X-plane wires and U-plane wires are at an angle of 30 degrees with respect to each other. The geometry of the wire planes is shown in Fig. 4.6(b). The transformation of U coordinate to Y coordinate is done as follows: $U = (X + \Delta X) \cos 30°$ and $\Delta X = Y \tan 30°$, thus giving $U = (X + Y \tan 30°) \cos 30°$. This leads to the relation

$$U = \frac{\sqrt{3}}{2} X + \frac{1}{2} Y .$$

(4.16)

Since Y is measured as positive in the downward direction

$$Y = \sqrt{3} X - 2U .$$

(4.17)

Scintillation Detectors

In addition to the multiwire drift chambers, the detection system includes several plastic scintillation detectors in two different geometries. A charged particle loses some of its energy in traversing the scintillator mainly in ionizing the atoms. It also excites the atoms in the medium and the following de-excitation results in low energy photons. The subsequent scintillation inside the material is converted into an electronic pulse by the attached photomultiplier tube. The photomultiplier output is fed to a charge sensitive preamplifier and then to an analog-to-digital converter (ADC) for further processing. The charge-integrating ADCs digitize charge pulses from the charge sensitive preamplifiers, giving a digital value proportional to the energy deposited in the scintillator by each particle. Signals from the scintillators contribute to the particle identification and to the SASP trigger, in combination with signals from the multiwire chambers. Five scintillator paddles are utilized above the focal plane VDCs and a single large scintillator is used at the top of the detector tower (see Fig. 4.4).

4.2.4 SASP Trigger and Electronics

Nuclear reaction products passing through SASP are observed by means of an interfaced system of electronics and computers. The master trigger generated by the electronics accepts only the valid events of interest, which are subsequently passed on to the data acquisition computer. The definition of a valid event is software controllable during data acquisition. A flexible event trigger also minimizes hardware changes of the

41

electronics during the data taking. For these reasons, the detector electronics are interfaced with the computer through CAMAC (Computer Automated Measurement & Control) electronic modules. The logic functions defined on each CAMAC module can be changed as desired to modify the trigger, and hence the experiment can be monitored and computer-controlled.

A valid event consists of a coincidence between signals from the detectors at the front-end and the top-end of the spectrometer. The relative timing of the various signals is crucial since the different types of detectors have different response times and they are located at different positions on the flight path. A schematic block diagram of the SASP trigger electronics is shown in Fig. 4.7.
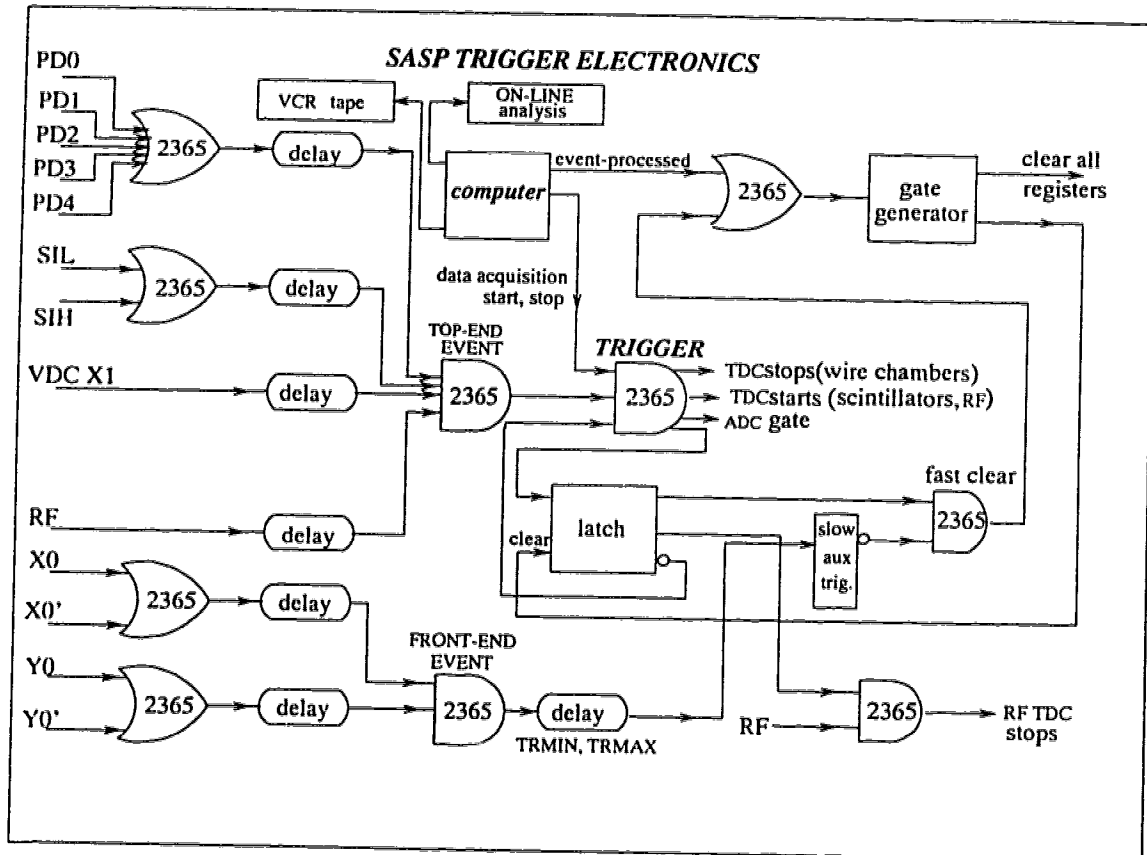
Figure 4.7: A schematic diagram for the electronic trigger set-up of the SASP spectrometer. Only the major components set for pion detection are shown. A detailed description of the SASP electronics is found in reference [Wa96].

A separate CAMAC crate houses the TDC modules connected to the anode wires

42

of the vertical drift chambers and the front-end chamber. These TDCs are started by the anode wire signals and stopped at a fixed time by the final trigger signal—the master TRIGGER. The final trigger is generated by two primary triggers that come from the FRONT-END EVENT and the TOP-END EVENT, respectively. When the final trigger signal is generated the TDC controller transfers the addresses and data from only those TDCs that are digitized to a CAMAC-controlled interface buffer which holds the data for the computer to read the whole event.

TRMIN and TRMAX are CAMAC-specified variables representing a given delay and duration of the front-end trigger signal to allow for the particle flight-times through the spectrometer. The master trigger is then produced by combining the front-end signal with that coming from the top-end detection system. The trigger operation includes an option of requiring hits in the front-end chamber. This feature is provided by introducing an auxiliary trigger called *slow aux*, which is set to 1 if the front-end chamber is to be excluded from the final trigger requirement or set to the front-end trigger logic if the other option is preferred. Generally, a nuclear reaction produces a high event-rate which saturates the processing capability of the data acquisition computer. Therefore, the latch operates as a lock which allows an event to be triggered only if the computer is ready to process it. The events which are lost in this way are taken into account by correcting the triggered event sample for the computer live time during the measurements.

As shown in Fig. 4.7, if the front-end chamber is required in the final trigger, all the signals will be fast cleared until the computer says that it has processed the earlier event and is ready to accept the next event. This message from the gate generator clears all the ADC and TDC registers as well as the latch (busy gate), preparing for the next event to be triggered. All the information of the event, such as the fired wires, pulse-heights from the scintillators, flight-times, etc. are registered and then passed to the computer buffer. This occurs when the scintillator ADC outputs are held and the TDCs of all drift chambers are enabled. The master trigger signal is also delayed by a fixed time before the TDCs are stopped. At this instant the computer, having stopped its on-line data analysis, transfers the information from its buffer to magnetic tape. During this process, the latch blocks any other events until the ready-signal from the computer is generated. One can also see in Fig. 4.7 that if the front-end trigger is required in the final trigger, all the events which are not detected at the front-end will be fast-cleared.

Stopping the vertical drift chamber TDCs with a common signal, generated at a fixed or set time after the start signals and after the last of the relevant signals reach the master trigger gate, does not affect the determination of the coordinates of a particle

passing through the drift chamber. Only time differences are involved with this calculation as discussed in section 4.2.3.

Typically in an experiment, millions of events are dumped to magnetic tape. These events are analyzed off-line after the experiment. The data acquisition allows one to perform an online data analysis so that the data quality can be monitored. This allows the experimenter to introduce any changes when necessary. Total numbers and rates of scaled quantities, such as the number of trigger events, busy latches, etc., are also recorded by the acquisition program, which periodically dumps these scalars onto tape. This scalar information is necessary to determine the total beam current, computer live time, detection efficiencies, rates, and other quantities essential for the final analysis.

Chapter 5

Data Analysis

Data sorting, calculations, and spectra processing were carried on the VMS/VAX cluster at TRIUMF. A set of software user-routines running within the command environment of the analysis program NOVA [Gr95] was used to analyse, event-by-event, the data stored on magnetic tapes. These user-routines include all the mathematical manipulations that are necessary for reconstructing the spectra which display various physical quantities of the nuclear reactions involved.

5.1 Data Stream

The data written on the tape in event-by-event format has a particular record structure. An event record is a data stream which consists of three major components; a header, a fixed length component, and a variable length component. The header contains the record length and an event type flag to identify the data stream either as an event or a set of scaler values which was read out at five second intervals. For event data, the header contains a flag to distinguish real particle events and pulser-generated pseudo-events. ADC and TDC information for the scintillators is contained in the fixed length component of the data stream. The variable length component of the event record consists of addresses and values for wire chamber TDCs that registered hits.

The first part of the analysis is to filter the useful data and skim out the unwanted events, thus reducing the number of events for further processing. In the first stage of data processing, both one- and two-dimensional spectra were produced to examine calculated variables and to obtain diagnostics for detector efficiencies, beam polarization, and beam

45

intensity variation. Appropriate conditions were imposed using software cuts and only acceptable data were retained for further processing. Details will be given in sections 5.3 and 5.4. Scaler tables for each data run were also made. Incident beam polarization was calculated using the scaler values from the in-beam polarimeter. The event-by-event analysis procedure is described by the flow chart shown in Fig. 5.1.

5.2 Particle Identification

Particle identification is crucial in the experiment since the focal plane spectra must correspond to the particular reaction products of interest, for (p,π^+) reactions, the π spectrum at the focal plane. Therefore, pions have to be precisely distinguished from protons and deuterons, which may also appear at the focal plane. The various particles have different rest masses. For a given momentum, they have different velocities, deposit different amounts of energies and do not have the same flight times through the spectrometer. The energy losses and times-of-flight are essential in purifying the spectra.

Two-dimensional spectra of energy-loss versus time-of-flight are used to identify the particle types. One then introduces an appropriate two-dimensional software gate to select pions for the rest of the analysis. The cyclotron radio frequency time is used as a time reference instead of the time-of-flight if the front-end chamber is not used in the data taking. To illustrate this, two dimensional spectra shown in Fig. 5.2 show the different particle types in each case. This way, one can select the required particle type (pions in this case) by eliminating the other particle types and most of the background events as well.

5.3 SASP Optics

A precise understanding of the spectrometer optics is essential in the data analysis. The ultimate objective is to determine the true focal plane position of the scattered particles provided that the flight path of the particle through the spectrometer is well understood. The focal plane of the spectrometer is an imaginary surface where all the particles of a given momentum from a point on the target come together, regardless of what angle they emerge from the target. A histogram of events at the focal plane should show sharp peaks corresponding to the different excited energy states in the residual nucleus. In practice, these peaks are broadened by optical aberrations of the spectrometer,
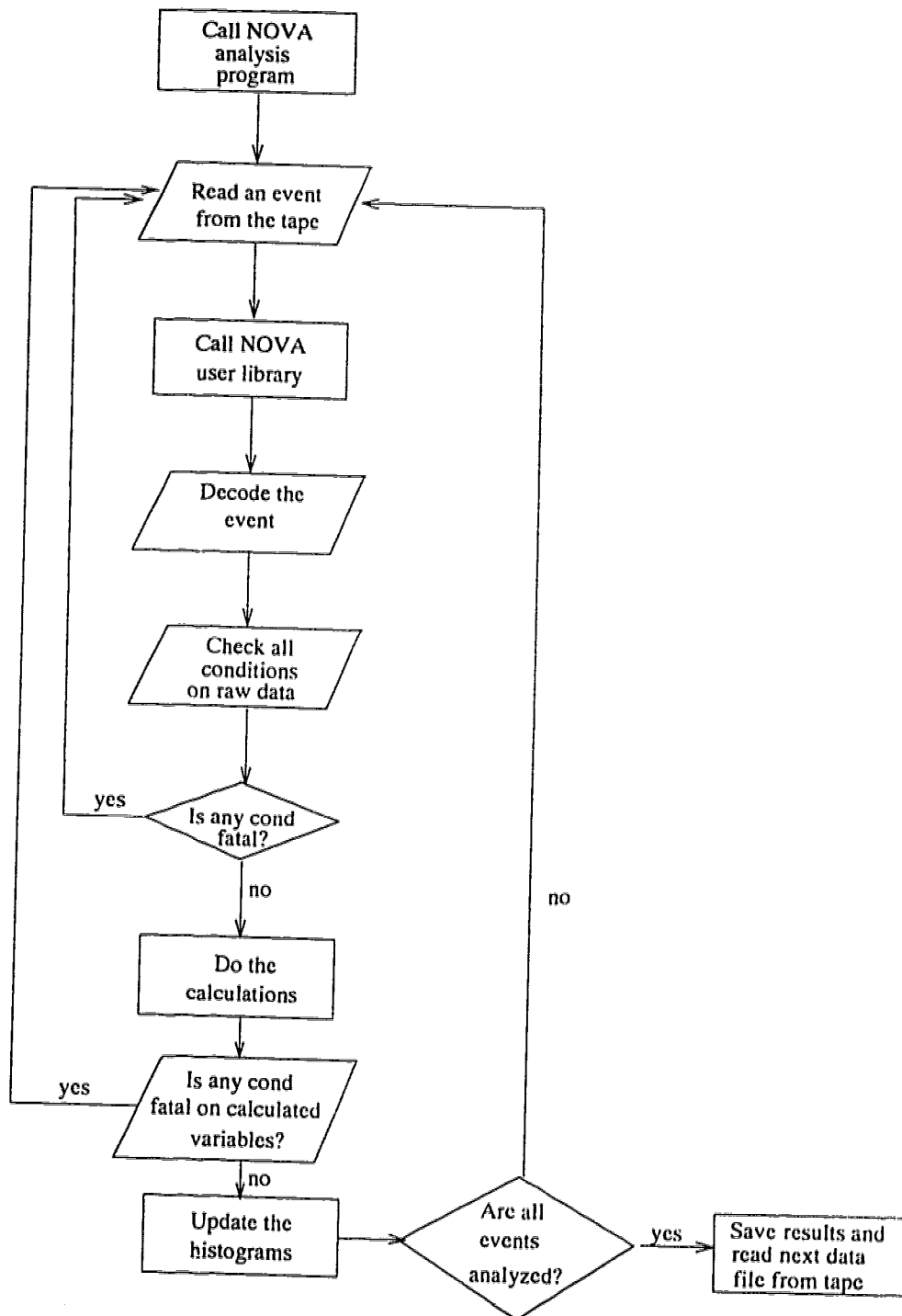
Figure 5.1: The flow chart diagram showing the event-by-event data analysis procedure.

Particle Identification
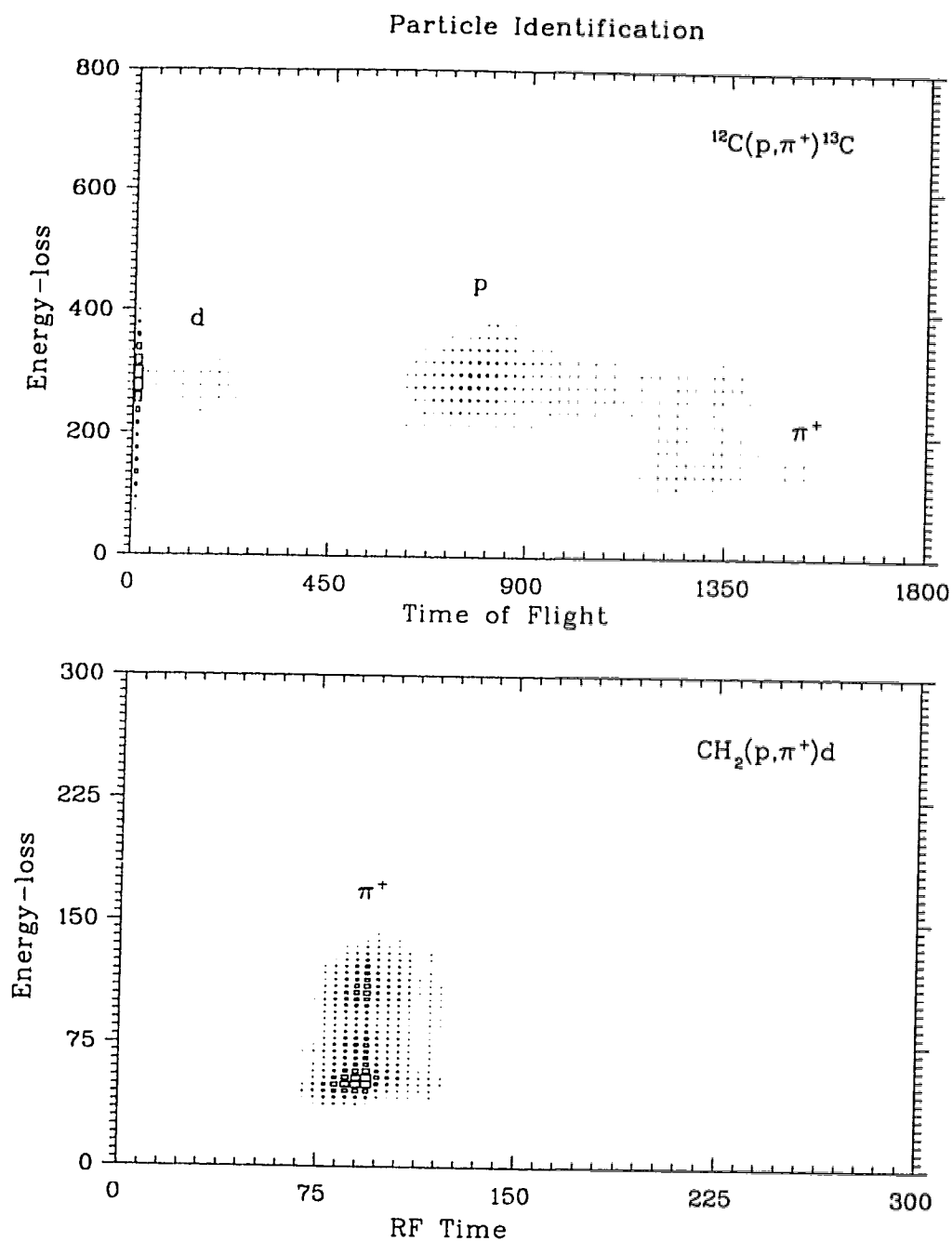
Figure 5.2: The two-dimensional histograms used for particle identification, showing the different types of particles appearing at the spectrometer focal plane. In the first plot, front-end chamber information is used to distinguish the different particles along with their energy losses. RF time is used in the second plot for the particle identification.

and the kinematical change of the momentum of a scattered particle within the spectrometer solid angle. Therefore, the focal plane spectra have to be corrected for these aberrations and kinematic shifts to improve the momentum resolution.

5.3.1 Focal Plane Reconstruction

Information for the calculation of the focal position for each event is provided by the $X1, X2$ (bend plane) and $Y1, Y2$ (non-bend plane) coordinates from the focal plane VDCs. The geometry used is shown in Fig. 5.3 where a planar approximation (the focal surface is assumed to be a plane) is used to calculate its approximate position. This position is then projected onto the true, curved, focal surface to obtain the accurate position at the spectrometer focus. The $X1$ and $X2$ information allows one to calculate the angle of the ray in the bend plane while the position and the angle calculation in the non-bend plane is achieved using Y1 and Y2 information.

In the side view of the bend plane shown in Fig 5.3, H is the separation between the two VDCs and $X1C$ is their offset. The distance from VDC1 to the focal plane (planar approximation) is F and θ is the angle of a particle ray to the VDC planes. Using the position information of $X1$ and $X2$ from each VDC (see Fig. 5.3), one can write,

$$\tan\theta = \frac{H}{DX12} = \frac{F}{X1 - XF},$$

(5.1)

where, XF is the approximate focal plane position in the (x1,y1,z1) coordinate system, and can be written as,

$$XF = \frac{X1\,H - (X2 - X1)\,F}{H}.$$

(5.2)

SASP has a curved focal surface located immediately below VDC1 because of its large momentum bite (25 %), as illustrated in Fig. 5.3. This curved focal surface was determined empirically by analyzing the data taken during the commissioning experiments. It can be parameterized conveniently by a fourth-order polynomial. From the direct information of the vertical drift chambers at the top-end, the trajectory of a particle ray can be determined and the ray's focal plane position (SXF) is obtained by its intersection point with the focal surface.

The curved focal surface is given as

$$Z = P_0 + P_1 \cdot XF + P_2 \cdot XF^2 + P_3 \cdot XF^3 + P_4 \cdot XF^4.$$

(5.3)

49
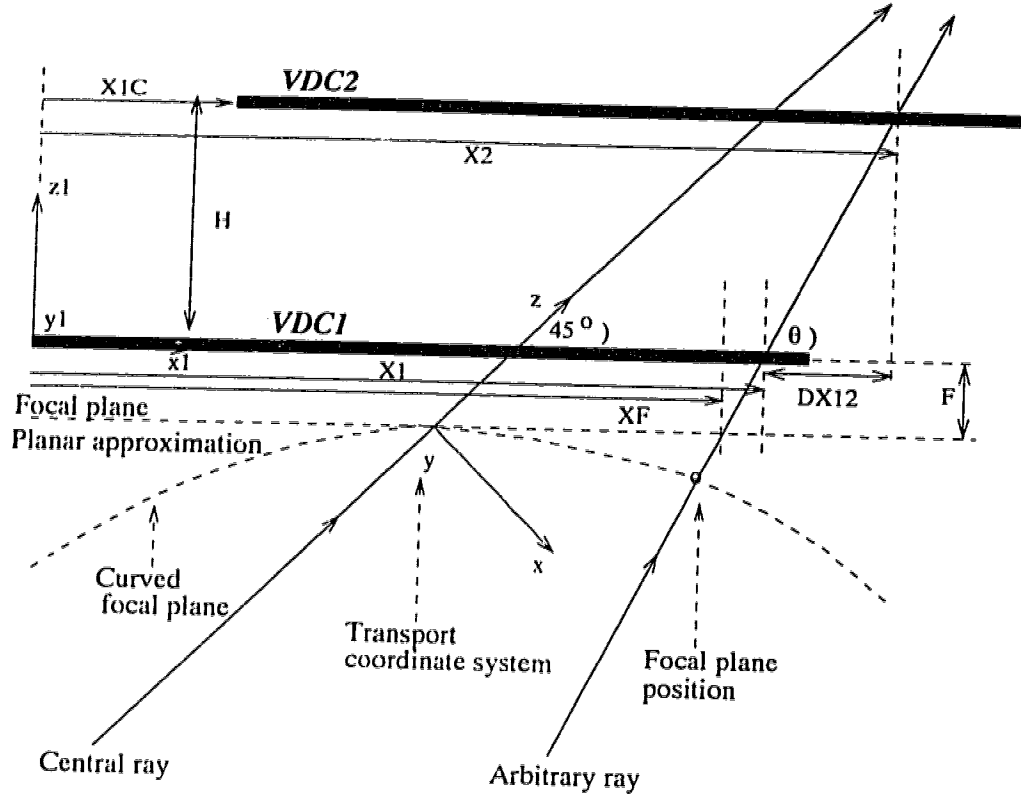
Figure 5.3: The geometry used to define the focal plane position of a given particle ray passing through the second arm spectrometer (SASP).

The XF position is first calculated in the X1 (VDC1) coordinate system using the planar approximation. In the same coordinate system, the equation of a given particle ray is written as

$$Z = M \cdot XF + B ,$$ (5.4)

where, M and B are provided directly by the VDC information. The focal position (SXF) is, therefore, given by the solution of the following equation:

$$0 = (P_0 - B) + (P_1 - M) \cdot XF + P_2 \cdot XF^2 + P_3 \cdot XF^3 + P_4 \cdot XF^4 .$$ (5.5)

5.3.2 Newton-Raphson Method

One has to solve a fourth-order equation to determine the focal position. Instead of solving this analytically, which consumes considerable computer cpu time, a numerical
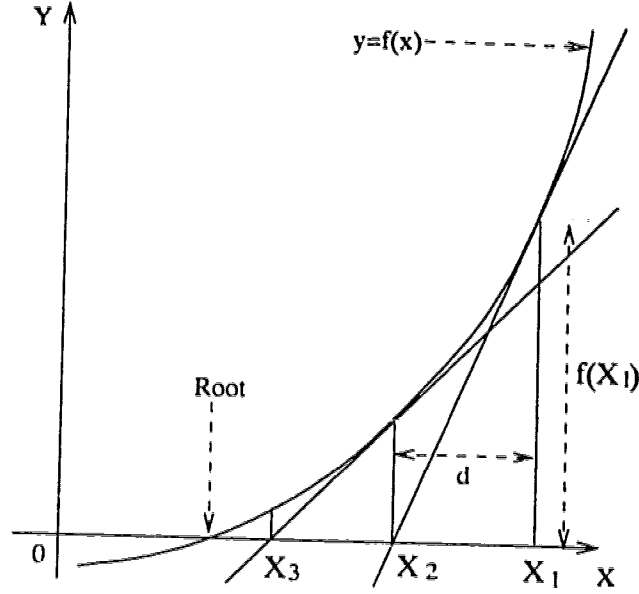
Figure 5.4: The Newton-Raphson method for solving $f(X) = 0$.

method called the Newton-Raphson method [Co72] was adopted to calculate the intersection point on the focal surface. The equation to be solved is of the type, $f(X) = 0$. An initial approximation X_1 to a root of $[f(X) = 0]$ is first chosen. This approximation is then improved by defining

$$X_2 = X_1 - d = X_1 - \left[\frac{f(X_1)}{f'(X_1)} \right] . \tag{5.6}$$

The derivative $f'(X)$ measures the slope of the tangent line to $y = f(X)$. Continuing as in the above equation, we obtain the Newton-Raphson iterative root-finding procedure which is illustrated in Fig. 5.4,

$$X_{n_1} = X_n - \left[\frac{f(X_n)}{f'(X_n)} \right] . \tag{5.7}$$

A very rapid convergence is typical in the Newton-Raphson method, but convergence is not guaranteed. For our application in particular, the Newton-Raphson method was observed to always converge. It is clear that if a sequence produced by the above equation converges to α, then α is a root of $f(X) = 0$, which in our case is the focal plane position (SXF) for the given particle ray.

In the running mode in which there is no front-end chamber, the front-end coordinate vector is determined using the top-end coordinate vector in conformity with the

51

conventional beam transport calculation. The transport matrix elements of the spectrometer magnet system are used in combination with the top-end information. The front-end and top-end quantities of the reaction particles in SASP are related to each other in beam transport convention according to the expression [Ye80],

$$
\begin{bmatrix} X_F \\ \Theta_F \\ Y_F \\ \Phi_F \\ L_F \\ \delta_F \end{bmatrix} = \begin{bmatrix} R_{11} & 0.00 & 0.00 & 0.00 & 0.00 & R_{16} \\ R_{21} & R_{22} & 0.00 & 0.00 & 0.00 & R_{26} \\ 0.00 & 0.00 & R_{33} & R_{34} & 0.00 & 0.00 \\ 0.00 & 0.00 & R_{43} & R_{44} & 0.00 & 0.00 \\ -- & -- & -- & -- & -- & -- \\ 0.00 & 0.00 & 0.00 & 0.00 & 0.00 & R_{66} \end{bmatrix} \begin{bmatrix} X_I \\ \Theta_I \\ Y_I \\ \Phi_I \\ L_I \\ \delta_I \end{bmatrix}
\tag{5.8}
$$

The left side of the matrix equation represents the coordinate vector of the outgoing particle at the top-end of the spectrometer. The right side shows the unknown coordinate vector of the ingoing particle, which is being operated on by the transfer matrix, $\mathbf{R}$, of the overall SASP magnet system. Here, $X(\Theta)$ is the position(angle) in the bend plane and $Y(\Phi)$ the corresponding non-bend plane quantities with F and I denoting the top-end and front-end quantities, respectively. L is the distance travelled by the particle, which in this case is not essential since the entire flight path of the scattered pion up to the top-end detection is calculated using a different method to determine the pion survival fraction (see section 5.12). δ is the momentum of the particle. This simply means that the $\mathbf{R}$ matrix contains the beam-optics transport properties of the SASP. The origin of the initial coordinate system is chosen at the target with the z-axis along the central ray and the x-axis downward in the vertical plane (bend-plane). The final coordinate system is chosen in the same way with its origin being the intersection point of the outgoing cental ray and the focal plane.

The final position and the associated angle (X_F, Θ_F) in the bend plane depend only on the initial position and angle (X_I, Θ_I) in the same plane. This is also true for the non-bend plane quantities, and hence some of the coefficients in the $\mathbf{R}$ matrix are zero. The fact that the particle momentum remains constant along the flight path means $R_{66} = 1$. Since SASP was designed to achieve a point-to-point focus, $R_{12} = 0$. Among the remaining coefficients, R_{11}, R_{16}, R_{21}, R_{22}, and R_{26} are associated with parameters in the bend plane whereas R_{33}, R_{34}, R_{43}, and R_{44} are non-bend plane parameters. These first-order transfer matrix elements for the SASP are described in details elsewhere [Pu94].

52

5.4 Scattering Angle Calculation

The scattering angle of the reaction has two components: the bend plane angle (Θ_I) and the non-bend plane angle (Φ_I). These angles can be determined directly from the position information provided by the front-end chamber (FEC method). However, when this chamber is absent a trace-back method using the position information provided by the vertical drift chambers at the focal plane is used. The $A(p,\pi)A+1$ data accumulated with the front-end chamber during the spectrometer commissioning are used to compare the above two methods of calculating the scattering angle. This comparison is supposed to show a one-to-one mapping between the two methods. In practice however, the trace-back method is influenced by the aberrations of the spectrometer, and requires corrections. When these are applied much better agreement between the two calculations is achieved as illustrated in Fig. 5.5.

The scattering angle can readily be calculated from the trace-back method using the first-order optical transfer elements. However, some of the significant higher-order terms based on the needed corrections to achieve a one-to-one mapping between first and second methods were taken into account. These corrections were obtained as polynomial functions of the exit angles at the focal plane (Θ_F, Φ_F) as well as the momentum of the particle over the total momentum bite of the spectrometer. For example, Θ_I is calculated in the trace-back method with first-order transfer matrix elements as

$$\Theta_I \approx \frac{\Theta_F}{R_{22}} , \tag{5.9}$$

where Θ_F is the bend plane angle of the outgoing particle at the VDCs. This calculation, which assumes that the target coordinate (X_I) is small, is further improved by determining the higher-order corrections according to

$$\frac{\Theta_F}{R_{22}} = \Theta_I + A(\delta) + B(\delta) \cdot \Theta_I + C(\delta) \cdot \Theta_I^2 . \tag{5.10}$$

The coefficients A, B, and C were obtained as functions of the momentum deviation (δ) by comparing the two methods of calculation for Θ_I. Θ_I, corrected for higher-order aberrations, is determined by solving the quadratic equation (5.10). A similar procedure was applied to determine the higher-order corrections for the Φ_I calculation using the trace-back method. Assuming that the target coordinate (Y_I) in the non-bend plane is small, the first-order calculation of Φ_I is given by

$$\Phi_I = \frac{\Phi_F}{R_{44}} , \tag{5.11}$$

where Φ_F is the non-bend plane angle of the outgoing particle at the VDCs. It was realized that the higher-order corrections for the Φ_I calculation were more significant than those for Θ_I. The improved Φ_I angle is obtained by solving higher-order equation

$$\frac{\Phi_F}{R_{44}} = \Phi_I + A'(\delta, \Theta_F) + B'(\delta, \Theta_F) \cdot \Phi_I + C'(\delta, \Theta_F) \cdot \Phi_I^2 + D'(\delta, \Theta_F) \cdot \Phi_I^3 .$$
(5.12)

The coefficients A', B', C' and D' were determined as functions of both δ and Θ_F by comparing the two methods of Φ_I calculations.

The comparisons of the Θ_I and Φ_I calculations are shown in Fig. (5.5) which has four different two-dimensional plots. (a) shows the comparison between the Θ_I calculated from the first-order transfer matrix elements and VDC information, and directly from the FEC information. The comparison in (b) shows one-to-one mapping between the improved Θ_I versus that calculated directly from the FEC. The slight smearing in the vertical direction is due to the fact that the target position (X_I) was assumed to be zero in applying the higher-order corrections. Similarly, (c) and (d) in Fig. (5.5) show the comparisons of initial and improved trace-back calculations of Φ_I versus that from the FEC method. A dramatic improvement in Φ_I corrected for the higher-order effects can be seen in (d). The improved trace-back calculations for Θ_I and Φ_I were used in the missing-mass calculations for the reactions that were measured without the front-end chamber.

5.5 Optical Aberrations of the Spectrometer

The resolution of the focal plane spectrum can be improved by applying corrections for the optical aberrations of the spectrometer. The focal position, SXF, as calculated from eqn. (5.5), still suffers from aberrations in the bend plane, and hence a major contribution to the total uncertainty in the focal position is caused by the scattering angle Θ_I. Before determining corrections for these aberrations, SXF was first corrected for the kinematic shift. The kinematic correction, $FKIN$, is calculated as

$$FKIN = \left[g'(\delta)\Delta\delta \cdot \frac{1}{p_0} \cdot \frac{dp}{d\Phi} \right] \cdot \Phi_I ,$$
(5.13)

where the momentum deviation $\delta = f(SXF)$ and $SXF = g(\delta)$. The central momentum of the spectrometer is p_0, and $\frac{dp}{d\Phi}$ is determined from the two-body kinematics as explained in the next section. For pion detection in SASP below the saturated magnetic field

$$\delta = D_0 + D_1 \cdot SXF + D_2 \cdot SXF^2 + D_3 \cdot SXF^3 .$$
(5.14)

54

The D-coefficients in ascending order were determined to be 4.22209×10^{-7}, 3.5096×10^{-1}, 7.16481×10^{-4}, and 2.97777×10^{-5}, respectively. The corrected focal position, $SXFK$, is obtained from SXF by correcting for the kinematic shift, and applying the higher-order aberration corrections as

$$SXFK = SXF - FKIN - C_1 - C_2 \cdot \Theta_I - C_3 \cdot \Theta_I^2 - C_4 \cdot \Theta_I^3 - C_5 \cdot \Theta_I^4 - C_6 \cdot \Theta_I^5 .$$

(5.15)

The C-coefficients were determined by considering a single isolated peak at a known specific point of the focal plane. These coefficients were obtained as functions of δ using similar data sets with different magnetic field settings in order to scan the entire focal plane.

The $SXFK$ histogram was examined as a function of the Φ_I angle to see if there were any optical aberrations in the non-bend plane. No aberration corrections were determined for Φ_I dependence because these aberrations were very small. The effects of aberrations and the corrections are illustrated in Fig. (5.6) which has six different plots. (a) and (b) show the dependence of $SXFK$ and SXF on Θ_I. while (c) and (d) demonstrate that there are almost no aberrations left to $SXFK$ as functions of Φ_I and $\Theta_I \cdot \Phi_I$. The one dimensional histograms in (e) and (f) show a dramatically improved resolution in $SXFK$ compared to SXF, illustrating that more of the final states can be clearly resolved with this resolution optimization.

5.5.1 SASP Momentum Calibration

Two-body kinematics of the reaction gives the momentum (p) of the particle detected in the SASP. Suppose we identify a strong peak that corresponds to a well-defined final state of the observed reaction, and obtain the mean peak position from the focal plane spectrum. This peak position moves across the focal plane for different magnetic field settings (B) of the SASP magnet. The relationship between p/B and $SXFK$ is the momentum calibration of the spectrometer. The SASP momentum calibration for pion detection below the saturated magnetic field condition was determined as a function of the focal position, and is given by

$$p_\pi = B \cdot \left[E_0 + E_1 \cdot SXFK + E_2 \cdot SXFK^2 + E_3 \cdot SXFK^3 \right] ,$$

(5.16)

where p_π is the momentum of the pion detected in SASP. The bending magnetic field is denoted by B. The E-coefficients, $E_0 - E_3$, were found to be $4.996977 \times 10^{+1}$, 1.75371×10^{-1}, 3.580239×10^{-4}, and 1.487987×10^{-5}, respectively. The π-momentum is used along with

the reaction kinematics to calculate the missing mass of the residual nucleus for the reaction $A(p, \pi)A+1$. The missing mass histogram is the ultimate data spectrum that is to be processed in further analysis to extract reaction observables.
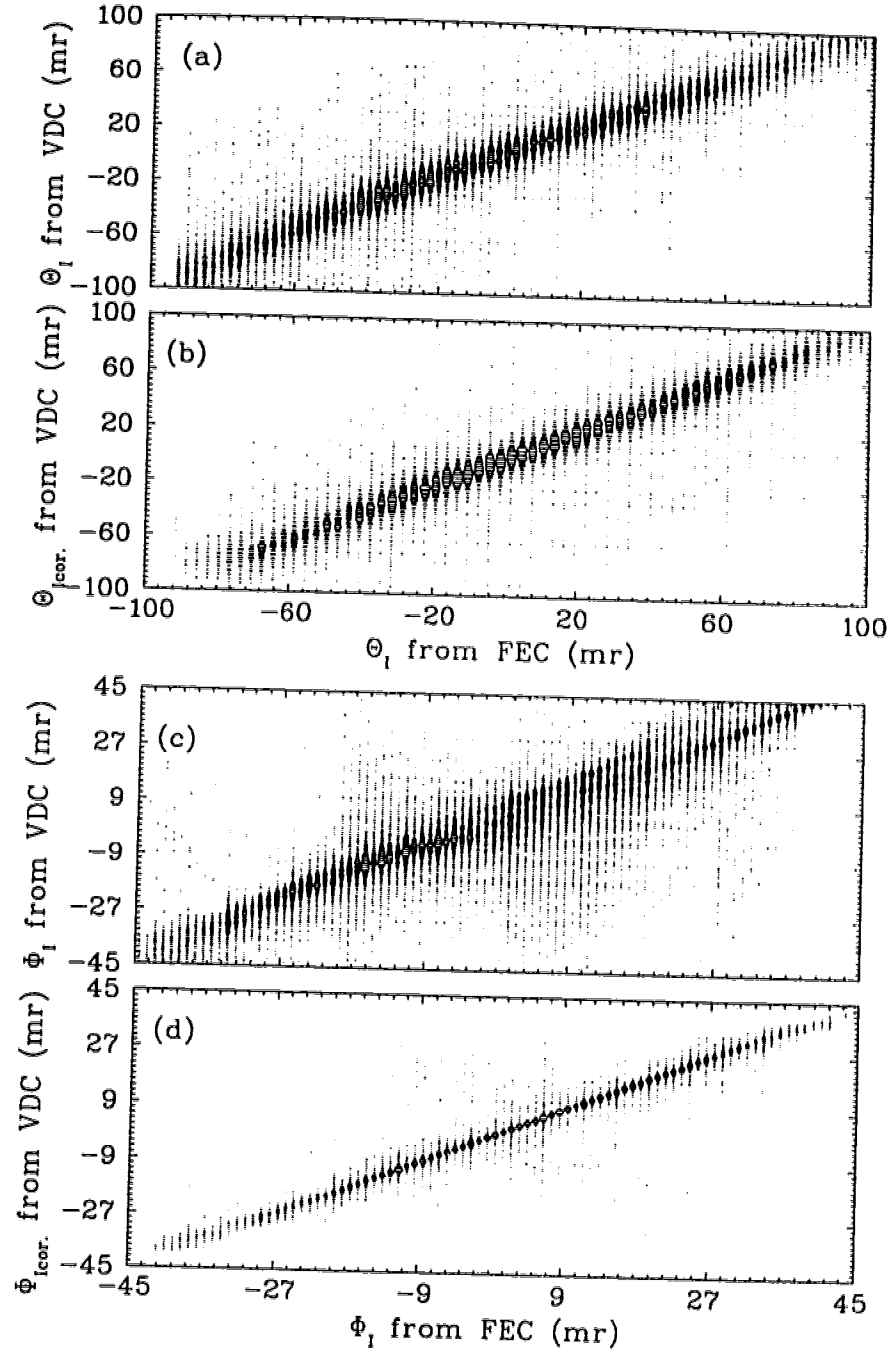
Figure 5.5: Comparisons of two different calculations for Θ_I and Φ_I angles are shown. The upper plots illustrate the improvement of the Θ_I calculation using the trace-back method with (b) and without (a) the higher-order optical aberrations. Similar plots for Φ_I are shown in (c) and (d). In each case, the calculated values are compared to those obtained directly from the front-end chamber.
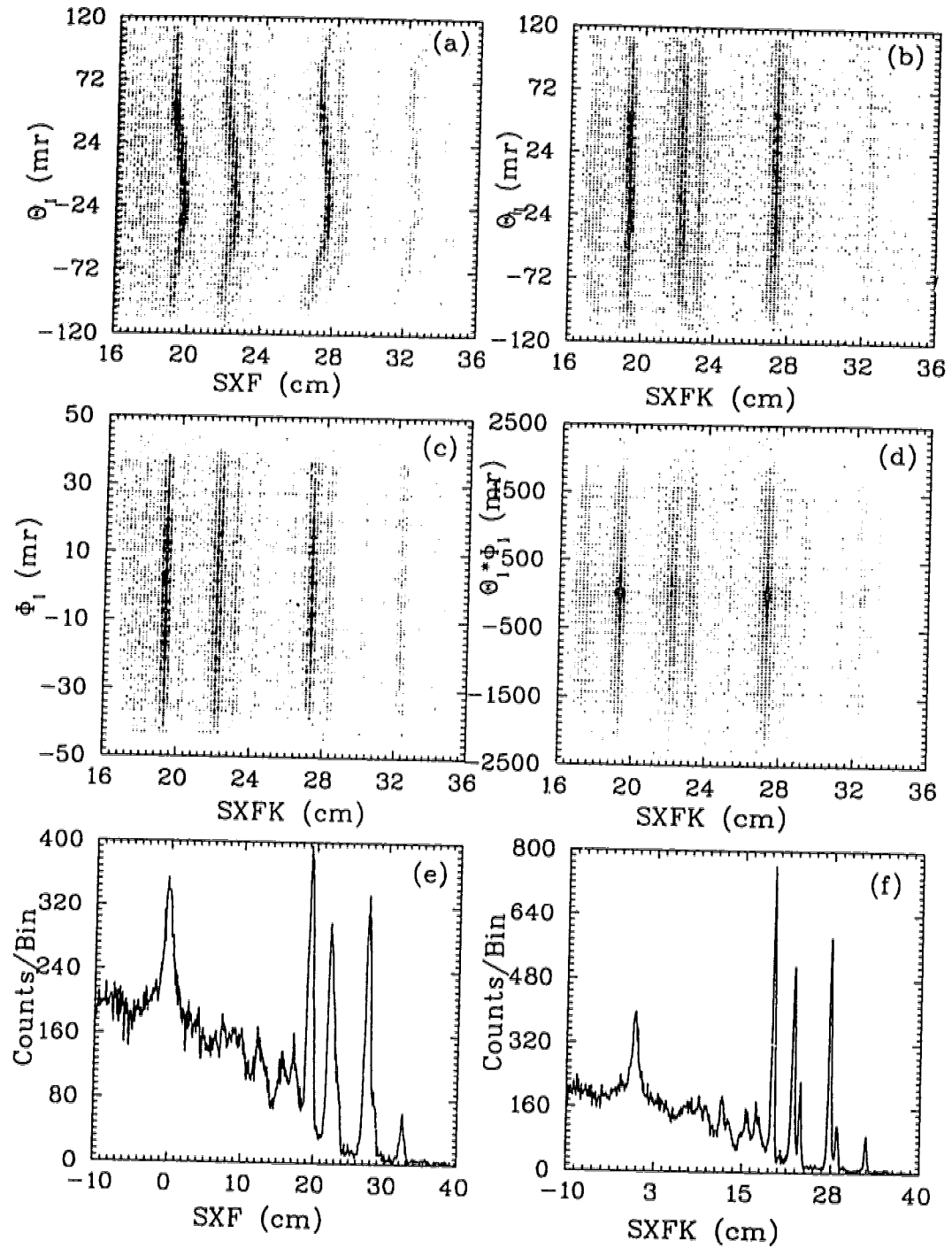
Figure 5.6: The focal position (SXF) and the aberration-corrected focal position ($SXFK$) are shown. The Θ_I aberrations and their removal are demonstrated in (a) and (b), while $SXFK$ shows almost no Φ_I or $\Phi_I \cdot \Theta_I$ dependence as illustrated in (c) and (d). The improved $SXFK$ can be compared to SXF in (e) and (f).

58

5.6 Missing Mass Calculation

Missing mass implies the determination of nuclear excitation energy of the residual nucleus of the reaction. Therefore, the missing mass spectrum is the chief agent that displays the physics of the reaction. Using two-body reaction-kinematics, which are illustrated in Fig. 5.7, the nuclear excitation energy can be calculated as follows. Considering the two-body process, where the incident proton interacts with the target nucleus to produce the outgoing pion and the recoil nucleus, one can write relativistic four-momentum conservation for the system as
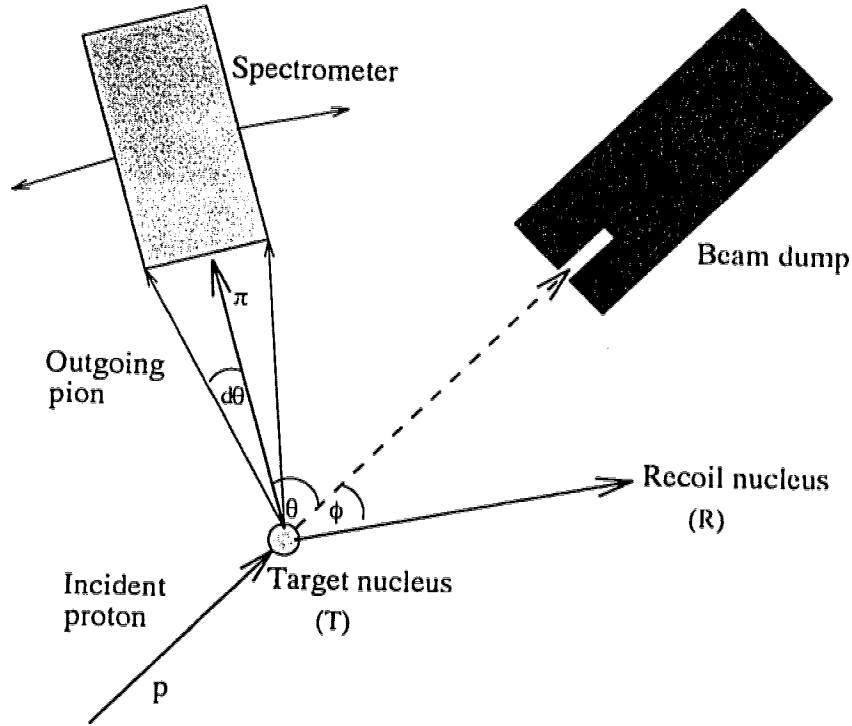
Figure 5.7: Geometry of the two-body reaction as observed using the spectrometer system in the proton hall.

$$P_p + P_T = P_\pi + P_R \, , \tag{5.17}$$

where P denotes the four-momenta of the incident proton (p), target nucleus (T), outgoing pion (π), and recoil nucleus (R). By definition, four-momentum is

$$P_\nu \equiv (E, \, p_x, p_y, p_z) \, , \tag{5.18}$$

where E is the total energy of the particle which is related to the particle mass m and 3-momentum by

$$E^2 = p^2 + m^2 .$$

(5.19)

Equation (5.17) can be manipulated to get

$$P_p^2 + P_T^2 + P_\pi^2 + 2P_p \cdot P_T - 2P_p \cdot P_\pi - 2P_T \cdot P_\pi = P_R^2 .$$

(5.20)

Using the energy relation [eqn. (5.19)], one can obtain,

$$\left(m_p^2 + m_T^2 + m_\pi^2\right) + 2\left(E_p E_T - p_p \cdot p_T\right) - 2\left(E_p E_\pi - p_p \cdot p_\pi\right) - 2\left(E_T E_\pi - p_T \cdot p_\pi\right) = m_R^2 .$$

(5.21)

Since the target nucleus is at rest in the lab frame, $p_T = 0$. Therefore,

$$\left(m_p^2 + m_T^2 + m_\pi^2\right) + 2m_T\left(E_p - E_\pi\right) - 2\left(E_p E_\pi - p_p\,p_\pi\,\cos\theta\right) = m_R^2 = \left((m_0)_R + \Delta_{EX}\right)^2 ,$$

(5.22)

where $(m_0)_R$ and Δ_{EX} represent the rest mass and the excitation energy of the residual nucleus. Thus, the missing mass of the nuclear reaction is obtained as

$$\Delta_{EX} = \sqrt{\left(m_p^2 + m_T^2 + m_\pi^2\right) + 2m_T\left(E_p - E_\pi\right) - 2\left(E_p E_\pi - p_p\,p_\pi\,\cos\theta\right)} - (m_0)_R .$$

(5.23)

In this equation:

$$p_p = \left(E_p^2 - m_p^2\right)^{\frac{1}{2}} .$$

$$E_p = (m_p + T_p) ,$$

$$E_\pi = \left(p_\pi^2 + m_\pi^2\right)^{\frac{1}{2}} ,$$

and m_p, m_T, and m_π denote the rest masses of the proton, target nucleus, and the scattered pion, respectively. The kinetic energy of the incident proton is labelled as T_p. The momentum of the scattered pion (p_π) is given by the momentum calibration of the spectrometer. Excitation energy of the reaction is calculated for spin-up and spin-down incident protons separately and increment the corresponding histograms for the extraction of reaction cross sections.

5.7 Kinematic Correction

The momentum of a particle emitted in a nuclear reaction is a function of its angle of emission with respect to the primary beam. The spectrometer subtends a solid angle $d\Omega$ at the target so the pions (if a particular state is concerned) entering the spectrometer from the target will have a small momentum spread and will reach the focal plane at slightly different positions, resulting in a broadening of the momentum spectrum at the focal plane. In order to obtain point-to-point focusing in the spectrometer, the momenta of the pions originating from the target must be corrected for this kinematic shift.

This correction can be obtained by taking the derivative of eqn. (5.22), as

$$-2m_T dE_\pi - 2E_p\, dE_\pi + 2p_p\cos\theta\, dp_\pi - 2p_p\, p_\pi\sin\theta\, d\theta = 2m_R dm_R \ .$$

$$(5.24)$$

The right hand side is zero because the recoil mass, m_R, is constant for a particular event. Using the expression for the total energy of the pion,

$$E_\pi = \sqrt{p_\pi^2 + m_\pi^2} \ ,$$

the change in pion energy as a function of its momentum is given by

$$dE_\pi = \frac{p_\pi}{\sqrt{p_\pi^2 + m_\pi^2}}dp_\pi = \frac{p_\pi}{E_\pi}dp_\pi = \beta_\pi\, dp_\pi \ ,$$

where $\beta_\pi = \frac{p_\pi}{E_\pi} = \frac{v_\pi}{c}$.

Substituting for dE_π in eqn. (5.24) gives

$$2\left(m_T\beta_\pi + E_p\beta_\pi - p_p\cos\theta\right)dp_\pi + 2p_\pi p_p\sin\theta\, d\theta = 0 \ ,$$

$$(5.25)$$

or,

$$\frac{dp_\pi}{d\theta} = \frac{-p_p\, p_\pi\sin\theta}{\{\beta_\pi(m_T + E_p) - p_p\cos\theta\}} \ .$$

$$(5.26)$$

The kinematic correction is included in the missing mass calculation itself by accounting for the correlation between the particle momentum and the corresponding scattering angle.

5.8 Spectrometer Acceptance/Solid Angle

The pion yield varies from place to place on the focal plane due to the variation of the acceptance of the spectrometer. Therefore, the acceptance variation must be measured

so that the pion yield can be corrected. Data for the acceptance scan were taken by measuring the reaction $p + p \rightarrow d + \pi$ at 500 MeV and 60°. The pion peak was moved across the focal plane by changing the magnetic field setting of the spectrometer. The peak yield was obtained at each field setting to determine the shape of the acceptance variation. The pion yields at different points on the focal plane are shown in Fig. 5.8 for different field settings.

The dependence of the focal plane acceptance is defined by the relative intensity of the pion peak at different points on the focal plane. Typically the acceptance curve is flat for the central region, and decreases at the low- and high-momentum regions of the focal plane. The relative intensity of the pion peak was determined by normalizing the peak-yield to the computer live-time, wire chamber detection efficiency, and the integrated total beam charge collected at the beam-dump. The acceptance calculation can be extended further to determine the spectrometer solid angle using a known cross section of $pp \rightarrow d\pi^{+}$. Some of the pions decay in their flight path through the spectrometer, hence the measured pion yield at the focal plane has to be corrected for the pion survival fraction as well.

The relation between the yield and the reaction cross section is

$$Yield = I \cdot \eta t \cdot \frac{d\sigma}{d\Omega} \cdot \Delta\Omega \cdot E_{ff} \cdot S_{\pi} , \qquad (5.27)$$

where the yield is the net number of counts in the peak corrected for the computer live time, I is the total beam charge, $\frac{d\sigma}{d\Omega}$ is the reaction cross section, and $\Delta\Omega$ is the effective spectrometer solid angle. E_{ff} is the detection efficiency and $\eta t = 2(\rho t N_0 / 14)$ denotes the total number of scattering centers in the target per unit area for the CH_2 target. The target thickness is given by ρt (ρ = density and t = physical thickness), and N_0 is Avogadro's number. The atomic mass of the CH_2 target is 14 amu and the factor 2 is included to account for the two scattering centers for each molecule. A correction for the pion survival fraction, S_{π}, in the flight path has also been included in the calculation. The solid angle variation across the focal plane is shown in Fig. 5.9 as a function of the focal position. This solid angle was evaluated with front-end software cuts of -103 mr $< \Theta_I < +103$ mr and -37 mr $< \Phi_I < +37$ mr. The restricted front-end opening corresponding to these software cuts defined the spectrometer solid angle, which in turn was used in calculating the reaction cross sections. The geometrical opening is shown in Fig. 5.10 where $SX0$ represents the vertical position and $SY0$ the horizontal position, both in units of 50 microns at the front-end.

62
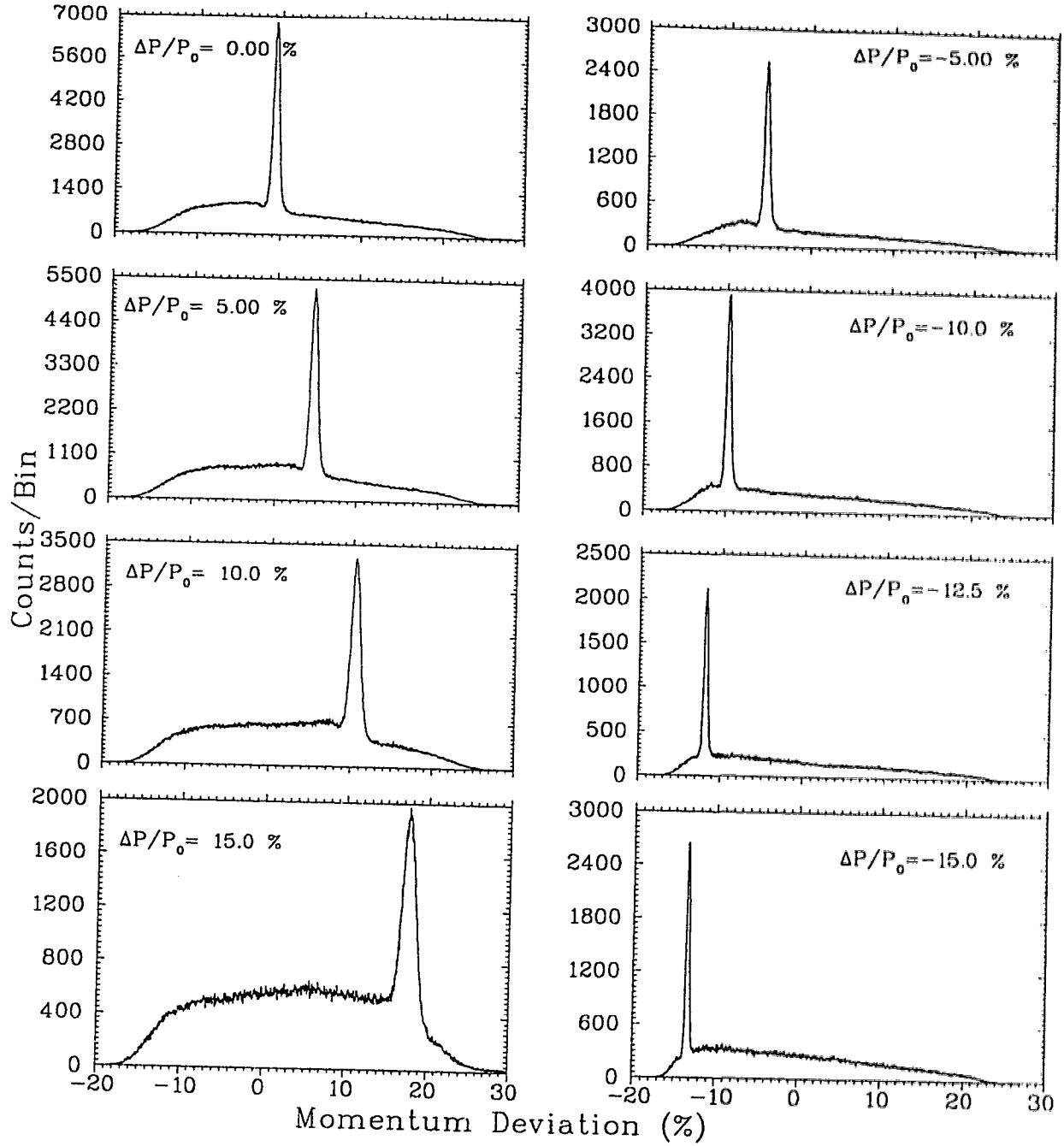
Figure 5.8: Focal plane spectra showing the pion yields for different field settings of the spectrometer. The net peak yield is extracted to calculate the solid angle in each case. These data were taken for the $pp \rightarrow d\pi^+$ reaction at 500 MeV and $\theta_\pi = 60°$ in the lab.
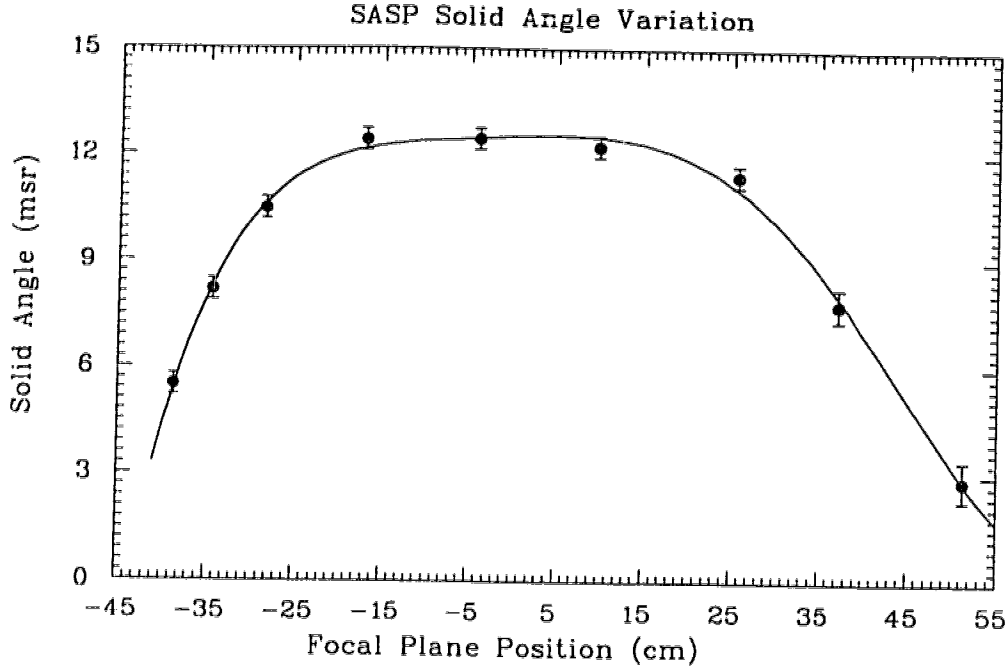
Figure 5.9: The solid angle variation of the SASP spectrometer as a function of focal plane position $SXFK$. The data used for this calculation are from $pp \rightarrow d\pi^+$ reaction at 500 MeV and $\theta_\pi = 60°$ in the lab.

5.9 Reaction Measurements

The main objective of the present experimental study was to measure several nuclear reactions to investigate the nuclear pion production in the bombarding proton energy range from 200 MeV up to 400 MeV. We have measured both the $A(p, \pi^+)A+1$ and the $A(p, \pi^-)A+1$ reactions on two p-shell nuclei and one d-shell nucleus at four different energies. The cross section and analyzing power angular distributions were determined for each reaction with kinematics chosen as shown in Table 5.1.

5.10 Cross Section Calculation

The cross sections for the nuclear transitions involved in each reaction were calculated by extracting the corresponding peak-yields of the observed bound states of the residual nucleus. The missing mass spectra for spin-up and spin-down incident protons
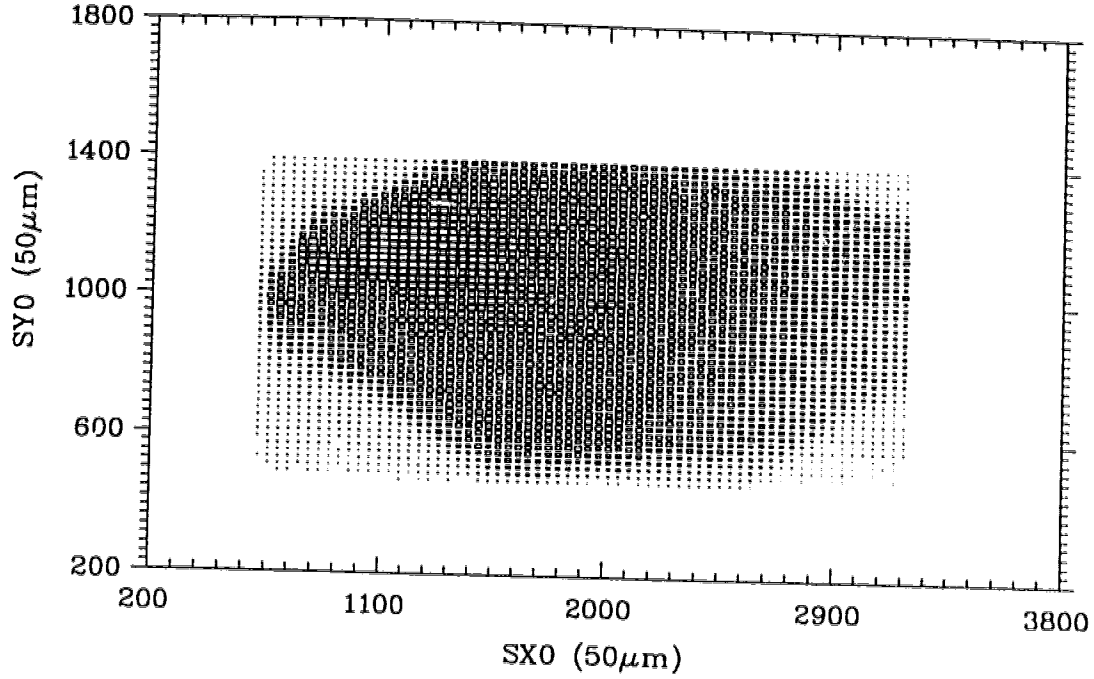
Figure 5.10: The selected front-end aperture of the spectrometer is shown. It defines the solid angle used for the absolute spectrometer normalization in calculating the reaction cross sections. See the text for details.

were obtained separately. A sample set of focal plane spectra is shown in Fig. 5.11 to illustrate the production yields of both positive pions and negative pions, with sufficiently good energy resolution to resolve the discrete final states of the residual nucleus. The major contribution to the resolution came from the energy straggling in the target because fairly thick targets had to be used to obtain sufficiently high count-rates. The energy spread of the incident beam also made some contribution. The energy resolution in the shown spectra is ~180 keV.

5.10.1 Differential Cross Section

The pion yields (Y_π) for the discrete final states in the residual nucleus are extracted from the experimental data. This yield has to be normalized using several experimental quantities to obtain the reaction cross section for any particular nuclear transition. The spin-dependent cross section is

$$\frac{d\sigma}{d\Omega_{c.m.}} = \frac{Y_\pi \cdot (Computer\ Live\ Time)}{I \cdot \eta t \cdot \Delta\Omega \cdot E_{ff} \cdot S_\pi} \left(\frac{d\Omega_{Lab}}{d\Omega_{c.m.}}\right) . \tag{5.28}$$

Table 5.1: The list of reactions and the associated kinematics selected for the present study is shown.

Reaction	Energy (MeV)	Angular Range in Lab (degrees)
$^{12}C(p,\pi^+)^{13}C$	250	25°, 30°, 50°, 62.5°, 70°, 80°, 90°, 100°
	280	25°, 30°, 40°, 50°, 70°, 100°
$^{13}C(p,\pi^+)^{14}C$	250	25°, 30°, 50°, 62.5°, 70°, 80°, 90°, 100°
	280	25°, 30°, 40°, 50°, 70°, 100°
$^{13}C(p,\pi^-)^{14}O$	221	25°, 45°, 65°, 85°
	280	25°, 45°, 65°, 85°, 105°
	350	25°, 45°, 65°, 85°
$^{26}Mg(p,\pi^-)^{27}Si$	280	25°, 45°
	350	25°, 45°
$^{40}Ca(p,\pi^+)^{41}Ca$	250	25°, 30°
	280	25°, 30°, 40°, 50°, 70°, 100°

The conversion factor, $\frac{d\Omega_{Lab}}{d\Omega_{c.m.}}$, is the jacobian of the solid angle transformation from the laboratory to the center-of-mass frame. Since the data acquisition computer is not able to process all the events at all times, the yield has to be corrected for the actual computer live time. E_{ff} is the overall detection efficiency of the system which is assumed to be determined entirely by the wire chambers. Also, one has to normalize the pion yield to the total number of incident protons (I), the effective solid angle of the spectrometer ($\Delta\Omega$), and the total number of scattering centers per unit target area (ηt). The pion decay while traversing the spectrometer is taken into account by correcting the yield for the pion survival fraction (S_π). Inserting these normalizations and corrections, the differential cross section is calculated as

$$\frac{d\sigma}{d\Omega_{c.m.}} = \frac{P(\downarrow)d\sigma/d\Omega_{c.m.}(\uparrow) + P(\uparrow)d\sigma/d\Omega_{c.m.}(\downarrow)}{P(\uparrow) + P(\downarrow)} , \qquad (5.29)$$

where, $\uparrow$ and $\downarrow$ denote the *up* and *down* incident beam polarization directions, respectively. The analyzing power is given by

$$A_y = -\left\{ \frac{d\sigma/d\Omega_{c.m.}(\uparrow) - d\sigma/d\Omega_{c.m.}(\downarrow)}{P(\downarrow)d\sigma/d\Omega_{c.m.}(\uparrow) + P(\uparrow)d\sigma/d\Omega_{c.m.}(\downarrow)} \right\} . \qquad (5.30)$$

The minus sign in front of the above expression is due to the fact that the SASP accepts the particles scattering to the right when looking in the beam direction.

66

5.11 Beam Current Normalization

The beam intensity was monitored with two independent devices throughout the experiment, once by using a secondary emission monitor (SEM), the second by the in-beam polarimeter (IBP). Both devices had been previously calibrated against a Faraday cup. The IBP is located upstream of the target while the SEM is downstream of the nuclear target on the beamline. There are several thin aluminum foils in the SEM which collect electrons from surface emission as the proton beam passes through the device. The number of electrons emitted by each proton is proportional to its energy loss in the foils. The total number of counts from the $p - p$ elastic scattering in the IBP target provides a measure of the total beam current. The agreement between the two methods should be within 1 to 2 % if both monitors work properly. However, the IBP target changes dimensions due to radiation damage after being exposed to the proton beam for a long time and gave a slightly lower value for the total beam current. It is more reliable to obtain the integrated beam charge from the SEM. The corresponding calibration of SEM versus Faraday cup shown in Fig. 5.12 as a function of the incident beam energy is a 4th order polynomial fit to the data points.
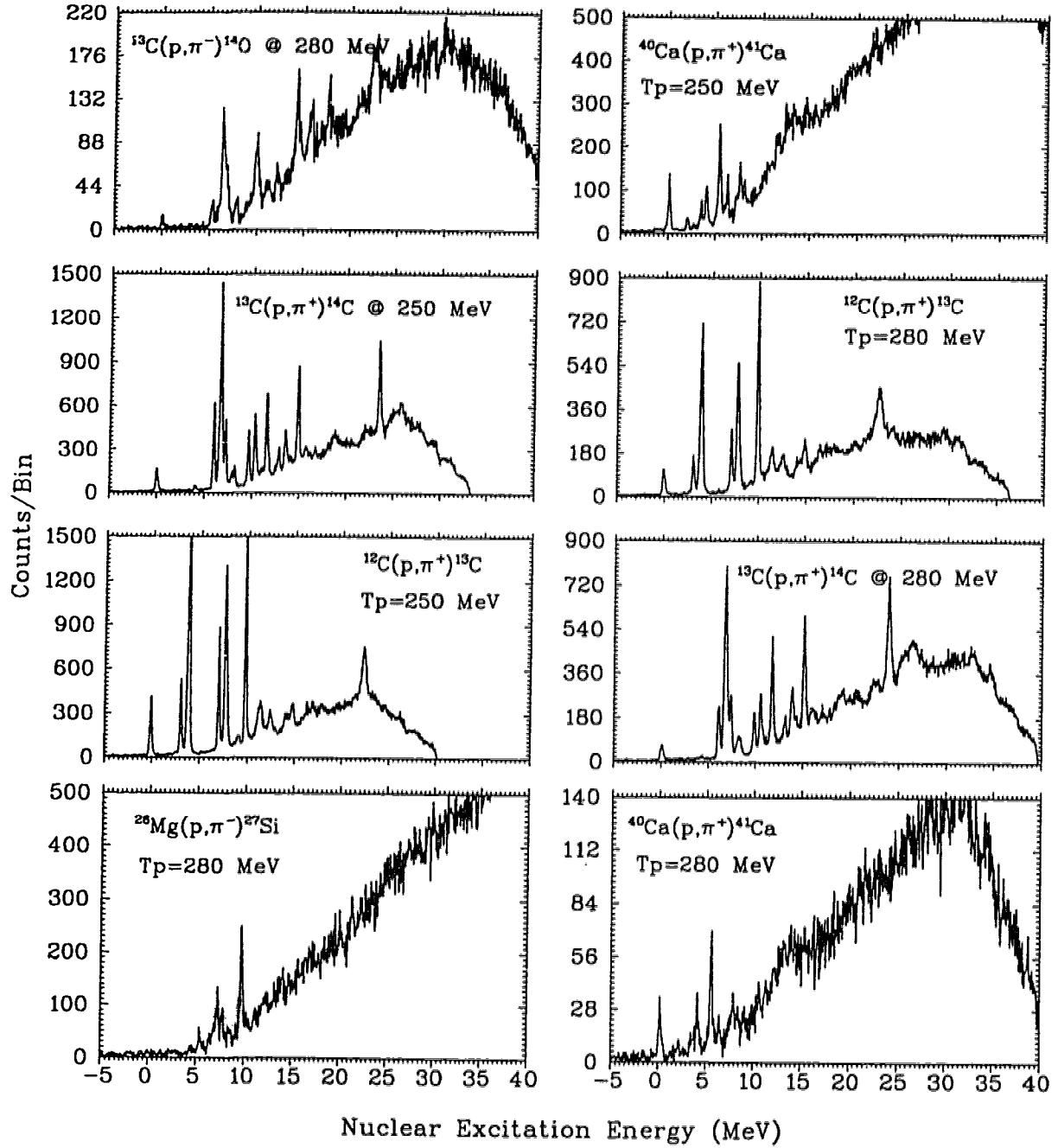
Figure 5.11: Examples of spectra showing the nuclear excitation energy of the residual nucleus in each reaction. Pion yields from positive and negative pion production are shown at bombarding energies of 250 MeV and 280 MeV at a lab scattering angle of $25°$.

68
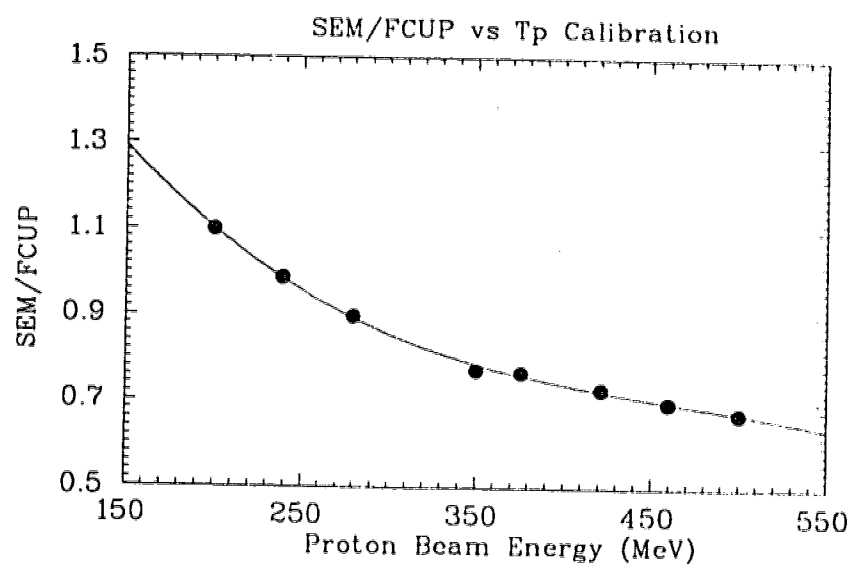
Figure 5.12: The calibration of the secondary emission monitor (SEM) against the Faraday cup is shown as a function of incident beam energy. This calibration is used for the beam current normalization.

5.12 Pion Decay Correction

Some of the pions decay along their flight paths through the spectrometer. A correction for the pion survival fraction is necessary in extracting the pion yield. The pion survival fraction is calculated by the relation

$$S_\pi = \exp\left[-\frac{t}{\gamma \tau_0}\right] = \exp\left[-\frac{L_\pi}{\gamma \beta c \tau_0}\right] = \exp\left[-\frac{m_\pi L_\pi}{p_\pi c \tau_0}\right] , \qquad (5.31)$$

where t is the pion survival time in the spectrometer. The pion decay length, $c\tau_0$, is 7.803 m. The decay fraction depends on the effective flight-path (L_π), which varies along the focal plane detectors and with the pion momentum. In calculating the effective flight-path through SASP one has to take into account the geometrical positions of the multiwire chambers and the scintillator paddles as well as the pion decay into muons and the associated directions of these decay-muons. A Monte Carlo calculation [Fa96] to obtain the effective flight-path for pions traversing SASP. as a function of the central momentum and the momentum deviation of the pions has been done. A detailed description of this calculation is found in [Be96].

5.13 Detection Efficiency

Another important characteristic in the cross section normalization of the system is the total detection efficiency. The scintillation detectors used were almost 100 % efficient so that the detection efficiency is dominated by the VDC chambers: (the FEC was not in use). An accountable background enters for pion detection in (p, π) measurements since a relatively high beam intensity has to be used to compensate for the low cross section. This leads to a situation where the background seen in VDC1 is not the same as that in VDC2. Therefore, each plane of the two VDCs was independently examined for its own detection efficiency. It turned out that the efficiencies of $X1$ and $U1$ in VDC1 were almost equal as were those of VDC2. However, the efficiency of VDC1 was higher than that of VDC2 (typically the efficiency of VDC1 was 90% and that of VDC2 was 87%). In the second step, a good event sample was isolated by removing the background and in order to check the efficiencies of the $U1$ and $U2$ wire planes. It was found that the X planes had same efficiencies as the U planes in each VDC so that the total detection efficiency was calculated as

$$Eff = \left[E_{ff}(U1) * E_{ff}(U2)\right]^2 . \qquad (5.32)$$

5.14 Error Calculations

Only the statistical errors have been included in the results. A detailed description of the error calculation is given in Appendix C. The statistical error in spin-up polarization is calculated as

$$\Delta P^+ = \frac{1}{A} \left[\Delta^2 \varepsilon^+ + (P^+)^2 \Delta^2 A \right]^{\frac{1}{2}} , \qquad (5.33)$$

and that in spin-down case is calculated with the corresponding spin-down variables in the same way (see section 4.1.2). The error in the analyzing power (ΔA) for the IBP target is assumed to be 0.01, and that in the left-right asymmetry is given by

$$\Delta \varepsilon = \sqrt{\frac{1 - \varepsilon^2}{L + R}} . \qquad (5.34)$$

The statistical error in the calculation of differential cross section is determined as

$$d\sigma = \frac{1}{(P^+ + P^-)} \left\{ \left((P^-)^2 \Delta^2 \sigma^+ + (P^+)^2 \Delta^2 \sigma^- \right) + \left(\frac{\sigma^+ - \sigma^-}{P^+ + P^-} \right)^2 \right.$$

$$\left. \times \left[(P^+)^2 \Delta^2 P^- + (P^-)^2 \Delta^2 P^+ - \frac{2}{A^2} \left(\frac{\varepsilon^+ \cdot \varepsilon^-}{A^2} \right)^2 \Delta^2 A \right] \right\}^{\frac{1}{2}} . \qquad (5.35)$$

where σ is the differential cross section and $\Delta\sigma$ is its statistical error, while $+$ and $-$ indicate the spin-up and spin-down cases, respectively. The $\Delta\sigma$ for each case is obtained from the yield of the corresponding final state in the missing mass spectrum. A similar calculation gives the statistical error in the analyzing power as

$$\Delta A_y = \left(\frac{1}{P^- \sigma^+ + P^+ \sigma^-} \right)^2 \left\{ (P^+ + P^-)^2 \left[(\sigma^-)^2 \Delta^2 \sigma^+ + (\sigma^+)^2 \Delta^2 \sigma^- \right] \right.$$

$$\left. + (\sigma^+ - \sigma^-)^2 \left[(\sigma^-)^2 \Delta^2 P^+ + (\sigma^+)^2 \Delta^2 P^- + \frac{2\sigma^+ \sigma^- P^+ P^-}{A^2} \Delta^2 A \right] \right\}^{\frac{1}{2}} . \qquad (5.36)$$

The analyzing power of the $p - p$ elastic scattering on the thin CH_2 target in IBP is required in order to measure the beam polarization. This quantity is determined by obtaining the data from phase shift analysis of $p - p$ elastic scattering data [Ar95] and correcting the analyzing powers for the Carbon contamination of the CH_2 target [Wa96]. This calibration shown in Fig. 5.13 as a function of the incident energy is a 4th order polynomial fit and the errors shown are indicative of the accuracy of the partial wave analysis [Ar95].
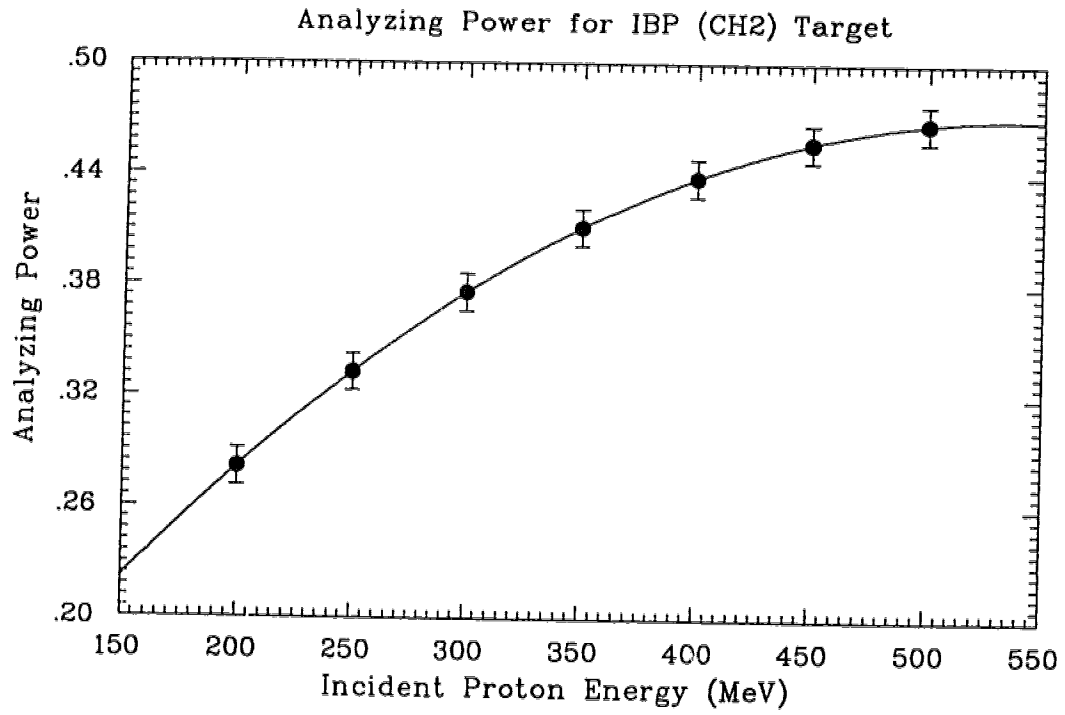
Figure 5.13: The calibration of the analyzing power for $p - p$ elastic scattering from the thin CH_2 target in the IBP as a function of the incident beam energy. The error bars are based on uncertainties of phase shift solutions.

72

Chapter 6

Results

The results extracted from the present study of the reactions $A(p, \pi^{\pm})A+1$ and $A(p, \pi^{\pm})X$ are summarized in this chapter. The former process allows one to study the discrete bound states of the residual nucleus, while pion production to the continuum can be used to study the mechanism of pion production process. The cross section and analyzing power angular dependencies have been determined only for the strongly-populated discrete final states as well as for two or more nuclear excitations in the continuum region of each reaction. The differential cross section, $d\sigma/d\Omega$, for each of the observed nuclear transitions is given in units of (nb/sr) in conformity with the usual convention. The analyzing power, A_y, a unitless quantity, is a measure of the asymmetry of π production at a given setting between beam protons polarized up and down with respect to the reaction plane. The variation of $d\sigma/d\Omega$ and A_y with momentum transfer provides information on the production process in the case of the continuum production and can lead to nuclear structure information in the case of production to discrete states. The physics content of the results will be presented in the next chapter.

6.1 Analysis of the Discrete Final States

The cross section and analyzing-power angular distributions calculated for the bound states of $A(p, \pi)A+1$ are given in this section. The spin and parity assignments for these states are taken from the most recent compilation [Aj91]. Some of these spin-parity designations will be questioned in this present study (see the discussion). Reactions involved in this (p, π) study are $^{12}C(p, \pi^+)^{13}C$, $^{13}C(p, \pi^+)^{14}C$, $^{40}Ca(p, \pi^+)^{41}Ca$ for positive pion production, and $^{13}C(p, \pi^-)^{14}O$ for the production of negative pions. These reactions

73

were measured at different incident proton energies and momentum transfers. All the angular distributions of the calculated results are plotted as a function of the scattering angle in the center-of-mass frame. See Appendix A for the numerical values of the results which include statistical errors only. A discussion on systematic and normalization errors is also included in this appendix.

6.1.1 $^{12}C(p, \pi^+)^{13}C$ Reaction at 250 and 280 MeV

The reaction information is obtained by detecting the outgoing pions in an exclusive measurement. A typical pion spectrum observed at the spectrometer focus is shown in Fig. 6.1 which illustrates the relative strengths of the nuclear excited states of the residual nucleus, ^{13}C. The reaction was observed up to 40 MeV excitation in a single momentum bite because of the large momentum acceptance of the spectrometer.
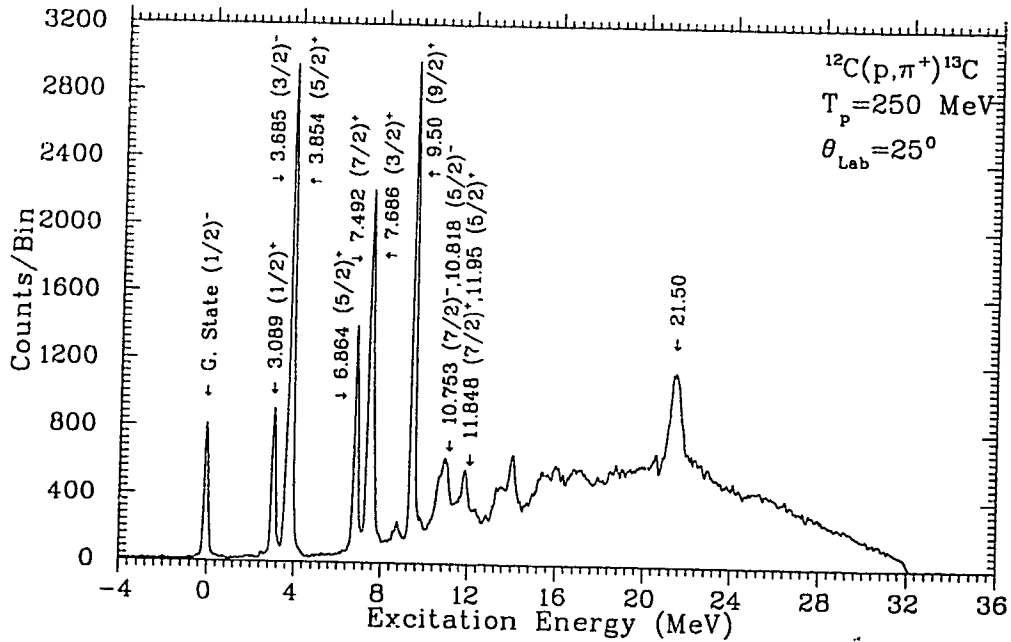
Figure 6.1: The recoil nucleus excitation spectrum for $^{12}C(p, \pi^+)^{13}C$ reaction at 250 MeV and 25° laboratory scattering angle.

The peaks sitting on the background continuum correspond to excited nuclear levels (or states) of the final nucleus. The background continuum was fitted by a 8th-order polynomial and subtracted from the spectrum, leaving only the resultant spectrum of final states, which were fitted to gaussian shapes using a peak-fitting program [Ma96].

In this program the line widths were set to the value obtained for a single isolated final state with relatively higher statistics (eg. the $\frac{9}{2}^+$ at 9.5 MeV) and the centroids to the values recorded in the literature [Aj91]. Only the numerical yields in the peaks were allowed to vary. This procedure allows yields to be extracted not only from fully resolved peaks but also from peaks which are not fully resolved (eg. the 3.685 and 3.854 MeV states). The single state line shape and the calibration of the focal plane were known well enough to permit such a procedure (see appendix B). The extracted peak yields are proportional to the strengths of the observed transitions, and were used to obtain the physical observables, the differential cross section and analyzing power. The results, for the strongest transitions, are shown in Figs. 6.2 and 6.3.

The calculated differential cross sections and analyzing powers for $^{12}C(p, \pi^+)^{13}C$ at 280 MeV are plotted as a function of the center-of-mass angle and shown in Figs. 6.4 and 6.5 for the same nuclear transitions as shown in the case of 250 MeV. The over-lapping data points are those determined from two different measurements with similar kinematic settings.
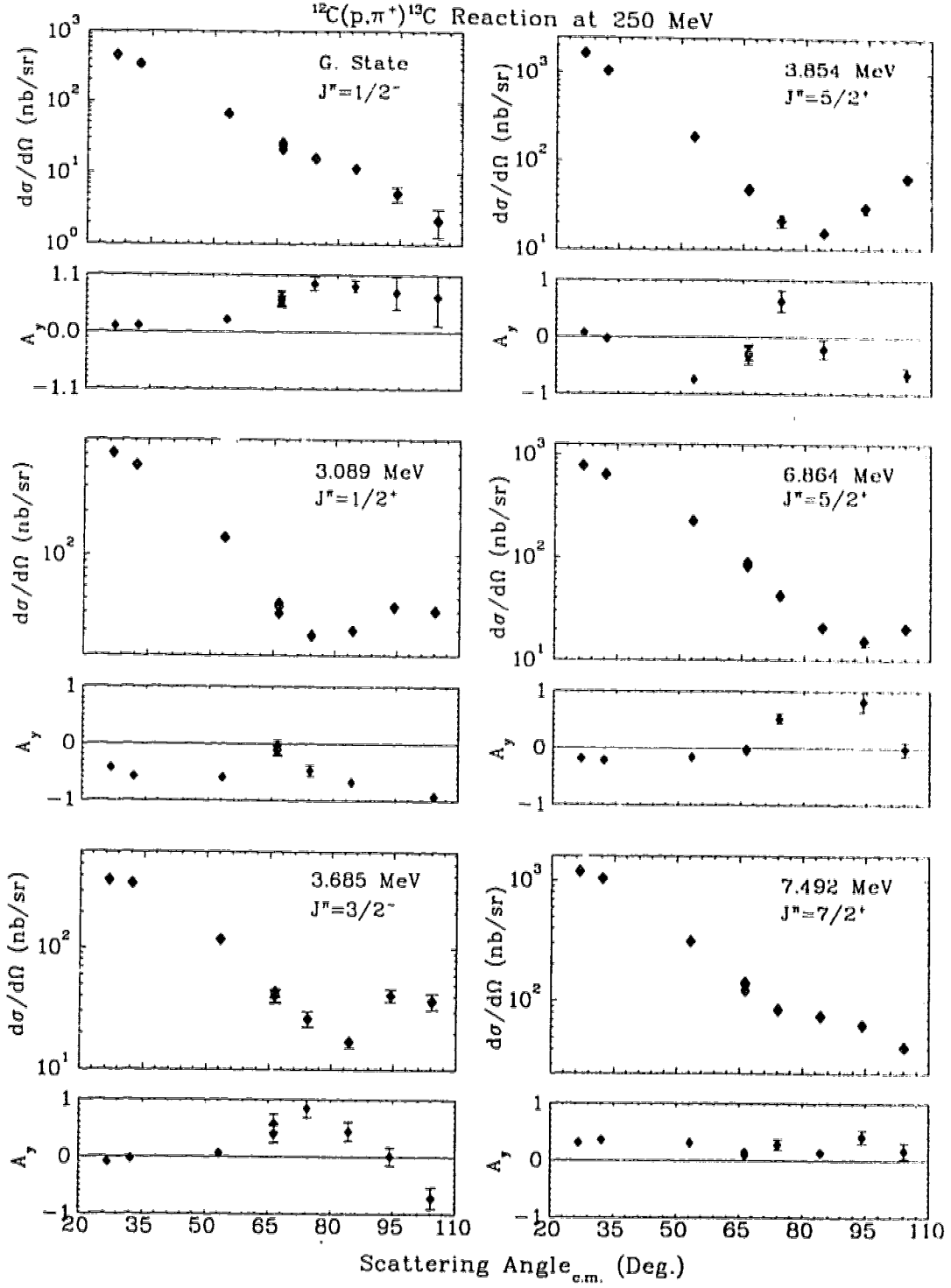
Figure 6.2: The differential cross section and analyzing power angular distributions for the $^{12}C(p, \pi^+)^{13}C$ reaction measured at 250 MeV.
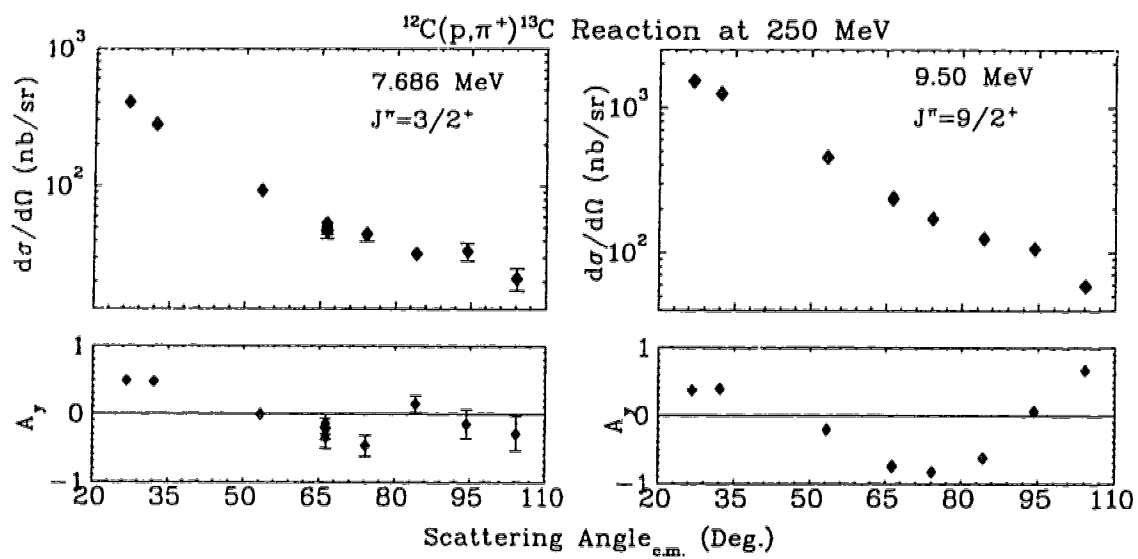
Figure 6.3: The differential cross section and analyzing power angular distributions for the $^{12}C(p, \pi^+)^{13}C$ reaction measured at 250 MeV.
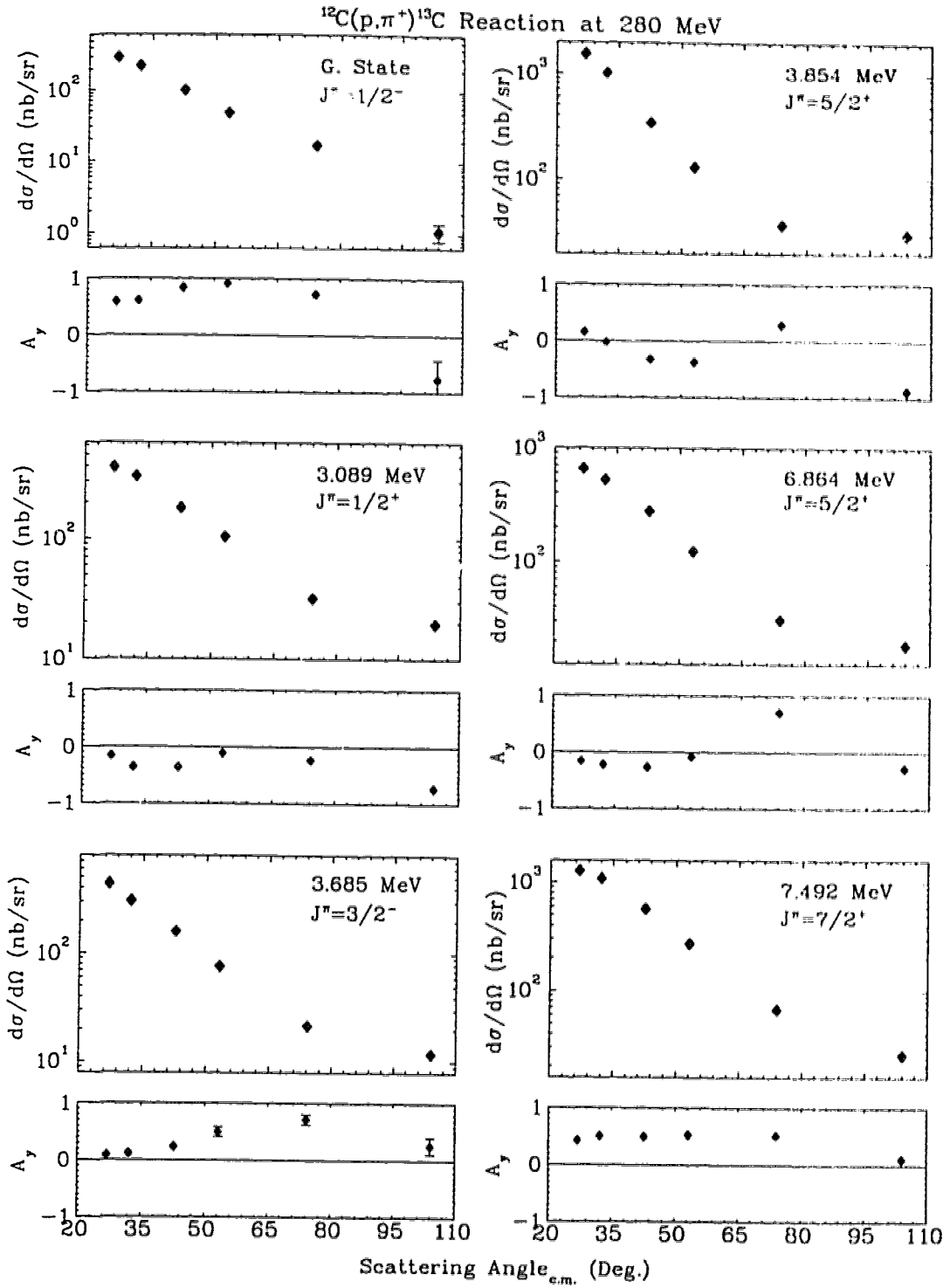
Figure 6.4: The differential cross section and analyzing power angular distributions for the ^{12}C(p, π^+)^{13}C reaction measured at 280 MeV.
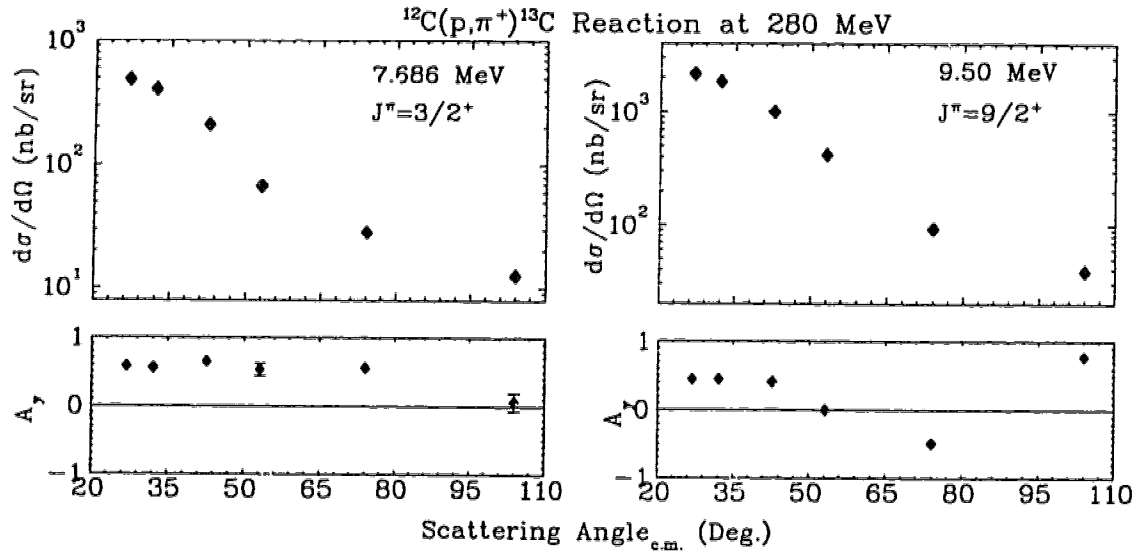
Figure 6.5: The differential cross section and analyzing power angular distributions for the $^{12}C(p, \pi^+)^{13}C$ reaction measured at 280 MeV.

6.1.2 $^{13}C(p, \pi^+)^{14}C$ Reaction at 250 and 280 MeV

The observed recoil nuclear excitation spectrum derived from the outgoing pions detected at the spectrometer focus is shown in Fig. 6.6 which indicates the relative strengths of different nuclear channels to the bound states as well as to the continuum. The spin and parity assignments listed for different bound states of the residual nucleus are based on known information [Aj91]. New evidence found in the present study for spin and parity assignments of some of the high-spin states will be discussed in the next section. The differential cross sections and analyzing powers have been extracted for the strongest transitions. In Fig. 6.7 are plotted $d\sigma/d\Omega$ and A_y for the ground, 6.094, 6.728, 7.012, 7.341, and 8.318 MeV states as a function of center-of-mass angle, and in Fig. 6.8 are those of the 9.801, 10.425, 10.736, 11.666, 14.868, and 23.288 MeV states.
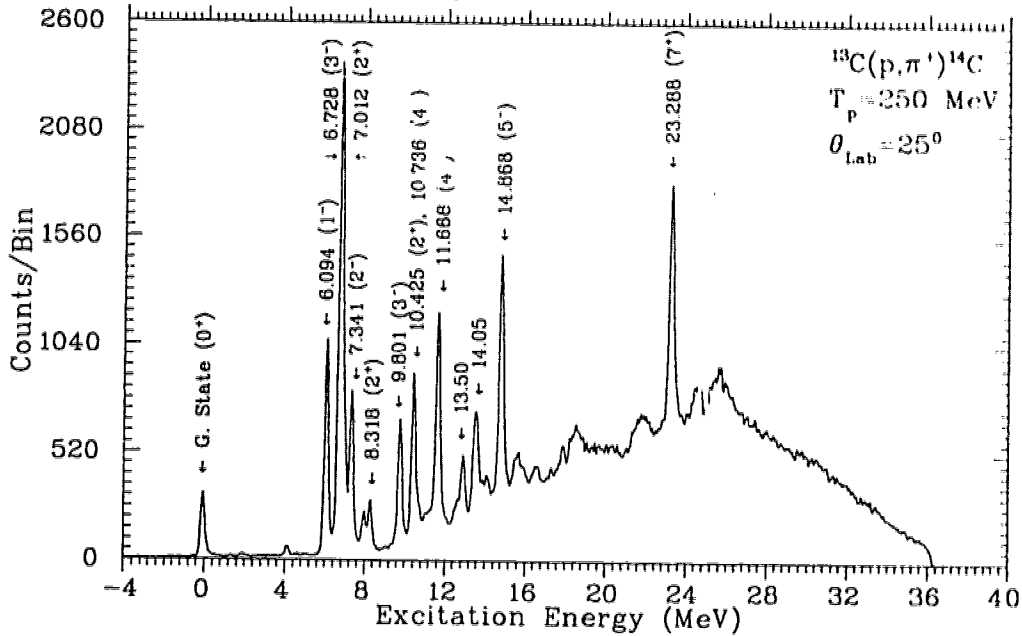
Figure 6.6: The recoil nucleus excitation spectrum for the $^{13}C(p, \pi^+)^{14}C$ reaction at 250 MeV and 25° laboratory scattering angle.

The same measurements were repeated for $^{13}C(p, \pi^+)^{14}C$ with 280 MeV beam protons. The extracted differential cross sections and analyzing powers for the same transitions as observed at 250 MeV are plotted as a function of the center-of-mass scattering angle in Figs. 6.9 and 6.10.

$^{13}C(p,\pi^+)^{14}C$ Reaction at 250 MeV
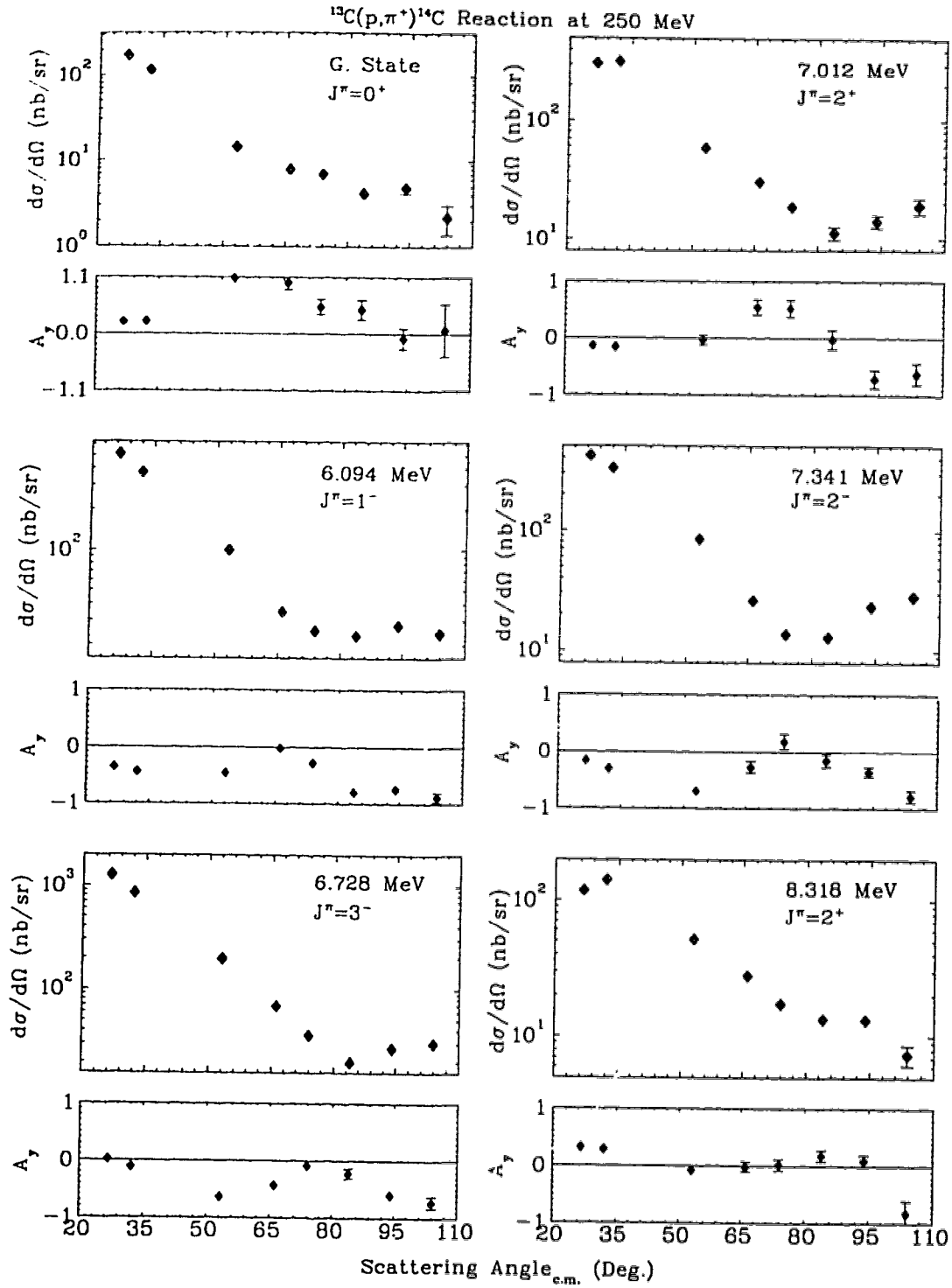
Figure 6.7: The differential cross section and analyzing power angular distributions for the $^{13}C(p, \pi^+)^{14}C$ reaction measured at 250 MeV.
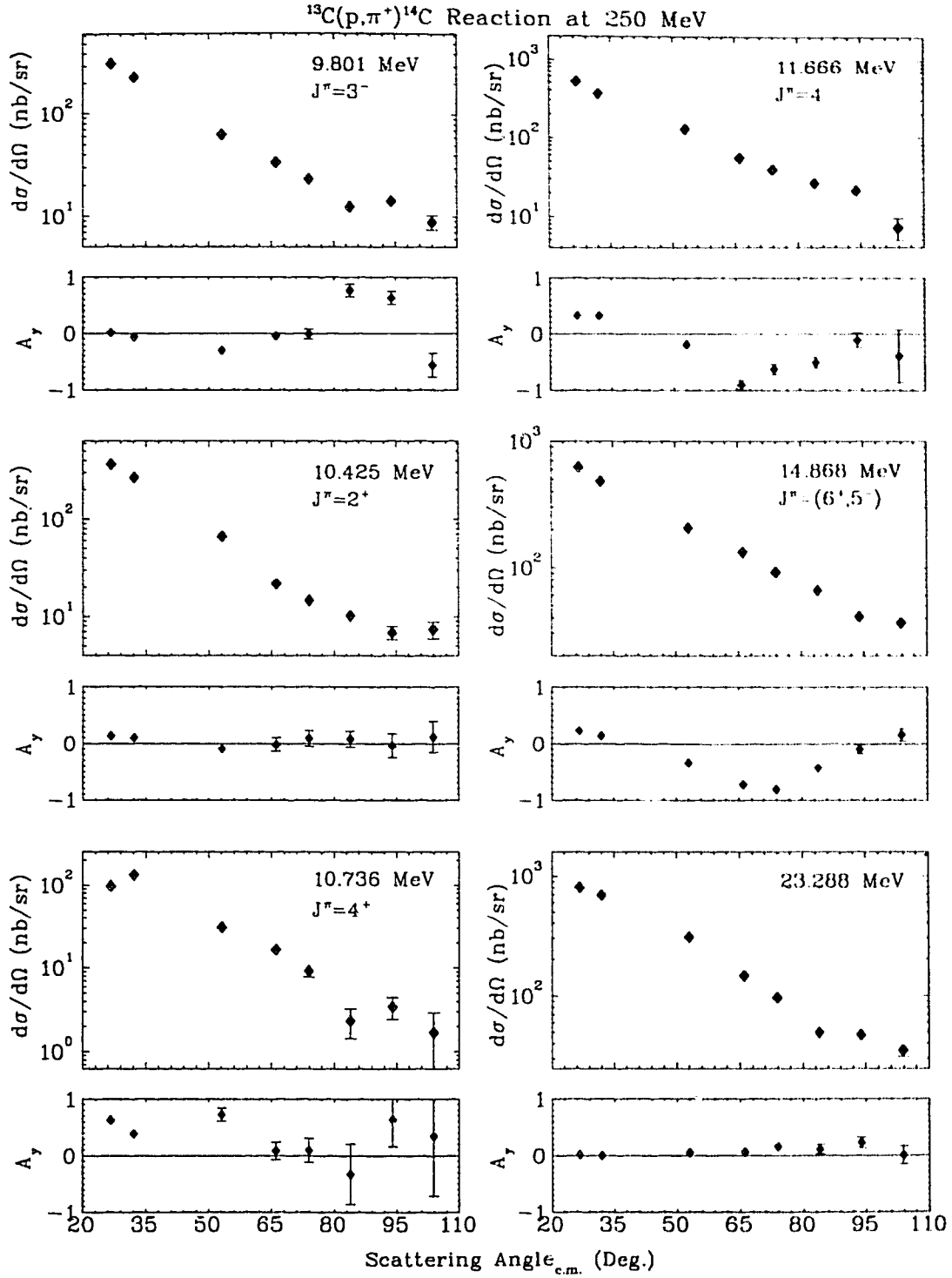
Figure 6.8: The differential cross section and analyzing power angular distributions for the $^{13}C(p, \pi^+)^{14}C$ reaction measured at 250 MeV.
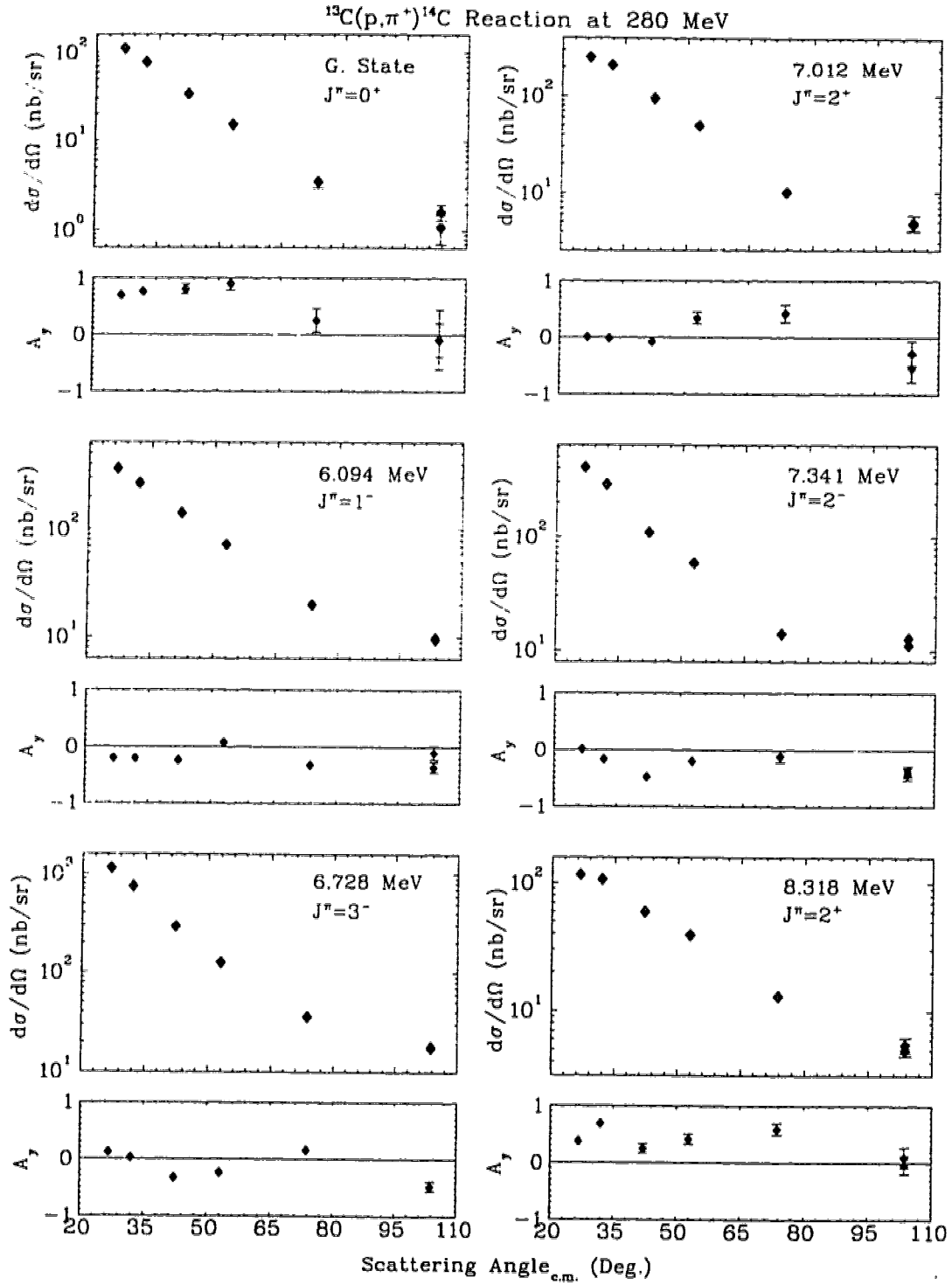
Figure 6.9: The differential cross section and analyzing power angular distributions for the $^{13}C(p, \pi^+)^{14}C$ reaction measured at 280 MeV.
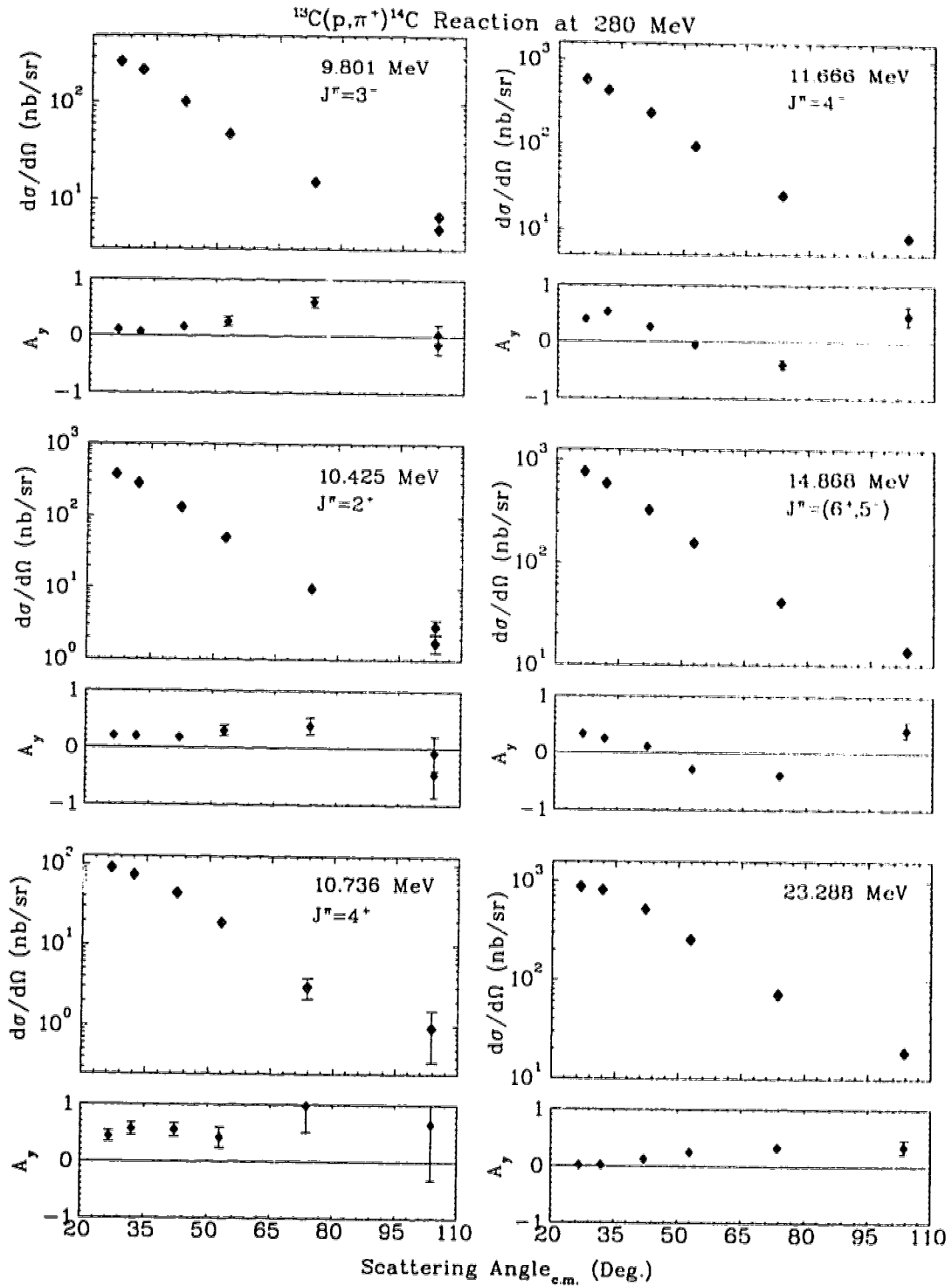
Figure 6.10: The differential cross section and analyzing power angular distributions for the $^{13}C(p, \pi^+)^{14}C$ reaction measured at 280 MeV.

6.1.3 $^{40}Ca(p, \pi^+)^{41}Ca$ Reaction at 250 and 280 MeV

Due to the restrictions imposed by the allocated beam time it was only possible to take data on the $^{40}Ca(p, \pi^+)^{41}Ca$ reaction at laboratory scattering angles of 25° and 30° at 250 MeV. Therefore, the angular distributions of the differential cross sections and analyzing powers were not obtained. A typical recoil nucleus excitation spectrum is shown in Fig. 6.11 which displays the observed low-lying bound states of the residual nucleus (^{41}Ca) as well as the continuum.
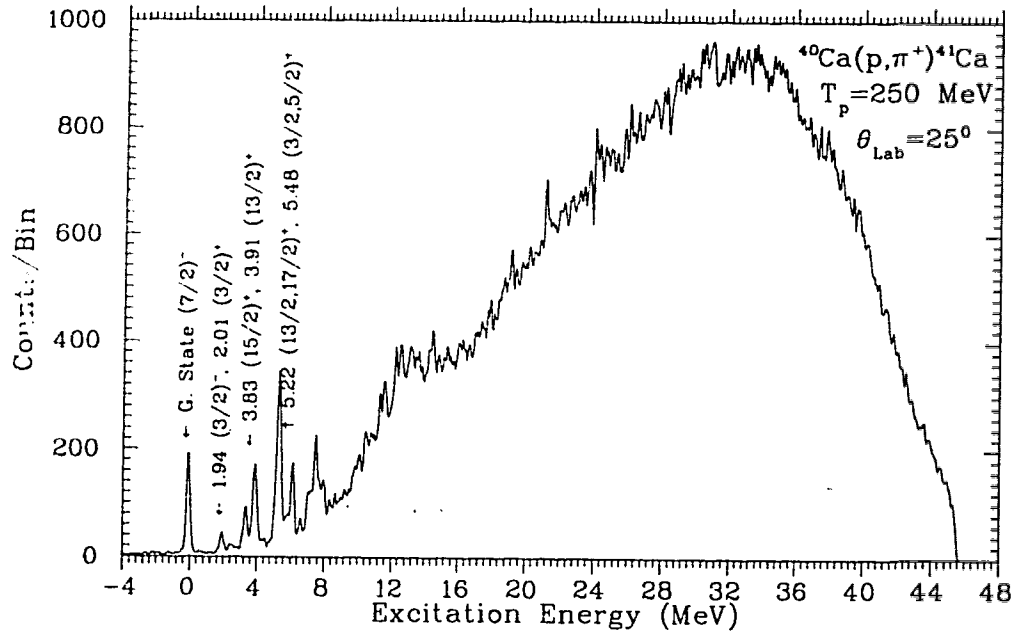
Figure 6.11: The recoil nucleus excitation spectrum for the $^{41}Ca(p, \pi^+)^{41}Ca$ reaction at 250 MeV and 25° laboratory scattering angle.

The relative strength of the bound states was observed to drop sharply with increasing momentum transfer for the $^{40}Ca(p, \pi^+)^{41}Ca$ reaction at 280 MeV. As a result, the measurement of cross sections and analyzing powers for the bound states was limited to three forward scattering angles (25°, 30°, and 40°), and hence the angular distributions were not well determined. The cross section and analyzing power angular dependencies will be given in section 6.2.3 for three different excitations in the continuum region for $^{40}Ca(p, \pi^+)^{41}Ca$ at this beam energy.

6.1.4 $^{13}C(p, \pi^-)^{14}O$ Reaction at 221, 280 and 350 MeV

The differential cross sections and analyzing powers for the production of negative pions were determined at 221 MeV. Population of bound states of the final nucleus for the (p, π^-) reaction is weak compared to that for the (p, π^+) reaction shown in the previous sections. The reaction was measured at four different scattering angles and the results were determined only for the strongly-populated states of the ^{14}O recoil nucleus. The missing mass spectrum for $^{13}C(p, \pi^-)^{14}O$ observed with 280 MeV incident protons at $25°$ lab angle is shown in Fig. 6.12 which displays the strongly populated excited states of the residual nucleus (^{14}O). The spin and parity assignments of these bound states are based on known information [Aj91]. The differential cross sections and analyzing powers extracted for these bound states are plotted in Figs. 6.13 and 6.14 as a function of the scattering angle in the center-of-mass frame for this reaction at 221 MeV.
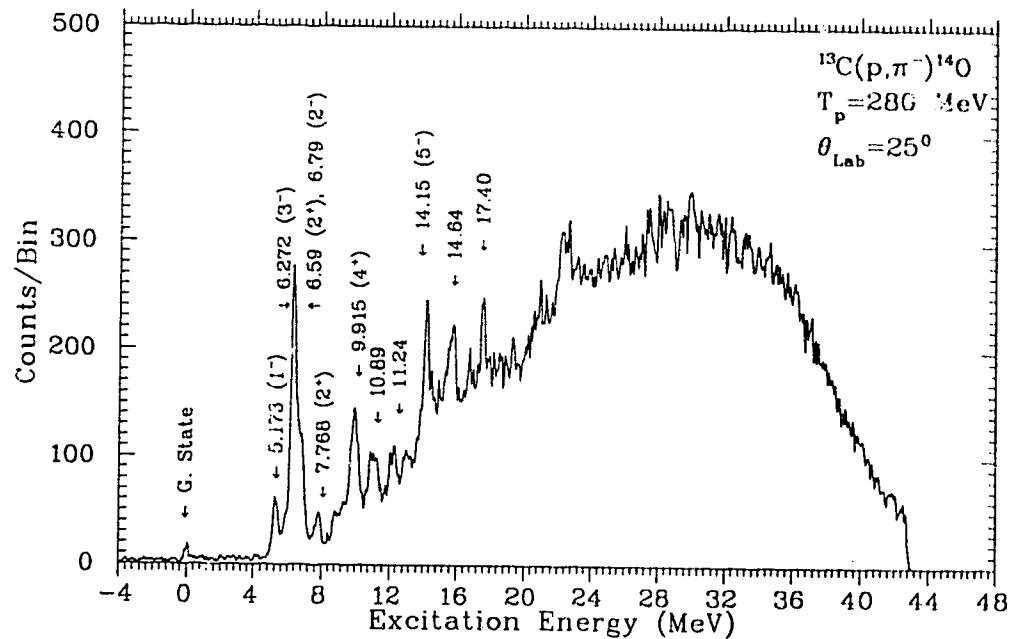
Figure 6.12: The recoil nucleus excitation spectrum for the $^{13}C(p, \pi^-)^{14}O$ reaction at 280 MeV and 25° laboratory scattering angle.
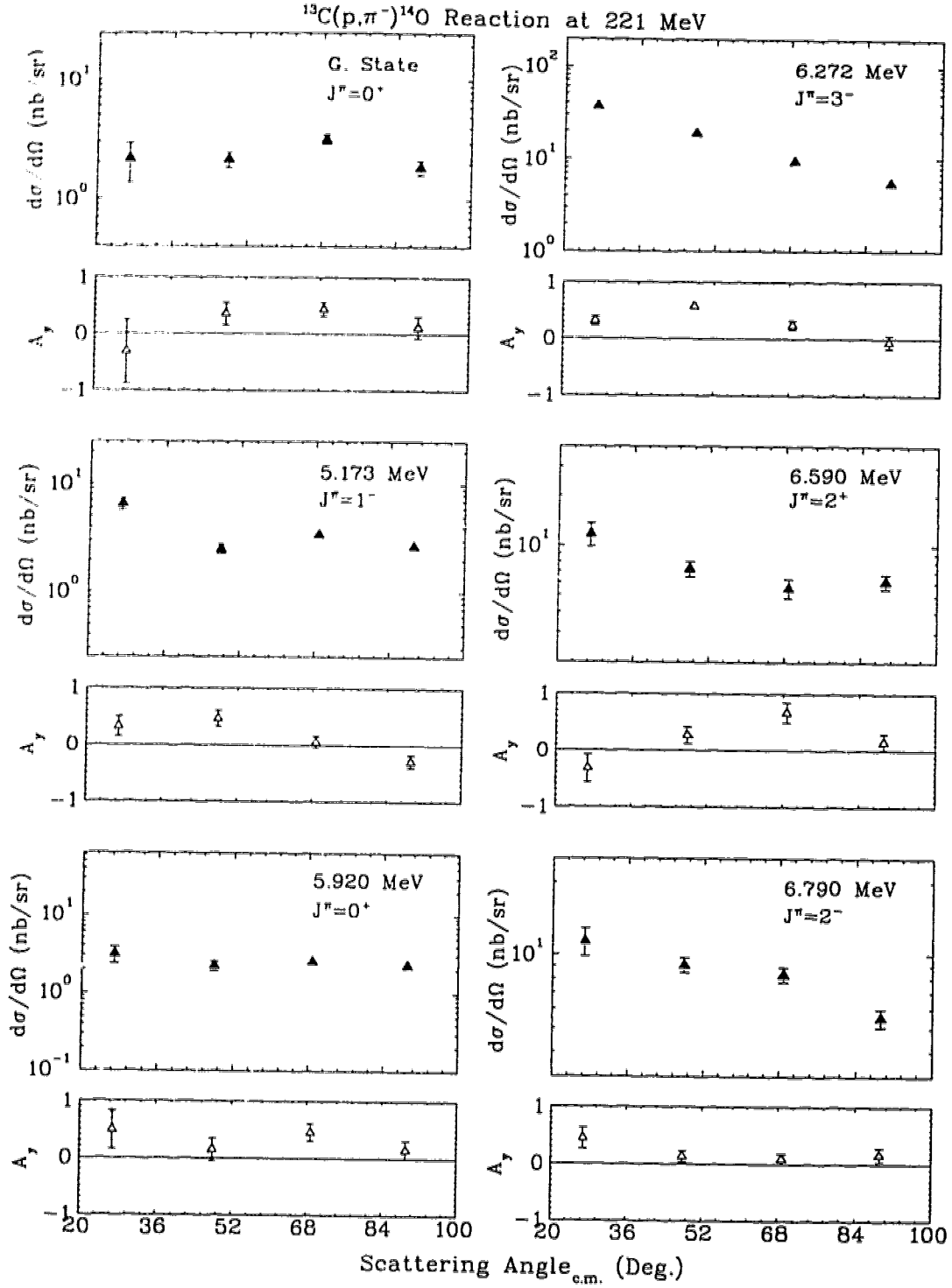
Figure 6.13: The differential cross section and analyzing power angular distributions for the $^{13}C(p, \pi^-)^{14}O$ reaction measured at 221 MeV.
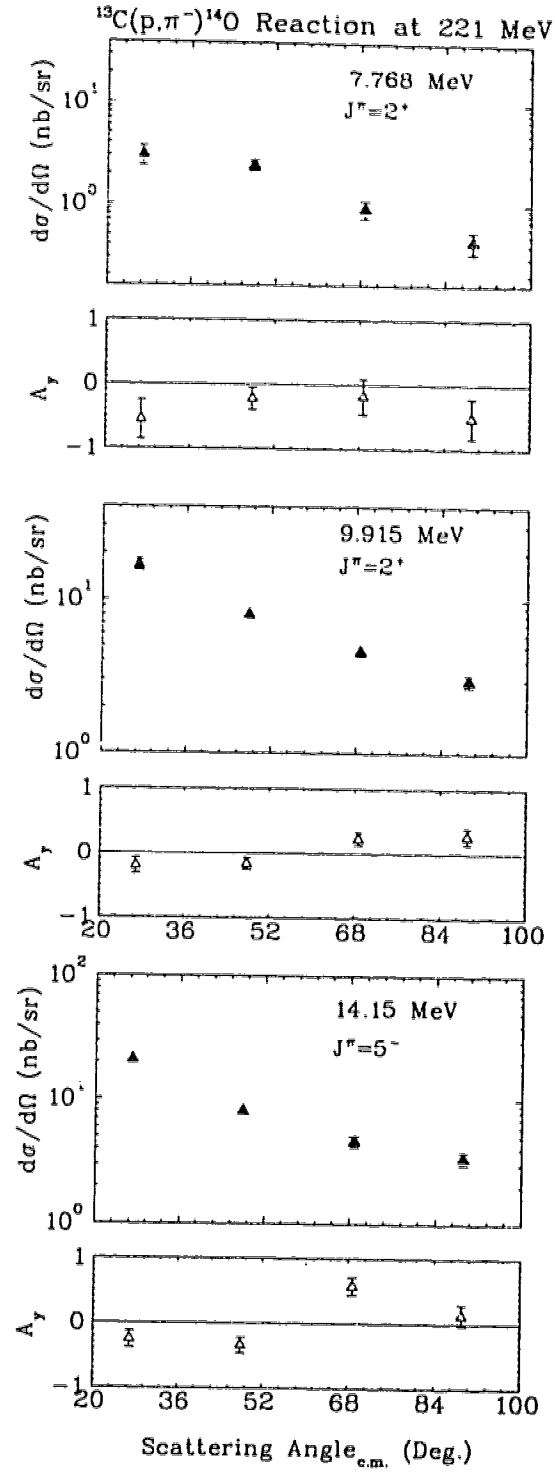
Figure 6.14: The differential cross section and analyzing power angular distributions for the $^{13}C(p, \pi^-)^{14}O$ reaction measured at 221 MeV.

The measurements described for 221 MeV were repeated for the same reaction at a beam energy of 280 MeV. The calculated differential cross sections and analyzing powers are plotted as a function of the center-of-mass angle. These results are shown in Figs. 6.15 and 6.16 for the excited states shown in Fig. 6.12.

The third energy at which the production of negative pions was investigated was 350 MeV. The cross section is very low at this energy. The differential cross section and analyzing power results for the discrete final states are given in Figs. 6.17 and 6.18 where the results are plotted as a function of the center-of-mass scattering angle.
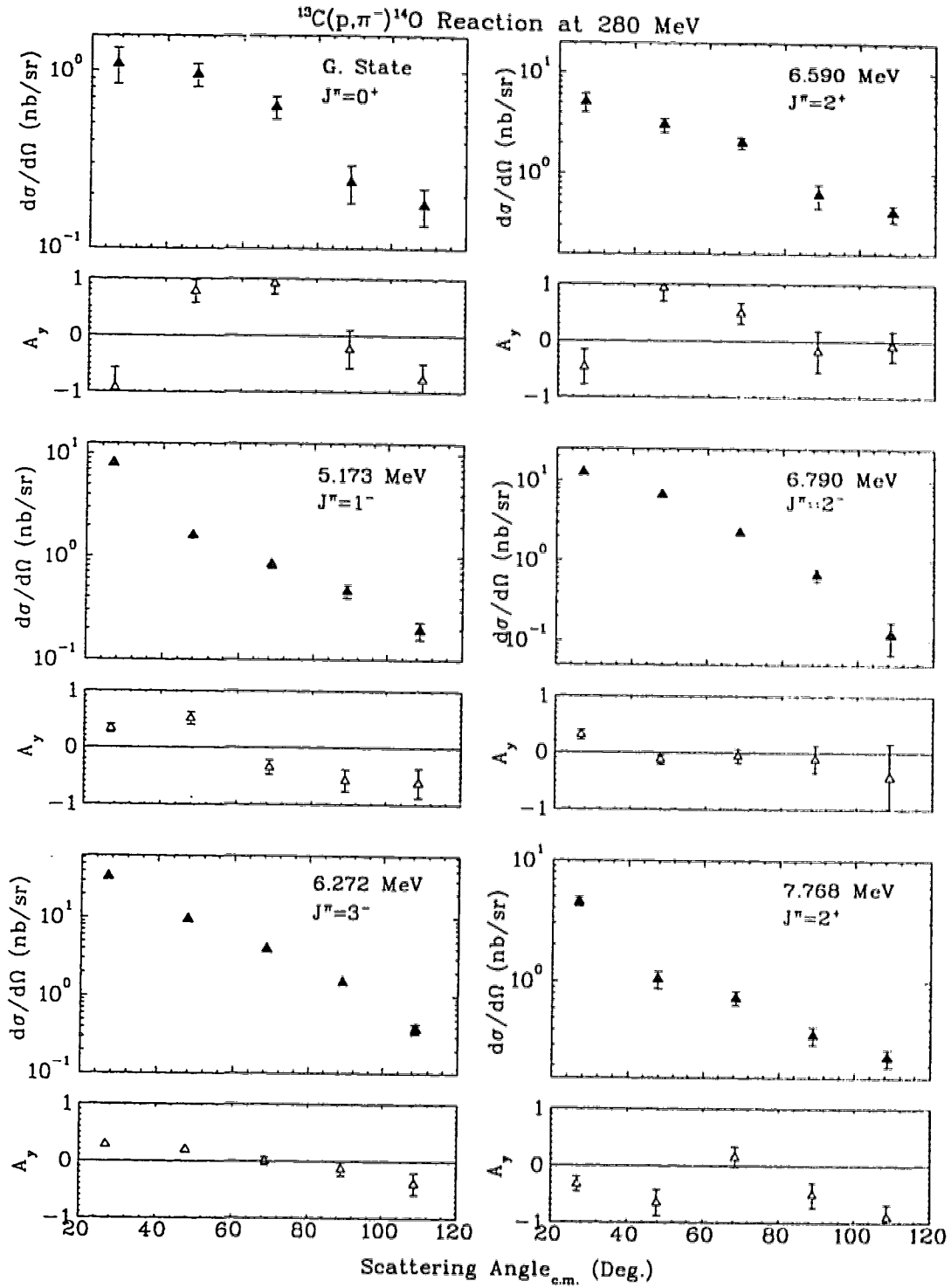
Figure 6.15: The differential cross section and analyzing power angular distributions for the $^{13}C(p, \pi^-)^{14}O$ reaction measured at 280 MeV.
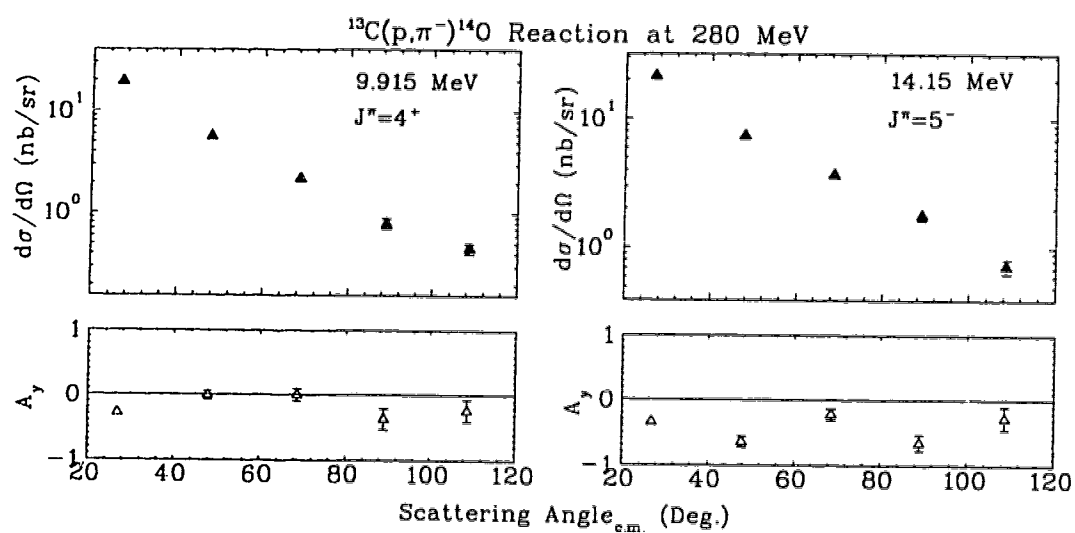
Figure 6.16: The differential cross section and analyzing power angular distributions for the $^{13}C(p, \pi^-)^{14}O$ reaction measured at 280 MeV.
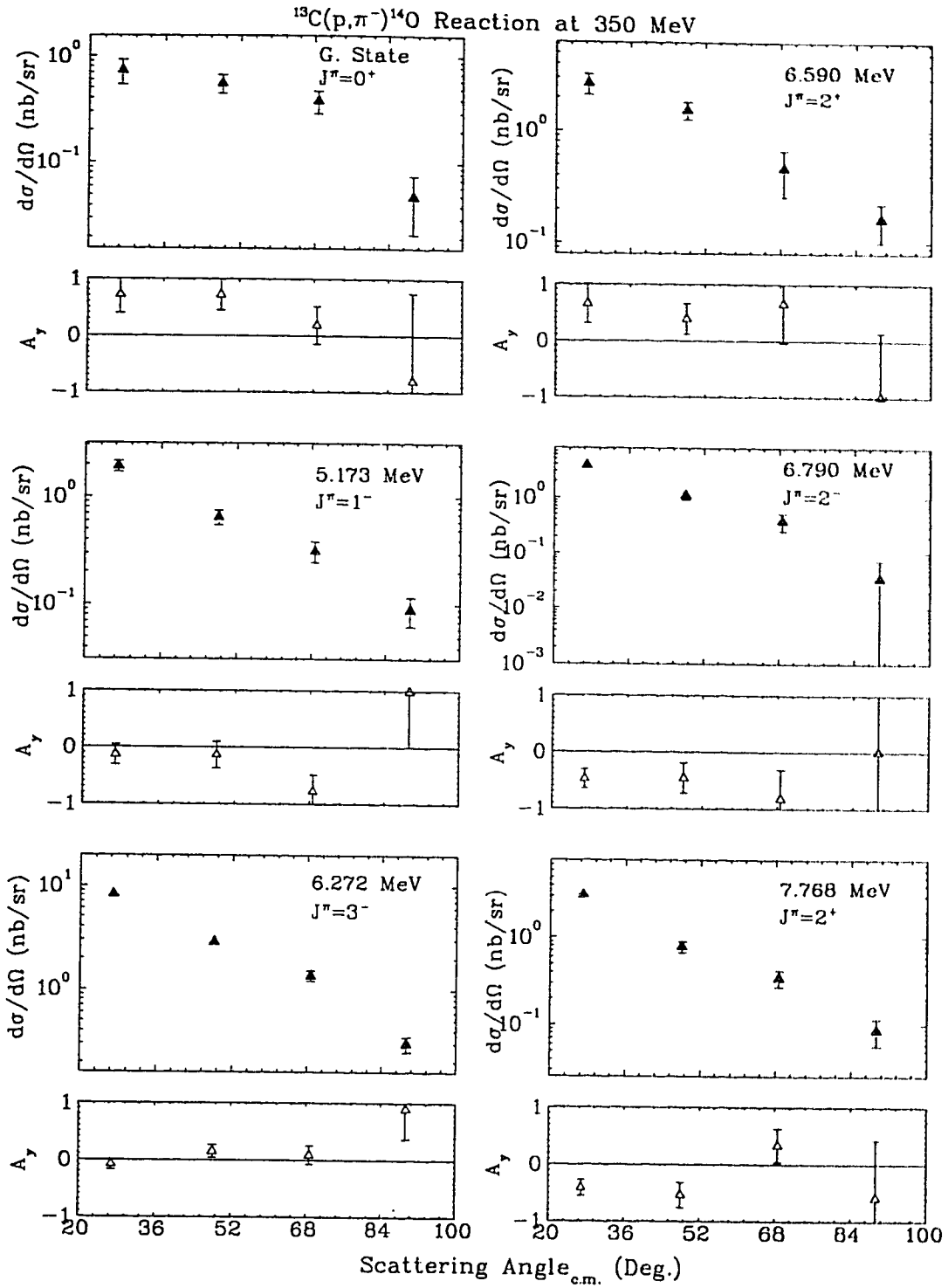
Figure 6.17: The differential cross section and analyzing power angular distributions for the $^{13}C(p, \pi^-)^{14}O$ reaction measured at 350 MeV.
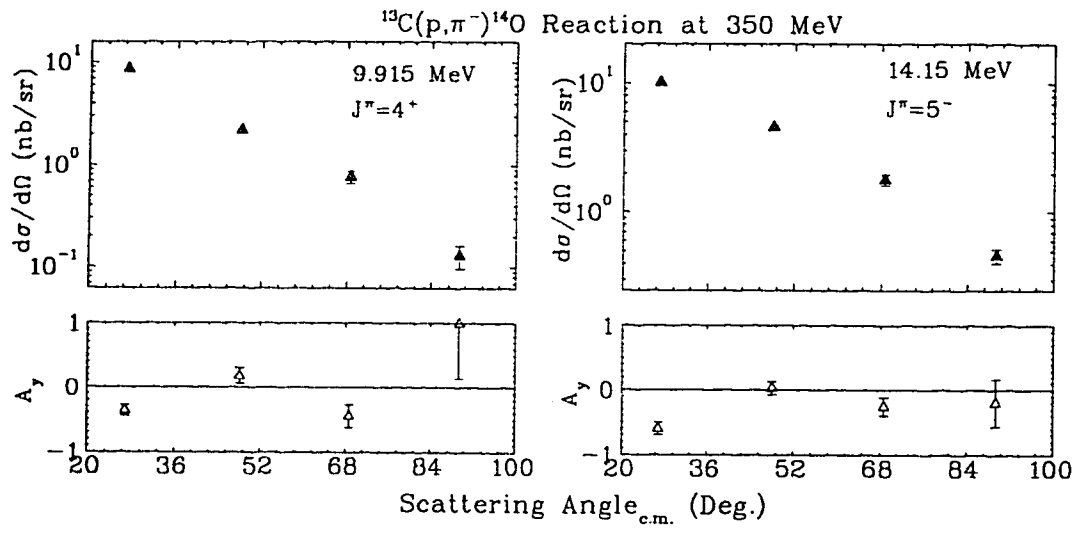
Figure 6.18: The differential cross section and analyzing power angular distributions for the ^{13}C(p, π^-)^{14}O reaction measured at 350 MeV.

6.2 Analysis of the Continuum Region

The continuum region of the nuclear excitation energy spectrum (for example Fig. 6.1) was studied for each reaction in the same way the bound states were treated. Continuum slices, 1.6 MeV wide. were chosen clear of the bound states to calculate differential cross sections and analyzing powers. The recoil nuclear excitation energy was set at the mean value for the slice. Two or more continuum slices were chosen for each reaction. See the next Chapter for a detailed discussion.

6.2.1 Continuum of $^{12}C(p,\pi^+)^{13}C$ Reaction

Two continuum slices which correspond to 15.5 MeV and 19 MeV excitation were chosen for the reaction $^{12}C(p.\pi^+)^{13}C$ at 250 and 280 MeV. The measured differential cross sections and analyzing powers as a function of the center-of-mass scattering angle are shown in Figs. 6.19 and 6.20.
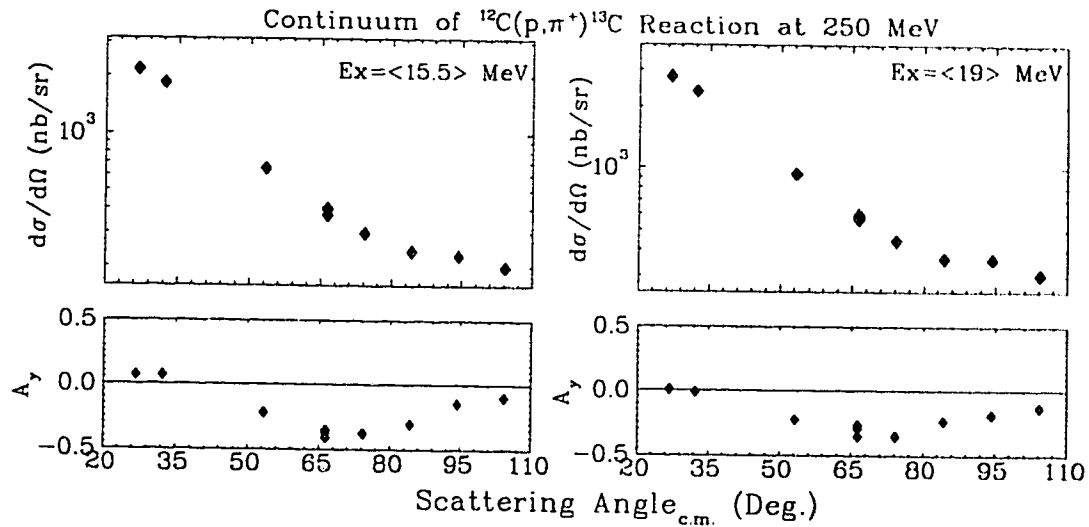
Figure 6.19: The differential cross section and analyzing power angular distributions for the continuum of $^{12}C(p,\pi^+)^{13}C$ at 250 MeV. The continuum slices were 1.6 MeV wide.

Two continuum slices were selected at 17 MeV and 19 MeV for the $^{13}C(p,\pi^+)^{14}C$ reaction. The measured differential cross section and analyzing power angular distributions at 250 MeV and 280 MeV are given in Figs 6.21 and 6.22, respectively.

To study the continuum behaviour for the reaction $^{40}Ca(p,\pi^+)^{41}Ca$, three contin-
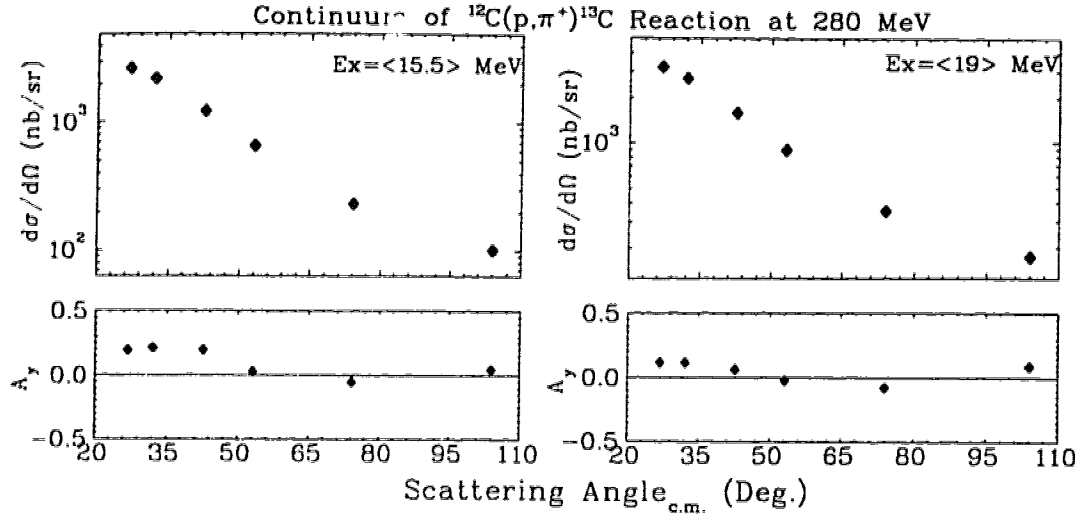
Figure 6.20: The differential cross section and analyzing power angular distributions for the continuum of $^{12}C(p, \pi^+)^{13}C$ at 280 MeV. The continuum slices were 1.6 MeV wide.
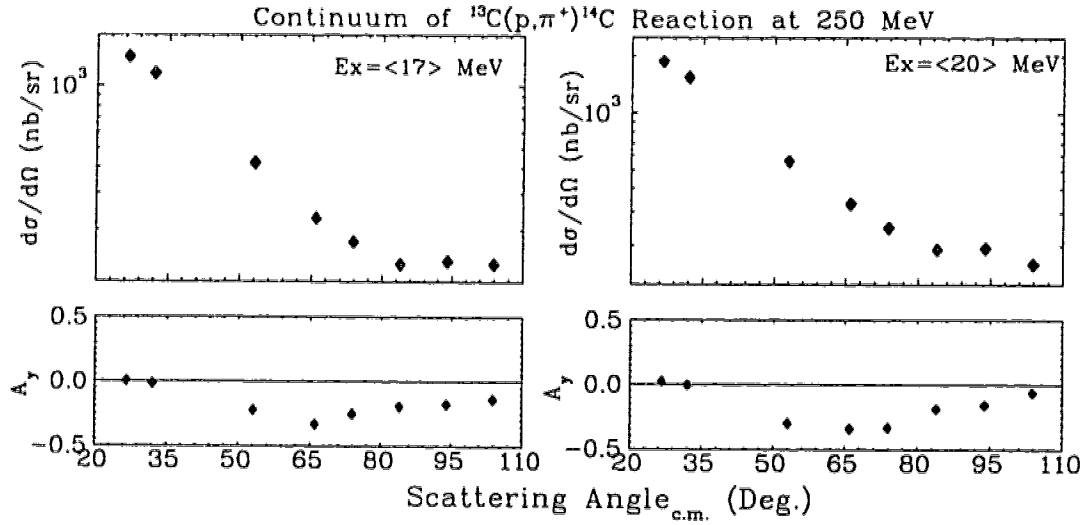
Figure 6.21: The differential cross section and analyzing power angular distributions for the continuum of $^{13}C(p, \pi^+)^{14}C$ at 250 MeV. The continuum slices were 1.6 MeV wide.

uum slices, 1.6 MeV wide, were selected at 16, 20, and 24 MeV excitation energy. The measured differential cross sections and analyzing powers at 280 MeV are shown in Fig. 6.23.

The continuum region of the missing mass spectrum for the $^{13}C(p, \pi^-)^{14}O$ reaction

95
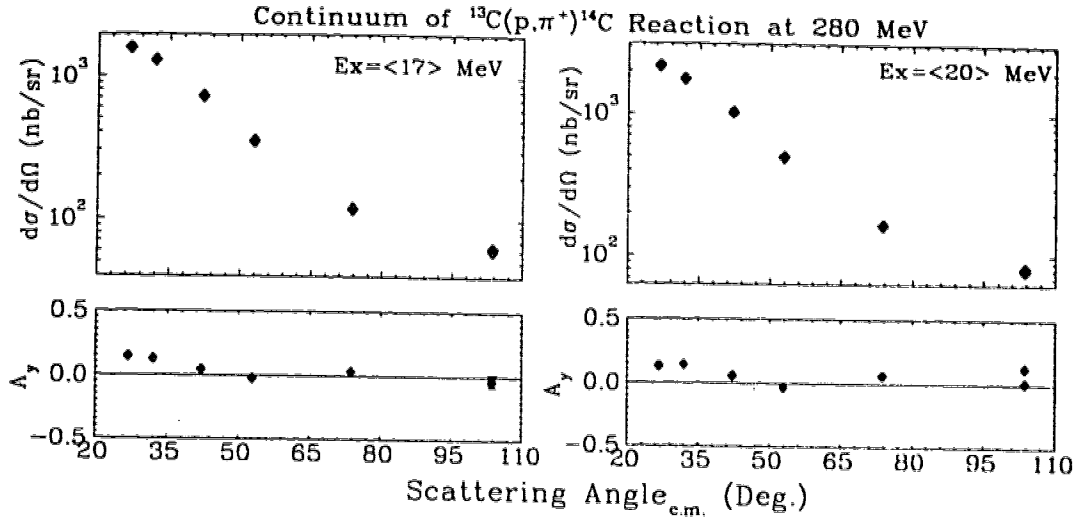
Figure 6.22: The differential cross section and analyzing power angular distributions for the continuum of $^{13}C(p, \pi^+)^{14}C$ at 280 MeV. The continuum slices were 1.6 MeV wide.

was studied at three excitation energies for 221 MeV and at four excitations at each of 280 MeV and 350 MeV. At 221 MeV, the 1.6 MeV wide slices were chosen at 17, 19, and 21 MeV, while the four excitations selected for the 280 MeV data were 19, 21, 24, and 27 MeV. The yields in the continuum were even stronger at 350 MeV. The four continuum excitations selected for this energy were at 19, 21, 25, and 30 MeV. The differential cross sections and analyzing powers for 221, 280, and 350 MeV are shown in Figs. 6.24, 6.25, and 6.26, respectively.
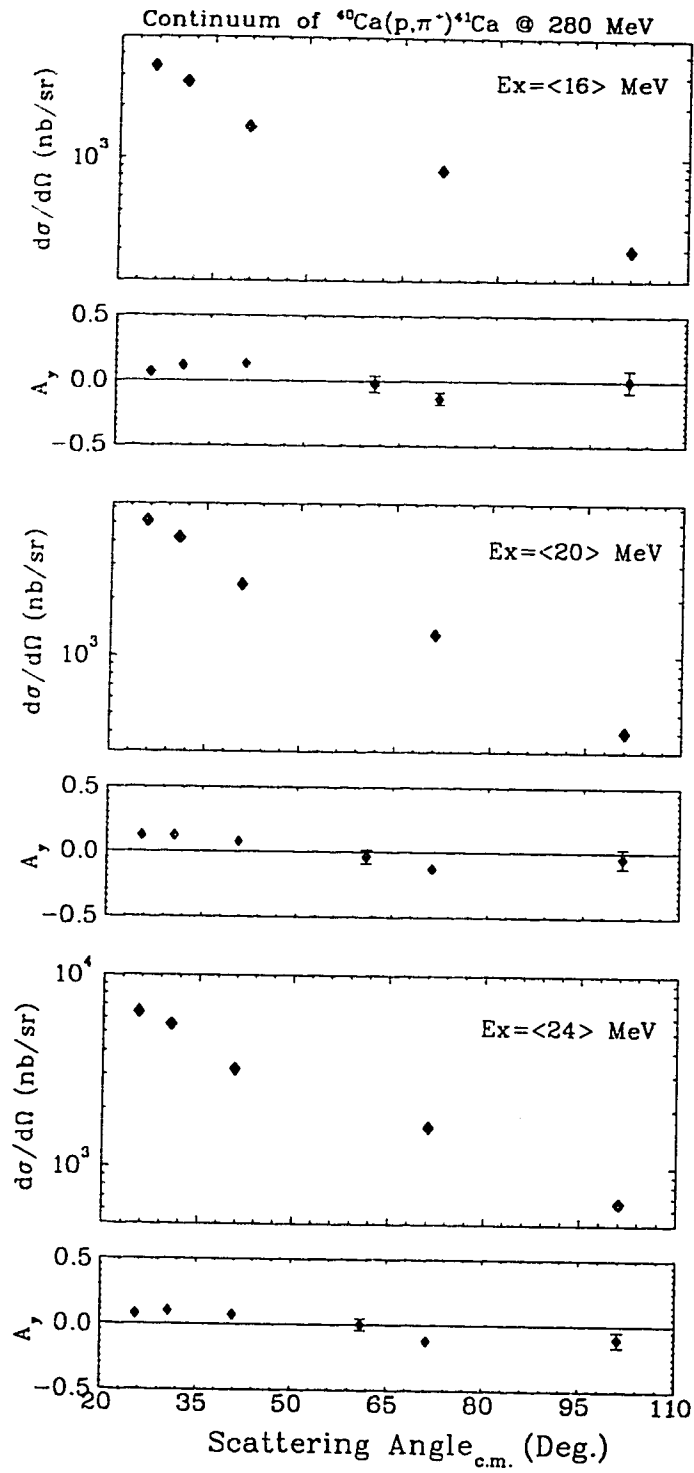
Figure 6.23: The differential cross section and analyzing power angular distributions for the continuum of ^{40}Ca$(p, \pi^+)^{41}$Ca at 280 MeV. The continuum slices were 1.6 MeV wide.
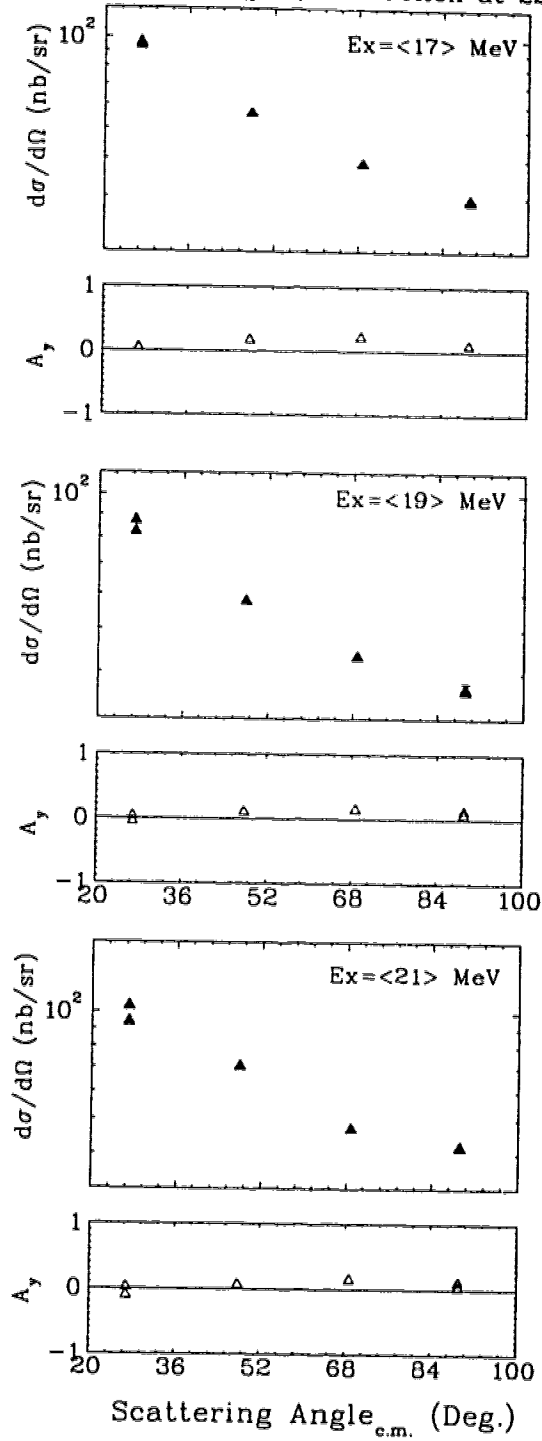
Figure 6.24: The differential cross section and analyzing power angular distributions for the continuum of $^{13}C(p,\pi^-)^{14}O$ at 221 MeV. The continuum slices were 1.6 MeV wide.
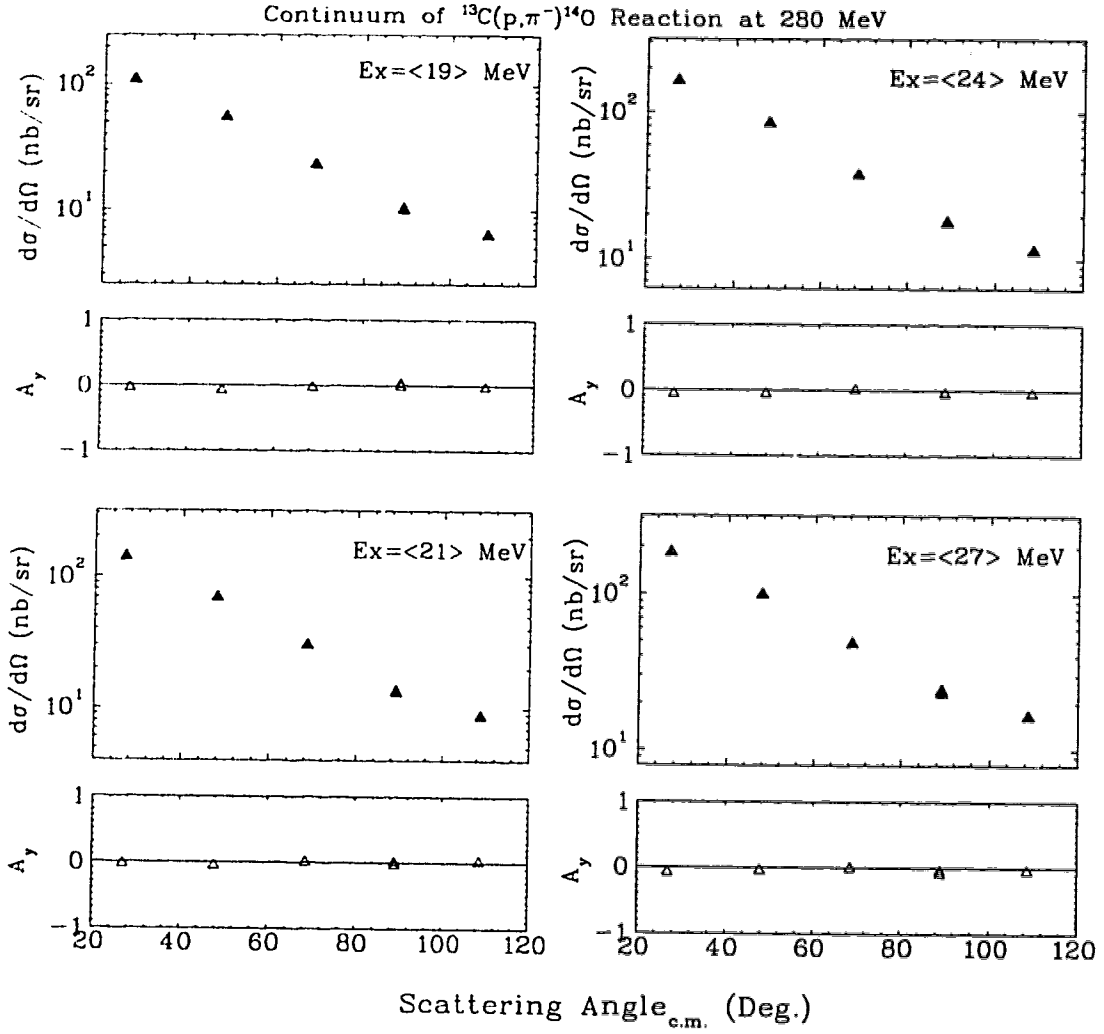
Figure 6.25: The differential cross section and analyzing power angular distributions for the continuum of $^{13}C(p, \pi^-)^{14}O$ at 280 MeV. The continuum slices were 1.6 MeV wide.
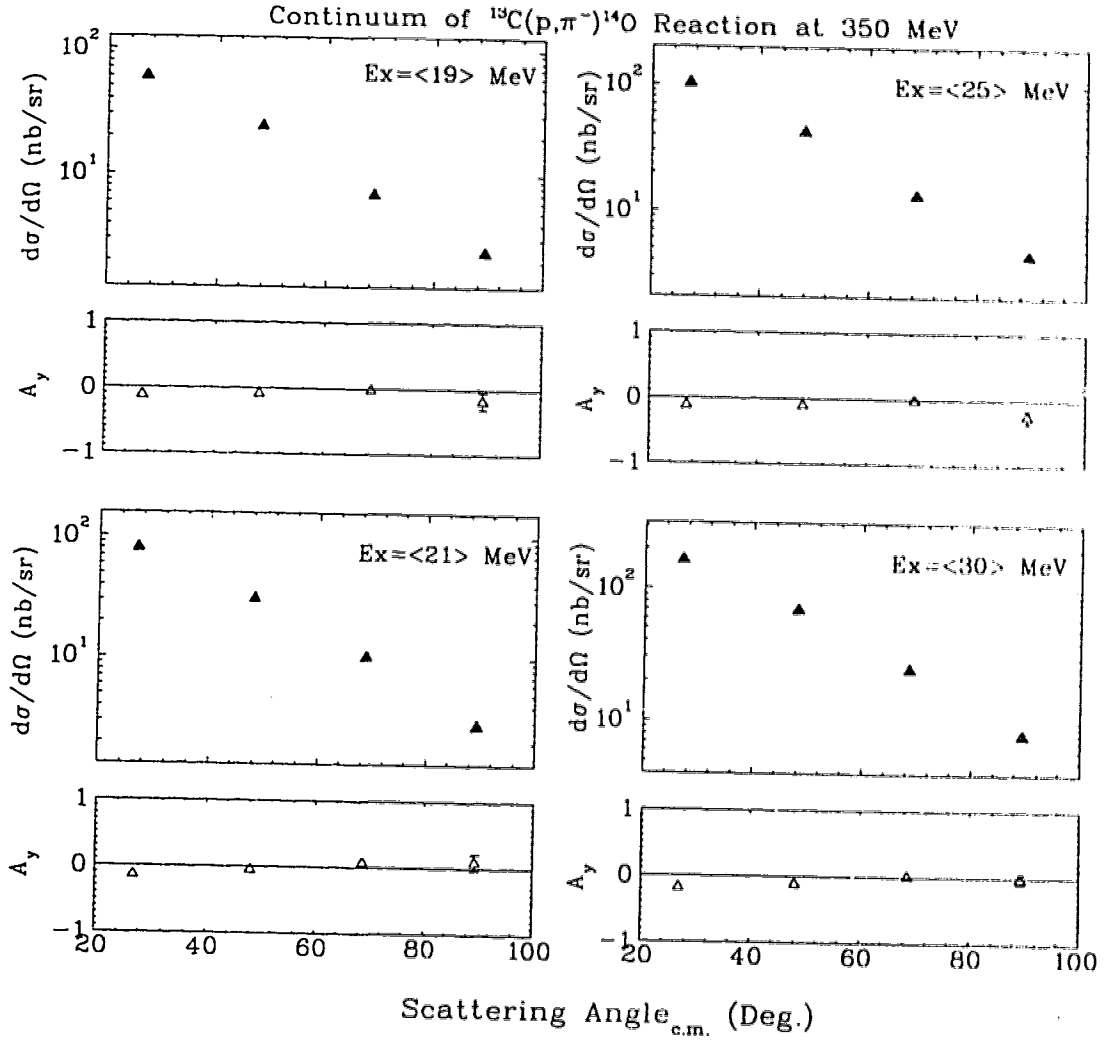
Figure 6.26: The differential cross section and analyzing power angular distributions for the continuum of $^{13}C(p, \pi^-)^{14}O$ at 350 MeV. The continuum slices were 1.6 MeV wide.

Chapter 7

Discussion

The results extracted from the data in the present $(p, \pi^{\pm})$ study are discussed in this chapter. One of the major objectives of the study is to find information about the reaction mechanism for nuclear pion production. This has been pursued by measuring the angular distributions of cross sections, $\frac{d\sigma}{d\Omega}$, and analyzing powers, A_y, at high excitations in the continuum region of missing mass spectra for the observed reactions. On the basis of these results we discuss the results determined for the discrete final states of each reaction using a model for the reaction mechanism. Finally, the role of the Δ-isobar resonance in nuclear pion production is discussed in the light of the present observations as well as some of the previous studies.

7.1   Continuum Studies from Inclusive Measurements

The continuum of the missing mass spectrum was studied for each reaction to investigate the behaviour of the $A(p, \pi)X$ reaction mechanism. Differential cross section and analyzing power angular distributions were extracted at several high nuclear excitations in these continua, which show a nearly linear rise in the spectra up to about 25 MeV excitation (see Figs. 6.1, 6.6, 6.11, and 6.12 as examples). Results were obtained for selected slices, 1.6 MeV wide, at two or more nuclear excitations depending on how far the continuum extended beyond the bound state region in each reaction. The results are tabulated by the mean nuclear excitation for each slice. The angular dependence of the cross section reflects the reaction strength at different momentum transfers, while that of the analyzing power provides information on the dominant reaction channels through which the pions are produced.

101

The analyzing power angular distributions obtained from the data for $A(p, \pi)X$ transitions are compared with those calculated for the free $pp \to d\pi^+$ and $pn \to pp\pi^-$ processes through a kinematical transformation from the nuclear process into a free two-nucleon process. Thus, we are looking for evidence that nuclear pion production is merely a two-nucleon sub-process occurring within the nucleus. This kinematical transformation and the subsequent calculation of the analyzing powers in the equivalent free two-nucleon process are discussed in the following section.

We are looking for evidence that the (p, π^+) reaction proceeds through $pp \to pn(^3S_1)\pi^+$, where the final pn is considered to be either a deuteron or just an unbound state. However, the reaction also proceeds via $pn \to nn\pi^+$ and $pp \to pn(^1S_0) \pi^+$ channels if we assume that the two-nucleon mechanism is the dominant underlying process. We estimate that the contribution from the latter two processes is small on the following grounds:

1. The $pp \to pn\pi^+$ cross section is larger than the $pn \to nn\pi^+$ cross section [Ve82]. The former process has isospin channels σ_{10} and σ_{11} while the latter goes via σ_{11} and σ_{01} where $\sigma_{10} > \sigma_{11} > \sigma_{01}$ (see section 2.1 for details).

2. It has been shown by applying kinematics and nuclear wave function considerations (see the next section) that the effective two-nucleon mass for the final NN state tends to favour as small a mass as possible. This means there is very little relative momentum in the NN system. This favours a $^3S_1$ configuration for pn from $pp \to d\pi^+$ (i.e., a deuteron) and a $^1S_0$ configuration for nn from $pn \to nn\pi^+$. The final state for $pn \to nn(^1S_0) \pi^+$ has zero spin, thus the J^π final states are determined by the relative angular momentum of the π^+ with respect to the $nn(^1S_0)$ and the parity of the π, i.e., 0^-, 1^+, 2^-, 3^+, ... The prominent $NN \to \Delta N \to NN\pi$ states have J^π of 2^+ and 3^-, which are not possible for $pn \to nn(^1S_0) \pi^+$. Thus, in the Δ-region [the energy range used for these $(p, \pi^\pm)$ measurements], the $pp \to pn(^3S_1) \pi^+$ cross section is substantially larger than that for $pn \to nn(^1S_0) \pi^+$.

3. The only viable $NN \to NN\pi$ process which can explain (p, π^-) is $pn \to pp\pi^-$. By isospin conservation, the cross section for this process is the same as that for $pn \to nn\pi^+$. Comparing the cross sections for (p, π^+) to those for (p, π^-) shows that the $pn \to nn\pi^+$ contribution to (p, π^+) must be very small. Hence for (p, π^+), the process almost always proceeds via an interaction with a nuclear proton. It does not rule out $pn \to nn\pi^+$, but the excitation of states requiring this transition would be quite weak. In fact experiments on π^- absorption on ^{3}He, i.e., $\pi^-{}^3\text{He} \to pnn$ involving quasi-free $\pi^-pp(^1S_0) \to pn$ with a n spectator, and $pd \to ppp\pi^-$ where

102

there is quasi-free $pn \to pp(^1S_0)\, \pi^-$ with a spectator p [Du96] have shown that in this case the dominant process is σ_{01} which is a $T = 0$ process (i.e., it is impossible to excite the Δ which requires $T = 1$). Thus, most of the strength in $pn \to pp\pi^-$ or, equivalently, $pn \to nn\pi^+$ comes from the case where the final pp or nn have a reasonable amount of relative internal momentum and are in a P-wave or higher. This is not favoured by nuclear transitions.

4. The $pp \to pn(^1S_0)\, \pi^+$ component has a $T = 1$ pn final state which is reached via the σ_{11} isospin channel, and hence has a cross section which is about the same order of magnitude as that for $pn \to pp(^1S_0)\, \pi^-$. Therefore, this contribution to the total (p, π^-) cross section is also small compared to the contribution from $pp \to pn(^3S_1)\, \pi^+$.

7.1.1 Kinematical Transformation into $pp \to d\pi^+$ Equivalent

In order to compare the analyzing-power angular distributions for pion production from the free, two-nucleon process $(pp \to d\pi^+)$ to those from the bound nucleon in the nuclear medium, one has to determine the effective kinetic energy of the incident proton and the corresponding scattering angle for the free process, taking into account the Fermi momentum associated with the struck target nucleon in a nucleon-nucleon collision within the nucleus. This calculation is performed by decomposing the $A(p, \pi)A+1$ process into two sub-processes. We change

$$p + A \to \pi + (A + 1)\,, \tag{7.1}$$

to

$$p + p' + (A - 1) \to \pi + d' + (A - 1)\,, \tag{7.2}$$

where, p and p' are the incident proton and the target nucleon, respectively. After the collision, the assumed final nucleon pair in the nuclear medium is represented by d', leaving the rest of the nucleus, $(A - 1)$, as a spectator.

Transformation

The pion momentum, p_π, in the process described by eqn. (7.1) can be calculated using two-body kinematics, whereas that for the process given in eqn. (7.2) has to

103

be determined in a different way. The center-of-mass 4-momentum vector, W, for the $A(p, \pi)A+1$ reaction is

$$W = P_p + P_A . \tag{7.3}$$

where P_p, and P_A are the four momenta of the incident proton and the target nucleus. In the center-of-mass system, $W = (w, 0, 0, 0)$ i.e., W has no three momentum by definition. Thus, $W \cdot W = w^2$. This is a relativistic invariant, so W also has the same value in the laboratory frame:

$$w^2 = (P_p + P_A) \cdot (P_p + P_A) = m_p^2 + m_A^2 + 2m_A E_p .$$

Here m_p and m_A are the rest masses of the proton and the target nucleus, respectively, and $E_p = T_p + m_p$ is the total energy of the proton. where T_p is its kinetic energy.

To determine the pion energy in the center-of-mass system (E_π^*) one can write $W - P_\pi^* = P_{A+1}^*$ where P_π^* and P_{A+1}^* denote the four-momenta of the pion and the target nucleus in the center-of-mass system, respectively. Evaluating $(P_{A+1}^*) \cdot (P_{A+1}^*)$ and using

$$W \cdot P_\pi^* = (w, 0) \cdot (E_\pi^*, p_\pi^*) = w E_\pi^* .$$

one gets.

$$E_\pi^* = \frac{w^2 + m_\pi^2 - m_{A+1}^2}{2 w} , \tag{7.4}$$

where m_π is the rest mass of the pion.

To relate E_π^* to p_π, the Lorentz transformation between the laboratory and center-of-mass systems must be known. To obtain this the relativistic γ and β for the center-of-mass systems are needed. In the laboratory $W = (E_p + m_A, p_p) = (\gamma w, \gamma \beta w)$. Therefore, $\beta = p_p/(E_p + m_A)$. and $\gamma = 1/\sqrt{1 - \beta^2}$. The pion momentum is determined by applying the Lorentz transformation

$$E_\pi^* = \gamma \left(E_\pi - \beta p_\pi \cos\theta \right) . \tag{7.5}$$

where θ is the laboratory scattering angle. Manipulating this expression, one obtains a quadratic equation in p_π

$$\left(E_\pi^* + \gamma\beta p_\pi \cos\theta \right)^2 = \gamma^2 \left(p_\pi^2 + m_\pi^2 \right) ,$$

$$\left[\gamma^2 \left\{ 1 - (\beta \cos\theta)^2 \right\} \right] p_\pi^2 - \left[2E_\pi^* \gamma\beta \cos\theta \right] p_\pi + \left[\gamma^2 m_\pi^2 - E_\pi^{*2} \right] = 0 . \tag{7.6}$$

The solution of this expression is the pion momentum for the process given in eqn. (7.2).

The struck proton momentum, $(p_{p'})$, is calculated by considering the four-momenta of the processes shown in eqns. (7.1) and (7.2):

$$P_p + P_A = P_\pi + P_{A+1} .$$

and

$$P_p + P_{p'} + P_{A-1} = P_\pi + P_{d'} + P_{A-1} .$$

The latter equation is equivalent to

$$P_p - P_\pi + P_{p'} = P_{d'} . \qquad (7.7)$$

Also, one can write the square of the four-momentum transfer, t, for the process as $t = (P_p - P_\pi) \cdot (P_p - P_\pi)$, which leads to

$$t = m_p^2 + m_\pi^2 - 2(E_p E_\pi - p_p p_\pi \cos\theta) . \qquad (7.8)$$

t can be calculated because all the parameters in this expression are known. Taking the dot product of each side of the eqn. (7.7) with itself, one obtains the expression,

$$t + m_p^2 + 2(E_p E_{p'} + p_p p_{p'}) - 2(E_{p'} E_\pi + p_{p'} p_\pi \cos\theta) = m_d^2 . \qquad (7.9)$$

Note that for this expression:

1. $P_{p'} = (E_{p'}, 0, 0, -p_{p'})$, i.e., the struck nucleon is headed straight at the beam proton to minimize the nuclear momentum. $p_{p'}$, required for the process. Any other direction for the struck nucleon will require higher target proton momenta and, since the nucleon wave function probability drops off as $1/p_{p'}^8$, the relative probability of a struck nucleon with a direction other than opposite to the beam proton is greatly diminished. Thus, it is assumed that **the struck nucleon direction is peaked in the direction directly opposite to that of the beam proton.**

2. Both the struck nucleon and the absorbed deuteron are on the mass shell. Since they are internal particles in the reaction, they are virtual particles and, by the uncertainty principle, they do not have to be on the mass shell, i.e., $P_{p'} \cdot P_{p'} = m_p^2$ and $P_{d'} \cdot P_{d'} = m_d^2$ are not required. However, there are three internal particles, p', d', and $(A-1)$. Their propagators $1/(P_{p'}^2 - m_p^2)$, $1/(P_{d'}^2 - m_d^2)$, and $1/(P_{A-1}^2 - m_{A-1}^2)$ are all present in the matrix element calculation, and each propagator, in principle, becomes

105

infinite if the particle is on its mass shell. Actually they are Dirac delta functions, and give finite numbers in the integration. In the kinematics being considered, either $(A-1)$ is on its mass shell, or p' and d' are on their mass shells, or nothing is on its mass shell. Here p' and d' may be considered to be on their mass shell, while $(A-1)$ carries all the virtuality in this calculation.

3. The reason that the p and n, which are swallowed back into the nucleus, are considered to have the mass m_d is that as $(p_p + p_n)^2$ increases beyond m_d^2, $p_{p'}$ goes up and, by the $1/p_{p'}^8$ argument above, the probability for the transition to occur begins to fall rapidly. Thus, the kinematics and nuclear wave function considerations favour $(p_p + p_n)^2$ to be small as possible, and the minimum is m_d^2.

Taking these into account, we can proceed to obtain $p_{p'}$ from eqn. (7.9). This results in a quadratic equation in $p_{p'}$

$$\left[4(E_p - E_\pi)^2 - (p_p - p_\pi \cos\theta)^2\right] p_{p'}^2 + \left[4(p_p - p_\pi \cos\theta)K\right]p_{p'} + \left[4\left\{(E_p - E_\pi)m_p\right\}^2 - K^2\right] = 0, \quad (7.10)$$

where $K = (m_d^2 - m_p^2 - t)$. The solution to this equation is the momentum of the proton, $p_{p'}$, in the process shown in eqn. (7.2).

A typical case is presented to give the reader some idea of these arguments by showing the required $p_{p'}$ as a function of the average nuclear momentum. The average nuclear momentum is

$$p_{avg} = \frac{1}{2M_n}\sqrt{\left[\left\{(m_1 + m_2)^2 - M_n^2\right\}\left\{M_n^2 - (m_1 - m_2)^2\right\}\right]},$$

where the nuclear mass breaks up into $M_n \to m_1 + m_2$. One example in our case is $^{13}C \to p + ^{12}B$ where $M_n(^{13}C) = 12109.58$ MeV, $m_1(p) = 938.2796$ MeV, and $m_2(^{12}B) = 11188.83$ MeV. For this example $p_{avg} =$ is 173.52 MeV/c. For the argument to work, $p_{p'}$ should be greater than p_{avg}, i.e., in the $1/p^8$ region. However, $p_{p'}$ should not be much greater than p_{avg} or else the process becomes extremely unlikely. The needed $p_{p'}$ increases as the effective pn mass goes up. For example, calculations of $^{13}C(p, \pi^+)^{14}C$ at $T_p = 280$ MeV and $\theta_{Lab} = 30°$ show that for the final pn to stay together as a deuteron $p_{p'} = 221.14$ MeV/c, whereas $p_{p'}$ increases up to 243.01 MeV/c if an extra 10 MeV is added to the pn system. In fact, one has to add about 21 MeV [Wa96] for the pn system to go into a P-wave at which point the $p_{p'}$ becomes 266.49 MeV/c. If the probability rule of the wave function ($1/p^8$) is applied, one will see that the latter process is much less likely than the

former by about a factor of five in the probability. This suppression becomes even larger at higher incident proton energies, particularly in the Δ-region (300 - 350 MeV).

Having given a detailed insight into the presumed reaction mechanism, we continue the calculations. We calculate the effective beam energy of the incoming proton for the $pp \rightarrow d\pi^+$ process. The center-of-mass energy squared for the pp system is

$$w_c^2 = (P_p + P_{p'}) \cdot (P_p + P_{p'}) = 2m_p^2 + 2(E_p E_{p'} + p_p p_{p'}) \, .$$

For a pp system in which the target proton is at rest, one can write

$$w_c^2 = 2m_p^2 + 2E_{pe} m_p.$$

Here, $E_{pe} = T_{pe} + m_p$ is the total effective energy of the incident proton. Therefore, the effective kinetic energy of the incident proton is given by

$$T_{pe} = \frac{w_c^2 - 4m_p^2}{2m_p} \, . \tag{7.11}$$

In order to calculate the effective scattering angle, θ_e^*, in the pp center-of-mass, the following method is used. The effective momentum of the incident proton in the pp center-of-mass system is

$$p_{pe}^* = \sqrt{E_{pe}^{*2} - m_p^2} \, ,$$

where

$$E_{pe}^* = w_e/2 \, .$$

Similarly, the effective momentum of the pion in the pp center-of-mass system can be determined as

$$p_{\pi e}^* = \sqrt{E_{\pi e}^{*2} - m_\pi^2} \, ,$$

where

$$E_{\pi e}^* = \left[w_e^2 + m_\pi^2 - m_d^2 \right] / [2w_e] \, ,$$

by reference to eqn. (7.4).

Since $t = (P_p - P_\pi)^2$ is a relativistic invariant, evaluating it in the effective pp center-of-mass system gives

$$t = m_p^2 + m_\pi^2 - 2\left\{ E_{pe}^* E_{\pi e}^* - p_{pe}^* p_{\pi e}^* \cos \theta_e^* \right\} \, . \tag{7.12}$$

The quantity t is also found in eqn. (7.9). By combining it with eqn. (7.12) the effective scattering angle in the pp center-of-mass system can be found. Thus, for each T_p and θ in the laboratory system, T_{pe}^- and θ_c^- can be calculated for the effective free case of the $pp \to d\pi^+$ reaction. The nuclear excitation energy corresponding to the selected continuum slice is already included in the ground state mass of the residual nucleus (m_{A+1}). Using the interactive dial-in SAID program [Ar96] the analyzing power for the free process for each T_{pe}^- and θ_c^- pair used in the data taking was obtained so that the analyzing powers extracted from the experiment could be directly compared with the equivalent free $pp \to d\pi^+$ process.

7.2   Analyzing Power Comparison with the Free Process

In this section, the analyzing power angular distributions calculated from the nuclear excitation continuum are compared with those calculated from the equivalent free $NN \to NN\pi$ process.

7.2.1   Continuum Analyzing Powers of A(p, π^+)X Reactions

The final two-nucleon pair in the $pp \to pn\pi^+$ sub-process for A(p, π^+)X is assumed to be in a $^3S_1$ triplet state (see section 7.1). Therefore, this nucleon pair is either in its bound state, which is the deuteron, or the nucleons are unbound, but with small relative momentum. Furthermore, the proton-induced positive-pion production reaction has been observed to proceed through a strong intermediate state of virtual $\Delta(1232)$ formation[Hu87] where dominant amplitude comes from the $^3S_1$ state of the final two nucleons. To help understand this mechanism, the analyzing powers of A(p, π^+)X have been compared with those of the free $pp \to d\pi^+$ process.

Continuum of ^{12,13}C(p, π^+)X Reactions

The analyzing-power angular distributions extracted from the nuclear excitation continuum of the ^{12}C(p, π^+)X and ^{13}C(p, π^+)X reactions at 250 and 280 MeV are compared with the $pp \to d\pi^+$ equivalents in Fig. 7.1 where two continuum excitation values have been chosen for each reaction. The dotted line represents the kinematical calculation of the $pp \to d\pi^+$ for the actual incident beam energy, while the solid line represents the same calculation of $pp \to d\pi^+$ performed for a lower effective beam energy. This is

108

explained below.

In Fig. 7.1 the calculation represented by the solid line is in better agreement with the experiment in each case than the dotted line. In the comparison, for example at 250 MeV, the solid line represents the $pp \to d\pi^+$ equivalent process for 230 MeV while the dotted line represents the free case for the actual beam energy of 250 MeV. The comparison is also shown for the data taken at 280 MeV, where the solid line shows the free process equivalent to 265 MeV. The overall results in Fig. 7.1 show that pion production within the nucleus displays a $NN \to NN\pi$ signature. The better agreement between the experiment and the transformation (solid line) calculated for a lower effective proton beam energy can be best attributed to the effects of nuclear distortions in both the incoming and outgoing channels. Distortions lead to a lowering of the effective center-of-mass energy of the internal process plus a reduced momentum transfer. Lowering the effective beam energy of the transformation does both of these. However, it remains true that the ability of the kinematic transformation to map the analyzing powers of $pp \to d\pi^+$ onto $A(p, \pi^+)A+1$ is suggestive of the underlying mechanism.

Continuum of $^{40}Ca(p, \pi^+)X$ Reactions

A similar comparison of analyzing powers to equivalent $pp \to d\pi^+$ results was repeated for a d-shell nucleus using the $^{40}Ca(p, \pi^+)X$ data at 280 MeV beam energy. This is shown in Fig. 7.2 where three continuum excitation values (16, 20, 24 MeV) were considered. It is also apparent in this case that the analyzing power angular distribution shapes of the (p, π^+) reaction are in close agreement with the free $pp \to d\pi^+$ process when the effective beam energy is reduced slightly. Note that in this case the effective beam energy had to be reduced by 30 MeV in order to get a satisfactory comparison whereas only a 15 MeV decrease was needed for the carbon isotopes. This indicates that the distortions are larger for ^{40}Ca, as would be expected for a larger nucleus. This is the first nucleus other than $1s$ and $1p$ shell nuclei to display the $pp \to d\pi^+$ signature. Thus, it seems, our data show consistent evidence that the (p, π) reaction on nuclei proceeds through an elementary $NN \to NN\pi$ process.

109
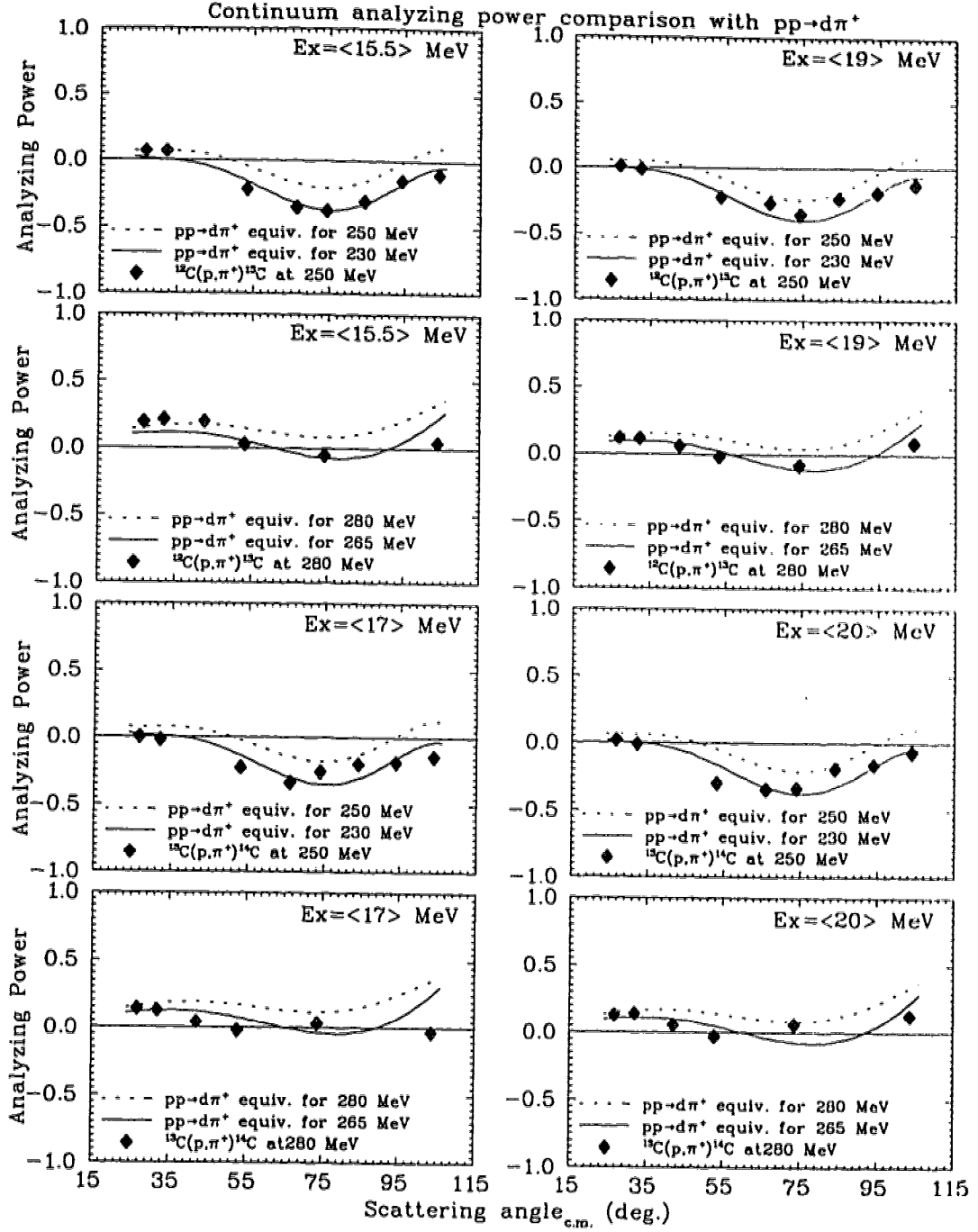
Figure 7.1: The analyzing powers of $^{12}C(p,\pi^+)X$ and $^{13}C(p,\pi^+)X$ are compared with those calculated for the free $pp \to d\pi^+$ equivalent process (see the text for details). Dotted lines show the calculated values for the actual beam energy used in the data taking, while the solid lines show those for a lower beam energy in an attempt to account for nuclear distortions.

110
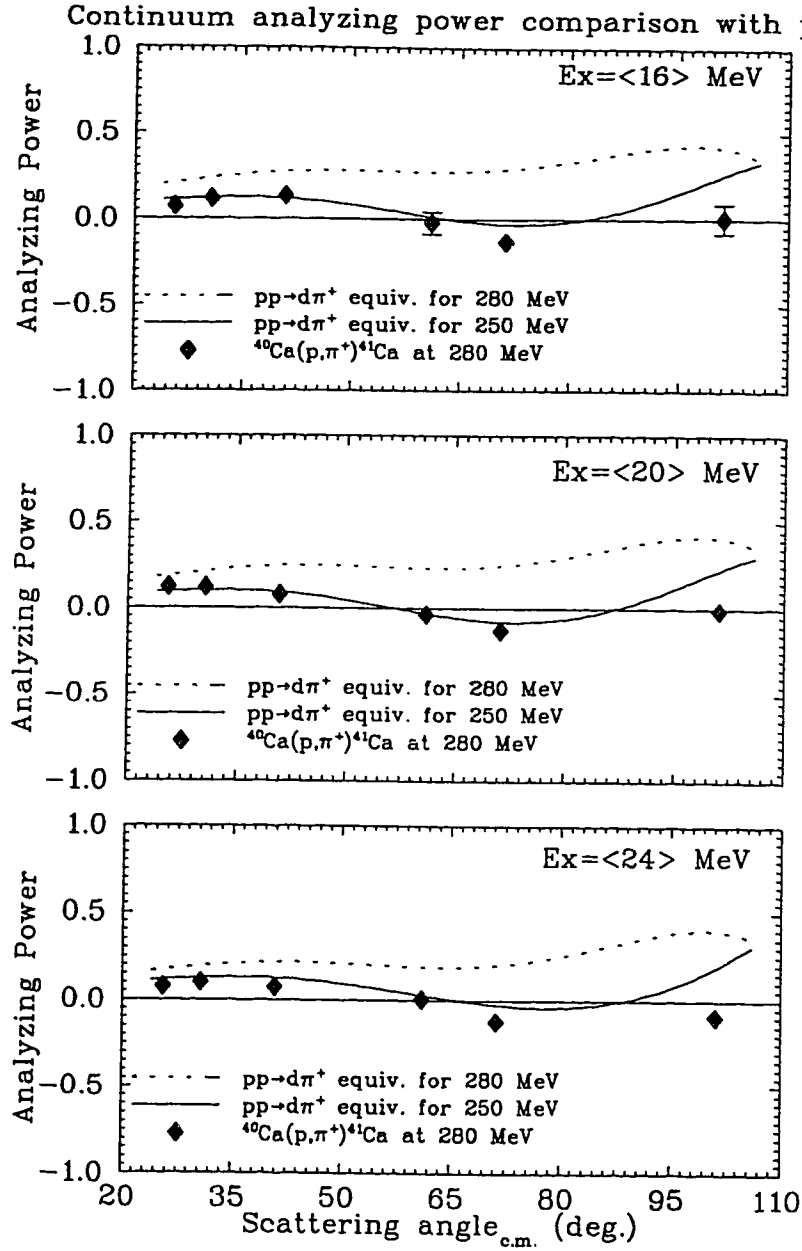
Figure 7.2: The analyzing powers of ^{40}Ca(p, π^+)X at 280 MeV are compared with those calculated for the free $pp \rightarrow d\pi^+$ equivalent (see text for details). Dotted lines show the calculated values for the actual beam energy used in the data taking, while the solid lines show those for a lower beam energy in an attempt to account for nuclear distortions.

111

7.3 Analyzing Power Shapes of the 2p1h Stretched States

Taking the lead that the 5^- 2p1h stretched state of $^{13}C(p, \pi^+)^{14}C$ displays $pp \rightarrow d\pi^+$ analyzing-power characteristics, the analyzing-power angular distributions for the 5^- state in ^{14}O from $^{13}C(p, \pi^-)^{14}O$ at beam energies of 200 and 221 MeV (200 MeV data were obtained from reference [Ko89]) were compared in Fig 7.3(a) with those of the equivalent free $pn \rightarrow pp(^1S_0)\pi^-$ process. The transformation calculation for the free case was carried out using the measured $pn \rightarrow pp(^1S_0)\pi^-$ analyzing power data [Du96]. The results in this figure show reasonable agreement between the nuclear case and the free case within the low-momentum transfer region. The most impressive characteristic in this comparison is the close agreement of the cross-over point of the analyzing power angular distributions. This characteristic is also observed at lower energies [Gr84] where the $pn \rightarrow pp(^1S_0)\pi^-$ analyzing power has been mapped onto the analyzing power of many (p, π^-) reactions to a variety of final states in A+1 nuclei where the A+1 is in a high-spin 2p1h stretched state [Ko91].

A comparison of analyzing-power angular distributions between the $A(p, \pi^+)X$ and the free $pp \rightarrow d\pi^+$ (see Figs. 7.1 and 7.2) present evidence for a $pp \rightarrow pn(^3S_1)\pi^+$ sub-process. However, the analyzing power data (see A_y distributions in chapter 6) for most of the $A(p, \pi^+)A+1$ transitions do not show this basic shape. However, the $pp \rightarrow pn(^3S_1)\pi^+$ hypothesis is still valid. Because of the spin-coupling considerations and Pauli blocking both the $A \rightarrow (A-1) + p$ decomposition of the initial state and the $d + (A-1) \rightarrow$ A+1 recomposition of the final state restrict the full set of $pp \rightarrow pn(^3S_1)\pi^+$ amplitudes available. Since the analyzing power is an interference between amplitudes, the resultant analyzing power can easily be quite different from that for the $pp \rightarrow pn(^3S_1)\pi^+$ case [for example, see the A_y distributions for $J^\pi = \frac{5}{2}^+$ (6.864 MeV) and $J^\pi = \frac{7}{2}^+$ (7.492 MeV) in Fig. 6.2, and $J^\pi = 3^-$ (9.801 MeV) and $J^\pi = 2^+$ (10.425 MeV) in Fig. 6.8]. A fully developed microscopic model which uses the $pp \rightarrow d\pi^+$ amplitudes as inputs to derive (p, π^+) analyzing powers is necessary to explain the analyzing-power behaviour in the reaction $A(p, \pi^+)A+1$. Similar model calculations [Fa94] have been applied to an investigation of the (p, π^+) reaction on ^2H, ^3He, ^4He, and ^{12}C where a reasonably good agreement is found for light nuclei. The most important thing is that a successful microscopic model can be employed as a means of determining nuclear structure from the analyzing power signature.

In contrast to the A_y behaviour of the exclusive final states discussed above, there are some states which do display characteristics similar to those of the free $pp \rightarrow pn(^3S_1)\pi^+$

process. The 2p1h stretched state of $J^\pi = \frac{9}{2}^+$ in ^{13}C and that of $J^\pi = 5^-$ in ^{14}C are examples of such final states for which the results are shown in Fig. 7.3(b) and (c). The reasons for these states displaying such analyzing power characteristics are not known.

The $A(p, \pi^-)X$ data would probably not have analyzing powers similar to those for $pn \rightarrow pp(^1S_0)\pi^-$ since the kinematics in the continuum which favour an S-wave would be overwhelmed by the strong tendency for the $pn \rightarrow pp\pi^-$ reaction to go through a P-wave since that channel allows Δ production. This is in contrast to $pn \rightarrow pp(^1S_0)\pi^-$ which does not proceed via a Δ intermediate state. However, the analyzing power angular distribution of $A(p, \pi^-)A+1$ could be expected to favour a $pp(^1S_0)$ final state in the confines of the nucleus[1]. We find the signature of $pn \rightarrow pp(^1S_0)\pi^-$ in the very same state (the 5^-) which displays a $pp \rightarrow pn(^3S_1)\pi^+$ signature. The combination of $\frac{9}{2}^+$, 5^- states (of similar structure) and the mirror 5^- in ^{14}O all displaying $NN \rightarrow NN\pi$ A_y signatures is suggestive of an underlying $NN \rightarrow NN\pi$ mechanism.

It is to be noticed that the analyzing-power angular distributions determined for the 4^- (11.666 MeV) and 5^- (14.868 MeV) states in ^{14}C via ^{13}C$(p, \pi^+)^{14}$C reaction at 250 and 280 MeV (see Figs. 6.8 and 6.10) are very similar to those of $\frac{9}{2}^+$ (9.5 MeV) in ^{13}C via ^{12}C$(p, \pi^+)^{13}$C reaction (see Figs. 6.3 and 6.5) at the same beam energies. These two states in ^{14}C are also 2p1h high-spin stretched states showing the similarity in their analyzing power shapes with the $pp \rightarrow d\pi^+$ process to support the TNM model, suggesting once again the dominance of the σ_{10} isospin channel. Having shown that the reaction mechanism of the nuclear pion production is indeed an elementary two-nucleon process, we discuss the results from our bound state analyses in the following section on the basis of the $NN \rightarrow NN\pi$ considerations.

---

[1]The relative spectroscopic abundance of the A+1 final state was successfully duplicated for the (p, π^-) reaction on $1f_{\frac{7}{2}}$ nuclei (eg. ^{48}Ca) by hypothesizing a $pn \rightarrow pp(^1S_0)\pi^-$ subprocess [Br83].
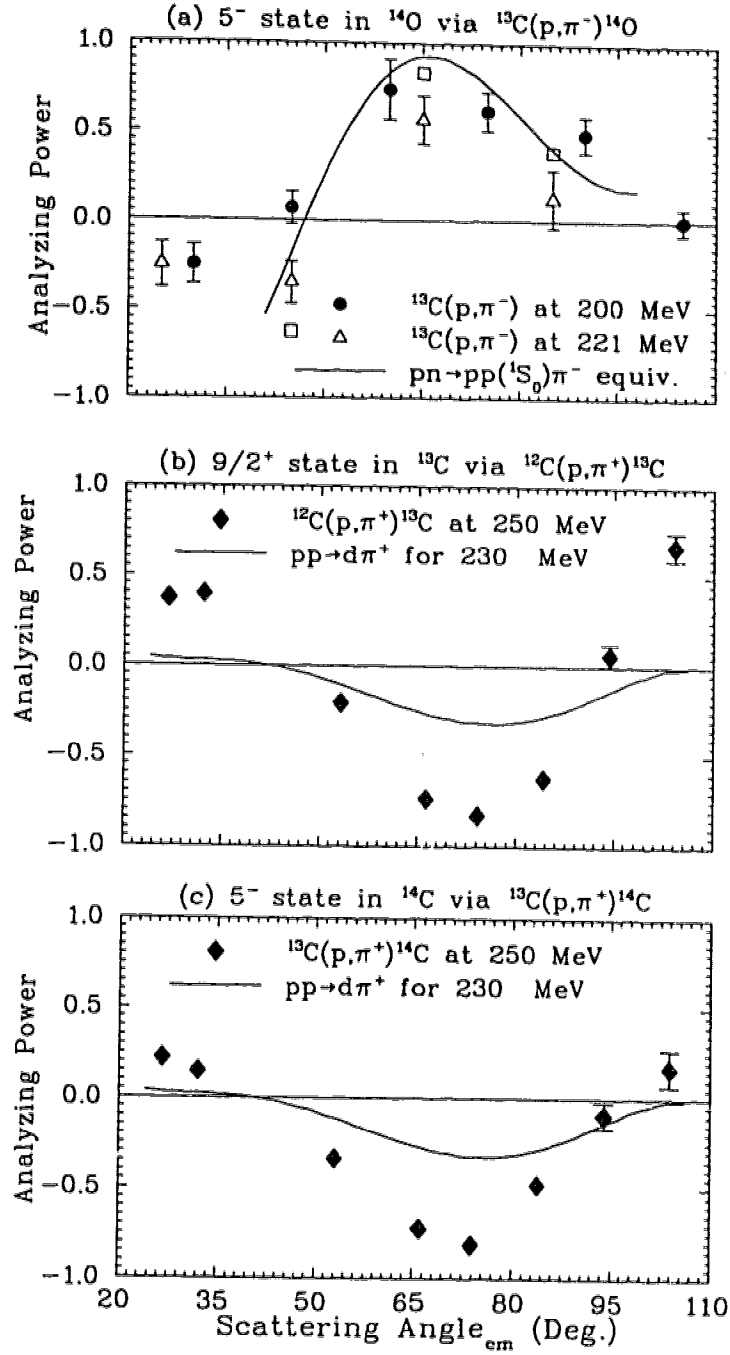
Figure 7.3: The analyzing power angular distributions for a 2p1h high-spin stretched state in ^{14}O, ^{13}C, and ^{14}C are compared with the corresponding quasi-free $NN \rightarrow NN\pi$ process. The results for A(p, π^-)A+1 compared to $pn \rightarrow pp\pi^-$ are shown in (a), while (b) and (c) show those for A(p, π^+)A+1 compared to $pp \rightarrow d\pi^+$. The experimental data at 200 MeV are from the reference [Ko89].

114

7.4 Bound State Analyses of $A(p, \pi^{\pm})A + 1$ Reactions

This section discusses the relative strengths of discrete final states, their spin and parity assignments, as well as additional evidence found from the present investigation that support some of the previously suggested nuclear configurations.

7.4.1 Study of Discrete Final states from Exclusive Measurements

Due to the typical high momentum transfers involved and the peripheral nature of the $A(p, \pi)A+1$ reaction, the resultant recoil nuclear spectrum shows a preference for higher spin configurations, especially the high-spin stretched states. The (p, π^-) reaction, in particular, can only excite 2p1h states with respect to the initial nucleus. Consider the recoil excitation spectra of ^{14}C and ^{14}O in Figs. 6.6 and 6.12. The final states are mirror nuclei since they are the $T_z = -1$ and $+1$ members of a $T = 1$ triplet. A qualitative comparison of the spectra shows that the mirror nuclei are similar with transitions of similar relative strengths. However, there are some differences which can be understood on the basis of simple, free TNM ($NN \to NN\pi$) considerations. Table 7.1 shows for a selection of the most prominent states, the presumed nuclear configurations of the final states in ^{14}C and ^{14}O. The final column lists the proposed struck nucleon based on a $NN \to NN\pi$ hypothesis. Certain features of the spectra can be understood by considering this column as explained below. Similarly, the final-state configurations of ^{13}C and ^{41}Ca are listed in Tables 7.2 and 7.3. showing the anticipated nuclear transitions in reactions ^{12}C(p, π^+)^{13}C and ^{40}Ca(p, π^+)^{41}Ca, respectively.

7.4.2 Mirror Final States in ^{14}C and ^{14}O Nuclei

Shell model configurations of the strongly excited nuclear states in ^{14}C and ^{14}O given in Table 7.1 show some differences in the intermediate states to reach the final states from ^{13}C($p, \pi^{\pm}$). For example, the 6^+ state is impossible to reach via $NN \to NN\pi$ for the ^{14}C configuration, but it is possible for the ^{14}O configuration. Such differences are manifested by some possible high-spin ($J \geq 3$) mirror configurations being stronger or weaker for one nucleus compared to the other. The spectra showing the reaction yields as a function of the nuclear excitation for the ^{13}C($p, \pi^{\pm}$) reactions are given in Figs. 6.6 and 6.12 for $T_p = 250$ MeV at 25° scattering angle. The J^{π} notation represents the quantum state of a given nuclear configuration, where J denotes the total angular momentum and π the parity of the system. Also in the given notation, $\nu(\pi)$ denotes a neutron(proton) in

115

Table 7.1: Final-state nuclear configurations in ^{14}C and ^{14}O for the observed transitions in ^{13}C$(p, \pi^{\pm})$ reactions. The incident proton interacts with the listed struck-nucleon which is labelled according to the shell-model structure of ^{13}C.

Residual Nucleus	J^{π}	Final-state Configuration of the Residual Nucleus	Excitation (MeV)	Struck Nucleon
^{14}C	0^+	$|^{12}C \otimes (\nu p_{1/2})^2_{0+}\rangle$	Ground State	any n or p
^{14}C	1^-	$|^{12}C \otimes (\nu p_{1/2})(\nu 2s_{1/2})\rangle$	6.094	any n or p
^{14}C	3^-	$|^{12}C \otimes (\nu p_{1/2})(\nu d_{5/2})\rangle$	6.728	any n or p
^{14}C	4^+	$|^{12}C \otimes (\nu d_{5/2})^2\rangle$	10.736	$p_{1/2}\,n$
^{14}C	4^-	$|^{12}C \otimes (\nu p_{1/2})^2_{0+}(\pi p_{3/2})^{-1}(\pi d_{5/2})\rangle$	11.666	$p_{3/2}\,p$
^{14}C	5^-	$|^{12}C \otimes (\pi p_{3/2})^{-1}(\pi p_{1/2})(\nu p_{1/2})(\nu d_{5/2})\rangle$	14.868	$p_{3/2}\,p$
^{14}C	6^+	$|^{12}C \otimes (\pi p_{3/2})^{-1}(\pi p_{1/2})(\nu d_{5/2})^2_{4+}\rangle$		none
^{14}C	7^+	$|^{12}C \otimes (\pi p_{3/2})^{-1}(\nu p_{1/2})(\pi d_{5/2})(\nu d_{5/2})\rangle$	23.288	$p_{3/2}\,p$
^{14}O	0^+	$|^{12}C \otimes (\pi p_{1/2})^2_{0+}\rangle$	Ground State	$p_{1/2}\,n$
^{14}O	1^-	$|^{12}C \otimes (\pi p_{1/2})(\pi 2s_{1/2})\rangle$	5.173	$p_{1/2}\,n$
^{14}O	3^-	$|^{12}C \otimes (\pi p_{1/2})(\pi d_{5/2})\rangle$	6.272	$p_{1/2}\,n$
^{14}O	4^+	$|^{12}C \otimes (\pi d_{5/2})^2\rangle$	9.915	$p_{1/2}\,n$
^{14}O	4^-	$|^{12}C \otimes (\pi p_{1/2})^2_{0+}(\nu p_{3/2})^{-1}(\nu d_{5/2})\rangle$		none
^{14}O	5^-	$|^{12}C \otimes (\nu p_{3/2})^{-1}(\nu p_{1/2})(\pi p_{1/2})(\pi d_{5/2})\rangle$	14.15	$p_{3/2}\,n$
^{14}O	6^+	$|^{12}C \otimes (\nu p_{3/2})^{-1}(\nu p_{1/2})(\pi d_{5/2})^2_{4+}\rangle$		$p_{3/2}\,n$
^{14}O	7^+	$|^{12}C \otimes (\nu p_{3/2})^{-1}(\pi p_{1/2})(\nu d_{5/2})(\pi d_{5/2})\rangle$		none

a particular sub-shell [for example, $(\pi d_{5/2})$ means a proton in the $d_{5/2}$ sub-shell] and the superscript "-1" represents a neutron- or proton-hole in the considered sub-shell.

$J^{\pi} = 4^+$ States

The spectroscopic evidence gathered from our data re-affirm that the known 4^+ state in ^{14}O at 9.915 MeV is strong, while that in ^{14}C at 10.736 MeV is weak with respect to the relative population in the final state. The weakness of the 4^+ state in ^{14}C is most easily discernable in Fig. B.1(d) in appendix B where the 4^+ state appears as a minor peak next to the more dominant 10.425 MeV (2^+) state. In contrast the 4^+ state in ^{14}O at 9.915 MeV in Fig. 6.12 is quite discernable. This was previously observed in $(p, \pi^{\pm})$ studies near-threshold [Ko89]. The $|^{12}C \otimes (\nu d_{5/2})^2\rangle$ and $|^{12}C \otimes (\pi d_{5/2})^2\rangle$ mirror configurations

are widely believed to represent these states [Fo78]. They can be excited from the ground state of ^{13}C only through the mirror channels $pn \to pp\pi^-$ and $pn \to nn\pi^+$.

The reason why the ^{13}C$(p,\pi^+)^{14}$C $(4^+, 10.736$ MeV$)$ transition is weak is that in the $NN \to NN\pi$ hypothesis it proceeds via $pn \to nn\pi^+$. This is a σ_{11} or σ_{01} reaction channel which is substantially smaller than σ_{10} reaction channel i.e., $pp \to pn(^3S_1$ or $d)$ π^+ (see section 7.1). This is especially so if the nn is forced into a $T = 1, S = 0$ configuration (which seems possible for $A(p,\pi^-)A+1$ to discrete final states) because in that case $pn \to nn\pi^+$ cannot proceed via the Δ. Therefore, any (p,π^+) reaction which cannot proceed via $pp \to pn(^3S_1)\,\pi^+$ is weak with respect to the other final states. Since ^{13}C$(p,\pi^+)^{14}$C $(4^+, 10.736$ MeV$)$ can only go via $pn \to nn\pi^+$, it will be weak. Thus, we have a really good example where the $NN \to NN\pi$ hypothesis provides a clear-cut explanation for the observations and also supports the assumption of a $|^{12}C \otimes (\nu d_{5/2})^2\rangle$ configuration for ^{14}C $(4^+, 10.736$ MeV$)$ and a $|^{12}C \otimes (\pi d_{5/2})^2\rangle$ configuration for ^{14}O $(4^+, 9.915$ MeV$)$. Excitation of ^{14}C to its 4^+ state may proceed via small admixtures from other configurations to the 4^+ state such as to $|^{12}C\otimes(\nu p_{1/2})(\nu f_{7/2})\rangle_{4^+}$, which is accessible in (p,π^+) via the dominant σ_{10} channel. This however lends support to the hypothesis that the 4^+ states are predominantly $(d_{5/2})^2$ configurations.

$J^\pi = 5^-$ States

The nuclear wave function of ^{14}C in 5^- state is given in Table 7.1 as

$$|^{12}C \otimes (\pi p_{3/2})^{-1}(\pi p_{1/2})(\nu p_{1/2})(\nu d_{5/2})\rangle_{5^-} \,,$$

and that of ^{14}O in the same state as

$$|^{12}C \otimes (\nu p_{3/2})^{-1}(\nu p_{1/2})(\pi p_{1/2})(\pi d_{5/2})\rangle_{5^-} \,.$$

Spectra in Figs. 6.6 and 6.12 show that both of these states are excited with similar strengths with respect to the rest of the spectrum. Both these states are high-spin 2p1h states with respect to ^{13}C. As long as there exists a $NN \to NN\pi$ channel to excite these states they are expected to be strongly excited because of the large momentum transfer and peripheral nature of the (p,π) reaction. According to table 7.1, these states can be reached via a $pp \to pn(^3S_1)\,\pi^+$ reaction for ^{14}C and a $pn \to pp(^1S_0)\,\pi^-$ reaction for ^{14}O. These are the predominant reaction mechanisms for both reactions according to the $NN \to NN\pi$ hypothesis and consequently both states should be relatively strong and this is confirmed experimentally.

117

The differential cross sections for these states, shown in Figs. 6.8 and 6.10 for $^{13}C(p, \pi^+)^{14}C$ at 250 and 280 MeV, decrease with increasing momentum transfer in a similar way to the data shown in Figs. 6.14, 6.16, and 6.18 for the $^{13}C(p, \pi^-)^{14}O$ reaction at beam energies of 221, 280, and 350 MeV. Furthermore, these states are not reachable by 1p1h excitations from the ground states of ^{14}C and ^{14}O. As far as the TNM is concerned, the only reaction channel available via (p, π^-) is $pn \rightarrow pp\pi^-$ which excites the residual nucleus only to a 2p1h state. In the latest compilation of $N = 14$ nuclei [Aj91], the 14.868 MeV state in ^{14}C is listed as a possible 5^- or a 6^+ configuration. The 14.15 MeV state in ^{14}O is listed as a possible 5^- state. If the ^{14}C state is 6^+, it could not be accessed via (p, π^+) (see Table 7.1). The fact that both states are strongly represented in their appropriate spectra strongly suggests an assignment of 5^- for both states.

$J^\pi = 7^+$ States

The anomalous bound state in ^{14}C observed at 23.288 MeV excitation seems to be quite strong via $^{13}C(p, \pi^+)$ at forward angles (see Fig 6.6). Spectroscopic information from our data reveals that this nuclear excitation is prominent at low momentum transfers but weakens fast at higher momentum transfers. The differential cross sections for this state at 250 MeV and 280 MeV are given in Figs. 6.8 and 6.10, showing that the relative population of this state is comparable to those of the other strongest low-lying states of the spectrum. As can be seen in these figures, the analyzing power angular distributions show nearly zero values for all angles, which is a rather different characteristic compared to all the other strongly excited states of this nucleus. The final state configuration for this strong transition in ^{14}C is proposed to be

$$|^{12}C \otimes (\pi p_{3/2})^{-1}(\pi p_{1/2})(\pi d_{5/2})(\nu d_{5/2})\rangle_{7^+}.$$

Our 7^+ assignment to this state is a guess based on the observed tendency of the (p, π) reaction to selectively excite high-spin stretched 2p1h states through its peripheral nature and inherent intrinsic high-momentum transfer. A similar, but weakly populated and rather broad state is observed in the mirror nucleus (^{14}O) at nearly the same nuclear excitation. Because of its broad nature, it is doubtful that this enhancement represents a single state, in particular the 7^+ state. As can be seen in Table 7.1, the final state configuration in this case is anticipated to be

$$|^{12}C \otimes (\nu p_{3/2})^{-1}(\pi p_{1/2})(\nu d_{5/2})(\pi d_{5/2})\rangle_{7^+}.$$

According to our observations, a 7^+ state in ^{14}C would be strong since it would be reached from ^{13}C via the dominant $pp \rightarrow pn(^3S_1) \pi^+$ process, whereas $^{14}O(7^+)$ from the

same target nucleus is not possible via $pn \rightarrow pp\pi^-$. However the latter channel is possible in $^{13}C(p,\pi^-)$ if the ground-state neutron configuration in ^{13}C is

$$(\nu 1p_{3/2})^{-1}(\nu 1d_{5/2})^2 \Rightarrow (1/2)^{-1}.$$

This should only be a small fraction of the initial quantum state of the ^{13}C ground state. Hence the 7^+ state seen in $^{13}C(p,\pi^-)^{14}O$ spectrum (see Fig 6.12) should be weak. It may be possible that the enhancement at 22 MeV can be associated with a 7^+ state. The asymmetry and the relative strengths of the proposed 7^+ state in $(p,\pi^{\pm})$ supports the $NN \rightarrow NN\pi$ hypothesis and the 7^+ assignment.

7.4.3 Transitions to Low-spin States in $^{13}C(p,\pi^{\pm})$ Reactions

^{14}C and ^{14}O are members of the same isospin T=1 triplet. Therefore spectra for both the $^{13}C(p,\pi^+)^{14}C$ and $^{13}C(p,\pi^-)^{14}O$ reactions should display a similar set of states. This should be especially true for the low-lying states. This is seen in a comparison of Figs. 6.6 and 6.12. The low-lying states follow the pattern 0^+, 1^-, 0^+, 3^-, 2^+, 2^-, and 2^+ in both cases, with the 3^- states dominating both spectra. This is to be expected for the highest angular momentum states because of the large momentum transfer of the (p,π) reaction. Conversely the 0^+ states are weak. The 0^+ ground states can be resolved only because of their isolation from all other states. The 0^+ 6.5844 MeV state in ^{14}C is not seen at all as there appears to be no need for such a state in deconvoluting the 3^- 6.728 MeV peak. The 0^+ 5.92 MeV state in ^{14}O is only discernable at 221 MeV. Above this energy this state is also lost in the dominant 3^- (6.272 MeV) state.

7.4.4 Discrete Final States in $^{12}C(p,\pi^+)^{13}C$ Reaction

A typical excitation spectrum showing the discrete final states of ^{13}C via $^{12}C(p,\pi^+)^{13}C$ is given in Fig. 6.1. A strongly excited group of states in ^{13}C has been identified involving nuclear excitations of $0.00(\frac{1}{2}^-)$, $3.089(\frac{1}{2}^+)$, $3.685(\frac{3}{2}^-)$, $3.854(\frac{5}{2}^+)$, $6.864(\frac{5}{2}^+)$, $7.492(\frac{7}{2}^+)$, $7.668(\frac{3}{2}^+)$, and $9.50(\frac{9}{2}^+)$ MeV. Broad peaks in the spectrum beyond 9.50 MeV excitation seem to consist of admixtures of several states and hence a meaningful analysis is very complex. The final nuclear configurations of the discrete states in ^{13}C are presumed to be those given in Table 7.2 where only the strong transitions are listed. The $6.864(\frac{5}{2}^+)$, $7.492(\frac{7}{2}^+)$ and $7.668(\frac{3}{2}^+)$ MeV states are not listed as these can be different combinations of the $9.50(\frac{9}{2}^+)$ configuration.

119

Table 7.2: Nuclear configurations for the strongly-excited final states in ^{13}C via ^{12}C$(p, \pi^+)^{13}$C transitions. The incident proton interacts with the listed struck nucleon which is labelled according to the shell-model structure of ^{12}C.

Residual Nucleus	J^π	Final-state Configuration of the Residual Nucleus	Excitation (MeV)	Struck Nucleon
^{13}C	$\frac{1}{2}^-$	$\lvert^{12}C \otimes (\nu p_{1/2})\rangle$	Ground State	any n or p
^{13}C	$\frac{1}{2}^+$	$\lvert^{12}C \otimes (\nu 2s_{1/2})\rangle$	3.089	any n or p
^{13}C	$\frac{3}{2}^-$	$\lvert^{12}C \otimes (\pi p_{3/2})^{-1}(\pi p_{1/2})(\nu p_{1/2})\rangle$	3.685	$p_{3/2}\, p$
^{13}C	$\frac{5}{2}^+$	$\lvert^{12}C \otimes (\nu d_{5/2})\rangle$	3.854	any p or n
^{13}C	$\frac{9}{2}^+$	$\lvert^{12}C \otimes (\pi p_{3/2})^{-1}(\pi p_{1/2})(\nu d_{5/2})\rangle$ or $\lvert^{12}C \otimes (\pi p_{3/2})^{-1}(\pi d_{5/2})(\nu p_{1/2})$	9.50	$p_{3/2}\, p$

As explained in Chapter 2, the experimental spectra illustrate single particle and 2p1h (and their possible admixtures) final states excited by the (p, π^+) reaction. Differential cross section and analyzing power angular distributions determined for the strong transitions $\leq$ 10 MeV are shown in Figs. 6.2 and 6.3 at 250 MeV while those at 280 MeV are shown in Figs. 6.4 and 6.5. Some of these states are not completely resolved in the spectra. However, the unresolved groups of states were unfolded into their component states in the peak-fitting procedure to extract their yields. Differential cross sections calculated from these data for some low-lying states are compared with those from two previous studies [Lo84, Hu88] in Fig. 7.4 which shows a close agreement between our data and [Hu88]. The ground state cross section in [Lo84] seems to have had some problems at large angles. The agreement with [Hu88] indicates Lolos [Lo84] may have had problems with background for $d\sigma/d\Omega$ lower than 10 nb/sr.

$J^\pi = \frac{9}{2}^+$ State in ^{13}C

The $\frac{9}{2}^+$ final state in ^{13}C is strongly populated (see Fig. 6.1), and is identified as a high-spin 2p1h stretched state. This can be reached via a TNM channel, $pp \to pn(^3S_1)\, \pi^+$, and has equally strong contributions corresponding to the following final nuclear configurations

$$\lvert^{12}C \otimes (\pi 1p_{3/2})^{-1}(\pi 1p_{1/2})(\nu 1d_{5/2})\rangle_{\frac{9}{2}^+}$$
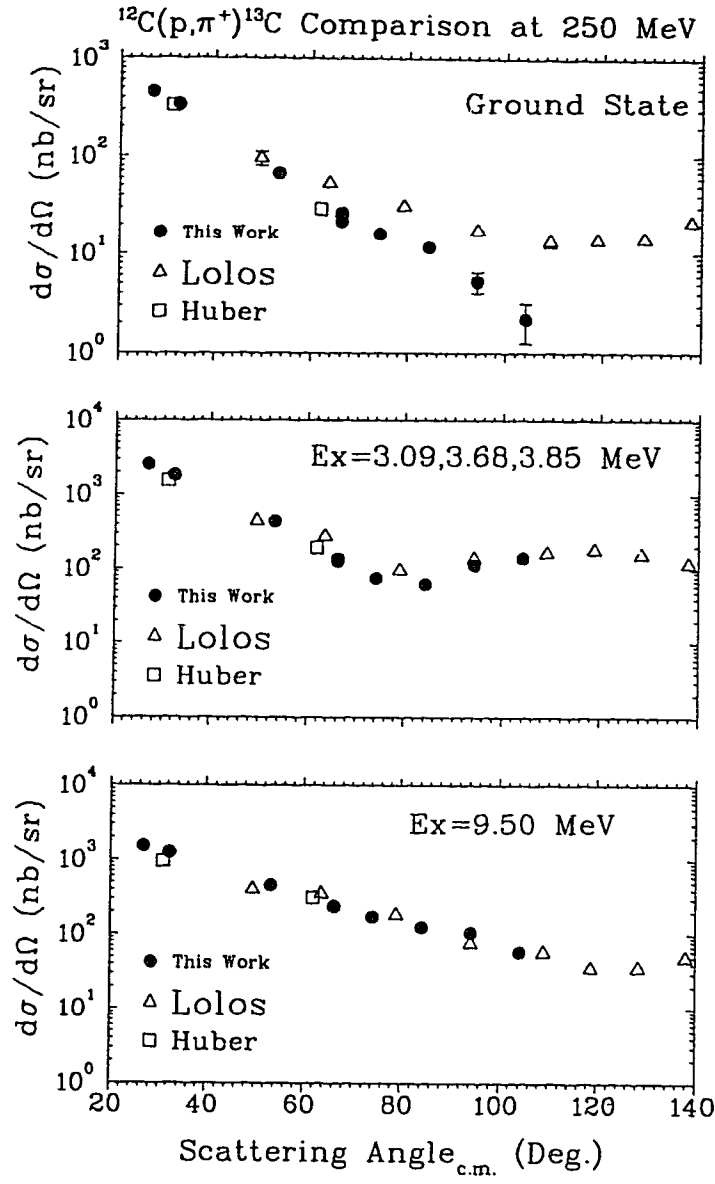
Figure 7.4: A comparison of differential cross sections for the low-lying final states of $^{12}C(p, \pi^+)^{13}C$ at 250 MeV. The Lolos results are from reference [Lo84] and the Huber results are from [Hu88].

and

$$|^{12}C \otimes (\pi 1p_{3/2})^{-1}(\nu 1p_{1/2})(\pi 1d_{5/2})\rangle_{\frac{9}{2}^+} \;.$$

This nuclear transition can be understood on the basis of the two nucleon mechanism with the dominance of the σ_{10} isospin channel. Here, the incident proton interacts with one proton from the $p_{3/2}$ sub-shell and the subsequent collision leaves a hole, while the final proton and the neutron are bound in $p_{1/2}$ and $d_{5/2}$ sub-shells, thus creating a 2p1h high-spin stretched state in the ^{13}C residual nucleus. The analyzing power angular distributions (see Figs. 6.3 and 6.5) calculated at 250 and 280 MeV have similar shapes as one expects from the free $pp \rightarrow d\pi^+$ case. A common thread should be discerned here. In all (p, π) spectra beyond the initial set of low-lying states, the states which are strongly excited are those in 2p1h configurations with respect to the initial state nuclei and in those configurations the combination which gives the highest spin is the one that is the most strongly excited. This is so for the 5^- state of ^{14}C and ^{14}O, the 4^+ state of ^{14}O, and the same for the $\frac{9}{2}^+$ state of ^{13}C.

21.50 MeV Excitation in ^{13}C

One can see a strong peak in the excitation spectrum shown in Fig. 6.1, which corresponds to a high nuclear excitation at 21.50 MeV in ^{13}C via ^{12}C(p, π^+). This is similar to what is observed in ^{14}C nucleus via ^{13}C(p, π^+) in Fig. 6.6. However, the peak in ^{13}C is not as narrow as that in ^{14}C. This broad nature makes the interpretation of this strong excitation complicated. There seems to be an admixture of several transitions responsible for this excitation. We believe that a major component of this state might be $\frac{13}{2}^-$ with a final configuration, $|^{12}$C$\otimes(\pi 1p_{3/2})^{-1}(\pi 1d_{5/2})(\nu 1d_{5/2})\rangle_{\frac{13}{2}^-}$, which can be reached via $pp \rightarrow pn\pi^+$ through σ_{10} isospin channel.

7.4.5 Discrete Final States in ^{41}Ca via ^{40}Ca(p, π^+) Transitions

The differential cross sections and analyzing powers have been extracted from the exclusive measurements of ^{40}Ca$(p, \pi^+)^{41}$Ca at 250 MeV and 280 MeV. A typical missing mass spectrum of this reaction is shown in Fig. 6.11 from the data collected at 250 MeV and 25° angle in the lab. The ground state and some low-lying excited states have been identified at nuclear excitations of 1.94, 2.01, 3.83, 3.91, 5.22, and 5.48 MeV. The yields to these bound states in ^{41}Ca were observed to decrease drastically with the increase of momentum transfer. Therefore, the differential cross sections and the analyzing powers for the bound states have been calculated only for the data collected at forward angles. These results are given in Appendix A.

The ^{40}Ca spectrum is very ambiguous with many closely-spaced levels beyond the

first excited state at 1.943 MeV. The only unambiguous state is the ground state, a spin $\frac{7}{2}^-$ single-particle state with a neutron in the $1f_{\frac{7}{2}}$ shell (see Table 7.3). This state is quite strongly excited as one would expect from its high spin value. The $\nu 2p_{3/2}$ state might be identified with the first excited state at 1.94 MeV which is a single-particle neutron state or it could be the $\frac{3}{2}^+$ state at 2.101 MeV which would necessitate a 2p1h configuration (see Table 7.3). In either case this experiment is unable to distinguish between the two. However, the former seems more likely because of its simple configuration.

Table 7.3: Nuclear configurations for strongly-excited final states in ^{41}Ca via ^{40}Ca$(p, \pi^+)^{41}$Ca transitions. The incident proton interacts with the listed struck nucleon which is labelled according to the shell-model structure of ^{40}C.

Residual Nucleus	J^π	Final-state Configuration of the Residual Nucleus	Excitation (MeV)	Struck Nucleon
^{40}Ca	$\frac{7}{2}^-$	$\lvert ^{40}Ca \otimes (\nu 1 f_{7/2}) \rangle$	Ground State	$d_{3/2}\, p$
^{40}Ca	$\frac{3}{2}^-$	$\lvert ^{40}Ca \otimes (\nu 2 p_{3/2}) \rangle$	1.94	$d_{3/2}\, p$
^{40}Ca	$\frac{17}{2}^+$	$\lvert ^{40}Ca \otimes (\pi 1 d_{3/2})^{-1}(\pi 1 f_{7/2})(\nu 1 f_{7/2}) \rangle$	5.22	$d_{3/2}\, p$

At 3.8, 5.2, 6.1, and 7.4 MeV excitations there are some fairly prominent peaks. All of them, except for the last, fall in regions where there are states labelled $\frac{15}{2}^+$, $\frac{17}{2}^+$, and $\frac{11}{2}^+$. The most prominent peak falls, as expected in the $\frac{17}{2}^+$ region. This state at 5.219 MeV has a double assignment of ($\frac{13}{2}^+$ or $\frac{17}{2}^+$) [En90]. Experience with the (p, π^+) reaction would suggest that an assignment of $\frac{17}{2}^+$ is appropriate with a 2p1h configuration of $(\pi 1 d_{3/2})^{-1}(\pi 1 f_{7/2})(\nu 1 f_{7/2})$ with all components aligned, unlike the $\frac{3}{2}^+$ state (see Table 7.3). Similarly an assignment of $\frac{11}{2}^+$ to the 6.1 MeV state seems in order. At 7.4 MeV, there are no states listed in the literature [En90].

It should be pointed out that not all the high spin states (regions) have been picked out. There is a $\frac{13}{2}^+$ state at 4.52 MeV [En90] which is not seen. The reason for this is unknown. Perhaps it is a configuration which requires excitation from a neutron and naturally would be suppressed.

7.5 $\Delta(1232)$ Excitation in $(p, \pi^{\pm})$ Reaction

At this stage, we have good evidence that the nuclear pion production reaction proceeds through $NN \to NN\pi$ processes occurring within the nuclear medium. Thus, the effective reaction mechanism is such that the two nucleons interact strongly in the initial state. The most probable intermediate state is $\Delta + N$ where one of the nucleons is excited into its lowest excited state which is the $\Delta(1232)$ isobar, plus the other nucleon. This virtual Δ particle can propagate a very short time within the many-nucleon environment, experiencing some nuclear structure effects before decaying into a real pion and a nucleon, resulting in the final state of two nucleons and a pion. This Δ-excitation in the (p, π^-) reaction has different consequences compared to those for the (p, π^+) reaction. The allowed Δ-amplitudes are different in the two reaction modes. This leads to a situation where a strong Δ-resonance is observed in (p, π^+) while it is very weak in (p, π^-). This phenomenon can be understood in the context of the following arguments which are graphically illustrated in Fig. 7.5. In Fig. 7.5, we consider that the incoming projectile proton interacts with one of the target nucleons which is moving towards the projectile. After the interaction, the final nucleon pair, which is presumed to be left in a S-state with a small relative momentum between the two nucleons, is captured in the final A+1 residual nucleus. All the particle directions in this figure are considered in the center-of-mass system. Then we analyse the initial, intermediate, and final states of the $A(p, \pi)A+1$ reaction in detail on the basis of TNM by assuming a Δ-isobar excitation in the intermediate state.

In the context of TNM, the only reaction channel available for π^- production is $pn \to pp\pi^-$ where the final proton pair is presumed to be in a relative $^1S_0$ singlet state. This assumption is reasonable due to the large momentum transfer involved in the $A(p, \pi)A+1$ reaction which highly favours an optimal momentum sharing for the process to occur. This assumption seems borne out by the transformation discussed in section 7.1.1 which describes mapping $NN \to NN\pi$ measured analyzing powers onto those of $A(p, \pi)A+1$. The favourable comparison in sections 7.2 and 7.3 bears out the assumptions. The total spin of the initial pn state can be either a spin $S = 1$ triplet or $S = 0$ singlet with isospin $T = 1$ or $T = 0$. As illustrated in Fig. 7.5, the possible partial wave amplitudes which satisfy the $S = 1$ triplet are $^3S_{1+}$, $^3P_{2-,1-,0-}$, $^3D_{3+,2+,1+}$, $^3F_{4-,3-,2-}$, and so on. Similarly, those amplitudes which satisfy the $S = 0$ singlet are $^1S_{0+}$, $^1P_{1-}$, $^1D_{2+}$, $^1F_{3-}$, and so on. Since the total wave function of the initial fermion system must be completely antisymmetric one has $T=0(1)$ when $S=1(0)$. This leads to the amplitudes, $^3S_{1+}$, $^1P_{1-}$, $^3D_{3+,2+,1+}$, $^1F_{3-}$, and so on having $T=0$, while

124

$^1S_{0+}$, $^3P_{2-,1-,0-}$, $^1D_{2+}$, $^3F_{4-,3-,2-}$, and so on having $T=1$.

Now consider the intermediate ΔN state which has total spin $S=2$ or 1, and isospin $T=2$ or 1 because Δ is spin $\frac{3}{2}$, isospin $\frac{3}{2}$ and N is spin $\frac{1}{2}$, isospin $\frac{1}{2}$. Therefore, the J^π of ΔN in a S-wave can be either 2^+ or 1^+, while in P-wave it can be either 3^-, 2^-, 1^-, or 0^-. In an examination of what initial states satisfy both the $T = 1$ requirement ($T = 2$ is impossible for NN systems) and the J^π possibilities, only the $^1D_{2+}$ amplitude is possible for a ΔN S-wave and the $^3F_{3-}$, $^3F_{2-}$, $^3P_{2-}$, $^3P_{1-}$ and $^3P_{0-}$ amplitudes are possible for a ΔN P-wave. The final state, $pp(^1S_0)\pi^-$, because of the π, have unnatural parity J^π values of 0^-, 1^+, 2^-, 3^+, ... An examination of the initial states which satisfy $T = 1$, and the J^π of ΔN and $pp(^1S_0)$ π^- in Fig. 7.5 leaves only the amplitudes $^3P_{2-,0-}$ and $^3F_{2-}$ which are relatively very weak. The strong Δ amplitudes such as $^1D_{2+}$ and $^3F_{3-}$ are not allowed. However, both of these strong Δ amplitudes are allowed in reaction channels proceeding via $pp \rightarrow \Delta N \rightarrow pn(^3S_1)$ π^+. This inability of the $pn \rightarrow pp(^1S_0)$ π^- to proceed via strong ΔN intermediate states is a primary reason why the (p,π^+) reaction is much stronger than the (p,π^-) reaction.

Since the single particle wave function drops drastically with the increase of momentum transfer, one has to observe the $A(p,\pi)A+1$ reaction at constant momentum transfer in order to study the Δ-resonance. An examination of the reaction strength for a selected strongly-populated final states in the $^{13}C(p,\pi^\pm)$ at constant momentum transfer helps to understand this phenomenon. The relative matrix element squared, $|M|^2$, is plotted in Fig. 7.6 as a function of $\sqrt{s} - M_N$ at constant 4-momentum transfer squared $t = 0.527$ (GeV/c)^2 for the 3^- (6.272 MeV) state in ^{14}O to study the Δ-excitation in the $^{13}C(p,\pi^-)^{14}O$ reaction. Here s is the effective center-of-mass energy considering the $NN \rightarrow NN\pi$ two-nucleon process, and M_N is the average nucleon mass. The relative matrix element squared extracted from the differential cross section is free of any effects due to an increase in phase space as the energy increases. Thus, $|M|^2$ versus $\sqrt{s} - M_N$ at constant t is indicative of the energy dependence of the $NN \rightarrow NN\pi$ reaction. The relative $|M|^2$ is calculated as

$$| M |^2 = K \cdot S \left[\frac{k_p}{k_\pi}\right] \left[\frac{d\sigma}{d\Omega}\right], \tag{7.13}$$

where S is the total energy, and k_p and k_π are the momenta of the incident proton and the outgoing pion, respectively. All are calculated in the $(p + A)$ center-of-mass system. The constant K is

$$K = \frac{64\pi^2}{\hbar^2 c^2} \frac{(2J_A + 1)(2S_p + 1)}{(2J_{A+1} + 1)(2S_\pi + 1)} .$$

The results are given in Fig. 7.6(a) which shows that the cross section tends to be

125

smaller at the Δ invariant mass of 1232 MeV. The cross section enhancement in this figure for the lower invariant mass region reflects the threshold behaviour of the reaction. This demonstrates that the Δ-isobar excitation in the reaction $A(p, \pi^-)A+1$ is very weak as expected (see section 7.3).

The Δ excitation was also examined for the continuum region of the $A(p, \pi^-)X$ reaction at constant t. The relative matrix element squared was plotted against the $\sqrt{s} - M_N$ at a constant $t = 0.539$ (Gev/c)^2 for a selected high excitation region (21 MeV) of the $^{13}C(p, \pi^-)X$ continuum. Fig. 7.6(b) shows the results of this analysis indicating that the (p, π^-) reaction strength in the continuum region becomes more dominant with respect to the exclusive final states as beam energy increases. However, $|M|^2$ to the continuum shows no hint of a delta excitation, and the question would probably not have been answered by taking more data at higher energies.

According to the explanation (at the beginning of this section) on the Δ excitation in the $A(p, \pi^+)A+1$ reaction, one should see strong Δ effects in this case. This was studied previously [Hu88]. The invariant matrix elements were extracted from the differential cross sections of the reaction $A(p, \pi)A+1$ in order to remove any effects due to an increase in phase space as the energy increases. The matrix elements extracted from the $^{13}C(p, \pi^+)^{14}C$ are shown in Fig. 7.6(c) as a function of the invariant mass at a constant t for the 3^- (6.728 MeV) final state in ^{14}C. The results show a cross section enhancement for the invariant mass in the Δ region, indicating that the (p, π^+) reaction proceeds via strong Δ-isobar excitation. These observations provide evidence supporting that the nuclear pion production proceeds predominantly through $NN \rightarrow NN\pi$ two-nucleon reaction channels.

Reaction: $A(p, \pi^-)A+1$ $\qquad$ $pn \longrightarrow$ $\Delta N \longrightarrow$ $pp(^1S_0)\pi^-$

(1) Initial State : pn

$S \longrightarrow 1/2 \otimes 1/2$ $\qquad$ $S=1$

or

$T \longrightarrow 1$ or 0 $\qquad$ $S=0$

$T=0$	$T=1$	$T=0$	$T=1$
$^3S_{1^+}$	$^3P_{2^-,1^-,0^-}$	$^3D_{3^+,2^+,1^+}$	$^3F_{4^-,3^-,2^-}$
$^1S_{0'}$	$^1P_{1^-}$	$^1D_{2^+}$	$^1F_{3^-}$
$T=1$	$T=0$	$T=1$	$T=0$

(2) Intermediate State : ΔN

$S \longrightarrow 3/2 \otimes 1/2$ $\qquad$ J^π : $\boxed{2^+, 1^+}$ x $L = 1$

$T \longrightarrow 1$ or 2 $\qquad\qquad$ S wave

$$\boxed{\begin{array}{c} 3^-, 2^-, 1^- \\ 2^-, 1^-, 0^- \end{array}}$$

(3) Final State : $pp(^1S_0)\pi^-$ $\qquad\qquad$ P wave

This now has unnatural parity states

J^π : $0^-, 1^+, 2^-, 3^+, \dots$

$^1D_2^+$ and $^3F_3^-$ strong ΔN amplitudes are not present in $A(p, \pi^-)A+1$

Figure 7.5: A brief analysis to illustrate that the $\Delta(1232)$ excitation in the $A(p, \pi^-)A+1$ reaction is weak compared to that in the $A(p, \pi^+)A+1$ reaction. See the text for details.

Figure 7.6: An illustration of the Δ excitation in the $(p, \pi^{\pm})$ reaction. (a) shows the relative matrix element $|M|^2$ vs $NN \rightarrow NN\pi$ CM energy for the reaction $^{13}C(p, \pi^-)^{14}O$ at a constant 4-momentum transfer squared $t = 0.527$ $(GeV/c)^2$. A similar plot is shown in (b) for the (p, π^-) continuum at a $t = 0.539$ $(GeV/c)^2$. Matrix element vs CM energy for the reaction $^{13}C(p, \pi^+)^{14}C$ is shown at a constant $t = 0.50$ $(GeV/c)^2$ in (c). The data shown in (c) were obtained from reference [Hu88].

128

Chapter 8

Conclusions

For the present $A(p, \pi^{\pm})A+1$ study measurements were made using TRIUMF's Second Arm Spectrometer which was used for the first time for a complete experiment without having to require the presence of a front-end chamber. This was achieved by analyzing the beam optics of the overall spectrometer system, allowing the particle trajectories to be traced back to the target using only information from the top-end detectors. Thus SASP is capable of measuring low cross-section reactions, such as nuclear pion production, within a practical period of time by running at high beam currents and eliminating problems arising from high count rates in a front-end detection system.

This investigation is focused on the reactions $^{12}C(p, \pi^+)^{13}C$, $^{13}C(p, \pi^+)^{14}C$, $^{40}Ca(p, \pi^+)^{41}Ca$, and $^{13}C(p, \pi^-)^{14}O$ observed over the energy range of 220 - 350 MeV. Angular distributions of differential cross sections and analyzing powers have been determined for the strongly-populated discrete final states as well as for the continuum region. These analyzing-power angular distributions, for both the continuum and for some of the final states, have been compared to those for free $NN \to NN\pi$. Consistent agreement suggests that $NN \to NN\pi$ is the dominant reaction mechanism.

For the (p, π^+) reaction on nuclei, the $NN \to NN\pi$ process which is of interest is the free $pp \to d\pi^+$ reaction as it is by far the dominant component in the $pN \to NN\pi^+$ reaction in this experiment's energy region. The reasonable agreement of the analyzing power angular distributions between $pp \to d\pi^+$ and the continuum (p, π^+) is suggestive that the nuclear pion production occurs predominantly in a quasi-free $NN \to NN\pi$ process within the many-nucleon environment. This is a feasible hypothesis as the large momentum transfer in the collision is shared by the initial state and the two final state nucleons. The observed discrepancies can be accommodated by a change in the effective

beam energy by an amount that can be reasonably attributable to initial and final state nuclear distortions.

It is shown via the $pp \rightarrow d\pi^+$ variant that the $NN \rightarrow NN\pi$ hypothesis is applicable for nuclei heavier than the $1p$ valence shell nuclei (i.e., $A = 1$ to 16). A comparison of measured analyzing-power angular distributions in the continuum for the (p, π^+) reaction on a d-shell nucleus (^{40}Ca) with those for the free $pp \rightarrow d\pi^+$ equivalent process shows similar agreement, as did (p, π^+) on ^{12}C and ^{13}C. The only difference in the ^{40}Ca case as opposed to the $1p$ nuclei case is that a lower effective beam energy is required to gain reasonable agreement with the $pp \rightarrow d\pi^+$ analyzing power. This can be attributed to larger distortions in the ^{40}Ca case which is quite reasonable as ^{40}Ca is a larger nucleus. Hence, it can be concluded that the $NN \rightarrow NN\pi$ process in the $pp \rightarrow d\pi^+$ variant is the dominant (p, π^+) mechanism for any nuclei.

In contrast to the continuum analyzing power results, (p, π^+) to exclusive final states have analyzing power angular distributions which have decidedly non-characteristics of $pp \rightarrow d\pi^+$. This is not surprising as the constraints of removing one nucleon from the target nucleus and restoring a "d" (i.e., a $^3S_1$ pn pair) back into the recoil nucleus can restrict the available $pp \rightarrow d\pi^+$ amplitude set. The analyzing power, being an interference of amplitudes, is quite sensitive to small amplitude changes, thus radically different $A(p, \pi^+)A+1$ analyzing powers may not be unexpected. Nevertheless there are some exclusive final states which display characteristics of $pp \rightarrow d\pi^+$ analyzing powers. These are notably high-spin stretched nuclear excitations such as the $\frac{9}{2}^+$ (9.5 MeV) state of ^{13}C and the 5^- (14.868 MeV) state of ^{14}C.

It is interesting that the equivalent $T = 1$, 5^- state of ^{14}O at 14.15 MeV displays characteristics of the $pn \rightarrow pp(^1S_0) \pi^-$ analyzing power. A comparison of measured analyzing-power angular distributions for the reaction $A(p, \pi^-)A+1$ with those calculated for the free $pn \rightarrow pp(^1S_0) \pi^-$ equivalent process at energies of 200 and 221 MeV shows a favourable agreement. However, unlike the final state of the $A(p, \pi^+)X$ where the final nucleon pair (pn) is favoured to be in a relative $^3S_1$ state by both dynamics and kinematics, the final pp pair in the $A(p, \pi^-)X$ reaction is not favoured to be in a relative $^1S_0$ state. Therefore, a similarity in the comparison of analyzing powers between the $A(p, \pi^-)X$ continuum and the $pn \rightarrow pp(^1S_0) \pi^-$ free process, as is observed for (p, π^+), is not observed as expected. It is hypothesized that in the 5^- case the restrictions of absorbing a final pp pair favour a $^1S_0$ configuration.

It is not known why high-spin stretched states favour characteristics of $NN \rightarrow NN\pi^+$ analyzing power. It can be speculated that such states allow only one reaction

route from the initial target shell configuration and that the final NN pair is absorbed onto an unoccupied shell where the $NN \to NN\pi$ amplitude set is not compromised by spin and Pauli blocking considerations. However, the 7^+ state of ^{14}C at 23.288 MeV is also a high-spin stretched state, and displays a flat analyzing power in contrast to that of $pp \to d\pi^+$. Therefore, sorting out the observed characteristics of the exclusive (p, π) analyzing powers will require a fully developed theoretical treatment, hopefully using the $NN \to NN\pi$ amplitude sets as input.

The quantum numbers and/or configurations of the mirror states produced by the reactions ^{13}C$(p, \pi^\pm)$ can be understood to some degree by invoking an underlying $NN \to NN\pi$ processes. The difference in the prominence of the 4^+ state in ^{14}C and ^{14}O spectra is indicative that the 4^+ state in ^{14}C cannot be directly excited via a proton as required by $NN \to NN\pi$ and $pp \to d\pi^+$ dominance. The 5^- state is equally available via $NN \to NN\pi$ channel for both ^{14}C and ^{14}O and both are equally prominent. In contrast, the 7^+ (23.288 MeV) of ^{14}C is only accessible to (p, π^+), and the corresponding peak in ^{14}O at a similar excitation seems to be weak. It is the confidence in these $NN \to NN\pi$ signatures that a J^π of 5^- is assigned to the 14.868 MeV and 14.15 MeV of ^{14}C and ^{14}O, respectively as in agreement with Korkmaz [Ko89]. Similarly a J^π of 7^+ assignment is given to the ^{14}C state at 23.288 MeV.

Using the same arguments that (p, π^+) excites predominately the highest spin states, the peaks seen in the ^{40}Ca$(p, \pi^+)^{41}$Ca spectrum at 3.8, 5.2, and 6.1 MeV can be associated with the $\frac{15}{2}^+$ (3.83 MeV), the $\frac{17}{2}^+$ (5.219 MeV) and the $\frac{11}{2}^+$ (6.066 MeV) states. The latter two states are of uncertain assignment in the literature [En90] and their appearance in the (p, π^+) spectrum favours the highest possible J^π assignment.

There does not seem to be a strong role for the Δ-isobar excitation in the intermediate state of the reaction A(p, π^-)A+1. The relative strengths of the observed (p, π^+) and (p, π^-) cross sections indicate this. From previous work [Hu88] the energy dependence of the (p, π^+) reaction shows a Δ-excitation, but not such resonance is seen in the (p, π^-) reaction. This energy dependence of (p, π^-) reaction is confirmed in this experiment. The (p, π^-) energy dependence has been previously restricted to exclusive A+1 final states which favour $^1S_0$ final pp absorption. For (p, π^-) to the continuum, final pp pairs in a relative P-wave could be expected which can have a direct Δ-excitation. The energy dependence to the continuum was extracted in this experiment, but no definitive Δ-excitation could be seen. However, it is quite evident that (p, π^-) strength to the continuum quickly dominates over the exclusive final states as the beam energy increases. Whether Δ-excitation in the continuum is responsible cannot be determined from this

experiment.

In summary, strong evidence is found to support a $NN \rightarrow NN\pi$ model for the reaction mechanism of the nuclear pion production process. In particular the observed spectroscopic features of the measured reactions are interpreted on the basis of this model. The role of the Δ-isobar excitation in the (p, π^-) reaction is discussed on expectations of the described reaction mechanism. The analyzing power to the continuum of the reaction (p, π^+) constitutes strong $NN \rightarrow NN\pi$ signature.

With the data of Huber [Hu88], Korkmaz [Ko89] and this experiment, a solution to understanding the (p, π) reaction seems apparent. A fully developed theoretical model is required which uses $NN \rightarrow NN\pi$ amplitudes as specific input. It is essential that the model be fully relativistic. If such a theory is developed, the variety of differential cross section and analyzing power $(d\sigma/d\Omega$ and $A_y)$ information in exclusive (p, π) reactions may be interpreted on the basis of nuclear structure information. Also one can extend these measurements by choosing several other nuclei over a wider energy range. More physics information can be extracted from such measurements with further improved resolution and better statistics taken within a wider angular range.

Appendix A

Data Tables

Numerical values of the results extracted from this study are given in this section. The cross section and analyzing power data include only the statistical errors. The thickness of the nuclear targets, ^{12}C. ^{13}C, and ^{40}Ca, were 58.2, 96.0, and 15.68 mg/cm^2, respectively. The error of the target thickness is estimated to be $\sim$ 3%. There are also other systematic uncertainties coming from the solid angle (5%), pion survival fraction (3%), chamber efficiency (5%), background subtraction (4%) so that a total of $\sim$ ±9% systematic error is estimated in the results.

A.1 Data Tables for the Bound-state Analysis

Each data table has the reaction and the incident proton energy at which it was measured. Cross section and analyzing power data are tabulated for each bound state as a function of the center of mass angle.

Table A.1: The angular distributions of cross section and analyzing power data at 250 MeV for the bound states of the $^{12}C(p.\pi^+)^{13}C$ at excitation energies of 0.000 and 3.089 MeV.

$\theta_{c.m.}$ (Deg.)	Ground State		3.089 MeV	
	$d\sigma/d\Omega$ (nb/sr)	Ay	$d\sigma/d\Omega$ (nb/sr)	Ay
26.78	458 ± 8	0.115 ± 0.023	509 ± 8	-0.432 ± 0.025
32.22	343 ± 7	0.123 ± 0.029	418 ± 8	-0.588 ± 0.030
53.29	67.2 ± 2.5	0.239 ± 0.049	131 ± 3	-0.600 ± 0.036
66.31	21.4 ± 2.5	0.700 ± 0.137	46.0 ± 3.4	-0.096 ± 0.096
66.31	26.4 ± 2.6	0.582 ± 0.114	43.7 ± 3.0	-0.025 ± 0 091
66.31	24.5 ± 2.4	0.625 ± 0.125	39.2 ± 2.8	-0.139 ± 0.093
74.17	16.0 ± 1.7	0.935 ± 0.129	27.6 ± 2.0	-0.478 ± 0.100
84.21	11.7 ± 0.9	0.890 ± 0.110	29.9 ± 1.3	-0.683 ± 0.059
94.25	5.2 ± 1.2	0.759 ± 0.317	43.7 ± 2.8	-1.113 ± 0.075
104.18	2.2 ± 0.9	0.678 ± 0.559	40.7 ± 2.4	-0.933 ± 0.074

134

Table A.2: The angular distributions of cross section and analyzing power data at 250 MeV for the bound states of the $^{12}C(p,\pi^+)^{13}C$ at excitation energies of 3.685, 3.854, 6.864, 7.492, 7.686, and 9.500 MeV.

$\theta_{c.m.}$ (Deg.)	3.685 MeV		3.854 MeV	
	$d\sigma/d\Omega$ (nb/sr)	Ay	$d\sigma/d\Omega$ (nb/sr)	Ay
26.78	368 ± 9	-0.095 ± 0.031	1672 ± 16	0.070 ± 0.0127
32.22	345 ± 10	-0.032 ± 0.040	1055 ± 15	-0.030 ± 0.019
53.29	117 ± 6	0.063 ± 0.062	187 ± 6	-0.747 ± 0.044
66.31	40.2 ± 5.2	0.586 ± 0.163	47.0 ± 5.2	-0.327 ± 0.150
66.31	40.6 ± 4.9	0.414 ± 0.157	47.4 ± 4.8	-0.270 ± 0.135
74.17	26.1 ± 3.7	0.850 ± 0.162	21.2 ± 3.4	0.629 ± 0.186
84.21	17.0 ± 2.0	0.445 ± 0.164	15.4 ± 1.8	-0.213 ± 0.161
94.25	40.9 ± 4.8	0.009 ± 0.162	29.7 ± 4.3	-1.206 ± 0.161
104.18	36.7 ± 5.5	-0.723 ± 0.185	63.7 ± 5.5	-0.647 ± 0.107

$\theta_{c.m.}$ (Deg.)	6.864 MeV		7.492 MeV	
	$d\sigma/d\Omega$ (nb/sr)	Ay	$d\sigma/d\Omega$ (nb/sr)	Ay
26.78	780 ± 11	-0.187 ± 0.019	1187 ± 14	0.315 ± 0.018
32.22	643 ± 11	-0.221 ± 0.023	1039 ± 15	0.363 ± 0.021
53.29	226 ± 5	-0.164 ± 0.026	310 ± 7	0.313 ± 0.030
66.31	90.1 ± 4.8	-0.006 ± 0.070	122 ± 7.2	0.148 ± 0.076
66.31	89.6 ± 4.3	-0.022 ± 0.063	137 ± 7.1	0.092 ± 0.068
74.17	42.5 ± 2.6	0.518 ± 0.083	84.7 ± 5.4	0.280 ± 0.089
84.21	20.9 ± 1.3	1.102 ± 0.092	74.8 ± 3.0	0.137 ± 0.056
94.25	15.7 ± 2.0	0.824 ± 0.177	63.4 ± 5.2	0.420 ± 0.112
104.18	20.5 ± 1.9	-0.022 ± 0.125	41.3 ± 4.1	0.169 ± 0.137

$\theta_{c.m.}$ (Deg.)	7.686 MeV		9.500 MeV	
	$d\sigma/d\Omega$ (nb/sr)	Ay	$d\sigma/d\Omega$ (nb/sr)	Ay
26.78	404 ± 10	0.487 ± 0.035	1520 ± 15	0.370 ± 0.017
32.22	277 ± 10	0.471 ± 0.047	1247 ± 15	0.395 ± 0.020
53.29	92.3 ± 5.4	-0.007 ± 0.075	456 ± 7	-0.207 ± 0.020
66.31	50.3 ± 6.1	-0.224 ± 0.160	240 ± 8	-0.737 ± 0.043
66.31	53.4 ± 6.0	-0.148 ± 0.146	239 ± 7	-0.741 ± 0.040
74.17	44.6 ± 4.9	-0.467 ± 0.159	173 ± 5	-0.829 ± 0.044
84.21	31.9 ± 2.8	0.142 ± 0.119	126 ± 3	-0.624 ± 0.034
94.25	33.3 ± 5.0	-0.145 ± 0.211	107 ± 5	0.062 ± 0.059
104.18	21.0 ± 3.8	-0.290 ± 0.252	58.7 ± 3.3	0.671 ± 0.077

Table A.3: The angular distributions of cross section and analyzing power data at 280 MeV for the bound states of the $^{12}C(p,\pi^+)^{13}C$ at excitation energies of 0.000, 3.089, 3.685, 3.854, 6.864, 7.492, 7.686, and 9.500 MeV.

	Ground State		3.089 MeV	
$\theta_{c.m.}$ (Deg.)	$d\sigma/d\Omega$ (nb/sr)	Ay	$d\sigma/d\Omega$ (nb/sr)	Ay
26.85	300 ± 10	0.586 ± 0.047	393 ± 12	-0.161 ± 0.042
32.09	226 ± 9	0.609 ± 0.053	329 ± 11	-0.363 ± 0.046
42.67	100 ± 4	0.840 ± 0.057	181 ± 6	-0.369 ± 0.048
53.12	48.6 ± 2.5	0.918 ± 0.070	104 ± 4	-0.104 ± 0.047
74.06	17.2 ± 0.9	0.729 ± 0.072	31.9 ± 1.2	-0.233 ± 0.050
104.00	1.10 ± 0.29	-0.766 ± 0.333	19.7 ± 0.9	-0.732 ± 0.063

	3.685 MeV		3.854 MeV	
$\theta_{c.m.}$ (Deg.)	$d\sigma/d\Omega$ (nb/sr)	Ay	$d\sigma/d\Omega$ (nb/sr)	Ay
26.85	439 ± 18	0.087 ± 0.058	1534 ± 26	0.148 ± 0.024
32.09	306 ± 15	0.118 ± 0.071	1021 ± 22	-0.029 ± 0.030
42.67	160 ± 9	0.239 ± 0.078	343 ± 11	-0.324 ± 0.044
53.12	76.3 ± 4.5	0.495 ± 0.084	130 ± 5	-0.372 ± 0.056
74.06	21.5 ± 1.3	0.714 ± 0.083	37.4 ± 1.6	0.286 ± 0.057
104.00	11.9 ± 1.1	0.256 ± 0.144	30.0 ± 1.4	-0.878 ± 0.065

	6.864 MeV		7.492 MeV	
$\theta_{c.m.}$ (Deg.)	$d\sigma/d\Omega$ (nb/sr)	Ay	$d\sigma/d\Omega$ (nb/sr)	Ay
26.85	655 ± 16	-0.168 ± 0.034	1270 ± 24	0.425 ± 0.028
32.09	524 ± 14	-0.230 ± 0.038	1087 ± 22	0.505 ± 0.031
42.67	278 ± 8	-0.277 ± 0.040	570 ± 13	0.493 ± 0.033
53.12	124 ± 4	-0.083 ± 0.046	273 ± 7	0.532 ± 0.036
74.06	31.0 ± 1.2	0.710 ± 0.053	67.5 ± 2.0	0.519 ± 0.041
104.00	18.6 ± 0.933	-0.287 ± 0.070	25.6 ± 1.3	0.110 ± 0.075

	7.686 MeV		9.500 MeV	
$\theta_{c.m.}$ (Deg.)	$d\sigma/d\Omega$ (nb/sr)	Ay	$d\sigma/d\Omega$ (nb/sr)	Ay
26.85	486 ± 18	0.580 ± 0.051	2162 ± 28	0.445 ± 0.021
32.09	406 ± 16	0.559 ± 0.056	1850 ± 26	0.444 ± 0.023
42.67	210 ± 10	0.648 ± 0.065	999 ± 15	0.400 ± 0.023
53.12	66.9 ± 4.8	0.529 ± 0.094	419 ± 7	-0.002 ± 0.025
74.06	28.3 ± 1.5	0.553 ± 0.073	93.2 ± 2.1	-0.496 ± 0.032
104.00	12.6 ± 1.1	0.063 ± 0.127	38.6 ± 1.4	0.770 ± 0.051

Table A.4: The angular distributions of cross section and analyzing power data at 250 MeV for the bound states of the $^{13}C(p,\pi^+)^{14}C$ at excitation energies of 0.000, 6.094, 6.728, 7.012, 7.341, and 8.318 MeV.

$^{13}C(p,\pi^+)^{14}C$ Reaction at 250 MeV				
	Ground State		6.094 MeV	
$\theta_{c.m.}$ (Deg.)	$d\sigma/d\Omega$ (nb/sr)	Ay	$d\sigma/d\Omega$ (nb/sr)	Ay
26.63	171 ± 4	0.225 ± 0.032	511 ± 7	-0.362 ± 0.021
32.04	115 ± 3	0.239 ± 0.037	373 ± 5	-0.445 ± 0.023
53.02	14.4 ± 1.2	1.081 ± 0.084	99.9 ± 2.6	-0.460 ± 0.036
66.00	7.92 ± 1.00	0.992 ± 0.134	34.8 ± 1.8	-0.018 ± 0.069
73.85	6.96 ± 0.76	0.524 ± 0.146	25.2 ± 1.3	-0.287 ± 0.072
83.87	4.18 ± 0.59	0.466 ± 0.189	23.2 ± 1.1	-0.805 ± 0.059
93.93	4.86 ± 0.70	-0.094 ± 0.200	27.6 ± 1.3	-0.744 ± 0.059
103.84	2.20 ± 0.82	0.072 ± 0.512	24.2 ± 1.7	-0.887 ± 0.085
	6.728 MeV		7.012 MeV	
$\theta_{c.m.}$ (Deg.)	$d\sigma/d\Omega$ (nb/sr)	Ay	$d\sigma/d\Omega$ (nb/sr)	Ay
26.63	1273 ± 12	0.020 ± 0.012	308 ± 7	-0.149 ± 0.028
32.04	857 ± 10	-0.110 ± 0.015	318 ± 9	-0.166 ± 0.039
53.02	198 ± 4	-0.632 ± 0.032	58.5 ± 4.0	-0.038 ± 0.089
66.00	69.0 ± 3.0	-0.431 ± 0.058	30.2 ± 2.9	0.544 ± 0.132
73.85	36.1 ± 1.9	-0.084 ± 0.074	18.6 ± 1.9	0.527 ± 0.147
83.87	19.8 ± 1.3	-0.220 ± 0.089	11.3 ± 1.4	-0.031 ± 0.169
93.93	27.1 ± 1.6	-0.600 ± 0.078	14.1 ± 1.7	-0.718 ± 0.157
103.84	30.3 ± 2.5	-0.726 ± 0.102	18.9 ± 2.8	-0.624 ± 0.184
	7.341 MeV		8.318 MeV	
$\theta_{c.m.}$ (Deg.)	$d\sigma/d\Omega$ (nb/sr)	Ay	$d\sigma/d\Omega$ (nb/sr)	Ay
26.63	414 ± 7	-0.174 ± 0.022	118 ± 4	0.321 ± 0.046
32.04	328 ± 7	-0.306 ± 0.027	141 ± 4	0.290 ± 0.038
53.02	85.2 ± 3.0	-0.701 ± 0.047	51.6 ± 2.2	-0.075 ± 0.055
66.00	26.0 ± 2.0	-0.274 ± 0.102	27.8 ± 1.8	-0.015 ± 0.089
73.85	13.8 ± 1.3	0.184 ± 0.132	17.3 ± 1.2	0.024 ± 0.094
83.87	13.0 ± 1.1	-0.157 ± 0.115	13.4 ± 0.9	0.183 ± 0.096
93.93	23.3 ± 1.5	-0.355 ± 0.087	13.2 ± 1.0	0.091 ± 0.104
103.84	28.2 ± 2.3	-0.783 ± 0.103	7.36 ± 1.26	-0.829 ± 0.217

Table A.5: The angular distributions of cross section and analyzing power data at 250 MeV for the bound states of the $^{13}C(p, \pi^+)^{14}C$ at excitation energies of 9.801, 10.425, 10.736, 11.666, 14.868, and 23.288 MeV.

	9.801 MeV		10.425 MeV	
$\theta_{c.m.}$ (Deg.)	$d\sigma/d\Omega$ (nb/sr)	Ay	$d\sigma/d\Omega$ (nb/sr)	Ay
26.63	318 ± 6	0.011 ± 0.026	364 ± 7	0.134 ± 0.025
32.04	229 ± 5	-0.060 ± 0.029	269 ± 6	0.106 ± 0.030
53.02	62.8 ± 2.5	-0.299 ± 0.053	66.7 ± 2.9	-0.091 ± 0.058
66.00	34.0 ± 2.0	-0.042 ± 0.077	21.7 ± 2.0	-0.019 ± 0.122
73.85	23.3 ± 1.5	-0.010 ± 0.087	14.6 ± 1.5	0.095 ± 0.141
83.87	12.5 ± 1.0	0.766 ± 0.116	10.2 ± 1.1	0.086 ± 0.141
93.93	14.3 ± 1.1	0.632 ± 0.115	6.87 ± 1.07	-0.039 ± 0.215
103.84	8.86 ± 1.42	-0.558 ± 0.211	7.42 ± 1.47	0.118 ± 0.273

	10.736 MeV		11.666 MeV	
$\theta_{c.m.}$ (Deg.)	$d\sigma/d\Omega$ (nb/sr)	Ay	$d\sigma/d\Omega$ (nb/sr)	Ay
26.63	97.5 ± 4.7	0.631 ± 0.064	520 ± 8.8	0.325 ± 0.023
32.04	133 ± 5	0.390 ± 0.053	364 ± 9	0.325 ± 0.033
53.02	30.8 ± 2.5	0.724 ± 0.112	129 ± 5	-0.187 ± 0.046
66.00	16.6 ± 2.0	0.086 ± 0.156	55.6 ± 3.8	-0.901 ± 0.087
73.85	9.19 ± 1.40	0.098 ± 0.210	39.2 ± 2.8	-0.627 ± 0.090
83.87	2.35 ± 0.91	-0.324 ± 0.532	26.6 ± 1.9	-0.503 ± 0.097
93.93	3.46 ± 1.03	0.637 ± 0.478	21.1 ± 1.9	-0.111 ± 0.126
103.84	1.70 ± 1.26	0.343 ± 1.053	7.13 ± 2.24	-0.391 ± 0.467

	14.868 MeV		23.288 MeV	
$\theta_{c.m.}$ (Deg.)	$d\sigma/d\Omega$ (nb/sr)	Ay	$d\sigma/d\Omega$ (nb/sr)	Ay
26.63	625 ± 10	0.229 ± 0.022	805 ± 14	0.016 ± 0.022
32.04	483 ± 11	0.145 ± 0.028	693 ± 13	-0.001 ± 0.024
53.02	207 ± 5	-0.338 ± 0.031	308 ± 7	0.053 ± 0.031
66.00	133 ± 4	-0.722 ± 0.043	147 ± 6	0.064 ± 0.054
73.85	92.8 ± 3.1	-0.811 ± 0.050	96.8 ± 4.3	0.162 ± 0.062
83.87	66.2 ± 2.3	-0.426 ± 0.048	49.9 ± 3.1	0.114 ± 0.085
93.93	40.9 ± 2.4	-0.096 ± 0.081	47.6 ± 3.0	0.228 ± 0.089
103.84	36.6 ± 2.9	0.163 ± 0.109	35.4 ± 4.0	0.008 ± 0.157

Table A.6: The angular distributions of cross section and analyzing power data at 280 MeV for the bound states of the $^{13}C(p, \pi^+)^{14}C$ at excitation energies of 0.000, 6.094, 6.728, 7.012, 7.341, and 8.318 MeV.

| $\theta_{c.m.}$ (Deg.) | Ground State | | 6.094 MeV | |
	$d\sigma/d\Omega$ (nb/sr)	Ay	$d\sigma/d\Omega$ (nb/sr)	Ay
26.71	110 ± 4	0.696 ± 0.054	363 ± 8	-0.205 ± 0.031
31.92	77.0 ± 4.1	0.757 ± 0.068	265 ± 7	-0.214 ± 0.039
42.08	33.6 ± 2.3	0.802 ± 0.089	141 ± 4	-0.245 ± 0.044
52.85	15.3 ± 1.5	0.903 ± 0.122	72.4 ± 3.1	0.076 ± 0.060
73.64	3.51 ± 0.55	0.249 ± 0.212	19.8 ± 1.0	-0.328 ± 0.073
103.67	1.64 ± 0.32	-0.097 ± 0.295	9.54 ± 0.60	-0.363 ± 0.094
103.67	1.10 ± 0.42	-0.083 ± 0.523	9.86 ± 0.85	-0.107 ± 0.121
$\theta_{c.m.}$ (Deg.)	6.728 MeV		7.012 MeV	
	$d\sigma/d\Omega$ (nb/sr)	Ay	$d\sigma/d\Omega$ (nb/sr)	Ay
26.71	1144 ± 14	0.119 ± 0.018	253 ± 9	0.004 ± 0.048
31.92	748 ± 13	0.023 ± 0.024	210 ± 8	-0.020 ± 0.056
42.08	292 ± 7	-0.322 ± 0.032	94.7 ± 4.6	-0.078 ± 0.068
52.85	126 ± 4	-0.238 ± 0.049	49.5 ± 3.4	0.341 ± 0.100
73.64	35.9 ± 1.5	0.157 ± 0.057	10.0 ± 1.1	0.419 ± 0.151
103.67	18.0 ± 0.9	-0.477 ± 0.073	4.70 ± 0.67	-0.281 ± 0.213
103.67	17.5 ± 1.2	-0.474 ± 0.088	4.87 ± 0.89	-0.539 ± 0.248
$\theta_{c.m.}$ (Deg.)	7.341 MeV		8.318 MeV	
	$d\sigma/d\Omega$ (nb/sr)	Ay	$d\sigma/d\Omega$ (nb/sr)	Ay
26.71	406 ± 9	0.011 ± 0.031	116 ± 6	0.369 ± 0.067
31.92	287 ± 8	-0.170 ± 0.039	107 ± 6	0.683 ± 0.077
42.08	109 ± 4	-0.481 ± 0.054	59.6 ± 3.6	0.248 ± 0.081
52.85	58.8 ± 3.0	-0.207 ± 0.071	39.0 ± 2.5	0.406 ± 0.089
73.64	14.0 ± 1.0	-0.116 ± 0.102	13.0 ± 1.0	0.592 ± 0.101
103.67	11.2 ± 0.7	-0.381 ± 0.094	5.00 ± 0.52	-0.030 ± 0.158
103.67	12.8 ± 1.0	-0.431 ± 0.105	5.49 ± 0.70	0.096 ± 0.181

Table A.7: The angular distributions of cross section and analyzing power data at 280 MeV for the bound states of the $^{13}C(p, \pi^+)^{14}C$ at excitation energies of 9.801, 10.425, 10.736, 11.666, 14.868, and 23.288 MeV.

$\theta_{c.m.}$ (Deg.)	9.801 MeV $d\sigma/d\Omega$ (nb/sr)	Ay	10.425 MeV $d\sigma/d\Omega$ (nb/sr)	Ay
26.71	269 ± 8	0.101 ± 0.040	377 ± 9	0.211 ± 0.035
31.92	217 ± 8	0.063 ± 0.049	284 ± 9	0.202 ± 0.044
42.08	102 ± 4	0.161 ± 0.060	132 ± 5	0.184 ± 0.054
52.85	47.5 ± 2.8	0.250 ± 0.083	50.9 ± 3.2	0.306 ± 0.087
73.64	15.5 ± 1.1	0.600 ± 0.095	9.76 ± 1.04	0.386 ± 0.147
103.67	5.18 ± 0.56	0.039 ± 0.166	1.75 ± 0.46	-0.466 ± 0.398
103.67	7.01 ± 0 80	-0.150 ± 0.159	2.94 ± 0.64	-0.090 ± 0.307

$\theta_{c.m.}$ (Deg.)	10.736 MeV $d\sigma/d\Omega$ (nb/sr)	Ay	11.666 MeV $d\sigma/d\Omega$ (nb/sr)	Ay
26.71	89.9 ± 6.4	0.442 ± 0.099	571 ± 12	0.396 ± 0.031
31.92	73.8 ± 6.2	0.573 ± 0.115	429 ± 12	0.521 ± 0.039
42.08	44.0 ± 3.7	0.553 ± 0.119	235 ± 7	0.267 ± 0.043
52.85	18.9 ± 2.5	0.425 ± 0.182	94.2 ± 4.8	-0.057 ± 0.071
73.64	2.99 ± 0.87	0.985 ± 0.468	25.0 ± 1.6	-0.402 ± 0.088
103.67	0.337 ± 0.419	-0.910 ± 2.024	6.94 ± 0.77	0.244 ± 0.164
103.67	0.938 ± 0.588	0.657 ± 0.980	7.91 ± 0.97	0.469 ± 0.170

$\theta_{c.m.}$ (Deg.)	14.868 MeV $d\sigma/d\Omega$ (nb/sr)	Ay	23.288 MeV $d\sigma/d\Omega$ (nb/sr)	Ay
26.71	766 ± 16	0.335 ± 0.031	879 ± 18	0.012 ± 0.029
31.92	591 ± 15	0.259 ± 0.037	819 ± 19	0.025 ± 0.032
42.08	329 ± 10	0.117 ± 0.042	521 ± 12	0.129 ± 0.033
52.85	157 ± 7	-0.289 ± 0.060	255 ± 9	0.246 ± 0.048
73.64	41.2 ± 2.3	-0.393 ± 0.078	71.4 ± 3.0	0.329 ± 0.059
103.67	13.9 ± 1.2	0.412 ± 0.134	18.6 ± 1.5	0.346 ± 0.124

Table A.8: The cross section and analyzing power data at 250 MeV for the bound states of the ^{40}Ca$(p, \pi^+)^{41}$Ca at scattering angles of 25.51° and 30.71°.

| | $\theta_{c.m.}$=25.51° | | $\theta_{c.m.}$=30.71° | |
Excitation (MeV)	$d\sigma/d\Omega$ (nb/sr)	Ay	$d\sigma/d\Omega$ (nb/sr)	Ay
0.00	369 ± 15	-0.089 ± 0.056	313 ± 33	0.042 ± 0.138
2.01	70.0 ± 7	0.348 ± 0.126	52.7 ± 11.8	0.465 ± 0.290
3.37	84.2 ± 8.9	0.383 ± 0.144	70.2 ± 26.9	0.100 ± 0.494
3.53	70.1 ± 9.1	0.178 ± 0.176	121 ± 32	0.447 ± 0.329
4.01	232 ± 17	0.316 ± 0.099	242 ± 24	0.573 ± 0.125
5.05	34.1 ± 7.1	-0.051 ± 0.280	12.2 ± 19.9	-0.568 ± 2.417
5.34	245 ± 18	0.429 ± 0.095	366 ± 59	0.349 ± 0.206
5.48	396 ± 20	0.227 ± 0.068	91.4 ± 62.1	0.709 ± 0.934
5.75	26.3 ± 10.0	-0.022 ± 0.513	81.4 ± 28.9	-0.054 ± 0.465
6.24	212 ± 12	0.047 ± 0.077	205 ± 25	-0.032 ± 0.159

141

Table A.9: The cross section and analyzing power data at 280 MeV for the bound states of the ^{40}Ca$(p, \pi^+)^{41}$Ca at scattering angles of 25.57°, 30.67°, and 40.83°.

	$\theta_{c.m.}$=25.57°		$\theta_{c.m.}$=30.67°	
Excitation (MeV)	$d\sigma/d\Omega$ (nb/sr)	Ay	$d\sigma/d\Omega$ (nb/sr)	Ay
0.00	242 ± 22	0.178 ± 0.128	205 ± 18	0.432 ± 0.118
2.01	20.8 ± 8.1	0.470 ± 0.553	40.5 ± 7.9	1.270 ± 0.210
3.20	62.6 ± 15.2	0.031 ± 0.343	30.4 ± 9.8	0.469 ± 0.439
3.37	55.5 ± 22.6	0.705 ± 0.600	53.7 ± 16.7	0.771 ± 0.425
3.53	66.7 ± 20.0	0.234 ± 0.409	36.5 ± 14.5	1.019 ± 0.592
3.83	217 ± 25	0.325 ± 0.160	110 ± 17	-0.078 ± 0.212
4.01	62.5 ± 17.2	0.344 ± 0.380	119 ± 15	0.132 ± 0.181
5.19	445 ± 36	0.352 ± 0.110	98.5 ± 18.5	0.712 ± 0.261
5.34	160 ± 31	0.257 ± 0.266	380 ± 26	0.278 ± 0.093
5.75	111 ± 18	0.281 ± 0.222	53.9 ± 11.6	0.505 ± 0.313
5.93	164 ± 21	-0.300 ± 0.186	73.4 ± 14.3	-0.039 ± 0.274
	$\theta_{c.m.}$=40.83°			----
Excitation (MeV)	$d\sigma/d\Omega$ (nb/sr)	Ay	......	
0.00	80.9 ± 6.8	0.145 ± 0.119	—	...
2.01	14.9 ± 3.2	-0.815 ± 0.315	—	......
3.20	26.6 ± 5.2	0.202 ± 0.272	—	......
3.37	25.9 ± 6.8	0.588 ± 0.367	—	...
3.83	88.3 ± 7.2	0.198 ± 0.115	—	...
4.01	22.5 ± 4.7	-0.339 ± 0.304	—	...
5.19	216 ± 10	0.345 ± 0.065	—	...
5.34	64.6 ± 7.6	0.278 ± 0.163	—	...
5.75	16.1 ± 4.7	-0.306 ± 0.433	—	......
5.93	43.4 ± 5.8	0.342 ± 0.187	—	......

Table A.10: The angular distributions of cross section and analyzing power data at 221 MeV for the bound states of the $^{13}C(p, \pi^-)^{14}O$ at excitation energies of 0.000. 5.173. 5.920, 6.272, 6.590, 6.790, 7.768, 9.915. and 14.150 MeV.

	Ground State		5.173 MeV	
$\theta_{c.m.}$ (Deg.)	$d\sigma/d\Omega$ (nb/sr)	Ay	$d\sigma/d\Omega$ (nb/sr)	Ay
26.87	2.13 ± 0.78	-0.323 ± 0.562	6.50 ± 0.80	0.328 ± 0.174
47.90	2.14 ± 0.32	0.354 ± 0.204	2.51 ± 0.26	0.466 ± 0.138
68.77	3.19 ± 0.29	0.436 ± 0.121	3.43 ± 0.24	0.058 ± 0.097
89.13	1.86 ± 0.25	0.116 ± 0.192	2.69 ± 0.21	-0.290 ± 0.110

	5.920 MeV		6.272 MeV	
$\theta_{c.m.}$ (Deg.)	$d\sigma/d\Omega$ (nb/sr)	Ay	$d\sigma/d\Omega$ (nb/sr)	Ay
26.87	3.12 ± 0.75	0.496 ± 0.334	36.6 ± 2.0	0.305 ± 0.080
47.90	2.19 ± 0.31	0.147 ± 0.197	18.9 ± 0.76	0.575 ± 0.056
68.77	2.52 ± 0.28	0.453 ± 0.149	9.35 ± 0.54	0.245 ± 0.079
89.13	2.28 ± 0.25	0.155 ± 0.156	5.41 ± 0.42	-0.057 ± 0.113

	6.590 MeV		6.790 MeV	
$\theta_{c.m.}$ (Deg.)	$d\sigma/d\Omega$ (nb/sr)	Ay	$d\sigma/d\Omega$ (nb/sr)	Ay
26.87	11.7 ± 1.9	-0.32 ± 0.241	11.4 ± 1.5	0.449 ± 0.184
47.90	7.27 ± 0.75	0.274 ± 0.143	9.05 ± 0.63	0.130 ± 0.098
68.77	5.57 ± 0.71	0.674 ± 0.177	8.29 ± 0.57	0.083 ± 0.095
89.13	6.12 ± 0.62	0.158 ± 0.145	5.53 ± 0.48	0.163 ± 0.124

	7.768 MeV		9.915 MeV	
$\theta_{c.m.}$ (Deg.)	$d\sigma/d\Omega$ (nb/sr)	Ay	$d\sigma/d\Omega$ (nb/sr)	Ay
26.87	3.06 ± 0.66	-0.555 ± 0.306	16.7 ± 1.4	-0.203 ± 0.116
47.90	2.42 ± 0.29	-0.220 ± 0.168	8.03 ± 0.50	-0.164 ± 0.087
68.77	0.909 ± 0.176	-0.187 ± 0.276	4.64 ± 0.33	0.230 ± 0.098
89.13	0.438 ± 0.105	-0.514 ± 0.313	2.98 ± 0.25	0.279 ± 0.122

	14.150 MeV		—	
$\theta_{c.m.}$ (Deg.)	$d\sigma/d\Omega$ (nb/sr)	Ay	—	—
26.87	20.9 ± 1.8	-0.255 ± 0.125	—	—
47.90	8.04 ± 0.66	-0.349 ± 0.119	—	—
68.77	4.59 ± 0.46	0.569 ± 0.136	—	—
89.13	3.39 ± 0.38	0.124 ± 0.162	—	—

Table A.11: The angular distributions of cross section and analyzing power data at 280 MeV for the bound states of the $^{13}C(p, \pi^-)^{14}O$ at excitation energies of 0.000, 5.173, 6.272, 6.590, 6.790, 7.768, 9.915, and 14.150 MeV.

$\theta_{c.m.}$ (Deg.)	Ground State $d\sigma/d\Omega$ (nb/sr)	Ay	5.173 MeV $d\sigma/d\Omega$ (nb/sr)	Ay
26.89	1.09 ± 0.25	-0.937 ± 0.367	8.09 ± 0.44	0.327 ± 0.071
47.83	0.948 ± 0.141	0.778 ± 0.196	1.62 ± 0.14	0.516 ± 0.110
68.62	0.627 ± 0.089	0.925 ± 0.193	0.837 ± 0.077	-0.346 ± 0.127
89.02	0.237 ± 0.058	-0.243 ± 0.335	0.462 ± 0.064	-0.578 ± 0.188
108.70	0.176 ± 0.042	-0.782 ± 0.283	0.194 ± 0.037	-0.622 ± 0.260

$\theta_{c.m.}$ (Deg.)	6.272 MeV $d\sigma/d\Omega$ (nb/sr)	Ay	6.590 MeV $d\sigma/d\Omega$ (nb/sr)	Ay
26.89	34.0 ± 1.0	0.282 ± 0.039	5.10 ± 1.07	-0.469 ± 0.313
47.83	9.48 ± 0.37	0.193 ± 0.053	3.04 ± 0.48	0.939 ± 0.238
68.62	3.98 ± 0.20	-0.002 ± 0.069	2.03 ± 0.26	0.492 ± 0.184
89.02	1.51 ± 0.13	-0.134 ± 0.115	0.615 ± 0.164	-0.179 ± 0.364
108.70	0.379 ± 0.053	-0.393 ± 0.192	0.404 ± 0.077	-0.085 ± 0.263

$\theta_{c.m.}$ (Deg.)	6.790 MeV $d\sigma/d\Omega$ (nb/sr)	Ay	7.768 MeV $d\sigma/d\Omega$ (nb/sr)	Ay
26.89	12.7 ± 0.8	0.308 ± 0.087	4.52 ± 0.41	-0.326 ± 0.127
47.83	6.78 ± 0.41	-0.123 ± 0.082	1.04 ± 0.17	-0.653 ± 0.229
68.62	2.28 ± 0.20	-0.063 ± 0.124	0.731 ± 0.094	0.152 ± 0.179
89.02	0.668 ± 0.118	-0.110 ± 0.241	0.360 ± 0.060	-0.509 ± 0.217
108.70	0.119 ± 0.052	-0.432 ± 0.603	0.234 ± 0.040	-0.905 ± 0.225

$\theta_{c.m.}$ (Deg.)	9.915 MeV $d\sigma/d\Omega$ (nb/sr)	Ay	14.150 MeV $d\sigma/d\Omega$ (nb/sr)	Ay
26.89	19.4 ± 0.77	-0.284 ± 0.055	21.4 ± 1.0	-0.346 ± 0.065
47.83	5.65 ± 0.31	-0.009 ± 0.076	7.41 ± 0.44	-0.642 ± 0.085
68.62	2.19 ± 0.15	-0.004 ± 0.097	3.71 ± 0.24	-0.226 ± 0.088
89.02	0.789 ± 0.094	-0.373 ± 0.161	1.77 ± 0.16	-0.659 ± 0.120
108.70	0.451 ± 0.054	-0.243 ± 0.167	0.728 ± 0.092	-0.281 ± 0.173

Table A.12: The angular distributions of cross section and analyzing power data at 350 MeV for the bound states of the $^{13}C(p, \pi^-)^{14}O$ at excitation energies of 0.000, 5.173, 6.272, 6.590, 6.790, 7.768, 9.915, and 14.150 MeV.

$\theta_{c.m.}$ (Deg.)	Ground State		5.173 MeV	
	$d\sigma/d\Omega$ (nb/sr)	Ay	$d\sigma/d\Omega$ (nb/sr)	Ay
26.92	0.730 ± 0.191	0.710 ± 0.314	1.91 ± 0.23	-0.140 ± 0.176
48.07	0.555 ± 0.110	0.723 ± 0.272	0.645 ± 0.101	-0.136 ± 0.234
68.63	0.382 ± 0.091	0.191 ± 0.335	0.315 ± 0.069	-0.775 ± 0.287
89.33	0.048 ± 0.027	-0.806 ± 1.555	0.089 ± 0.027	0.990 ± 0.989
$\theta_{c.m.}$ (Deg.)	6.272 MeV		6.590 MeV	
	$d\sigma/d\Omega$ (nb/sr)	Ay	$d\sigma/d\Omega$ (nb/sr)	Ay
26.92	8.22 ± 0.48	-0.082 ± 0.086	2.64 ± 0.56	0.649 ± 0.345
48.07	2.86 ± 0.22	0.148 ± 0.114	1.53 ± 0.27	0.392 ± 0.271
68.63	1.36 ± 0.16	0.085 ± 0.161	0.458 ± 0.203	0.658 ± 0.692
89.33	0.301 ± 0.051	0.895 ± 0.523	0.159 ± 0.060	-0.993 ± 1.147
$\theta_{c.m.}$ (Deg.)	6.790 MeV		7.768 MeV	
	$d\sigma/d\Omega$ (nb/sr)	Ay	$d\sigma/d\Omega$ (nb/sr)	Ay
26.92	3.83 ± 0.44	-0.476 ± 0.170	3.08 ± 0.29	-0.417 ± 0.143
48.07	1.12 ± 0.20	-0.457 ± 0.267	0.785 ± 0.113	-0.539 ± 0.223
68.63	0.385 ± 0.133	-0.819 ± 0.508	0.345 ± 0.072	0.332 ± 0.295
89.33	0.034 ± 0.037	0.000 ± 3.272	0.086 ± 0.029	-0.595 ± 1.025
$\theta_{c.m.}$ (Deg.)	9.915 MeV		14.150 MeV	
	$d\sigma/d\Omega$ (nb/sr)	Ay	$d\sigma/d\Omega$ (nb/sr)	Ay
26.92	8.69 ± 0.49	-0.364 ± 0.084	10.10 ± 0.65	-0.604 ± 0.097
48.07	2.21 ± 0.19	0.179 ± 0.127	4.60 ± 0.31	0.029 ± 0.100
68.63	0.771 ± 0.103	-0.446 ± 0.180	1.80 ± 0.18	-0.257 ± 0.139
89.33	0.130 ± 0.033	0.998 ± 0.851	0.460 ± 0.057	-0.197 ± 0.367

A.2 Data Tables for the Continuum Analysis

This section shows the numerical values of cross section and analyzing power data extracted from the continua of the measured reactions. These continuum slices were selected to be 1.6 MeV wide at each excitation. Data are tabulated as a function of center of mass angle. Each table shows the reaction and the incident proton energy at which it was observed.

Table A.13: The angular distributions of cross section and analyzing power data at 250 MeV for the continuum of the $^{12}C(p, \pi^+)X$ at excitation energies of 15.5 and 19.0 MeV.

$\theta_{c.m.}$ (Deg.)	15.5 MeV		19 MeV	
	$d\sigma/d\Omega$ (nb/sr)	Ay	$d\sigma/d\Omega$ (nb/sr)	Ay
26.78	2167 ± 18	0.069 ± 0.011	2785 ± 21	0.008 ± 0.010
32.22	1841 ± 18	0.069 ± 0.013	2362 ± 21	-0.012 ± 0.012
53.29	652 ± 7	-0.218 ± 0.016	936 ± 9	-0.225 ± 0.014
66.31	403 ± 8	-0.373 ± 0.028	592 ± 10	-0.269 ± 0.024
66.31	399 ± 8	-0.410 ± 0.028	564 ± 10	-0.293 ± 0.024
74.17	298 ± 6	-0.376 ± 0.030	442 ± 8	-0.354 ± 0.025
84.21	240 ± 3	-0.305 ± 0.021	364 ± 4	-0.234 ± 0.018
94.25	227 ± 6	-0.147 ± 0.035	361 ± 8	-0.187 ± 0.029
104.18	197 ± 5	-0.097 ± 0.033	303 ± 6	-0.129 ± 0.028

Table A.14: The angular distributions of cross section and analyzing power data at 280 MeV for the continuum of the $^{12}C(p, \pi^+)X$ at excitation energies of 15.5 and 19.0 MeV.

$\theta_{c.m.}$ (Deg.)	15.5 MeV		19 MeV	
	$d\sigma/d\Omega$ (nb/sr)	Ay	$d\sigma/d\Omega$ (nb/sr)	Ay
26.85	2652 ± 30	0.192 ± 0.017	3198 ± 33	0.116 ± 0.015
32.09	2205 ± 27	0.211 ± 0.018	2694 ± 31	0.117 ± 0.016
42.67	1218 ± 16	0.196 ± 0.019	1575 ± 18	0.060 ± 0.016
53.12	657 ± 9	0.029 ± 0.019	895 ± 10	-0.022 ± 0.016
74.06	233 ± 3	-0.052 ± 0.019	353 ± 4	-0.079 ± 0.015
104.00	101 ± 2	0.044 ± 0.028	174 ± 3	0.088 ± 0.022

Table A.15: The angular distributions of cross section and analyzing power data at 250 MeV for the continuum of the $^{13}C(p, \pi^+)X$ at excitation energies of 17 and 20 MeV.

$\theta_{c.m.}$ (Deg.)	17 MeV		20 MeV	
	$d\sigma/d\Omega$ (nb/sr)	Ay	$d\sigma/d\Omega$ (nb/sr)	Ay
26.63	1391 ± 12	0.004 ± 0.011	1872 ± 14	0.021 ± 0.010
32.04	1151 ± 9	-0.018 ± 0.011	1542 ± 11	-0.007 ± 0.009
53.02	422 ± 5	-0.223 ± 0.017	559 ± 6	-0.299 ± 0.016
66.00	228 ± 4	-0.333 ± 0.026	334 ± 5	-0.341 ± 0.023
73.85	175 ± 3	-0.253 ± 0.027	250 ± 4	-0.331 ± 0.024
83.87	136 ± 2	-0.196 ± 0.025	192 ± 3	-0.189 ± 0.022
93.93	141 ± 3	-0.180 ± 0.026	195 ± 3	-0.158 ± 0.023
103.84	136 ± 4	-0.138 ± 0.039	161 ± 4	-0.064 ± 0.037

Table A.16: The angular distributions of cross section and analyzing power data at 280 MeV for the continuum of the $^{13}C(p, \pi^+)X$ at excitation energies of 17 and 20 MeV.

$\theta_{c.m.}$ (Deg.)	17 MeV		20 MeV	
	$d\sigma/d\Omega$ (nb/sr)	Ay	$d\sigma/d\Omega$ (nb/sr)	Ay
26.71	1582 ± 16	0.143 ± 0.015	2188 ± 19	0.132 ± 0.013
31.92	1295 ± 16	0.130 ± 0.017	1784 ± 19	0.144 ± 0.015
42.08	720 ± 10	0.044 ± 0.019	1026 ± 12	0.057 ± 0.016
52.85	350 ± 7	-0.020 ± 0.026	498 ± 8	-0.029 ± 0.022
73.64	119 ± 2	0.034 ± 0.028	166 ± 3	0.063 ± 0.024
103.67	63.5 ± 1.5	-0.040 ± 0.036	80.2 ± 1.7	0.130 ± 0.032
103.67	61.3 ± 2.0	-0.031 ± 0.046	82.3 ± 2.3	0.010 ± 0.040

Table A.17: The angular distributions of cross section and analyzing power data at 250 MeV for the continuum of the ^{40}Ca(p, π^+)X at excitation energies of 16, 20, and 24 MeV.

$\theta_{c.m.}$ (Deg.)	16 MeV		20 MeV	
	$d\sigma/d\Omega$ (nb/sr)	Ay	$d\sigma/d\Omega$ (nb/sr)	Ay
25.51	3524 ± 36	0.029 ± 0.013	3524 ± 36	0.029 ± 0.013
25.51	3740 ± 51	0.010 ± 0.018	5262 ± 62	-0.022 ± 0.015
30.71	3383 ± 72	0.010 ± 0.027	4670 ± 85	0.032 ± 0.023
$\theta_{c.m.}$ (Deg.)	24 MeV			
	$d\sigma/d\Omega$ (nb/sr)	Ay		
25.51	7235 ± 54	-0.008 ± 0.010		
25.51	7338 ± 74	-0.006 ± 0.013		
30.71	6488 ± 102	0.017 ± 0.020		

Table A.18: The angular distributions of cross section and analyzing power data at 280 MeV for the continuum of the ^{40}Ca(p, π^+)X at excitation energies of 16, 20, and 24 MeV.

$\theta_{c.m.}$ (Deg.)	16 MeV		20 MeV	
	$d\sigma/d\Omega$ (nb/sr)	Ay	$d\sigma/d\Omega$ (nb/sr)	Ay
25.57	3389 ± 70	0.069 ± 0.029	5135 ± 87	0.120 ± 0.024
30.67	2744 ± 54	0.115 ± 0.028	4193 ± 68	0.119 ± 0.023
40.83	1524 ± 22	0.131 ± 0.021	2385 ± 29	0.078 ± 0.017
61.01	—	-0.023 ± 0.064	—	-0.036 ± 0.053
71.26	857 ± 28	-0.133 ± 0.047	1294 ± 35	-0.130 ± 0.038
101.12	296 ± 17	0.004 ± 0.085	404 ± 20	-0.047 ± 0.073
$\theta_{c.m.}$ (Deg.)	24 MeV			
	$d\sigma/d\Omega$ (nb/sr)	Ay		
25.57	6431 ± 100	0.074 ± 0.022		
30.67	5506 ± 79	0.100 ± 0.020		
40.83	3231 ± 34	0.071 ± 0.015		
61.01	—	0.003 ± 0.045		
71.26	1624 ± 41	-0.123 ± 0.035		
101.12	655 ± 27	-0.104 ± 0.060		

Table A.19: The angular distributions of cross section and analyzing power data at 221 MeV for the continuum of the ^{13}C(p, π^-)X at excitation energies of 17, 19, and 21 MeV.

$\theta_{c.m.}$ (Deg.)	17 MeV		19 MeV	
	$d\sigma/d\Omega$ (nb/sr)	Ay	$d\sigma/d\Omega$ (nb/sr)	Ay
26.87	96.1 ± 2.2	0.031 ± 0.033	87.3 ± 2.1	-0.054 ± 0.035
26.87	93.7 ± 1.885	0.038 ± 0.028	82.6 ± 1.8	0.025 ± 0.030
47.90	56.4 ± 1.1	0.171 ± 0.028	57.8 ± 1.2	0.098 ± 0.028
68.77	38.6 ± 0.8	0.212 ± 0.028	43.5 ± 0.8	0.142 ± 0.026
89.13	29.6 ± 1.0	0.096 ± 0.047	36.9 ± 1.1	0.069 ± 0.043
89.13	29.1 ± 0.6	0.092 ± 0.032	36.5 ± 0.7	0.121 ± 0.029
$\theta_{c.m.}$ (Deg.)	21 MeV		—	
	$d\sigma/d\Omega$ (nb/sr)	Ay	—	—
26.87	104 ± 2	0.016 ± 0.033	—	—
26.87	94.0 ± 2.0	-0.109 ± 0.030	—	—
47.90	70.4 ± 1.	0.061 ± 0.026	—	—
68.77	47.1 ± 0.9	0.148 ± 0.026	—	—
89.13	41.9 ± 1.2	0.028 ± 0.042	—	—
89.13	41.6 ± 0.8	0.101 ± 0.028	—	—

149

Table A.20: The angular distributions of cross section and analyzing power data at 280 MeV for the continuum of the $^{13}C(p,\pi^-)X$ at excitation energies of 19, 21, 24, and 27 MeV.

	19 MeV		21 MeV	
$\theta_{c.m.}$ (Deg.)	$d\sigma/d\Omega$ (nb/sr)	Ay	$d\sigma/d\Omega$ (nb/sr)	Ay
26.89	108 ± 2	-0.054 ± 0.019	140 ± 2	-0.035 ± 0.017
47.83	54.8 ± 0.8	-0.088 ± 0.019	69.4 ± 0.9	-0.059 ± 0.017
68.62	22.9 ± 0.4	-0.035 ± 0.023	30.1 ± 0.5	-0.003 ± 0.021
89.02	10.3 ± 0.3	-0.015 ± 0.036	13.5 ± 0.3	0.000 ± 0.032
89.02	10.0 ± 0.2	0.025 ± 0.033	13.3 ± 0.3	-0.039 ± 0.029
108.70	6.19 ± 0.17	-0.031 ± 0.037	8.71 ± 0.20	0.011 ± 0.031
	24 MeV		27 MeV	
$\theta_{c.m.}$ (Deg.)	$d\sigma/d\Omega$ (nb/sr)	Ay	$d\sigma/d\Omega$ (nb/sr)	Ay
26.89	164 ± 2	-0.073 ± 0.016	183 ± 2	-0.086 ± 0.016
47.83	84.3 ± 0.994	-0.058 ± 0.016	99.0 ± 1.1	-0.053 ± 0.015
68.62	37.8 ± 0.5	0.000 ± 0.019	48.0 ± 0.6	-0.011 ± 0.017
89.02	18.3 ± 0.4	-0.051 ± 0.028	24.3 ± 0.4	-0.050 ± 0.025
89.02	18.1 ± 0.3	-0.040 ± 0.025	23.2 ± 0.4	-0.093 ± 0.023
108.70	11.4 ± 0.2	-0.057 ± 0.028	16.5 ± 0.3	-0.048 ± 0.024

150

Table A.21: The angular distributions of cross section and analyzing power data at 350 MeV for the continuum of the $^{13}C(p, \pi^-)X$ at excitation energies of 19, 21, 25, and 30 MeV.

	19 MeV		21 MeV	
$\theta_{c.m.}$ (Deg.)	$d\sigma/d\Omega$ (nb/sr)	Ay	$d\sigma/d\Omega$ (nb/sr)	Ay
26.92	59.7 ± 1.2	-0.124 ± 0.029	79.8 ± 1.4	-0.144 ± 0.026
48.07	24.3 ± 0.5	-0.085 ± 0.032	31.1 ± 0.6	-0.054 ± 0.029
68.63	6.94 ± 0.27	-0.020 ± 0.055	10.2 ± 0.3	0.066 ± 0.046
89.33	2.36 ± 0.10	-0.171 ± 0.130	2.79 ± 0.11	0.085 ± 0.122
	25 MeV		30 MeV	
$\theta_{c.m.}$ (Deg.)	$d\sigma/d\Omega$ (nb/sr)	Ay	$d\sigma/d\Omega$ (nb/sr)	Ay
26.92	102 ± 2	-0.118 ± 0.023	164 ± 2	-0.182 ± 0.020
48.07	42.2 ± 0.7	-0.105 ± 0.026	69.7 ± 1.0	-0.117 ± 0.022
68.63	13.4 ± 0.4	-0.015 ± 0.041	24.7 ± 0.6	0.005 ± 0.031
89.33	4.49 ± 0.15	-0.241 ± 0.097	7.88 ± 0.20	-0.022 ± 0.077

Appendix B

Peak Fitting Procedure

In order to extract the number of events ascribed to each final state in a resultant excitation spectrum, for example the $^{13}C(p, \pi^+)^{14}C$ spectrum in Fig. B.1(a), it was necessary to fit both the background and then each individual state to a gaussian. The entire procedure is depicted in Fig. B.1.

The first stage, shown in Fig. B.1, was to fit a polynomial to the background. This was done manually, first by marking points, by eye along the spectrum to correspond to the background and then fitting a polynomial through those points. This procedure avoided the background polynomial taking wild excursions when asking for a simultaneous fit to both peaks and background. The background, as given by the fit, was then subtracted from the spectrum. The result can be seen in Fig. B.1(b).

The next stage was to determine the line width of a single isolated nuclear excitation. This was obtained by fitting a single gaussian to [for example, 1^- (6.094 MeV) state in ^{14}C in Fig. B.1(d)]. The line shape for individual peaks is assumed to remain constant so the common width of all Gaussians was fixed to this value. Next the peak centroids (excitation energies of states corresponding to peaks) were fixed to the values given in the nuclear data tables [Aj91]. The calibration of the SASP focal plane was very good (see section B.1) so that this could be done. With both the centroid and the widths fixed, a peak fitting program [Ha95] was used to fit the the resultant spectrum after subtracting the polynomial background. The result is shown in Figs. B.1(c) and (d).

The fitting procedure determined the total number of events in each Gaussian peak which was subsequently used in the calculation of the cross sections and analyzing power. The fitting routine also extracted the number of events for peaks which were not fully

resolved [see inset in Fig. B.1(c)]. This was possible due to our knowledge of line width and peak position. The statistical error on the number of events in each peak was given by the program. For isolated peaks, this error was approximately $\sqrt{N}$ where N was the number of events in the peak given by the program. For states where there were overlapping peaks [for example the 2^+ (7.012 MeV) state in Fig. B.1(d) and the inset in (c)] the statistical error was appropriately larger than $\sqrt{N}$. Fig. B.1(a) shows the actual experimental data where the background is fit to a higher-order polynomial while the background subtracted spectrum is shown in (b). The yield extractions by fitting the data to gaussian peaks is illustrated in (c). More details of the single, and unfolded peaks and their corresponding nuclear states are given in (d) for the $^{13}C(p, \pi^+)^{14}C$ reaction measured at 250 MeV and $25°$ in the laboratory.

This statistical error had to be augmented for the contribution due to the background subtraction. To include the error in the background with the statistical error of the peak yield, a Monte Carlo study [Wa96] was carried out in which a data sample was generated for the hypothetical example of a gaussian lying atop of a smooth uniform background. Applying a least squares fit to a series of such examples, an empirical formula, eqn. (B.2), was found which adequately estimated the increased error in the yield due to the background subtraction.

In this study the least squares fit extracted a yield, N_l, and an average background, B_k (events/bin). The extraction of the yield is simple enough and the error matrix gives the error on the yield. However, the problem comes in when the background has already been subtracted before the peak fitting process is employed. If one has an estimate of the background, the error due to the background can be added later. For a simple case one has Total (T) = Yield (Y) + Background (B). and so

$$T = Y + B .$$

To extract Y, one has an estimate of B and let it B_{est}. Then

$$Y_{exp} = T - B_{est} ,$$

$$\Delta^2 Y_{exp} = \Delta^2 T + \Delta^2 B_{est} = Y + B + \Delta^2 B_{est} .$$

Therefore, one can write

$$\Delta Y_{exp} = \sqrt{Y + KB} . \qquad (B.1)$$

Now B is set to $B_k 4\sigma/\Delta$ where σ is the Gaussian σ and Δ is the histogram bin size, we get a generic formula for handling the error on the yield, Y, with a background B. $B_k 4\sigma/\Delta$

Table B.1: The data generated by a Monte Carlo study to obtain the coefficients α, β, and R for the calculation of K in eqn. (B.2). Here 'Bckgrnd' is the background as a fraction of the yield within $\pm\sigma$.

Bckgrnd	α	β	R	K
0.01	3.93	11	0.509402	2.9466
0.0625	3.762	7.75	0.633342	1.9889
0.125	3.648	6.75	0.69193	1.7214
0.25	3.509	5.87	0.749916	1.5137
0.5	3.32	5.56	0.811004	1.3734
1	3.14	5.365	0.866135	1.2701
2	2.99	5.23	0.911682	1.1963
4	2.87	5.22	0.947345	1.1484
8	2.82	5.12	0.960626	1.1269
16	2.805	5.02	0.97221	1.1086
32	2.763	5.08	0.977979	1.1041

is B_k integrated from -2σ to $+2\sigma$, which contains 0.9545 of the Gaussian yield, Y. The value of K can then be determined from the least squares fit. This results in the empirical formula,

$$K = \frac{1}{R\left[1 - \exp\left\{-\frac{(n-\alpha)}{\beta}\right\}\right]} .$$ (B.2)

where n is the range over which the least squares fit is applied in units of σ. R, α, and β are empirical constants. In Table B.1, Bckgrnd $= B/(0.9545 \cdot Y)$ is the background in $\pm 2\sigma$ as a ratio to the yield in 4σ.

Consider the following example for the reaction, $^{13}C(p,\pi^+)^{14}C$, at $T_p = 250$ MeV and a laboratory scattering angle of $25°$. The spin-up yield on the 23 MeV state was 3792 counts and the error was 61 counts from the peak fitting program. The background curve was

$$B = A_0 + A_1 X + A_2 X^2 + A_3 X^3 + A_4 X^4 + A_5 X^5 + A_6 X^6 + A_7 X^7 + A_8 X^8 ,$$

where B is the events/bin and X is the excitation energy. The A-coefficients in ascending order had the values 6.067, 5.635, 0.8248×10^{-1}, -0.8583, 0.1953, $-0.1698 \times$

154

10^{-1}, 0.7147×10^{-3}, -0.1452×10^{-4}, and 0.1130×10^{-6}. The peak fitting routine only contained a background fitting curve to the 4th power which was inadequate.

Putting in $X = 23.28$ MeV we get that the background under the 23 MeV peak is 320 events/bin. From the peak fitting the σ of the 23 MeV peak is 0.1104 MeV. The bin size is 0.05 MeV so that 4σ would cover $4(0.1104)/0.05 = 9$ bins. Thus B in the discussion above would be $319.95 \times 8.832 = 2826$ events.

Taking Bckgrnd $= B/(0.9545 \cdot Y)$ from above we get Bckgrnd $= 0.78078$. Taking $n = 16$. the extent in units of σ over which the background is determined (an arbitrary decision as there is certainly an extensive continuum to determine this) and interpolating from Table B.1 for Bckgrnd $= 0.78078$ we get $R = 0.8419634$, $\alpha = 3.2189$, and $\beta = 5.3958$. Using eqn. (B.2) we get $K = 1.3104$.

This gives the statistical error in the yield including background to be via the discussion above:

$$\sqrt{61^2 + 1.3104 \times 2826} = 86 .$$

B.1   Accuracy of the Calibration of SASP Focal Plane

To appreciate the accuracy of SASP focal plane calibration, it is instructive to consider the results of a method to determine the SASP momentum calibration[1] and the beam energy.

The SASP momentum calibration is given by

$$P_0 = C \cdot B ,\qquad\qquad (B.3)$$

where P_0 is the central SASP momentum (MeV/c), B is the SASP magnetic field (kG) as recorded by the Rawson-Lush rotating coil probe [Pu93], and C is the SASP momentum calibration in units of MeV/c/kG. Now each peak in the excitation spectrum has a momentum deviation, δ_s, given by

$$\delta_s = \left[\frac{P_s - P_0}{P_0} \right] .$$

Here P_s is the actual momentum associated with the peak in the excitation spectrum. Using two-body kinematics, it is possible to compute the beam energy, T_p, from P_s, and

---

[1]See section 5.5.1 for the discussion into the SASP momentum calibration.

Table B.2: Excitation energies and momenta corresponding to the strongly-populated final states in $^{13}C(p, \pi^+)^{14}C$ reaction as shown in Fig. B.1.

State	Ex (MeV)	T_p (MeV/c^2)	C (MeV/c/kG)
0^+	0.000		
4^-	11.666	249.910	49.972
5^-	14.868	250.156	50.044
7^+	23.288	249.707	49.912
Average		249.924	49.976
Stnd Dev.		0.225	0.066

the spectrometer angle setting. θ_s. Thus for any C, one can calculate

$$\Delta T_p = T_p(g.s.) - T_p(Excited\ State) .\qquad (B.4)$$

To find C and T_p, C is varied until $\Delta T_p = 0$. If the focal plane calibration is accurate, one will obtain the same T_p and C for each excited state in the spectrum. The results of this calculation are shown in Table B.2 determined for the $^{13}C(p, \pi^+)^{14}C$ example in Fig. B.1. The average and the standard deviation are given for the 4^-, 5^-, and 7^+ states only. The 2^+ state is 20% of the 3^- state at 6.775 MeV. For the 4^-, 5^-, and 7^+ states the C and T_p values are consistent. The only state with inconsistent T_p and C values is the 3^- at 6.728 MeV.

156
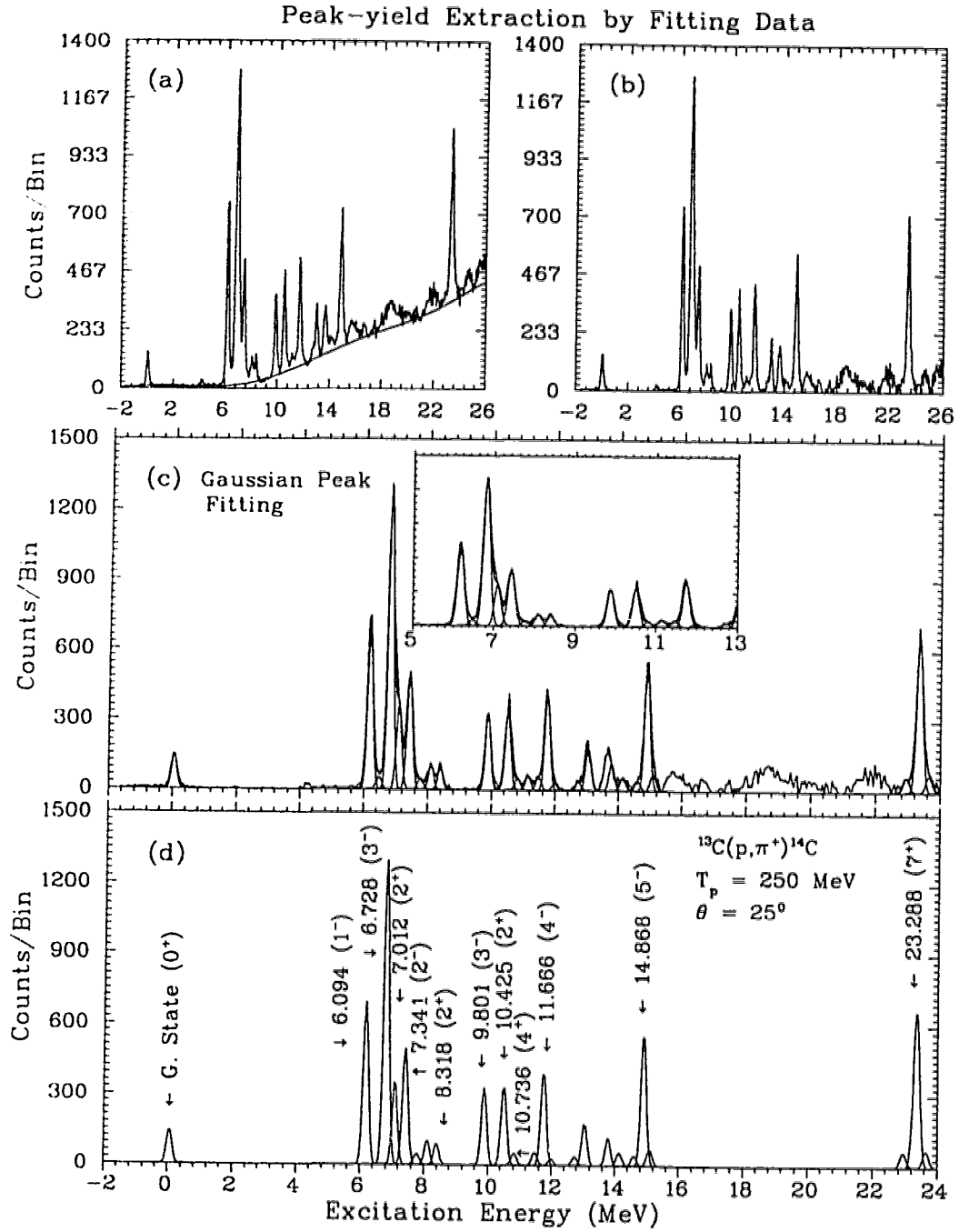
Figure B.1: Shown are the four different stages of the peak fitting procedure used for the extraction of peak yields. (a) and (b) show the background subtraction to separate the discrete final states. The data fitting to gaussian peaks is shown in (c). More details of the single and unfolded peaks corresponding to the different excited states are given in (d) for the $^{13}C(p, \pi^+)^{14}C$ reaction measured at 250 MeV and 25° in the laboratory.

Appendix C

Error Calculations

Mathematical manipulations used to calculate the statistical errors of the results are discussed in this appendix. The overall statistical error of the results includes the error of the asymmetry measurement, error of the polarization calculation, error of the analyzing power measurement for the IBP target, error of the efficiency calculation, error of the peak yield which includes the peak fitting error and the background subtraction error, error of the differential cross section calculation, and the error of the analyzing power calculation. Some of these error calculations are described in details below.

C.1 Error in the Asymmetry Measurements

The incident beam polarization is determined by measuring the left-right asymmetry (ε) of pp elastic scattering from the thin CH_2 target. Let $L(R)$ be the number of events scattered to left(right). The asymmetry is

$$\varepsilon = \frac{L - R}{L + R} ,$$

where $N = L+R$ is the total number of events detected. If N is fixed, then the asymmetry is determined from Binomial statistics where p is the probability for left scattering. In principle then

$$\varepsilon = \frac{2L - N}{N} = 2p - 1 \Rightarrow p = \frac{\varepsilon + 1}{2} .$$

$$\Delta^2 \varepsilon = \frac{4}{N^2} \Delta^2 L = \frac{4}{N^2}(p)(1 - p)N$$

$$\Delta^2 \varepsilon = \frac{4p(1 - p)}{N} = \frac{(\varepsilon + 1)(-\varepsilon + 1)}{N} = \frac{1 - \varepsilon^2}{N} .$$

Therefore, the statistical error in the asymmetry is,

$$\Delta\varepsilon = \sqrt{\frac{1-\varepsilon^2}{L+R}}.$$

(C.1)

C.2   Error in the Calculation of Polarization

The polarization is calculated as

$$P = \left(\frac{L-R}{L+R}\right) \cdot \frac{1}{A} = \frac{\varepsilon}{A} .$$

(C.2)

where A is the analyzing power for the pp elastic event at the IBP target. The error is calculated as follows:

$$\Delta P = \frac{1}{A}\Delta\varepsilon - \frac{\varepsilon}{A^2}\Delta A.$$

$$\Delta^2 P = \frac{1}{A^2}\Delta^2\varepsilon + \frac{\varepsilon^2}{A^4}\Delta^2 A.$$

where the cross term is zero because ε and A are independent of each other.

$$\Delta P = \frac{1}{A}\left[\Delta^2\varepsilon + P^2\Delta^2 A\right]^{\frac{1}{2}} .$$

Now one can write the error in spin up and spin down polarizations separately as

$$\Delta P^+ = \frac{1}{A}\left[\Delta^2\varepsilon^+ + (P^+)^2\Delta^2 A\right]^{\frac{1}{2}} ,$$

(C.3)

$$\Delta P^- = \frac{1}{A}\left[\Delta^2\varepsilon^- + (P^-)^2\Delta^2 A\right]^{\frac{1}{2}} .$$

(C.4)

Here, P^+ and P^- are not independent so that they have a covariance, $cov(P^+P^-)$, which can be calculated from

$$\Delta P^+ \cdot \Delta P^- = \left(\frac{1}{A}\Delta\varepsilon^+ - \frac{\varepsilon^+}{A^2}\Delta A\right) \cdot \left(\frac{1}{A}\Delta\varepsilon^- - \frac{\varepsilon^-}{A^2}\Delta A\right),$$

$$\Delta P^+ \cdot \Delta P^- = \frac{1}{A^2}\Delta\varepsilon^+ \cdot \Delta\varepsilon^- - \frac{1}{A^3}\varepsilon^-\Delta\varepsilon^+ \cdot \Delta A - \frac{1}{A^3}\varepsilon^+\Delta\varepsilon^- \cdot \Delta A + \frac{1}{A^4}\varepsilon^+\varepsilon^-\Delta^2 A.$$

159

Since ε^+, ε^-, and A are independent, their correlations are zero. Therefore, the $P^+ \cdot P^-$ covariance is

$$Cov(P^+P^-) = \frac{1}{A^4}\varepsilon^+\varepsilon^-\Delta^2 A \ . \tag{C.5}$$

where the error in the IBP analyzing power ($\Delta^2 A$) for pp elastic scattering is estimated to have 0.01 [Wa96] which comes from the accuracy of the phase shift analysis.

C.3 Error Calculation for the Cross Section

Let the differential cross sections for spin up and spin down be σ^+ and σ^-. The spin-averaged cross section, σ, is calculated as follows:

$$\sigma^+ = \sigma(1 + P^+A_y\cos\phi),$$

$$\sigma^- = \sigma(1 - P^-A_y\cos\phi),$$

$$P^-\sigma^+ = P^-\sigma + P^+P^-A_y\cos\phi,$$

$$P^+\sigma^- = P^+\sigma - P^+P^-A_y\cos\phi.$$

Here, $\cos\phi = -1$ because SASP accepts particles scattered to the right. Therefore, the total cross section is

$$\sigma = \left(\frac{P^-\sigma^+ + P^+\sigma^-}{P^+ + P^-}\right) \ . \tag{C.6}$$

Here, P^+ and P^- are the magnitudes of spin-up and spin-down polarizations corrected for the instrumental asymmetry by

$$P^+ = (P_m^+ - P_0), \quad P^- = (P_m^- + P_0) \ ,$$

where $P_0 = (1/2)[P_0^+ + P_0^-]$ is the average of the observed spin-up and spin-down polarizations due to the instrumental asymmetry when the beam protons were unpolarized. The sign convention (spin-up is +ve and spin-down is -ve) was taken into account when the measured polarizations were corrected for the instrumental asymmetry. Typically $P_0 \sim 1\%$ whereas the measured polarizations, P_m^+ and P_m^-, were $\sim 75\%$. A typical error in P_m^+ and P_m^- was $\sim 3\%$. The error in the instrumental asymmetry was typically $\sim 0.2\%$, and is assumed to be small in this error calculation.

The error formula for the total cross section is written as

$$\Delta\sigma = \left(\frac{\partial\sigma}{\partial P^-}\right)\Delta P^- + \left(\frac{\partial\sigma}{\partial P^+}\right)\Delta P^+ + \left(\frac{\partial\sigma}{\partial\sigma^-}\right)\Delta\sigma^- + \left(\frac{\partial\sigma}{\partial\sigma^+}\right)\Delta\sigma^+$$

160

$$\Delta\sigma = \left(\frac{P^-}{P^+ + P^-}\right)\Delta\sigma^+ + \left(\frac{P^+}{P^+ + P^-}\right)\Delta\sigma^-$$

$$+ \frac{P^+(\sigma^+ - \sigma^-)}{(P^+ + P^-)^2}\Delta P^- - \frac{P^-(\sigma^+ - \sigma^-)}{(P^+ + P^-)^2}\Delta P^+ \quad (C.7)$$

$$\Delta^2\sigma = \frac{1}{(P^+ + P^-)^2}\left[(P^-)^2\Delta^2\sigma^+ + (P^+)^2\Delta^2\sigma^-\right]$$

$$+ \frac{1}{(P^+ + P^-)^4}\left[(P^+)^2(\sigma^+ - \sigma^-)^2\Delta^2 P^- + (P^-)^2(\sigma^+ - \sigma^-)^2\Delta^2 P^+\right.$$

$$\left. - 2P^+ P^-(\sigma^+ - \sigma^-)^2 cov(P^+ P^-)\right] \quad (C.8)$$

Substitute $cov(P^+ P^-) = \frac{1}{A^4}\epsilon^+\epsilon^-\Delta^2 A$ from eq. (C.5) to get.

$$\Delta^2\sigma = \frac{1}{(P^+ + P^-)^2}\left[(P^-)^2\Delta^2\sigma^+ + (P^+)^2\Delta^2\sigma^-\right]$$

$$+ \frac{1}{(P^+ + P^-)^4}\left[(P^+)^2(\sigma^+ - \sigma^-)^2\Delta^2 P^- + (P^-)^2(\sigma^+ - \sigma^-)^2\Delta^2 P^+\right.$$

$$\left. - \frac{2P^+ P^-\epsilon^+\epsilon^-}{A^4}(\sigma^+ - \sigma^-)^2\Delta^2 A\right] \quad (C.9)$$

Therefore, the statistical error in the differential cross section calculation can be written as

$$\Delta\sigma = \frac{1}{(P^+ + P^-)}\left\{(P^-)^2\Delta^2\sigma^+ + (P^+)^2\Delta^2\sigma^- + \left(\frac{\sigma^+ - \sigma^-}{P^+ + P^-}\right)^2\right.$$

$$\left. \times \left[(P^+)^2\Delta^2 P^- + (P^-)^2\Delta^2 P^+ - \frac{2}{A^2}\left(\frac{P^+ P^-}{A^2}\right)^2\Delta^2 A\right]\right\}^{\frac{1}{2}} \quad (C.10)$$

Here, $\Delta\sigma^+(\Delta\sigma^-)$ is the statistical error of the normalized peak yield from the spin-up(spin-down) spectrum as determined by the peak fitting program.

C.4 Error Calculation for the Analyzing Power

Having determined the error in the cross section calculation, one can calculate the statistical error in the analyzing power as follows. The analyzing power is calculated using

161

the expression,

$$A_y = \left(\frac{\sigma^+ - \sigma^-}{P^-\sigma^+ + P^+\sigma^-} \right) .$$ (C.11)

The error formula is

$$\Delta A_y = \left(\frac{\partial A_y}{\partial \sigma^+} \right) \Delta \sigma^+ + \left(\frac{\partial A_y}{\partial \sigma^-} \right) \Delta \sigma^- + \left(\frac{\partial A_y}{\partial P^+} \right) \Delta P^+ + \left(\frac{\partial A_y}{\partial P^-} \right) \Delta P^-$$

$$\Delta A_y = \left[\frac{(P^+ + P^-)\sigma^-}{(P^-\sigma^+ + P^+\sigma^-)^2} \Delta \sigma^+ - \frac{(P^+ + P^-)\sigma^+}{(P^-\sigma^+ + P^+\sigma^-)^2} \Delta \sigma^- \right.$$

$$\left. - \frac{(\sigma^+ - \sigma^-)\sigma^-}{(P^-\sigma^+ + P^+\sigma^-)^2} \Delta P^+ - \frac{(\sigma^+ - \sigma^-)\sigma^+}{(P^-\sigma^+ + P^+\sigma^-)^2} \Delta P^- \right]$$ (C.12)

$$\Delta A_y = \frac{1}{(P^-\sigma^+ + P^+\sigma^-)^2} \left[(P^+ + P^-)(\sigma^- \Delta \sigma^+ - \sigma^+ \Delta \sigma^-) \right.$$

$$\left. - (\sigma^+ - \sigma^-)(\sigma^- \Delta P^+ + \sigma^+ \Delta P^-) \right]$$ (C.13)

$$\Delta^2 A_y = \frac{1}{(P^-\sigma^+ + P^+\sigma^-)^4} \left[(P^+ + P^-)^2 (\sigma^- \Delta \sigma^+ - \sigma^+ \Delta \sigma^-)^2 + \right.$$

$$\left. (\sigma^+ - \sigma^-)^2 (\sigma^- \Delta P^+ + \sigma^+ \Delta P^-)^2 \right]$$ (C.14)

$$\Delta^2 A_y = \frac{1}{(P^-\sigma^+ + P^+\sigma^-)^4} \left[(P^+ + P^-)^2 \left\{ (\sigma^-)^2 \Delta^2 \sigma^+ + (\sigma^+)^2 \Delta^2 \sigma^- \right\} \right.$$

$$\left. + (\sigma^+ - \sigma^-)^2 \left\{ (\sigma^-)^2 \Delta^2 P^+ + (\sigma^+)^2 (\Delta^2 P^- + 2\sigma^- \sigma^+ cov(P^+ P^-) \right\} \right]$$ (C.15)

$$\Delta^2 A_y = \frac{1}{(P^-\sigma^+ + P^+\sigma^-)^4} \left[(P^+ + P^-)^2 \left\{ (\sigma^-)^2 \Delta^2 \sigma^+ + (\sigma^+)^2 \Delta^2 \sigma^- \right\} \right.$$

$$\left. + (\sigma^+ - \sigma^-)^2 \left\{ (\sigma^-)^2 \Delta^2 P^+ + (\sigma^+)^2 \Delta^2 P^- + \frac{2\sigma^- \sigma^+ P^+ P^-}{A^2} \Delta^2 A \right\} \right],$$ (C.16)

162

where $cov(P^+P^-) = \frac{\epsilon^+\epsilon^-}{A^4}\Delta^2 A = \left(\frac{\epsilon^+}{A} \cdot \frac{\epsilon^-}{A}\right)\frac{\Delta^2 A}{A^2} = \frac{P^+ \cdot P^-}{A^2}\Delta^2 A$ has been substituted from eq. (C.5). Therefore, the statistical error in the analyzing power calculation is determined as

$$\Delta A_y = \left(\frac{1}{P^-\sigma^+ + P^+\sigma^-}\right)^2 \left\{ (P^+ + P^-)^2 \left[(\sigma^-)^2\Delta^2\sigma^+ + (\sigma^+)^2\Delta^2\sigma^-\right] \right.$$

$$\left. + (\sigma^+ - \sigma^-)^2 \left[(\sigma^-)^2\Delta^2 P^+ + (\sigma^+)^2\Delta^2 P^- + \frac{2\sigma^+\sigma^- P^+ P^-}{A^2}\Delta^2 A\right] \right\}^{\frac{1}{2}}. \quad \text{(C.17)}$$

Bibliography

[Aj91] F. Ajzenberg-Selove. Nucl. Phys. **A 523** (1991).

[Al67] G. Alexander et al., Phys. Rev. **154**. 1284 (1967).

[Al88] P. W. F. Alons et al.. Nucl. Phys. **A480**. 413 (1988).

[Ar95] R. A. Arndt, "http://clsaid.phys.vt.edu/ CAPS" (1995).

[Ar96] R. A. Arndt and D. Roper. VPI and SU Scattering Analysis Interactive Dial-in Program and Data Base.

[Au78] E. G. Auld et al.. Phys. Rev. Lett. **41**. 462 (1978).

[Be82] Proceedings of the Conference on Pion Production and Absorption in Nuclei, edited by R. D. Bent. AIP Conf. Proc. No. 79 (AIP, New York. 1982).

[Be92] R. D. Bent et al.. Nucl. Phys. **A548**. 637 (1992).

[Be96] M. J. Benjamintz, M. Sc. Thesis, University of Manitoba, Canada (1996).

[Br83] B. A. Brown et al., Phys. Rev. Lett. **51**. 1952 (1983).

[Br75] G. E. Brown and W. Weise, Phys. Reports **22** 279 (1975).

[Br83] G. E. Brown et al. . Nucl. Phys. **A397**, 447 (1983).

[Co72] S. D. Conte and Carl de Boor, Elementary Numerical Analysis: An Algorithmic Approach, New York. McGraw-Hill (1972).

[Co85] P. Couvert and M. Dilling. Phys. Rev. **C32**, 352 (1985).

[Cr77] M. K. Craddock, K. L. Erdman and J. T. Sample, Nature **270**, 671 (1977).

[Da71] S. Dahlgren, B. Hoistad, and P. Grafstrom, Phys. Lett. **35B**, 219 (1971).

164

[De79] D. Dehnhard et al., Phys. Rev. Lett. **43**. 1091 (1979).

[Du51] R. Durbin, H. Loar. J. Steinberger, Phys. Rev. **83**, 646 (1951).

[Du96] F. Duncan et al. to be published.

[En90] P. M. Endt. Nucl. Phys. **A521** 1 (1990).

[Fa85] W. R. Falk et al., Phys. Rev. **C32**, 1972 (1985).

[Fa94] W. R. Falk, Phys. Rev. **C50**, 1574 (1994).

[Fa96] Private Communication. Prof. W. R. Falk. University of Manitoba. Canada (1996).

[Fe81] H. W. Fearing. Prog. Part. Nucl. Phys. **7**. 113 (1981); B. Hoistad. Adv. Nucl. Phys. **11**, 35 (1979); D. F. Measday and G. A. Miller. Annu. Rev. Nucl. Sci. **29**, 121 (1979).

[Fo78] H. T. Fortune et al., Phys. Rev. Lett. **40**. 1236 (1978)

[Go64] M. L. Goldberger and K. M. Watson. Collison Theory. J. Wiley & Sons. Inc. New York (1964).

[Gr84] M. C. Green et al., Phys. Rev. Lett. **53**. 1893 (1984).

[Gr95] P. W. Green. Introduction to The NOVA Data Analysis System, University of Alberta (1995).

[Ha60] D. Harting et al., Phys. Rev. **119**. 1716 (1960).

[Ha74] P. Haapakoski, Phys. Lett. **48B**. 307 (1974).

[Ha95] Matthias Hartig. Institut fur Kernphysik. Universitat Munster, Germany (1995).

[Ho81] K. Holinde. Phys. Reports **68**. 121 (1981).

[Hu88] G. M. Huber et al., Phys. Rev. **C37**, 1161 (1988).

[Hu87] G. M. Huber et al., Phys. Rev. **C36**, 2683 (1987).

[Hu88] G. M. Huber et al., Phys. Rev. **C38**, 1304 (1988).

[Hu88] G. M. Huber, Ph. D. Thesis, University of Regina, Canada (1988).

[Iq85] M. J. Iqbal and G. E. Walker, Phys. Rev. **C32**, 556 (1985).

[Ja82] W. W. Jacobs et al., Phys. Rev. Lett. **49**, 855 (1982).

[Jo77] G. Jones, *Nucleon − Nucleon Interactions − −1977*, AIP conference Proceedings No. 41, edited by D. Measday, H. W. Fearing, and A. Strathdee, (American Institute of Physics, New York, 1978), p. 292.

[Jo84] G. Jones, Nucl. Phys. **A416**, 157c (1984).

[Ko87] E. Korkmaz et al., Phys. Rev. Lett. **58**, 104 (1987).

[Ko89] E. Korkmaz et al., Phys. Rev. **C40**, 813 (1989).

[Ko91] E. Korkmaz, TRIUMF E635 Experiment Proposal (1991).

[Ku89] K. Kume, Nucl. Phys. **A504**, 712 (1989).

[Lo84] G. J. Lolos et al., Phys. Rev. **C25**, 574 (1984).

[Ma96] M. J. Martin, J. K. Tuli, Nuclear Data Sheets, Volume **77**, Number 1, January 1996.

[Pa51] W. K. F. Panofsky et al., Phys. Rev. **81**, 565 (1951).

[Pi86] E. Piasetzky et al., Phys. Rev. Lett. **57**, 2135 (1986).

[Pu92] M. A. Punyasena, P. Walden and S. Yen, Hall Probe Calibration for Beam Line 4B and the MRS Spectrometer, *TRIUMF Internal Report*, TRI-DN-93-3 (1993).

[Pu93] M. A. Punyasena, M. Sc. Thesis, University of Alberta, Canada (1993).

[Pu94] M. A. Punyasena, S. Yen, M. Hartig and you Ke, Empirical Determination of the Focal Surface and First Order Transfer Matrix Elements of the SASP,*TRIUMF Internal Report* (1994).

[Re85] R. P. Redwine, Nucl. Phys. **A434**, 239c (1985), and references therein.

[Sc86] O. Scholten and H. Toki, Phys. Rev. **C34**, 601 (1986).

[Su68] H. Sugawara and F. von Hippel, Phys. Rev. **172**, 1764 (1968).

[Th83] T. G. Throwe et al., Bull Am. Phys. Soc. **28**, 672 (1983).

[Th87] T. G. Throwe et al., Phys. Rev. **C35**, 1083 (1987).

[To85] H. Toki and K. I. Kubo, Phys. Rev. Lett. **54**, 1203 (1985).

[Wa95] P. L. Walden, "http://www.triumf.ca/dass/homepage.html", DASS Home Page, Electronics Diagrams (1995).

[Wa96] P. L. Walden *et al.*. TRIUMF Internal Report 'New IBP Polarimeter Calibration Report', (1996).

[Wa96] Private Communication. Dr. Patrick. L. Walden. TRIUMF, Vancover, Canada (1996).

[Ve82] B. J. Verwest and R. A. Arndt. Phys. Rev. **C 25**. 1979 (1982).

[Vi82] S. E. Vigdor *et al.*. Phys. Rev. Lett. **49**. 1314 (1982), and Nucl. Phys. **A396**, 61c (1983).

[Vi87] S. E. Vigdor. W. W. Jacobs and E. Korkmaz. *et al.*,Phys. Rev. Lett. **58**, 840 (1987).

[We77] W. Weise. Nucl. Phys. **A278**. 402 (1977).

[Ye80] S. Yen. M.Sc. Thesis. University of Toronto (1980).